



GEORG-AUGUST-UNIVERSITÄT
GÖTTINGEN

Improving the analysis of aeroacoustic measurements
through machine learning

Dissertation

for the award of the degree
“Doctor rerum naturalium” (Dr. rer. nat.)
of the Georg-August-Universität Göttingen

within the doctoral program in Computer Science (PCS)
of the Georg-August University School of Science (GAUSS)

submitted by
Armin Goudarzi
from Berlin, Germany

Göttingen, 2023

Thesis Committee

Prof. Dr. rer. nat. Steffen Herbold
University of Passau
Faculty of informatics and mathematics

Prof. Dr. rer. nat. Alexander Ecker
Georg August University of Göttingen
Institute of Computer Science

Dr. ing. Carsten Spehr
German Aerospace Center
Institute of Aerodynamics and Flow Technology

Members of the Examination Board

First Reviewer

Prof. Dr. rer. nat. Steffen Herbold
University of Passau
Faculty of Informatics and Mathematics

Second Reviewer

Prof. Dr. rer. nat. Alexander Ecker
Georg August University of Göttingen
Institute of Computer Science

Further members of the Examination Board

Dr. ing. Carsten Spehr
German Aerospace Center
Institute of Aerodynamics and Flow Technology

Prof. Dr. rer. nat. Fabian Sinz
Georg August University of Göttingen
Institute of Computer Science

Prof. Dr. ing. Marcus Baum
Georg August University of Göttingen
Institute of Computer Science

Prof. Dr. rer. nat. Andreas Schröder
German Aerospace Center
Institute of Aerodynamics and Flow Technology,
and Brandenburg University of Technology
Institute of Transport Technology

Date of the oral examination: 06.11.2023

Contents

Nomenclature	V
Abstract	VII
1 Introduction	1
1.1 Research hypothesis	3
1.2 Outline	3
1.3 Impact	3
1.4 Acknowledgments	4
2 Theory	7
2.1 Aeroacoustics	7
2.1.1 Sound generation mechanisms	7
2.1.2 Similarity laws	10
2.1.3 Source definition	12
2.1.4 Compact, free-field Green's function	13
2.1.5 Cross spectral matrix	14
2.1.6 Distributed sources and source coherence	14
2.1.7 Propagation forward operator	17
2.2 Artificial neuronal networks	18
2.3 Clustering	19
3 Experimental data	23
3.1 Streamlined speaker, open test section	23
3.2 Dornier 728, closed test section	25
3.3 Airbus 320, closed test section	27
3.4 Embraer, closed test section	28
4 Beamforming	29
4.1 Steering vectors	30
4.2 Conventional beamforming	33
4.3 CLEAN-SC	36
4.4 B-CLEAN-SC	39
4.4.1 Methodology	40
4.4.2 CLEAN-SC and B-CLEAN-SC Results	42
4.5 Global Optimization	46
4.5.1 Methodology	47
4.5.2 Results	52
4.6 Grid-based supervised learning beamforming	60
4.6.1 Synthetic measurement setup	60
4.6.2 Metrics	61
4.6.3 ANN architectures	62
4.6.4 Results	65
4.7 Permutation invariant, gridless ANN beamforming	66
4.7.1 Architecture	67
4.7.2 Evaluation metrics	69
4.7.3 Cases and setup	70
4.7.4 Results	71
5 Regions Of Interest	77
5.1 Manual ROI definition	78
5.2 Source identification results	80
5.2.1 Source Identification based on spatial Normal Distributions (SIND)	82

5.2.2	Source Identification based on Hierarchical Clustering (SIHC)	89
5.2.3	Comparison of SIND and SIHC	90
5.2.4	SIND 3D	93
5.3	Method errors	97
6	Expert Decision Support System	101
6.1	Quasi-stationary, self-similar sources	102
6.2	Manual source identification	103
6.3	Source identification results	106
6.3.1	Do728	107
6.3.2	A320	107
6.3.3	Embraer model	110
6.4	Feature engineering	111
6.5	Feature results	119
6.6	Source-type clustering	124
6.6.1	Methodology	124
6.6.2	Results	125
7	Discussion	131
7.1	Beamforming	131
7.1.1	Conventional beamforming	131
7.1.2	CLEAN-SC and B-CLEAN-SC	132
7.1.3	Global Optimization	133
7.1.4	Grid-based ANN beamforming	134
7.1.5	Gridless ANN beamforming	135
7.2	Regions Of Interest	136
7.2.1	SIND	136
7.2.2	SIHC	137
7.2.3	Comparison of both methods	138
7.3	Expert Decision Support System	140
7.3.1	Manual classification	140
7.3.2	Aeroacoustic features	140
7.3.3	Clustering	143
7.4	Aeroacoustics	144
8	Summary	147
8.1	Beamforming	147
8.1.1	Conventional beamforming	147
8.1.2	CLEAN-SC	147
8.1.3	B-CLEAN-SC	148
8.1.4	Global Optimization	148
8.1.5	Supervised learning beamforming	149
8.2	Regions Of Interest	149
8.3	Expert Decision Support System	150
8.4	Aeroacoustics	151
8.5	Thesis conclusion	152
	Bibliography	i
	List of Figures	xi
	List of Tables	xiii
	Alphabetical Index	xiv

Nomenclature

Abbreviations

AE	Auto Encoder
ANN	Artificial Neuronal Network
BSS	Blind Source Separation
CFM	Covariance matrix Fitting Method
CL	Convolutional Layer
CLEAN-SC	CLEAN based on Source Coherence
CSM	Cross Spectral Matrix
CRAFT	Clustering sources based on Aeroacoustic Features
FC	Fully Connected
FP	False Positive
FSE	Flap Side Edge
FW-H	Ffowcs Williams and Hawkings
GMM	Gaussian Mixture Models
GO	Global Optimization
HDBSCAN	Hierarchical Density-Based Spatial Clustering of Applications with Noise
HL	Hidden Layers
LO	Local Optimization
MAE	Mean Absolute Error
MSE	Mean Squared Error
NPL	Neurons Per Layer
NR	Nacelle Region
NSR	Noise to Signal Ratio
OASPL	Overall Sound Pressure Level
OPTICS	Ordering points to identify the clustering structure
PDF	Probability Density Function
PSD	Power Spectral Density
PSF	Point Spread Function
RE	Reconstruction Error
ReLU	Rectified Linear Unit
ROI	Region Of Interest
SIHC	Source Identification based on Hierarchical Clustering
SIND	Source Identification based on spatial Normal Distribution
SNR	Signal to Noise Ratio
SSD	Source Strength Deviation
SSR	Signal to Signal Ratio
SPL	Sound Pressure Level
UMAP	Uniform Manifold Approximation and Projection for Dimension Reduction
VUT	Vectorized Upper Triagonal
WLR	Wing Leading Region
WTR	Wing Trailing Region

Mathematical Symbols

$\overline{(\cdot)}$ average

$(\cdot)^\dagger$	Hermetian transpose
$\langle \cdot \rangle$	averaged quantity
δ	Kroncker delta
Δ	delta or Laplace operator
∇	Nabla operator
\square	d'Alembert operator
\odot	Khatri-Rao product
\otimes	Hadamard product
$\#$	number of elements / cardinality

Variables

variable	unit	description
κ		power scaling weight
μ	Pa s	dynamic viscosity
ρ	kg m ⁻³	density
σ		standard deviation
$\mathcal{F}, \mathcal{G}, \mathcal{H}$		generic functions
a	m s ⁻¹	speed of sound
b		conventional beamforming source map
\mathbf{C}	Pa ² Hz ⁻¹	cross-spectral matrix
D	m	characteristic length
f	s ⁻¹	frequency
\hat{f}		generalized frequency
\mathbf{g}		Green's function
\mathbf{h}		steering vector
He		Helmholtz number
I	W m ⁻²	acoustic intensity
j		imaginary unit
k	m ⁻¹	wave number
m		frequency modification exponent
M		Mach number
\mathbf{M}		Mach number vector $M = \mathbf{M} $
M		number of microphones
n		power scaling exponent
N		number of sources or focus points
p	Pa	pressure fluctuations / complex pressure
p_a	Pa	ambient pressure
q	Pa ²	sound power
Re		Reynolds number
St		Strouhal number
SPL	dB	sound power level
$\widehat{\text{SPL}}$	dB	scaled sound power level
τ	Pa	shear stress
\mathbf{u}	m s ⁻¹	flow velocity vector $u = \mathbf{u} $
u	m s ⁻¹	flow velocity
w		weighting function
x_1, x_2, x_3	m	spatial coordinates
x, y, z	m	spatial coordinates
\mathbf{x}, \mathbf{y}	m	spatial coordinate vectors

Abstract

This thesis focuses on improving the analysis of aeroacoustic imaging methods using automated data processing and machine learning. Imaging methods result in beamforming maps that are challenging to explore manually since they comprise complex, high-dimensional data, including spatial coordinates, frequency, and flow properties. The manual, iterative analysis is time-consuming, biased, and typically based on 2D beamforming maps that only insufficiently capture the complex source distribution of airframe sources. Further, acoustic array imaging methods often assume monopole sources and, thus, suffer from mismatches between model assumptions and actual sources.

This thesis addresses these issues by proposing novel broadband beamforming methods based on the observation that most airframe noise sources are spatially compact and parameters such as their location do not change over frequency. A broadband approach improves the ratio of known to unknowns in the mathematical formulation of the problem, which allows for the inclusion of advanced model assumptions, such as dipoles and distributed sources. The resulting novel methods are broadband Global Optimization, a gridless covariance matrix fitting method, Broadband-CLEAN-SC, an adaptation of CLEAN based on Source Coherence (CLEAN-SC), and gridless beamforming using artificial neuronal networks with a permutation invariant loss. All proposed methods share that a beamforming solution is obtained for multiple frequencies simultaneously. The broadband approach improves the resolution at low frequencies. It suppresses side- and grating lobes (aliasing), improves the identification and spectra extraction from the results, and outperforms the corresponding small-band methods.

This thesis proposes two clustering methods that identify sources in the high-dimensional beamforming maps and extract their spectra to post-process the industrial gold standard conventional beamforming and CLEAN-SC methods. The proposed “Source Identification based on Spatial Normal Distribution” (SIND) method is a clustering algorithm similar to a Gaussian Mixture Model. It is tailored to the source identification problem, with spatial discretization, a large number of estimated sources, and statistical noise as its main challenges. To determine the number of clusters, SIND does not rely on a priori hyper-parameters but determines the unknown number of sources iteratively from the spatial distribution of the data. The proposed “Source Identification based on Hierarchical Clustering” (SIHC) method clusters the data directly in space and frequency using the established Hierarchical Density-Based Spatial Clustering of Applications with Noise (HDBSCAN) algorithm. The introduced automatic source identification capabilities allow the precise source identification and spectra extraction of 3D beamforming maps with no added effort, compared to the standard manual process, typically based on planar 2D beamforming maps with insufficient spatial resolution.

This thesis provides an overview and insight into the aeroacoustic theory and introduces numerical features that explicitly formulate physical properties, enabling the deduction of aeroacoustic source mechanisms. The proposed formulas are robust towards noisy and degenerate spectra typically resulting from deconvolution methods such as CLEAN-SC. They are independent of the measured object, the amount of measured Mach numbers, and the Mach numbers themselves. Thus, they offer a comparability of the properties across different measurements, which was previously impossible. Sources

can be visualized utilizing their high-dimensional feature space through dimensional-reduction methods and effectively clustered with HDBSCAN, offering a manual classification and interpretation guideline. This process facilitates the creation of an Expert Decision Support System (EDSS). The clusters proposed by the EDSS strongly correlate with the manually determined categories so that the expert can interpret them. Clustering results from industrial wind tunnel experiments on a Dornier 728 and Airbus 320 models are presented. The clustering accuracy, determined from a confusion matrix and a manual selection of its correct entries, is 77.04 % for the Dornier 728 and 61.52 % for the Airbus 320 experiment.

The thesis presents a detailed aeroacoustic analysis and manual classification of all occurring airframe sources. Novel aeroacoustic observations are described, such as that the flap side edge and strake are composed of two sources each with different mechanisms and that many sources depend on the Mach number weaker than the one of a true Strouhal number. Also, some sources, such as the strake and cavity noise, show a Mach number dependency, even at a constant Reynolds number, while most sources are self-similar within a large Reynolds number range.

In summary, this thesis presents an improved workflow for beamforming, post-processing, interpretation, and knowledge generation from aeroacoustic experiments. The proposed EDSS enables a complete aeroacoustic analysis of wind tunnel experiments, offering detailed insights into the nature of the sources. Further, the EDSS has proven its capabilities to be employed in situ to detect and fix spurious noise sources during experiments, offering new perspectives and a practical tool for researchers and practitioners in the field.

1 Introduction

Severe acoustic emissions and their associated health issues have been a persistent challenge since the beginning of industrialization. In 2011, the WHO estimated up to 1.6 million disability-adjusted life years in the EU alone due to environmental noise pollution, with traffic noise being the main burden [42] due to sleep disturbance-induced cardiovascular disease [100]. Consequently, social and governmental pressure is increasing to reduce sound emission levels. Although advancements in new technologies, such as the electrification of the transportation sector, hold promise for reducing traffic noise pollution, other scenarios, such as landing aircraft, continue to be dominated by aeroacoustic noise sources. These sources become even more significant once the currently dominating propulsion noise is reduced.

The assessment of aeroacoustic noise often relies on wind tunnel facilities, where microphone array technology, particularly beamforming, has proven to be a reliable method [87]. Beamforming, a correlation-based imaging technique, estimates the spatial sound power distribution by steering microphone cross-powers to different locations based on specific source assumptions, like a spatially compact, incoherent monopole. This assumption implies that the sound radiation originates from a point-like source and radiates its energy uniformly in all directions into the observed far-field. However, this established approach faces several challenges.

The main challenges are that the assumptions of beamforming often do not align with the actual nature of aeroacoustic noise, which typically involves dipole and quadrupole sources [40] that are not spatially compact and incoherent. Additionally, the resolution of beamforming depends on the wavelength. It deteriorates at low and high frequencies due to the Rayleigh limit and sensor spacing, resulting in aliasing and noisy beamforming maps. This poses challenges in manually identifying sources in the noisy maps. The beamforming maps are integrated within spatial regions into spectra to reduce visual complexity so that the estimated sound power depends solely on the frequency. However, the manual and biased process of defining integration regions for analysis can hinder the accurate deduction of properties of individual sources within these regions. Furthermore, the labor-intensive and expert-dependent analysis of integration areas and the resulting spectra leads to potential errors and biases in interpreting aeroacoustic properties and source mechanisms.

In detail, an expert has performed the time-consuming process of defining integration regions manually for decades and depends on implicit knowledge, experience, intuition, and the model geometry. It requires several iterations since one has to analyze the resulting spectra to determine if the integration regions are well chosen. This makes the process biased towards the expert's expectations and prone to errors, which contradicts the fundamental idea of beamforming – to measure the spatial sound distribution without assuming it a priori. Due to the precision limitation of this manual definition and the subsequent time-consuming analysis, large integration regions are often defined for 2D beamforming maps, encompassing regions like the whole slat, flap, and nacelle, without obtaining and analyzing spectra for all individual sources [4, 7]. This approach proves insufficient as such large regions usually contain multiple sources with different mechanisms, like the flap side edge, composed

of two different source mechanisms, making the deduction of their individual properties difficult.

The aeroacoustic analysis based on spectra has been performed manually and is susceptible to the same bias as the integration region definition. The noisy spectra and the limited range of measured Mach numbers strongly influence important scaling variables such as the source's power scaling or the determination of self-similarity over the Strouhal and Helmholtz number. Furthermore, the analysis relies on the expert's aeroacoustic background, experience, and knowledge of historical measurements. Often, properties are only implicitly assessed, such as tonal components, due to the lack of rigorous mathematical definitions. Consequently, comparing results obtained by different scientists becomes difficult. The manual spectra analysis process typically involves identifying the exact source location within the integration region when detecting interesting or atypical behavior in a spectrum, determining its nature, and connecting it to a geometric property (e.g., a slat track or a cavity). The source type and mechanism are then deduced based on manual spectrum analysis, attributing interesting observations to the identified source location. This knowledge generation process is extremely time-consuming, scaling linearly with the number of analyzed measurements and integration regions.

This thesis introduces novel methods to improve the analysis of beamforming results in aeroacoustic wind tunnel testing. It addresses the challenges above by introducing beamforming methods and automising the post-processing, thereby enhancing knowledge generation. In detail, the thesis introduces the gridless broadband Global Optimization method, which, in contrast to the established covariance fitting method "Global Optimization", improves reliability and resolution by obtaining a solution for all frequencies simultaneously and not sequentially. The thesis introduces B-CLEAN-SC, an improved broadband adaptation of the CLEAN-SC algorithm, which outperforms CLEAN-SC in resolution and noise. Additionally, beamforming methods are advanced using supervised machine learning, where an Artificial Neuronal Network (ANN) is trained with synthetic data. This problem is similar to inverse beamforming, as the ANN learns the inverse of the acoustic propagation operator to predict the source distribution. This approach is an ill-posed problem for grid-based methods, thus a permutation invariant loss function for a gridless ANN architecture is proposed.

This thesis proposes using two unsupervised learning methods to automatically extract individual sources from sound maps without a priori knowledge. Sources appear normally distributed in sparse beamforming maps, enabling identification by clustering. The thesis introduces the meta-clustering method "Source Identification based on spatial Normal Distribution" (SIND), specifically designed for deconvolved beamforming maps and iteratively fits normal distributions to a histogram of the spatial data distribution. Alternatively, the established algorithm Hierarchical Density-Based Spatial Clustering of Applications with Noise can cluster the source maps so that the resulting clusters are good approximations of sources.

Further, this thesis introduces the explicit and machine-readable formulation of several acoustic properties via feature engineering, visualization of aeroacoustic properties via dimensionality reduction, and clustering source types based on their aeroacoustic properties, forming an Expert Decision Support System. This system allows for a detailed and automated evaluation of aeroacoustic testing campaigns within minutes, reducing high-dimensional data to low-dimensional metadata that can

be compared to previous experiments by both the aeroacoustic expert and the machine. This thesis presents results from previously presented experiments, which have never been fully analyzed in full scope due to the aforementioned time consumption.

In the future, this enables researchers to improve, compare, and track the acoustic performance of their designs in the transport sector.

1.1 Research hypothesis

This thesis examines how machine learning techniques can be employed in aeroacoustic wind tunnel testing to find, identify, and analyze aeroacoustic source types and their physical properties. The main challenges are that data is often confidential, no ground truth exists, and many physical sound generation mechanisms are still up for debate. Also, the results must be usable in a scientific environment and, thus, cannot be „black-box“ results. The hypothesis is that machine learning methods can estimate the existence and type of aeroacoustic sources based on mathematically modeled data. Further, source types are assumed to be uniquely distinguishable based on their aeroacoustic properties. Thus, the hypothesis is that physically driven feature engineering allows the clustering of acoustic source types and enables a physical interpretation and knowledge generation through average cluster features. These help experts identify, classify, and quantify interesting sources and their properties.

1.2 Outline

The thesis is structured as follows. Chapter 2 presents the aeroacoustic theory and machine learning foundations on which the proposed methods are based. Chapter 3 presents wind tunnel experiments used to develop and test the methods. Chapter 4 presents established beamforming techniques and introduces new beamforming methods. Chapter 5 presents the definition of spatial integration regions, called Regions Of Interest, and discusses how acoustic spectra are obtained from beamforming maps. Chapter 6 presents aeroacoustic properties and corresponding machine-readable features used to cluster the identified acoustic sources. Chapter 7 presents the discussion of the presented results, and Chapter 8 presents a summary of the main findings.

1.3 Impact

This thesis is based on the original research in chronological order:

- A. Goudarzi, C. Spehr, S. Herbold. “Expert Decision Support System for Aeroacoustic Classification from Deconvolved Beamforming Maps”. AIAA Aviation, 2020 [46],
- A. Goudarzi, C. Spehr, S. Herbold. “Automatic source localization and spectra generation from deconvolved beamforming maps”. Journal of the aeroacoustic Society of America, 2021 [47], featured in the Council of European Aerospace Societies Aeroacoustics Specialists Committee’s (CEAS) 2020/21 aeroacoustic highlights report [94],

- A. Goudarzi, C. Spehr, S. Herbold. “Expert Decision Support System for aeroacoustic source type identification using clustering”. Journal of the aeroacoustic Society of America, 2022 [48], featured in the CEAS 2022 aeroacoustic highlights report [110],
- A. Goudarzi. “Frequency domain beamforming using neuronal networks”. Berlin Beamforming Conference, 2022 [51],
- T. Ahlefeldt, D. Ernst, A. Goudarzi, H. G. Raumer, C. Spehr. “Aeroacoustic testing on a full aircraft model at high Reynolds numbers in the European Transonic Windtunnel”. Journal of Sound and Vibration, 2023 [8],
- A. Goudarzi. “Global, and Local Optimization Beamforming for Acoustic Broadband Sources”, ArXiv preprint, 2023 [53],
- A. Goudarzi. “B-CLEAN-SC: CLEAN-SC for broadband sources”. JASA Express Letters, 2023 [52].

1.4 Acknowledgments

First and foremost, I would like to express my deepest appreciation to Dr. Carsten Spehr, my supervisor and mentor during the dissertation. He contributed support, guidance, and ideas and was available for fruitful discussions at any time. He encouraged me throughout the process to explore and investigate the nature of aeroacoustics and beamforming algorithms. Carsten’s ideas and inputs played a crucial role in shaping the direction of this thesis.

I deeply appreciate the excellent support and mentoring provided by Prof. Dr. Steffen Herbold in data science and unsupervised machine learning-related topics. Steffen’s guidance and expertise significantly contributed to the development and application of advanced techniques in clustering and source detection.

I would also like to express my gratitude to Prof. Dr. Alexander Ecker for his support in supervised learning machine learning. Alexander’s contributions and insights in this area were instrumental in refining the machine learning beamforming methodologies developed in this thesis.

I am deeply indebted to Dr. Daniel Ernst for his insightful discussions on steering vectors and his invaluable mathematical assistance throughout this research. Daniel’s guidance greatly contributed to the accuracy of the thesis.

A special word of appreciation is due to Dr. Hans-Georg Raumer for his remarkable mathematical expertise. Hans-Georg’s invaluable support significantly enhanced the quality and rigor of the mathematical work.

I sincerely thank Dr. Thomas Ahlefeldt for generously sharing his extensive knowledge of aeroacoustics, which was instrumental in designing the aeroacoustic features. Furthermore, Thomas’s provision of well-documented, state-of-the-art datasets was immensely valuable and greatly facilitated the research.

I would like to thank Florian Phillip for his exceptional assistance with the software and his tireless efforts in accelerating the code. Florian's expertise and dedication were instrumental in efficiently implementing features in the SAGAS beamforming software and parts of my machine learning code.

I want to thank all the anonymous reviewers who helped improve the published research. They helped with detailed comments and suggestions to improve the clarity and quality of the publications.

Last, I want to express my deepest appreciation and heartfelt acknowledgment to my wife Ann-Kathrin Goudarzi for her immeasurable contributions throughout the completion of this thesis. My wife's love and unwavering support were the pillars upon which this thesis was built. Without her, this journey would have been impossible.

I am truly thankful to all these individuals for their unconditional support, expertise, and collaboration. Their contributions have significantly impacted the outcome of this research, and I am immensely grateful for their assistance throughout this journey.

2 Theory

This chapter presents the theory necessary to follow the concepts and methods introduced in this thesis. Section 2.1 presents aeroacoustic theory, Section 2.2 presents a brief overview of supervised learning, and Section 2.3 provides an overview of different clustering methods. Beamforming will be discussed in detail in the following Chapter 4.

Variables will be denoted in italic (v), vectors in bold (\mathbf{v}), matrices in capitalized bold letters (\mathbf{V}). Due to the computational orientation of this thesis, italic indices and Einstein summation notation is used to indicate the dimensionality of the variables. Thus, an I -dimensional vector \mathbf{v} will be denoted with v_i , with $i = 1, \dots, I$. The averaging of a variable \mathbf{v} over its i -th dimension is denoted with $\langle v_i \rangle_i$

$$\langle v_i \rangle_i = \frac{\sum_{i=1}^I v_i}{I}, \quad (2.0.1)$$

and the corresponding standard deviation $\sigma_i(v_i)$ with

$$\sigma_i(v_i) = \sqrt{\frac{\sum_{i=1}^I (v_i - \langle v_i \rangle_i)^2}{I}}. \quad (2.0.2)$$

The imaginary unit is displayed with “j”.

2.1 Aeroacoustics

This section is based on original work [8, 46, 47, 48, 50, 51, 53] and presents the in aeroacoustics. This section provides an overview about aeroacoustics, sound generation mechanisms, and source modeling in the frequency domain. An overview of how to generate compact and distributed sources, and monopole and dipole sources is provided. The existence of N sources, located at the position $\mathbf{y}_n \in \mathcal{R}^3$ for $n = 1, \dots, N$ are assumed. The microphone positions are denoted by $\mathbf{x}_m \in \mathcal{R}^3$ for $m = 1, \dots, M$, observer positions are denoted with \mathbf{x} .

2.1.1 Sound generation mechanisms

This subsection is based on the lectures of Delfs [30] and will outline the theory necessary to understand the various mechanisms that drive aeroacoustic sound generation, such as the wave equation and acoustic analogies. In acoustics, the pressure p is the main variable of interest, which consists of a fluctuating part in a medium with an ambient pressure p_a . In this thesis, p describes the fluctuating part of the complex pressure in the frequency domain. The propagation of a disturbance with the speed a in a medium is described by the wave equation \square , where \square is the d'Alembert operator in Minkowski space and $\Delta = \nabla^2$ is the Laplacian and the ∇ is the Nabla operator

$$\square = \frac{1}{a^2} \frac{\partial^2}{\partial t^2} - \Delta. \quad (2.1.1)$$

The inhomogeneous pressure wave equation is

$$\square p = -Q \quad (2.1.2)$$

with the arbitrary source term Q , which yields the Helmholtz equation in the frequency domain

$$-k^2 p - \Delta p = -Q, \quad (2.1.3)$$

where the k is the wavenumber $k = 2\pi f/a$, f is the frequency. The corresponding convective Helmholtz equation for a uniform medium at flow is

$$-(k - \mathbf{jM}\nabla)^2 p - \Delta p = -Q, \quad (2.1.4)$$

where $\mathbf{M} = \mathbf{u}/a$ is the Mach number (non-dimensional flow velocity) for the medium speed $\mathbf{u} \in \mathcal{R}^3$.

To study how sound is generated in a medium one can derive Lighthill's wave equation [79, 80] from the Navier Stokes equations, assuming that only normal and shear stresses work on the medium, other forces such as gravity are abandoned. For Newtonian fluids the shear stresses can be expressed with the viscosity μ

$$\tau_{ij} = \mu \left(\frac{\partial u_i}{\partial x_j} + \frac{\partial u_j}{\partial x_i} \right). \quad (2.1.5)$$

This yields the Lighthill pressure wave equation

$$\square p = \frac{1}{a^2} \frac{\partial^2}{\partial x_i \partial x_j} (\rho u_i u_j - \tau_{ij}) + \frac{\partial^2}{\partial t^2} \left(\frac{p}{a^2} - \rho \right), \quad (2.1.6)$$

with

$$T_{ij} = (\rho + \rho_a) u_i u_j - \tau_{ij} + \delta_{ij} (p - a^2 \rho). \quad (2.1.7)$$

The far-field approximation solution is

$$\rho = -\frac{k^2}{4\pi a^2} \int_{V_Q} \mathbf{e}_{r_0} (\mathbf{T} \mathbf{e}_{r_0}) \exp(-\mathbf{j}kr) dV_Q, \quad (2.1.8)$$

where \mathbf{e}_{r_0} is the unit vector in the direction of the observer, so that it describes the projection of the source terms in the according direction.

No simplifications (except for the absence of gravitational forces) have been made. The equation is typically not used to calculate sound propagation since the pressure and density field have to be known beforehand. However, this equation allows the calculation of any kind of sound generation in fluids based on the inhomogeneous part of the equation. Thus, the right-hand part of the equation can be interpreted as sound-generating mechanisms in a flow. There are three main components on the source term: The Reynolds stresses ($\rho u_i u_j$), the shear stresses (τ_{ij}), and the nonlinear relationship between pressure and density ($p - a^2 \rho$). One can argue that for high Reynolds numbers, the changes in viscous friction stresses can be neglected, and for isentropic flows, the third term can be neglected so that the dominating term in flows is typically caused by the Reynolds stress tensor, which often originates from vortex interactions in turbulent flows. The two derivatives of the Tensor

indicate that it is a quadrupole source.

Similarly to the Lighthill equation, the Ffowcs-Williams and Hawkings (FW-H) equation can be derived for objects in flows, which describes the sound generation as a boundary integral instead of an integral over the whole domain. The far-field approximation is

$$p(\mathbf{x}, t) = \frac{1}{4\pi a^2 r_0} \frac{\partial^2}{\partial t^2} \int_{V_B^+} \frac{\mathbf{T} \mathbf{e}_{r_0}}{|1 - M_r|} dV(\eta) + \frac{1}{4\pi a r_0} \frac{\partial}{\partial t} \int_{V_B} \frac{\mathbf{e}_{r_0} (p' \mathbf{I} - \tau) \mathbf{n}}{|1 - M_r|} dS(\eta) + \frac{1}{4\pi r_0} \frac{\partial}{\partial t} \int_{V_B} \frac{\rho_\infty \mathbf{u} \mathbf{n}}{|1 - M_r|} dS(\eta), \quad (2.1.9)$$

with the isentropic pressure-density relation

$$p = a^2 \rho. \quad (2.1.10)$$

Here, $\mathbf{u} \mathbf{n}$ is the velocity normal to the rigid object surface, and \mathbf{I} is the identity matrix. The integration region V_B^+ is outside of the object body in the coordinate system that moves with η , so that $dV(\eta) = d\eta_n dS(\eta)$.

The equation describes the noise generated by an object moving through a flow (both the object and flow may move). Due to the motion a convective amplification of $|1 - M_r|$ is observed. The first term is the unsteady flow volume quadrupole noise term, already observed in the Lighthill equation. The second term is the so-called dipole "loading noise" and is related to the aerodynamic load on the object. The third term is the so-called monopole "thickness noise" and is related to the unsteady volume displacement of the body geometry and the kinematics in the medium.

These acoustic analogies can be used to assess the behavior of the source mechanisms using several simplifications. For the quadrupole sources, the dominating Reynolds stress tensor $\rho \mathbf{u} \mathbf{u}$ is of interest in eq. 2.1.9 and eq. 2.1.8. Assuming the density is approximately the ambient density $\rho \approx \rho_\infty$, and the velocity of the turbulence fluctuations is approx. the free-flow velocity $|\mathbf{u}| \approx u_\infty$. The temporal derivative on an eddy is proportional to its velocity u_∞ and inversely proportional to its size D , so that $\partial/\partial t \approx u_\infty/D$. This yields for the Lighthill equation 2.1.8

$$\rho \propto \frac{1}{a_\infty^4 r_0} \left(\frac{u_\infty}{D} \right)^2 \rho_\infty u_\infty^2 D^3. \quad (2.1.11)$$

With the isentropic pressure density relation, see eq.2.1.10, the acoustic intensity $I = \overline{p\dot{u}} \approx \overline{p}/(\rho_\infty a_\infty)$, the far-field pressure p^2 is

$$\frac{p_{\text{quadrupole}}^2 r_0^2}{\rho_\infty^2 a_\infty^4 D^2} \propto M_\infty^8. \quad (2.1.12)$$

This result shows that isentropic free-flow turbulence is mainly generated by a quadrupole source that scales in intensity by M^8 (for subsonic flows $u_\infty \ll a_\infty$).

The integral of the second term can be interpreted as a force $\mathbf{F} \approx \int (p\mathbf{I} - \boldsymbol{\tau})\mathbf{n}dS$. Using the previous approximation of a temporal derivative and assuming the force $F = |\mathbf{F}|$ is proportional to the surface pressure and surface area $F \approx pD^2 \approx \rho_\infty u_\infty^2 D^2$ this yields

$$\frac{p_{\text{com. dipole}}^2 r_0^2}{\rho_\infty^2 a_\infty^4 D^2} \propto M_\infty^6. \quad (2.1.13)$$

The source is a dipole and its axis is aligned with the force exerted on the body. For non-compact sources such as airfoil slats the intensity reduces to M^5 , but the reason for this is up to debate [40, 55, 54]. Most often, airframe noise sources are dipole sources [67, 55, 120, 31]

Finally, the intensity of a monopole source is a volume source with a volumetric flow $\hat{Q} \approx \rho u D^2$ in normal direction through V_B in the third term in eq. 2.1.9. The term is usually called “thickness noise” as sound is generated by the displacement of the medium through the moving body or by a volume flow of the source itself (e.g., a car exhaust system). With \hat{Q} and the approximations from above the far-field pressure then is

$$\frac{p_{\text{monopole}}^2 r_0^2}{\rho_\infty^2 a_\infty^4 D^2} \propto M_\infty^4, \quad (2.1.14)$$

so that the monopole scales at M^4 . Generally, one can deduce from the derivatives in the acoustic analogy source terms that it requires a change in the boundary or flow conditions for sound to be generated and that the intensity depends on the abruptness of the change.

2.1.2 Similarity laws

A basic assumption in aeroacoustic source modeling is that small changes in subsonic Mach numbers do not alter the source mechanism [66]. Also, a source may exist in extended spatial areas or frequency intervals, for instance, the sound generated from vertices in Kármán’s vortex street [102, 139]. Sources may have a frequency-dependent spatial location and shift their peak frequencies with changing Mach number. One example is jet noise, where the location of dominant sound generation shifts downstream, and the peak frequency decreases with increasing Mach number, while the power increases [79]. However, a normalization of the PSD or frequency using the Mach number reveals that the spectrum shape, Mach-normalized peak frequencies, and Mach-normalized PSDs collapse [104]. This is referred to as self-similarity. The underlying physical sound-generating mechanism has not changed; we only observe a different realization of the source mechanism. However, source mechanisms can change completely for large variations of their Reynolds numbers. One example is the radiated acoustics from a flow around a cylinder [139], where the flow properties may change due to, for instance, the transition from a laminar to a turbulent flow.

According to this theory, we consider aeroacoustic sources similar if the dimensionless quantities Reynolds number (Re), Mach number (M), and Strouhal number (St) or Helmholtz number (He) coincide.

$$M = \frac{u}{a} \quad (2.1.15)$$

$$St = \frac{fD}{Ma} \quad (2.1.16)$$

$$He = \frac{fD}{a} \quad (2.1.17)$$

$$Re = \frac{\rho Ma D}{\mu} \quad (2.1.18)$$

Depending on the quantity, the self-similarity implies different properties. If all dimensionless quantities are equal for different flow configurations, then the resulting dimensionless aeroacoustic nature is still the same, as they satisfy the dimensionless Navier Stokes equations. The Reynolds number determines the ratio of inertial and viscous forces and indicates the flow's chaoticness. At low Reynolds numbers, viscous forces dominate, resulting in a laminar flow. A laminar-turbulent transition is observed at Reynolds numbers above $Re \geq 2000$ and depends on the smoothness of the initial flow. In the receptivity phase, small disturbances, such as Tollmien–Schlichting waves, are introduced in the boundary layer and either decay or grow depending on their nature and amplitude. Depending on the Reynolds number, frequency, and boundary conditions, different mechanisms and instabilities lead to the observed flow characteristics. The Reynolds number is significant for assessing aeroacoustic noise since the flow drives sound generation in the medium. While the generated noise mechanism remains typically constant over some variations of the Reynolds number, it can also abruptly change [139]. Sources are typically not observed at constant Reynolds number over increasing Mach number, as an increase of the medium speed u also increases the Reynolds number, see eq. 2.1.18. Only an increase in medium density or decrease in temperature can counter this effect, which is how cryogenic wind tunnels operate.

Self-similarity over the frequency means that tonal components in a spectrum are observed at the same (normalized) frequency over a variation of the Mach number. The frequency can be normalized by the speed of sound a and a characteristic length D , resulting in a Helmholtz number, or by the Mach number M and D , resulting in the Strouhal number. The FW-H and Lighthill analogies show that the frequency of flow-induced noise typically depends on the flow itself. Thus, for turbulence-induced noise, one assumes it depends on the Strouhal number rather than the Helmholtz number. However, through resonance mechanisms and propagation effects such as spatial coherence, a Helmholtz number dependence may be observed in the far-field [90, 91], even though the driving mechanism is the flow itself and, thus, connected to the Strouhal number. The amplitude can be assumed to be subject to all dimensionless quantities, thus dependent on u_∞ , a , the density ρ , and a characteristic length D . Since the Strouhal number often depends on the convective Mach number M_C , which is unknown and can differ from the known free-flow Mach number M_∞ , observed sources often neither perfectly scale over the free-flow Strouhal or Helmholtz number. To overcome this issue this thesis introduces a generalized frequency \hat{f}

$$\hat{f} = \frac{fD}{M^m a} \quad (2.1.19)$$

with the modification exponent m , that can express a Helmholtz number for $m = 0$, a Strouhal number for $m = 1$, and everything in-between. A modification exponent $m \leq 0.5$ indicates a Helmholtz-like scaling and $m > 0.5$ indicates a Strouhal-like scaling behavior of the sources [48].

Self-similarity of the source power means that the (normalized) sound power does not change over a variation of the Mach number. This is true for an M^8 law for isothermal, subsonic quadrupole jet noise, see eq. 2.1.12, an M^6 law for short cylinders in a flow causing dipole noise, see eq. 2.1.13, and an M^4 law for automobile exhaust monopole noise, see eq. 2.1.14. The power scaling is expressed by the Mach number's exponent n , and results in a scaled level $\widehat{\text{SPL}}$ over the generalized frequency \hat{f}

$$\widehat{\text{SPL}}(\hat{f}) = \left\langle \text{SPL}(\hat{f}, M_i) - 10 \log_{10} \left(\frac{M_i}{M_0} \right)^n \right\rangle_i. \quad (2.1.20)$$

Here, the angle brackets indicate that averaging over the different Mach numbers i is performed. The $\widehat{\text{SPL}}$ is scaled with the given power exponent n from the given Mach number to the reference Mach number M_0 . The Sound Pressure Level (SPL) is given by

$$\text{SPL} = 10 \log_{10} \left(\frac{p^2}{4 \times 10^{-10} \text{ Pa}^2} \right). \quad (2.1.21)$$

If a source is self-similar for the given frequency type and power exponent, their spectra from different Mach numbers will collapse using eq. 2.1.20 so that the spectra averaged over the different Mach numbers show a low standard deviation. Then, the resulting averaged spectrum is valid for all flow conditions as long as self-similarity holds. If different normalized spectra show the same scaling behavior, frequency type, and spectral shape, independently of absolute levels or observed Mach numbers, we conclude that the driving aeroacoustic mechanism is the same. Further, the self-similarity parameters may indicate the driving mechanism, e.g., the quadrupole-like M^8 scaling, and Strouhal number scaling indicates free-flow turbulence, such as present in jet noise. In contrast, a M^5 scaling indicates a non-compact, dipole-like 2D object in the flow.

2.1.3 Source definition

This thesis defines a source as a phenomenon that radiates acoustic energy to the far-field. This thesis deals with quasi-stationary sources in the frequency domain, and thus, all source properties are assumed to be stationary and ergodic so that with the signal variance σ_p^2

$$\lim_{T \rightarrow \infty} \mathbb{E} \left[\left(\frac{1}{T} \sum_{t=1}^T (p'_t)^2 - \sigma_p^2 \right)^2 \right] = 0. \quad (2.1.22)$$

Ergodic signals are characterized by their statistical properties so that ensemble averages are equal to time averages. Thus, we can determine the statistical properties of a signal by observing a single realization of that signal for a sufficiently long period. In the case of acoustic signals, ergodicity implies that the statistical properties, such as the mean, variance, and power spectral density, can be accurately estimated by analyzing a sufficiently long segment of the signal. This assumption allows for the simplification of statistical analysis, as it eliminates the need to gather ensemble data or

average over multiple realizations of the signal.

A source has an amplitude $p_0(f)$ that typically depends on the frequency f , an arbitrary phase, a location \mathbf{y} that can be spatially distributed, and a spatial orientation described by the polar angles θ, φ . For monopole sources, the orientation angles can be neglected; for poles of higher order, the angles determine the sound radiation direction. While the orientation angle typically depends on the object's orientation in the flow, see eq. 2.1.9, this thesis assumes no prior knowledge of the source orientations.

This thesis introduces the definition of a source object to specify the nature of a source further. A source object describes an abstract source s with a collection of properties. These properties are all expressed by a finite number of numerical variables. The main idea is to define properties that hold for the idealized source independently of their location, frequency, and other parameters. A monopole source object has the following properties: A fixed location \mathbf{y} and a Power Spectral Density (PSD). A dipole has the additional properties: The spatial dipole rotation angles θ, φ , and the dipole PSD. Together, they can form a multipole source object with a single location, rotation, and separate monopole and dipole PSDs, as opposed to a conventional source that typically is defined as a power for a single frequency and location.

2.1.4 Compact, free-field Green's function

This subsection is based on the lectures of Delfs [30]. A free-field solution to the convective Helmholtz equation 2.1.2 is the convolution of the source term Q and a Green's function for compactly supported, radiating sources that satisfy the Sommerfield condition [122]. The convective free-field monopole Green's function is

$$g_0(\mathbf{x}, \mathbf{y}) = \frac{\exp(-jk r^+)}{4\pi r^*}, \quad (2.1.23)$$

where $r = \|\mathbf{x} - \mathbf{y}\|_2$, $\|\dots\|_2$ is the l_2 -norm between the source position \mathbf{y} and the observer position \mathbf{x} , $M_r = \mathbf{M}\mathbf{e}_r$, $M = |\mathbf{M}|$ and

$$r^+ = \frac{r^* - r M_r}{1 - M^2}, \quad (2.1.24)$$

$$r^* = r \sqrt{M_r^2 + 1 - M^2}, \quad (2.1.25)$$

which simplify to $r^* = r^+ = r$ for $M = 0$. The monopole has no directivity, so it radiates its energy equally distributed in all directions. All spatial derivatives of this equation are equally valid solutions to the Helmholtz equation and are called poles of higher orders such as the dipole g_1 , quadrupole g_2 , and further derivatives. They also result from the Taylor approximation of a general Green's function so that any Green's function can be expressed as a multipole, the superposition of $\sum_i^I g_i$.

The first derivative of this function is the so-called dipole, which in polar coordinates for $M = 0$ is given by

$$g_1(\mathbf{x}, \mathbf{y}) = \mathbf{e}_y^T \cdot \mathbf{e}_x \frac{\exp(-jkr)}{(4\pi r)^2} (-1 - jkr) \quad (2.1.26)$$

where \mathbf{e}_y is the normalized direction vector of the dipole at \mathbf{y} , and \mathbf{e}_x between the microphone position and source position with

$$\mathbf{e} = [\sin(\theta) \cos(\varphi), \sin(\theta) \sin(\varphi), \cos(\theta)]^T. \quad (2.1.27)$$

Thus, the dot product of unit vectors incorporates the dipole directivity, based on the dipole rotation and relative location of receiver and source.

2.1.5 Cross spectral matrix

The CSM is the most compact form for quasi-stationary, proper, and circular data [2]. This thesis assumes these properties. In closed wind tunnel data, where these assumptions can be violated, higher-order statistics improve the performance of the beamforming process [106]. The CSM corresponding to a source s is given by the complex microphone pressure vector p

$$p = \begin{pmatrix} p(x_1) \\ \vdots \\ p(x_N) \end{pmatrix} \quad (2.1.28)$$

with

$$\mathbf{C} = pp^\dagger \quad (2.1.29)$$

where \dagger denotes the Hermitian (conjugate transpose). In measurements, it is typically obtained with the Welch method, which splits the signal in $i = 1, \dots, I$ blocks, Fourier-transforms them, and then estimates $\mathbf{C} \approx \langle p_i(f)p_i^\dagger(f) \rangle_i$. Given a source signal $s(\mathbf{y}_n)$, the complex pressure at microphone position \mathbf{x}_m , is given by

$$p_m = s_n g_{nm} + \xi_m, \quad (2.1.30)$$

where ξ_m describes uncorrelated measurement noise such as sensor noise. Depending on the angle of incidence and the array's size, the signal offset can lead to a decrease in coherence [50] and can be compensated with pre-steering by shifting the signals in the time-domain. However, the offset is typically small compared to the Welch block length, and since often incoherent sources are of interest, the offset is neglectable [36].

2.1.6 Distributed sources and source coherence

In real-world scenarios, sources are often spatially distributed, and spatially distributed sources are typically (partially) coherent. We approximate a distributed source of any shape with a superposition of \hat{N} compact sub-sources $s_{\hat{n}}$ for $\hat{n} \in \hat{N}$ at source locations $\mathbf{y}_{\hat{n}}$

$$\mathbf{s} = \begin{pmatrix} s_1 \\ \vdots \\ s_{\hat{N}} \end{pmatrix}. \quad (2.1.31)$$

The number and distance of sub-sources should be chosen so that $|\Delta \mathbf{y}_{\hat{n}}| \ll \lambda$, to prevent aliasing in the resulting sound field. Using any Green's function g , the propagation matrix \mathbf{G} from all sub-sources to all microphones is given by

$$\mathbf{G}_{\hat{n}m} = g(x_m, y_{\hat{n}}) \quad \hat{n} = 1, \dots, \hat{N} \quad m = 1, \dots, M . \quad (2.1.32)$$

Given that $\mathbf{s} \in \mathbb{C}^M$ is a vector-valued random variable, its correlation matrix is $\mathbb{E}(\mathbf{s}\mathbf{s}^\dagger)$ and the CSM \mathbf{C} at the microphone array (without self-noise) is given by

$$\mathbf{C} = \mathbf{G}\mathbb{E}(\mathbf{s}\mathbf{s}^\dagger)\mathbf{G}^\dagger . \quad (2.1.33)$$

The expected value of $\mathbf{s}\mathbf{s}^\dagger$ depends on the coherence between the sub-sources and will result in a Hermitian matrix, with the sub-source strengths on the diagonal and the coherent parts on the upper and lower triangular matrix. For incoherent sub-sources, the expected value yields

$$\mathbb{E}(\mathbf{s}\mathbf{s}^\dagger) = \text{diag}(\mathbf{s}\mathbf{s}^\dagger) = |\mathbf{s}|^2 , \quad (2.1.34)$$

whereas for perfectly coherent sources, the expected value yields the matrix

$$\mathbb{E}(\mathbf{s}\mathbf{s}^\dagger) = \mathbf{s}\mathbf{s}^\dagger . \quad (2.1.35)$$

The unknown source covariance matrix is replaced with an explicit expression, depending on the sub-source vector $\hat{\mathbf{s}} \in \mathbb{C}^{\hat{N}}$ (defined later) and a coherence matrix $\mathbf{\Gamma} \in \mathbb{C}^{\hat{N} \times \hat{N}}$, $0 \leq |\mathbf{\Gamma}| \leq 1$ to obtain a formulation for partially coherent sources. More precisely, excluding self-noise, eq. 2.1.33 is replaced by

$$\mathbf{C} = \mathbf{G} \left(\mathbf{\Gamma} \otimes (\hat{\mathbf{s}}\hat{\mathbf{s}}^\dagger) \right) \mathbf{G}^\dagger , \quad (2.1.36)$$

where \otimes denotes the Hadamard (pointwise) product. A function for $\mathbf{\Gamma}$ can be freely defined, e.g. $\mathbf{\Gamma} = \mathbf{1}$ (matrix of ones) for coherent sub-sources or $\mathbf{\Gamma} = \mathbf{I}$ (identity matrix) for incoherent sources. Additionally, $\mathbf{\Gamma}$ may include phase relations between the sub-sources s_i and s_j under the condition that $\mathbf{\Gamma}$ must be Hermitian so that the CSM is also Hermitian. For the purpose of this thesis a simple variable coherence length L_c is defined based on the sub-sources wave-length λ and distance matrix between all sub-sources \mathbf{D} with

$$D_{ij} = \|\mathbf{y}_i - \mathbf{y}_j\|_2 , \quad (2.1.37)$$

the coherence matrix for exponential decay over the distance is

$$\mathbf{\Gamma} = \begin{cases} \mathbf{I} & \text{for } L_c = 0 \\ \exp\left(-\frac{2\mathbf{D}}{\lambda L_c}\right) & \text{for } 0 < L_c < \infty \\ \mathbf{1} & \text{for } L_c \rightarrow \infty \end{cases} . \quad (2.1.38)$$

The total power of a distributed source is the spatial integration of its source power. The sub-source powers must be deduced from the total strength based on the formulation in eq. 2.1.36, explicitly formulated based on the total source strength q . With increasing sub-sources of constant source strength, the total source strength increases (assuming no phase cancellation for coherent sources). Since the total source power is supposed to be independent of the number of sub-sources, it is

normalized by the number of sub-sources. However, it can be easily observed that the normalization must depend on the coherence between the sub-sources. Assuming they are located in the same position, doubling the number of sources will increase the sound power and far-field SPL by 6 dB, an incoherent source only by 3 dB. Thus, a simple normalization of the total power by the number of sub-sources is insufficient.

The exact normalization can be derived analytically by calculating the CSM entries for the given sub-sources s_i with amplitude $A_i = |s_i|$ and phase $Q_i = \angle s_i$, so that

$$s_i = A_i Q_i . \quad (2.1.39)$$

The coherence η_{ij} (not magnitude squared) between the sub-sources s_i and s_j is given by

$$\eta_{ij} = \sqrt{\frac{|s_{ij}|^2}{s_i^2 s_j^2}} = \mathbb{E} [Q_i Q_j^*] \quad (2.1.40)$$

with $0 \leq |\eta|^2 \leq 1$. We assume the sub-sources are located and evaluated in the same location since this thesis seeks a sub-source strength normalization based on the source description and not on a receiver position. The observed sound field might still experience deviations from the total source strength due to interference. For illustration purposes, the Cross Spectral Density (CSD) is calculated for the summed signals s_a and s_b from two sub-sources s_1 and s_2 with

$$s_a = A_1 Q_1 + A_2 Q_2 \quad (2.1.41)$$

$$s_b = A_1 Q_1 + A_2 Q_2 . \quad (2.1.42)$$

The CSD is defined as $C_{ab} = s_a s_b^*$.

$$C_{ab} = A_1^2 + 2A_1 A_2 \mathbb{E} [Q_i Q_j^*] + A_2^2 \quad (2.1.43)$$

All sub-sources are assumed to have the same amplitude $A_i = A$, so with eq. 2.1.40 the CSD is

$$C_{ab} = 2A^2 (\eta + 1) . \quad (2.1.44)$$

The amplitude of the super-positioned sources depends on their level of coherence. If the amplitude of the total source is supposed to be constant, the sub-sources have normalized by $\hat{N}^{\bar{\eta}}$. For a total amplitude of A^2 for $\hat{N} = 2$ sub-sources this yields

$$A^2 = 2 \left(\frac{A}{2^{\bar{\eta}}} \right)^2 (1 + \eta) , \quad (2.1.45)$$

which is the case for

$$\bar{\eta} = \frac{1}{2} \log_2 (2(\eta + 1)) . \quad (2.1.46)$$

Here, the normalization exponent $\bar{\eta}$ was derived, which explicitly depends on the coherence between the sub-sources. The original assumption that the difference between the sum of two coherent and incoherent sources is $\Delta\text{PSD} = 3\text{ dB}$ is validated when plugging $\eta_{\text{coher.}} = 1$ and $\eta_{\text{incoher.}} = 0$ in eq. 2.1.46. If C_{ab} is incoherent one simply expects $C_{ab} = 2A^2$ (see eq. 2.1.34), which yields a

normalization exponent of $\bar{\eta} = 0.5$. A normalization exponent of $\bar{\eta} = 1$ is obtained for coherent sources. It can easily be seen that this derivation works for \hat{N} sources and results in a normalization of $1/\hat{N}^{\bar{\eta}}$, thus $1/\sqrt{\hat{N}}$ for incoherent and $1/\hat{N}$ for coherent sub-sources. For a varying coherence level in $\mathbf{\Gamma}$ (e.g. with eq. 2.1.38) one simply uses the averaged coherence from the upper triangular matrix (without its diagonal)

$$\bar{\eta} = \langle |\gamma_{ij}^2| \rangle \quad \text{for } i \neq j. \quad (2.1.47)$$

It follows for a distributed source with total power A (that is the power integrated over all \hat{N} sub-sources) the normalized sub-source amplitudes in eq. 2.1.36 are with eq. 2.1.46

$$|\hat{s}_{\hat{n}}| = \frac{A}{\hat{N}^{\bar{\eta}}}. \quad (2.1.48)$$

Figure 4.2 shows for a monopole line source how the coherence length affects the CSM. Figure 4.2 (a) and (b) show the incoherent case $L_C = 0$, (c) and (d) show the partially coherent case $L_C = 3$, and (e) and (f) show the coherent case $L_C \rightarrow \infty$. In the resulting absolute CSM, a long source is visible with repeating side lobes, with a strong diagonal pattern in the corresponding phase for the incoherent case. The same is not true for the coherent case, where a checkerboard pattern is visible. The partially coherent case is a mix of both, where it is more related to the incoherent case in its absolute value but more similar to the coherent case in its phase.

2.1.7 Propagation forward operator

In beamforming literature, the CSM is often computed from eq. 2.1.29, since measurements obtain the pressure and the source strength is unknown. In terms of source strength, this implies that the CSM is

$$\mathbf{G}\mathbf{q}\mathbf{G}^\dagger = \mathbf{C}, \quad (2.1.49)$$

which requires the application of a Green's function to the source. This formulation is not computationally efficient for theoretic applications or if one seeks to calculate a synthetic CSM for a known source strength. It gives no direct description of a propagation operator. Instead, the acoustic propagation can be formulated as

$$\mathbf{T}\mathbf{q} = \mathbf{c}, \quad (2.1.50)$$

with \mathbf{c} being the vectorized CSM, $\mathbf{q}(\mathbf{y})$ are the source strengths, and \mathbf{T} being the propagation operator. The propagation operator \mathbf{T} is of dimension microphones $M \times$ focus points N , the source vector \mathbf{q} of dimension focus points, and the vectorized CSM \mathbf{c} of dimension M^2 . The propagation operator is derived from the Green's Matrix \mathbf{G} with

$$\mathbf{T} = \mathbf{G} \odot \mathbf{G}^\dagger, \quad (2.1.51)$$

where \odot is the Khatri-Rao product [130], a column-wise Kronecker product so that \mathbf{T} is of dimension $[F \times M^2 \times Q]$, where F is the number of frequencies, M is the number of microphones, and Q is the number of sources (or focus points). The advantage of this formulation is that the whole propagation problem is reduced to a matrix-vector product and that the propagation operator is formulated

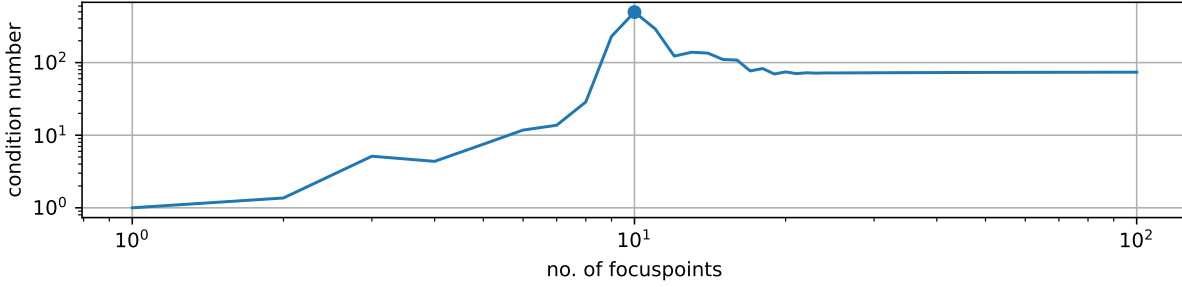


Figure 2.1: Conditioning number of the forward operator \mathbf{T} for $M = 5$ microphones with $x_1 = [-0.25 \text{ m}, \dots, 0.25 \text{ m}]^T$ and an increasing number of focus points at $-1 \text{ m} \leq y_1 \leq 1 \text{ m}$, $\Delta y_2 = 0.5 \text{ m}$, $f = 3400 \text{ Hz}$. The case where $N = (M^2 - M)/2$ (\mathbf{T} is bijective) is marked with a dot.

explicitly.

Given that for the beamforming problem \mathbf{c} is known, \mathbf{q} is wanted, the problem can be solved by obtaining \mathbf{T}^{-1}

$$\mathbf{q} = \mathbf{T}^{-1} \mathbf{c}. \quad (2.1.52)$$

\mathbf{T} has the rank $\min((M^2 - M)/2, N)$. Thus, \mathbf{T} is injective for $N \leq (M^2 - M)/2$. However, \mathbf{T} can be ill-conditioned, see Figure 2.1 for a sample 1D setup with $M = 5$ equidistantly spaced microphones. This is especially true for the bijective case. The strong peak at the bijective case originates from the equidistant array design and is relaxed with an array design with lower side lobes but never vanishes.

2.2 Artificial neuronal networks

Given enough training data, supervised learning has recently become widely popular and outperformed other classification and regression algorithms. Especially successful are multi-layer perceptrons, so-called Artificial Neuronal Networks (ANN), which are universal function approximators based on the universal approximation theorem [64]. They try to learn a mapping implicitly from training data. The ANN will learn any function if its learning capacity is large enough, there is a global minimum and no local minimum, and the amount of training data approaches infinity.

Deep learning refers to ANN with multiple hidden layers and typically a feed-forward model so that an ANN comprises a series of nested functions along multiple layers. A fully connected feed-forward architecture typically models each neuron by a linear function $\mathcal{F}(x) = ax + b$, where a and b are called weights and biases. A non-linear function $\mathcal{G}(x)$ is evaluated on \mathcal{F} to introduce non-linearity to the ANN, so that $\mathcal{G}(\mathcal{F}(x)) = \mathcal{G}(ax + b)$. Popular non-linear functions are the Rectified Linear Unit (ReLU), a softmax, and a sigmoid, depending on the use-case, such as regression or classification tasks.

For an input (or hidden) layer x_n with $n = 1, \dots, N$, the output layer y_m with $m = 1, \dots, M$ for a fully connected architecture then is defined by the sum

$$y_m = \mathcal{G}(a_{mn}x_n + b_{mn}). \quad (2.2.1)$$

The weights and biases are randomly initialized in the ANN and then optimized during supervised learning. Given that the output is known, an error metric can be defined as a loss L . Then, the loss gradient is calculated for the weights and biases via back-propagation (chain rule) through the nested functions. The loss is then minimized with a step towards the negative gradient with a step size $\alpha < 1$ for stability. A popular training algorithm is Adaptive Moment estimation, which will be used throughout this thesis.

2.3 Clustering

Opposed to supervised learning, where a function is learned from data with known input and output, clustering is an unsupervised learning method that does not require a known output or a training phase. Instead, data is analyzed based on its distribution and clustered into groups. This section provides an overview of clustering methods with an emphasis on Hierarchical Density-Based Spatial clustering of Applications with Noise [21] (HDBSCAN), which this thesis primarily employs.

Many clustering algorithms exist to group data into clusters. The typical problem associated with clustering methods is that the outcome strongly depends on hyper-parameters such as the expected number of clusters or that an underlying distribution is assumed. Other challenges include noisy data, outliers, or a large cluster-member-count mismatch.

Figure 2.2 shows exemplary popular clustering methods and their outcome for different problems for 2D spatially distributed data. The clustering problem in the first row contains two concentric circles. The second row contains two moon-shaped distributions. The third row contains three Gaussian distributions with different densities. The fourth row contains correlated Gaussian distributions. The fifth row contains a random uniform distribution. The different methods show different strengths and weaknesses, depending on their assumptions and the nature of the data. For example, Gaussian Mixture Models (GMM) show the best result for Gaussian distributions, as the data matches its assumptions. Clustering methods that show promising results throughout the different problems are Density-Based Spatial clustering of Applications with Noise [118] (DBSCAN), and its derivatives HDBSCAN, and Ordering points to identify the clustering structure [13] (OPTICS).

As shown in Figure 2.2, violating the clustering methods' assumptions results in wrong cluster estimations. The underlying distribution is typically unknown for real data and does not satisfy these models. DBSCAN is a two-parameter algorithm that accounts for clusters with different densities and noisy data, which does not assume an underlying distribution and, thus, performs well for all presented cases in Figure 2.2. Instead, the algorithm determines if a point belongs to a cluster based on the minimum number of neighbored points N_s and the distance ε to them. The algorithm distinguishes between core points, which are points that have at least N_s neighbored points within ε distance, reachable points, which are points that have at least one reachable core point within ε , and noise

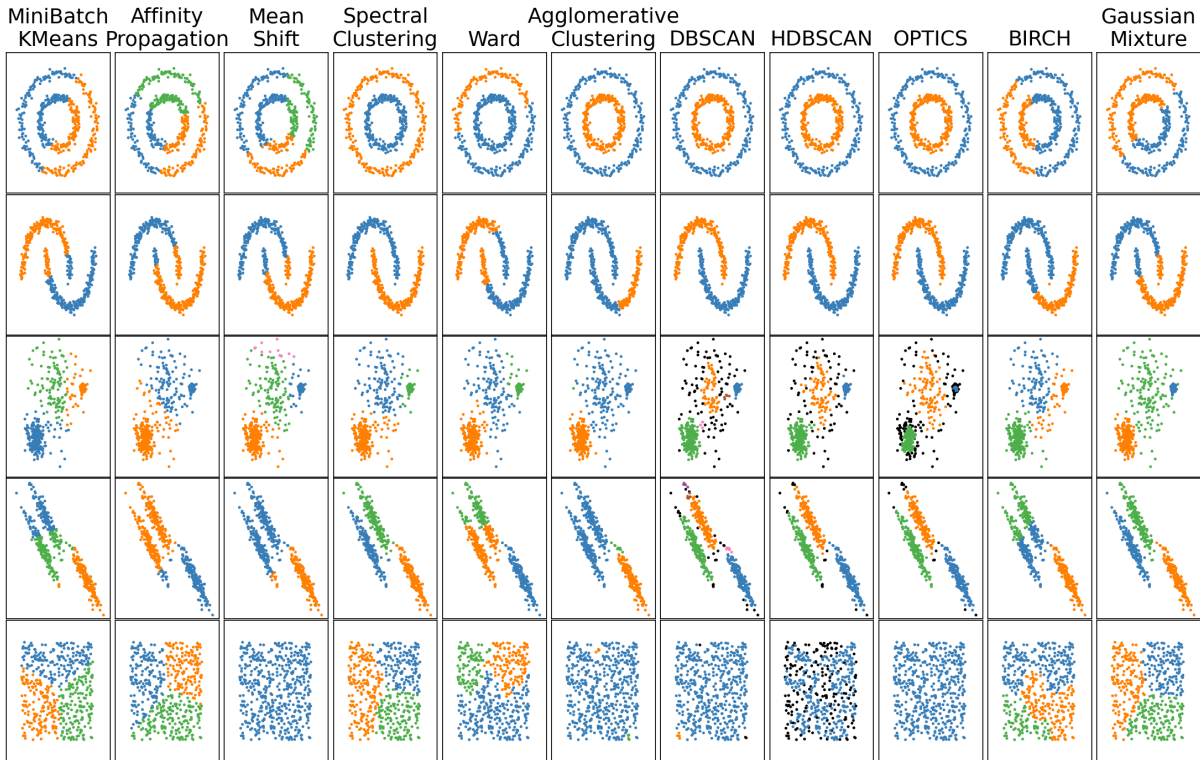


Figure 2.2: Outcome for popular clustering methods (shown on the columns) for different clustering problems (shown on the rows). The correct number is provided for algorithms that depend on the number of clusters. Taken from Scikit-learn’s standard examples [99].

points, which have no neighbors within ε . The advantages of DBSCAN over algorithms such as GMM or k-Means are that the number of clusters does not have to be predetermined, and the algorithm can cluster points with any underlying, unknown distribution. The underlying distribution can be estimated after the clustering process based on the density of the cluster members. The algorithm can also identify outliers, which typically distort the outcome of algorithms such as GMM and k-means. However, the two parameters N_s and ε must be set manually, and a fixed ε implies that all clusters have the same densities. This results in an unwanted behavior for the third case in Figure 2.2, where the middle distribution with little density is broken down into sub-clusters by the algorithm, and many points are wrongly estimated as noise. One can interpret N_s as a smoothing parameter for the estimated cluster PDF so that several sub-clusters will be merged with an increasing N_s . With a decreasing N_s , a cluster will break down into sub-clusters (for $N_s \rightarrow 1$, each point may form a cluster).

HDBSCAN is an extension to DBSCAN that allows a variable ε per cluster (that does not have to be determined manually). It uses $\lambda = 1/\varepsilon$ as an inverse distance measure and computes a spanning tree of the data using the mutual reachability distance. To do so, HDBSCAN constructs a cluster tree, an upside-down version of the estimated PDF, where λ is proportional to the underlying PDF value. Figure 6.17 shows an exemplary cluster tree for the Do728 sources, with a parent branch at $\lambda = 0$, splitting into the first branches at $\lambda \approx 1.5$. The width and color of the branches indicate the number of contained points, which shrink with increasing λ , as some points will first transition from core points to reachable points and then from reachable points to noise (so that they no longer belong to any cluster). The cluster tree always divides into branches if a super-cluster breaks into sub-clusters with a shrinking ε , which can be interpreted as local minima in the estimated PDF. A cut through

the cluster tree at any given ε is identical to the DBSCAN solution at the identical ε . The remaining question is how to choose λ on each branch to form either sub-clusters or super-clusters. The question relates to the overfitting problem so that sub-clusters are prone to fitting local maxima in the estimated PDF as individual distributions, even though they are only artifacts from the insufficient PDF estimation.

HDBSCAN solves this question with the persistence measure to determine λ for adjacent sub-clusters so that they are either merged at a low λ or separated for larger values of λ . The persistence is the integrated branch area, spanning from the number of points and the λ range, and for sub-clusters to maximize the persistence, their integrated area has to be larger than the area of their parent branch in the cluster tree. Figure 6.17 shows how this approach results in different λ -values for the different branches so that they have a different estimated density. The chosen branches are encircled, and the circles' colors represent the cluster number. The chosen λ value corresponds to the top splitting point in the branch, i.e., $\lambda \approx 1.5$ for cluster one. Note how cluster two is chosen as a super-cluster, while clusters seven to ten are chosen as sub-clusters in their branches due to the differences in their persistence.

Based on the clustering result, HDBSCAN estimates an underlying PSF for each cluster to yield a soft-clustering result. For each clustered point, it estimates the underlying PDF by calculating the probability of belonging to any cluster so that the clustering result is an $N_p \times N_c$ probability matrix, where N_p is the number of clustered points, and N_c is the number of resulting clusters. This probability can also be interpreted as a clustering confidence. The estimation is based on the distance between a point and the core cluster points, which are the points that persist longest within the cluster (independently from the corresponding cluster λ), and the persistence of the point compared to the persistence of the core points within the cluster.

3 Experimental data

This chapter provides an overview of the different experimental wind tunnel data used for this thesis. The data consists of four experiments. First, a generic dataset with a monopole speaker with known source position and sound power [47]. Second, a Dornier 728 1:10.8 half-model [4], based on which the methods presented in this thesis were developed. Third, an Airbus 320 1:13.6 half-model [7, 5, 123], based on which the developed methods were assessed. Fourth, an Embraer full-model [8] (confidential scale), where the developed methods were applied in situ during the measurement campaign for the first time.

Wind tunnel testing has a long history in the development, validation, and certification of aircraft [60, 96, 121]. In recent years, the demand for reliable aeroacoustic testing has increased due to the need for reduced sound emission levels [100, 134]. Nevertheless, one main driver of aircraft testing is still optimizing aerodynamics, thus reducing fuel consumption and other economic or ergonomic aircraft design improvements. Another challenge is the drive concept of the open rotor for passenger aircraft as part of the reduction in fuel consumption, leading to more noise [39, 68]. The resulting designs are driven by the increasing accuracy of computational predictions [119, 126], which require careful calibration and validation measurements [32, 41, 124]. Since these tests are performed before the build of actual prototypes, small-scale models must be built to fit in the wind tunnel facilities. One of the various challenges is to observe the model under realistic flight Reynolds numbers since many studies show that acoustic phenomena observed at low Reynolds numbers are vastly different [11, 4, 139]. Thus, pressurized and cryogenic wind tunnel facilities were developed, drastically increasing the range of observable Reynolds numbers [98, 103].

Aeroacoustic measurements often use half-models (i.e., the Do728 and A320 models). Half-models offer advantages over full-span models, such as a higher achievable Reynolds number and frequency range due to the increased model size and the upper limited measurement frequency [129]. On the downside, half-models impact the airflow close to the symmetry axis [43] and limit the measurement of acoustic directivity perpendicular to the flow direction in closed wind tunnels due to the floor and ceiling. Source directivity will not be studied as part of this thesis but may severely affect the observed sound radiation [49].

3.1 Streamlined speaker, open test section

A generic monopole dataset with known source location and sound power was acquired for this thesis [47] to test the capabilities of the presented imaging and source identification methods. The data features an equidistant 7×7 microphone array $-0.27 \text{ m} \leq x_{1,2} \leq 0.27 \text{ m}$, $x_3 = -0.65 \text{ m}$, with $\Delta x_1 = \Delta x_2 = 0.09 \text{ m}$, the sensors are mounted with $d = 30 \text{ cm}$ long rods on a 7 cm Basotect covered back-plate in a mostly reverberation-free environment. The source is a generic monopole



Figure 3.1: Experimental setup, the monopole source is located in the core flow of the open wind tunnel section (left), the housing opening is at the downstream end (positive x_1 direction). On the right, the equidistant 7×7 B&K 4961 multi-field microphone array is mounted with 30cm long rods on a back-plate that is then covered with 7cm Basotect absorbers. The coordinate system only indicates the directions, the actual coordinate origin lies roughly at the speaker housing opening.

source (streamlined housing with a circular $r = 2.5$ mm opening at the downstream end). The source is moved to the three locations

$$\begin{bmatrix} y_I \\ y_{II} \\ y_{III} \end{bmatrix} = \begin{bmatrix} -0.05 & 0.1 & 0.0 \\ 0.10 & 0.1 & 0.0 \\ 0.25 & 0.1 & 0.0 \end{bmatrix} \quad (3.1.1)$$

during separate measurements and uses uncorrelated white noise with different band-pass frequencies and amplitudes to generate different spectral shapes. Figure 3.1 shows the experimental setup. The source is positioned in the jet core of the open wind tunnel, and four different Mach numbers are measured $M = [0.00, 0.03, 0.06, 0.12]$. The CSM has a sampling frequency of $f_S = 2^{16}$ Hz. Results presented for Global Optimization in Section 4.5 use a blocksize of 2^6 , which results in around 6×10^4 Welch averages and $\Delta f = 2^{10}$ Hz. Results presented for SIND, SIHC in Chapter 4.5.1, and CLEAN-SC in Section 4.3 use a blocksize of 2^8 resulting in $\Delta f = 2^8$ Hz. The ground truth source powers are obtained by dividing the CSMs by the propagation matrices $\mathbf{T}' = \mathbf{G}^\dagger \mathbf{G}$, see eq. 2.1.32, for an ideal monopole source, see eq. 2.1.23. Then, the absolute upper triangular CSM entries \hat{i} are averaged to obtain an average ground truth spectrum with standard deviation.

$$\text{PSD}_{\text{true}}(f) = \left\langle \left| \frac{\mathbf{C}(f)}{\mathbf{T}'(f)} \right| \right\rangle_{\hat{i}} \quad (3.1.2)$$

The ground truth excludes self-noise since it does not use the CSM diagonal. The three measurements are super-positioned (addition of their CSM) to obtain a single CSM that contains three incoherent sources. To evaluate how close the real sound source is to an ideal monopole, a synthetic CSM is generated based on the average ground truth spectra, see eq. 3.1.2, the true source locations, and the compact monopole assumption. Thereafter, the Mean Absolute Error (MAE) of the upper triangular synthetic and measured CSM is calculated to measure the distance of the assumption and data. Figure 3.2 shows the resulting error, which is calculated for the absolute PSD difference (a)

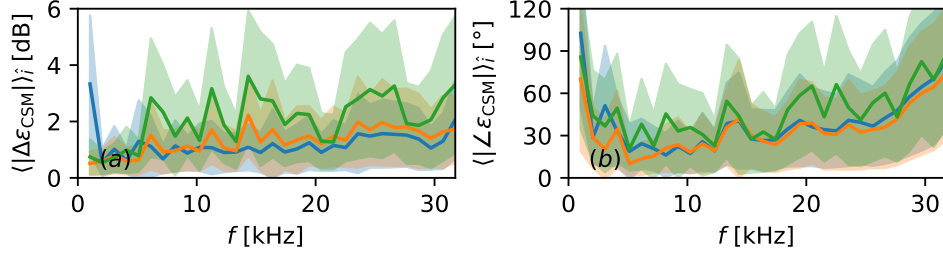


Figure 3.2: Differences between measurement and synthetic monopole. (a) shows the Mean Absolute Error (MAE) of the upper triangular CSM entries (\hat{i}) between the synthetic and measured CSMs for the three source positions (S_I depicted in blue, S_{II} in orange, S_{III} in green) with 1σ standard deviation (shaded area). (b) shows the MAE of the corresponding phase difference.



Figure 3.3: Photo of Do728 model and microphone array in the closed wind tunnel test section.

and absolute phase difference (b). The errors show that the monopole assumption is reasonable at $2 \text{ kHz} \leq f \leq 25 \text{ kHz}$. At lower frequencies, the assumption is probably violated by reflections of the array's back-plate, see Figure 3.1. At higher frequencies, the assumption is gradually violated by the speaker design (non-compactness, asymmetric orientation towards the array). The influence of the speaker's asymmetric orientation towards the array can also be observed from the increased error from source position y_I to y_{II} , and finally y_{III} , where the average observation angle further increases. It will be of particular interest how different methods perform at these very low and high frequencies, where the compact monopole assumptions are violated.

3.2 Dornier 728, closed test section

A large, cryogenic dataset of a Do728 [4] is used to develop the methods presented in this thesis. The Mach-averaged Reynolds numbers $\langle \text{Re} \rangle_M$, the ambient pressures p_0 and cryogenic temperatures

configuration	D1	D2	D3	D4	D5
$\langle \text{Re} \rangle_M [1 \times 10^6]$	1.4	1.8	2.5	3.8	10.6
$T [\text{K}]$	290	250	200	150	100
$p_0 [1 \times 10^5 \text{ Pa}]$	1.0	1.0	1.0	1.0	1.0

Table 3.1: Do728 flow configurations.

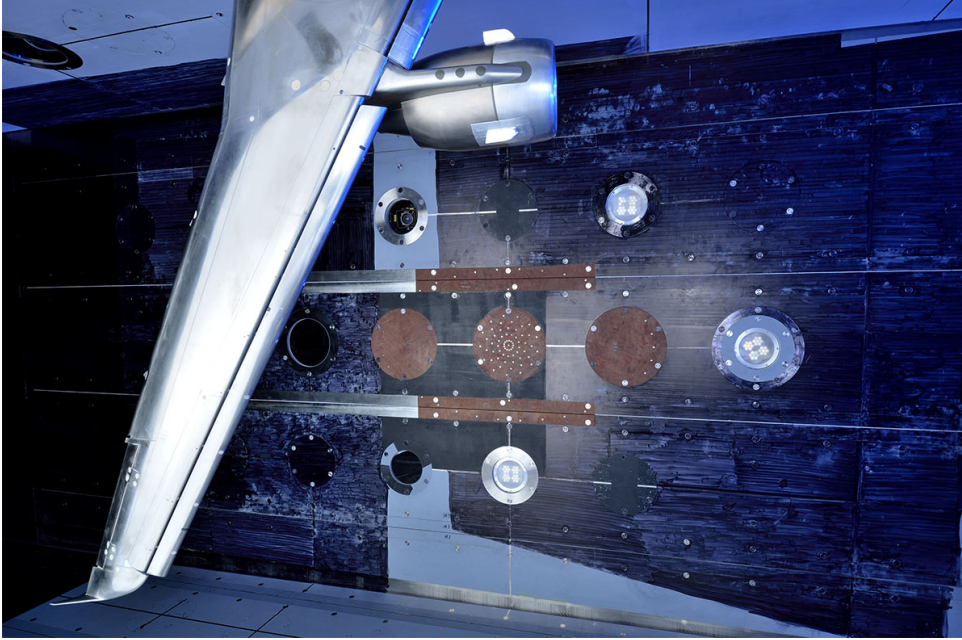


Figure 3.4: Photo of A320 model and microphone array in the closed wind tunnel test section.

T are shown in Table 3.1 based on the mean aerodynamic cord length $D_0 = 0.353 \text{ m}$. Values of $\alpha_a = [1^\circ, 3^\circ, 5^\circ, 6^\circ, 7^\circ, 8^\circ, 9^\circ, 10^\circ]$ were chosen for angle of attack for every Reynolds number configuration and $M_j = [0.125, 0.150, 0.175, 0.200, 0.225, 0.250]$ as Mach number for every angle of attack. In total, the Do728 dataset contains $5 \langle \text{Re} \rangle_M \times 8 \alpha \times 6 M = 240$ different flow configurations. The array consisted of 144 microphones at an oval aperture of $1.756 \text{ m} \times 1.3 \text{ m}$ and a data sample frequency of $f_S = 120 \text{ kHz}$ was used. Note that the Reynolds numbers are averaged over the Mach number, as the Reynolds number is not kept constant over varying Mach numbers. The CSM is calculated using Welch's method with a block size of 2^{10} samples and 50% overlap, which results in around 7000 averages. Conventional beamforming results for Chapter 5 and Chapter 6 is performed on an equidistant grid with a focus point resolution of $\Delta x = 0.5 \text{ mm}$. For 2D beamforming maps the focus plane is around $\Delta x_3 \approx 1 \text{ m}$ away from the $D = 1 \text{ m}$ spiral array, where D is the aperture.

configuration	A1	A2	A3	A4
$\langle \text{Re} \rangle_M [1 \times 10^6]$	1.4	5.1	5.1	19.9
$T [\text{K}]$	310	311	125	120
$p_0 [1 \times 10^5 \text{ Pa}]$	1.10	3.99	1.15	4.19

Table 3.2: A320 flow configurations.

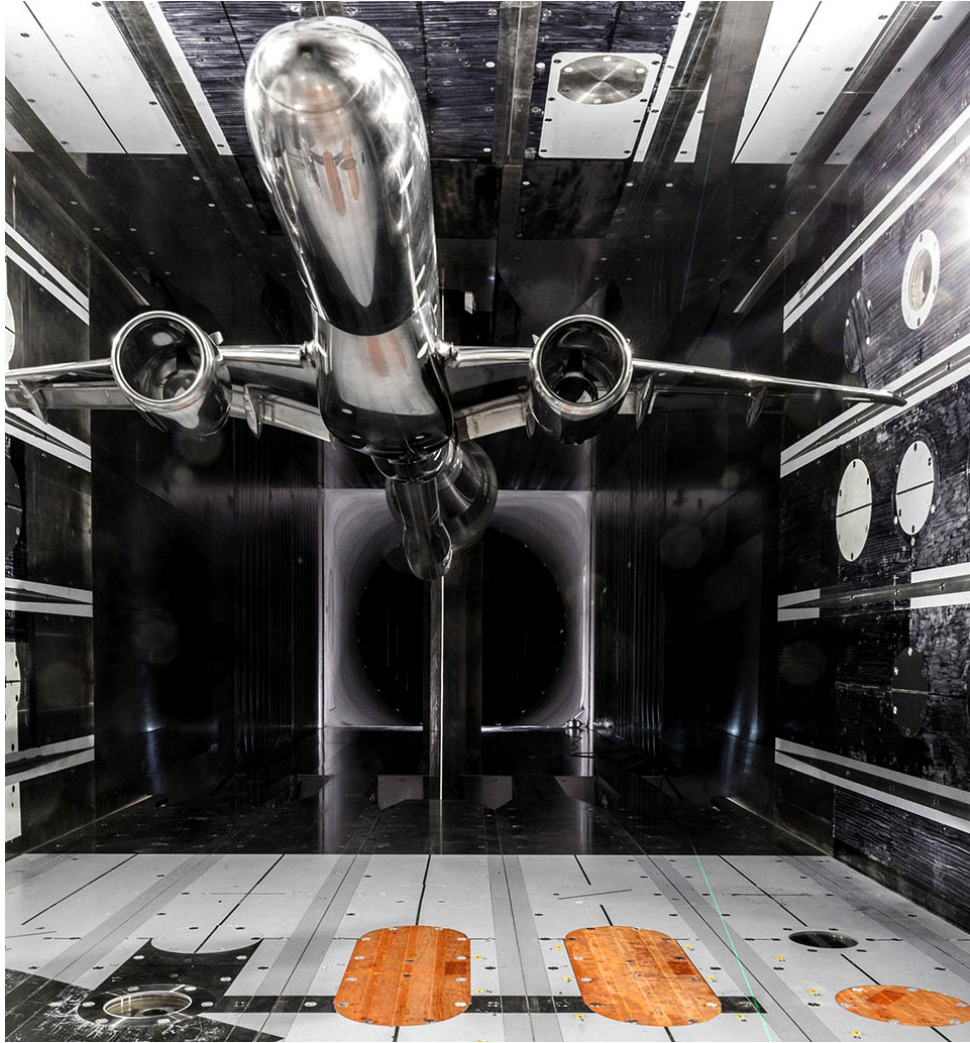


Figure 3.5: Photo of model and part of the microphone array in the closed wind tunnel test section. The microphones are positioned in the wooden cut-outs on the floor.

3.3 Airbus 320, closed test section

For the validation of the methods presented in Chapter 5 and Chapter 6, a second dataset of an Airbus 320 model [5] is used. The A320 model was observed at $\alpha_a = [3^\circ, 7^\circ, 7.15^\circ, 9^\circ]$ for every Reynolds number configuration, and $M_j = [0.175, 0.200, 0.225]$ for every angle of attack. The Mach averaged Reynolds numbers, the ambient pressures p_0 and cryogenic temperatures T are shown in Table 3.2 based on $D_0 = 0.353$ m. In total, the A320 dataset contains 48 different flow configurations. The array consisted of 96 microphones at an aperture of $1.06 \text{ m} \times 0.5704 \text{ m}$ and the data was recorded at $f_S = 150 \text{ kHz}$. The CSM is calculated using Welch's method with a block size of 2^{10} samples and 50% overlap, which results in around 9000 averages. Conventional beamforming for Chapter 5 and Chapter 6 is performed on an equidistant grid with a focus point resolution of $\Delta x = 0.5 \text{ mm}$. For 2D beamforming maps the focus plane is around $\Delta x_3 \approx 1 \text{ m}$ away from the $D_1 = 1.1 \text{ m}$, $D_2 = 0.6 \text{ m}$ oval array, where D are the apertures in x_1 and x_2 direction.

	M	T [K]	p_0 [kPa]	Re [10^6]
DP 1	0.220	137.4	134.10	03.33
DP 2	0.220	137.2	403.45	10.00
DP 3	0.220	115.0	405.50	13.00
DP 5	0.250	126.3	313.20	10.00
DP 6	0.289	115.0	235.00	10.00

Table 3.3: Embraer flow configurations.

3.4 Embraer, closed test section

In this study, a full-span aircraft model by Embraer is located in the center of the test section as depicted in Figure 3.5. The scaled model is installed in landing configuration, has a mean aerodynamic chord length of about 0.2 m, and is not equipped with landing gear. It is mounted around $\Delta z = 1$ m away from the randomly optimized array. The model's material was chosen so that its temperature dependence compensates the increased dynamic pressures q at increased static pressures p_a . Thus, the model deformation does not change at cryogenic conditions, which allows a wide range of combinations of temperatures T and static pressures p_a to achieve a desired Reynolds number. All selected data points were obtained at the elastic deformation, see Table 3.3. Each data point was recorded at $f_S = 250$ kHz.

In comparison to the model scale, the large array aperture produces a low depth of field, which in return leads to an increased depth resolution. Conventional beamforming results for Chapter 6 is performed on an equidistant grid with a focus point resolution of $\Delta x = 1$ mm. The increased spatial resolution is a significant difference compared to the other datasets. A second difference is that the Reynolds number is constant (for DP 2, 5, and 6) over the variation of the Mach number, as opposed to the increasing Reynolds number with increasing Mach number for the Do728 and A320 datasets. This dataset was acquired after developing the methods introduced in this thesis. Thus, it can be seen as a test set for the methods proposed in Chapter 5 and Chapter 6.

4 Beamforming

For the localization and estimation of the sound power of complex source geometries, beamforming (referring to any covariance matrix-based imaging method) is well-established [78, 87]. Each field of application in acoustical imaging has its own challenges. In aeroacoustic imaging, the number of sensors is typically favorably large compared to the number of observed sources. The array's aperture is favorably large compared to the observed object and its distance. However, the Signal to Noise Ratio is unfavorably low (the noise typically exceeds the signal by over 10 dB), so that blind source separation methods and signal subspace-based methods fail for this application.

Idealized, noise-free correlation measurements in a bounded measurement domain uniquely determine an unknown, compactly supported source power function [63]. However, it is well known that correlated sources are not uniquely determined from distant measurements of acoustic waves since so-called non-radiating sources exist. Additionally, most methods are grid-based so that in the area where sources are expected, focus points are defined in the area of interest. Beamforming is then evaluated on these predefined points. Due to the increasing computational power, many algorithms are now evaluated on 3D problems, where the number of focus points is typically vast compared to the number of microphones so that even a solution for radiating sources is no longer unique. Thus, various beamforming methods and algorithms emerged over the last decades to account for different use cases, configurations, and assumptions.

These include assumptions about the source and propagation, such as distributed sources [20, 34], the incorporation of wind tunnel flow effects, such as shear layer decorrelation [37, 38, 56, 58, 117], partially coherent source regions [25, 51, 73, 92, 97, 136], imposing real steering vectors through a measured or simulated flowing medium [77, 92], the speed of sound [6, 10, 83], and reflections [72], correlated in-flight or closed wind tunnel shear layer noise [9, 57, 59], beamforming on multiple CSMs at different subsonic flow speeds, assuming self-similarity and a Mach power law [4, 7, 48], multipoles such as dipoles and quadrupoles, and source directivity [44, 51, 97].

The main strategies can be summarized as follows. Solving the inverse problem leads to eq 2.1.52. Given that \mathbf{T} is known and can be inverted, the unknown source powers \mathbf{q} can be estimated based on the CSM \mathbf{c} . However, in real-world scenarios, neither \mathbf{T} nor the source positions and the number of sources are known. A propagation model for \mathbf{T} is assumed to solve this equation. Further, several estimated source positions are assumed, typically called focus points. Still, \mathbf{T} is rarely bijective since the number of unknowns (focus points) typically exceeds the number of equations ($(M^2 - M)/2$, given that the diagonal of the CSM is dominated by self-noise). To solve this problem, a regularization that enforces sparseness is introduced, commonly also known as compressive sensing. This approach is known as the inverse beamforming method [138, 125, 15, 28, 105].

A similar strategy is the gridless CSM Fitting Method (CFM) "Global Optimization", where a propagation model is modeled for \mathbf{T} , and both \mathbf{T} and \mathbf{q} are optimized in such a way that a norm between the observed CSM and the estimated CSM is minimized, see Section 4.5. The main dif-

ference between CFM and the inverse method is that one trades linearity for an improved ratio of equations to unknowns.

In the time domain, a delay-and-sum beamformer works by shifting the observed signals so that the shift negates the propagation time differences to the estimated source positions. Then, all observed time-shifted signals are averaged. The signals will interfere constructively if the estimated source position and propagation assumption are correct. Otherwise, they will randomly cancel each other out. This method is a naïve method in that it estimates a sound power for each focus point without determining if a source exists without considering the other focus point. In the frequency domain, this type of beamforming is known as conventional beamforming. Instead of performing the correlation-based signal averaging during the beamforming process, the coherence between the signals is calculated first, then the weighted matrix is steered to the focus points and summed. While this naïve estimation is a limitation of the method, it also makes it extremely robust, which is why it is still primarily used in wind tunnel applications. Since it will be used throughout this thesis, different weighting and steering strategies are discussed in detail in the next section.

More methods exist, such as subspace-based methods [109, 71, 14, 35, 34, 140], which will not be further discussed in this thesis. These methods assume that the CSM comprises eigenvectors representing individual sources. However, this is not true for closed wind tunnel measurements, where the CSM diagonal is strongly dominated by noise from the medium flow of the sensors, so the eigenvectors mainly represent self-noise.

The following sections discuss the mathematical foundations of beamforming and how the aforementioned limitations arise. Then, this thesis introduces two methods that seek to overcome these limitations by performing beamforming at all frequencies at once in Section 4.5. While the method's results are superior over traditional beamforming methods, the computational time makes the method in its current form not applicable to large-scale measurement campaigns. Section 4.6 and Section 4.7 discuss how these methods can be translated into data-driven machine learning models.

4.1 Steering vectors

Conventional beamforming requires a Green's function to model the propagation between the source and receiver. Four steering vectors h are typically regarded [107, 25] which differ in how the Green's function is normalized.

$$\mathbf{h}^I = \frac{1}{M} \frac{\mathbf{g}}{|\mathbf{g}|} \quad (4.1.1)$$

$$\mathbf{h}^{II} = \frac{1}{M} \frac{\mathbf{g}}{|\mathbf{g}|^2} \quad (4.1.2)$$

$$\mathbf{h}^{III} = \frac{\mathbf{g}}{\|\mathbf{g}\|_2^2} \quad (4.1.3)$$

$$\mathbf{h}^{IV} = \frac{1}{\sqrt{M}} \frac{\mathbf{g}}{\|\mathbf{g}\|_2} \quad (4.1.4)$$

Here, a steering vector is simply a normalized Green's function. The desired property of a steering vector is that the beamforming map $\mathbf{b}(\mathbf{y})$ achieves the correct level at the true source location \mathbf{y}_S , so that

$$q(\mathbf{y}_S) = \mathbf{h}^\dagger(\mathbf{x}, \mathbf{y}_S) \mathbf{C}(\mathbf{x}) \mathbf{h}(\mathbf{x}, \mathbf{y}_S) = b(\mathbf{y}_S). \quad (4.1.5)$$

Additionally, the source location is desired to be correct so that the maximum level of the source map appears at the source location

$$\mathbf{b}(\mathbf{y} = \mathbf{y}_S) > \mathbf{b}(\mathbf{y} \neq \mathbf{y}_S). \quad (4.1.6)$$

In the following, the different formulations are analyzed with respect to the two conditions for monopole sources, see eq. 2.1.23. Formulation I is normalized by the absolute value of the Green's function and, thus, only compensates the phase. While it satisfies the second conditions [107, 25] based on its spatial derivatives at the true source position, the first condition is only met at a reference position \mathbf{y}_R , so that $d_S = |\mathbf{x} - \mathbf{y}_S|$, $d_R = |\mathbf{x} - \mathbf{y}_R|$

$$g(\mathbf{x}, \mathbf{y}_S, \mathbf{y}_R) = \frac{\exp(-jk(d_S - d_R))}{4\pi(d_S - d_R)}, \quad (4.1.7)$$

and thus

$$\mathbf{b}(\mathbf{y}_S) = \left(\frac{1}{M} \sum_{m=1}^M \frac{d_R}{d_S} \right)^2 q. \quad (4.1.8)$$

With an increasing distance $d = |\mathbf{y} - \mathbf{y}_R|$, the source power estimation error will increase. Formulation II additionally compensates for the Green's function's amplitude and thus meets condition one. Condition two is violated so that the maximum in the beamforming map does not reassemble the true source location. Formulation III is typically connected to "conventional beamforming" and can be interpreted as the Maximum Likelihood Estimator because its l_2 -norm normalization

$$\mathbf{A} = \frac{\mathbf{g}^* \mathbf{C}}{\|\mathbf{g}\|^2} \quad (4.1.9)$$

minimizes the Mean Squared Error (MSE) between the observed CSM and the estimated source power

$$\text{MSE} = |\mathbf{C} - \mathbf{A}\mathbf{g}|^2. \quad (4.1.10)$$

The MSE and the variance of Formulation III are smaller or equal compared to Formulation II [25]. Formulation IV seeks to minimize the MSE with $h^*h = 1/N$, which satisfies condition two but only yields the power estimation

$$\mathbf{b}(\mathbf{y}_S) = \frac{1}{M} \sum_{m=1}^M \frac{d_R^2}{d_S^2} 2q, \quad (4.1.11)$$

of which the error is less or equal to formulation I [25]. D. Ernst [37] formalized the steering vector normalization with

$$h(\mathbf{y}) = \hat{h}(\mathbf{y}) \exp(j\varphi(\mathbf{y})) \quad (4.1.12)$$

and

$$\hat{h}(\mathbf{y}) = \frac{|g(\mathbf{y})|^{\beta-1}}{\left(\sum_m^M |g_m(\mathbf{y})|^\beta \right)^\alpha} \quad (4.1.13)$$

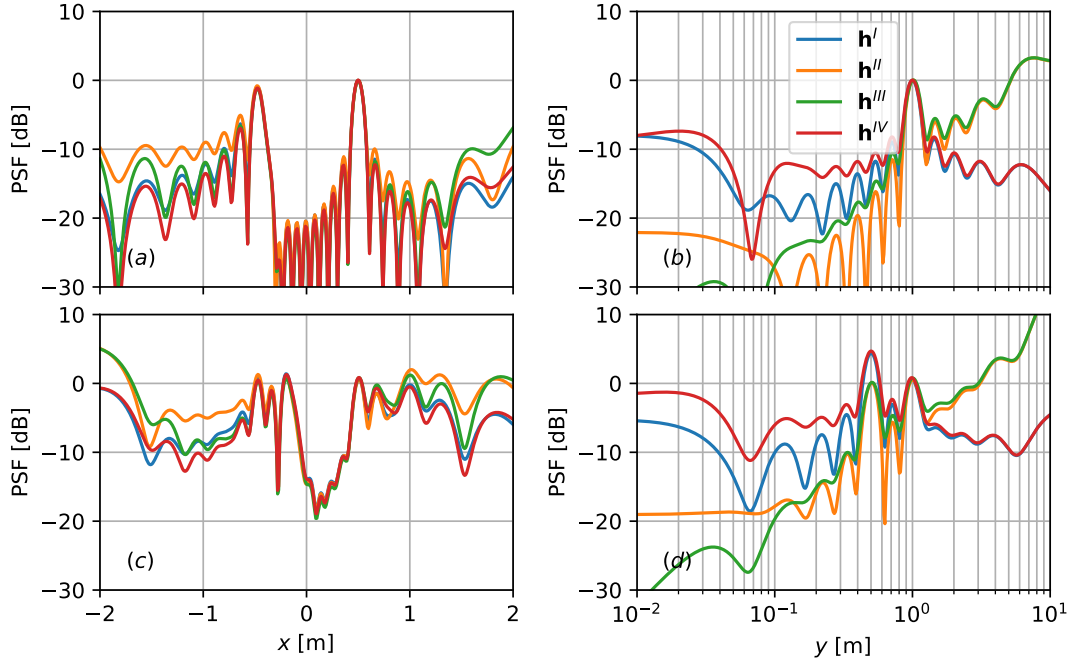


Figure 4.1: Comparison of the steering vector influence on the PSF at $f = 4096$ Hz for (a), (b) a source at $\mathbf{y} = [0.5, 1, 0]$, and (c), (d) two sources at $\mathbf{y}_I = [0.5, 1, 0]$, $\mathbf{y}_{II} = [0.5, 0.5, 0]$. The equidistant array is located at $y = z = 0$, and $-0.5 \leq x \leq 0.5$, $M = 11$ sensors. (a), (c) show the PSF for $y = 1, z = 0$, and (b), (d) show the PSF for $x = 0.5, z = 0$.

that satisfies condition one for $\alpha = 1, \beta \in \mathbb{R}$, and condition two for $\alpha = 1 - 1/\beta$. Both conditions can only be met at $\beta \rightarrow \infty$, where beamforming renders useless due to the weighting of the microphones. However, we can use the generalization to analyze the steering vector behavior. With

$$\angle h = \frac{h}{|h|} \quad (4.1.14)$$

the steering vectors result from eq. 4.1.13 with

$$\mathbf{h}^I \quad \alpha = 0 \quad \beta = 1 \quad \hat{\mathbf{h}} = \frac{1}{M} \quad (4.1.15)$$

$$\mathbf{h}^{II} \quad \alpha = 1 \quad \beta = 0 \quad \hat{\mathbf{h}} = \frac{1}{M} \frac{1}{|\mathbf{g}|} \quad (4.1.16)$$

$$\mathbf{h}^{III} \quad \alpha = 1 \quad \beta = 2 \quad \hat{\mathbf{h}} = \frac{|\mathbf{g}|}{\|\mathbf{g}\|_2^2} \quad (4.1.17)$$

$$\mathbf{h}^{IV} \quad \alpha = \frac{1}{2} \quad \beta = 1 \quad \hat{\mathbf{h}} = \frac{1}{\sqrt{M}} \frac{|\mathbf{g}|}{\|\mathbf{g}\|_2} \quad (4.1.18)$$

Figure 4.1 shows the PSF that results from the different steering vector formulation for two cases. First, a single source. Second, two sources are located behind each other in relation to the array. The PSF for formulations I and IV is scaled to yield the correct result at $y = 1$ m. Figure 4.1 (a) shows that the side lobes of formulation IV are lowest parallel to the array and increase through formulations I, III, and IV. The main lobe width and grating lobe strength are identical for the formulations. Figure 4.1 (c) shows that for two cases, the PSF of IV is not strictly lower for all focus points, but the general observation still holds. The grating lobe of the second source is projected to a different location due to the wrong focal plane. Figure 4.1 (b) shows that perpendicular to the array, the best

choice of the steering vector depends on the estimated source region. Formulations II and III suffer from distance normalization, producing distance-dependent side lobe strengths. While closely behind the source, the main lobe is still dominant. At increasing distances, the side lobe always dominates the PSF. Figure 4.1 (d) shows that the same is true for two sources. The main lobe strength for I and IV at \mathbf{y}_{II} shows that they do not produce the correct amplitude.

4.2 Conventional beamforming

The result of conventional beamforming depends on the employed steering vector, as discussed in Section 4.1. Throughout this thesis steering vector formulation III is used for planar beamforming at a fixed distance from the array, and steering vector formulation IV is used for 3D beamforming.

The conventional beamforming [115] result b is calculated with

$$b = \mathbf{h}^\dagger \mathbf{C} \mathbf{h}. \quad (4.2.1)$$

Since the CSM diagonal is dominated by self-noise, it is typically excluded in the beamforming process, known as Diagonal Removal (DR). If so, the steering vectors must be adjusted with weights. E.g., formulation IV [107] with diagonal removal then reads

$$\mathbf{h} = \frac{\mathbf{g}}{\left(M(M-1) \|\mathbf{g}\|_2^4 - \|\mathbf{g}\|_4^4\right)^{1/4}}. \quad (4.2.2)$$

If the medium is not at rest, the propagation vector \mathbf{g} is derived from the Green's function for the convective Helmholtz equation [106]. For the l -th focus point \mathbf{g} is given by

$$g_l(\mathbf{y}) = \frac{\exp\left(-\frac{-jk}{1-|\mathbf{M}|^2}(-(\mathbf{x}_l - \mathbf{y}) \cdot \mathbf{M} + |\mathbf{x}_l - \mathbf{y}|_{\mathbf{M}})\right)}{4\pi|\mathbf{x}_l - \mathbf{y}|_{\mathbf{M}}} \quad (4.2.3)$$

and depends on the frequency f , the speed of sound a , the mean flow velocity vector \mathbf{u}_∞ , the m -th microphone position \mathbf{x}_m and the focus position \mathbf{y} with

$$|\mathbf{x}_m - \mathbf{y}|_{\mathbf{M}} = \sqrt{((\mathbf{x}_m - \mathbf{y}) \cdot \mathbf{M})^2 + (1 - |\mathbf{M}|^2) |\mathbf{x}_m - \mathbf{y}|^2}, \quad (4.2.4)$$

$$\mathbf{M} = \frac{\mathbf{u}_\infty}{a}, \quad (4.2.5)$$

$$k = \frac{2\pi f}{a}. \quad (4.2.6)$$

Conventional beamforming has many similarities to optical imaging. While the focus points can be freely defined, an increase in focus points only yields an increase in pseudo resolution, as the array's aperture determines the resolution of the optical system. The Rayleigh criterion with a sinus small angle approximation ($\sin x \approx x$) yields

$$\Delta x \approx 1.22 \frac{\lambda d_z}{D} \quad (4.2.7)$$

where d_z is the source distance, and D is the array's aperture. Below the Rayleigh criterion, sources can no longer be spatially separated. For practical application, the true resolution depends on the

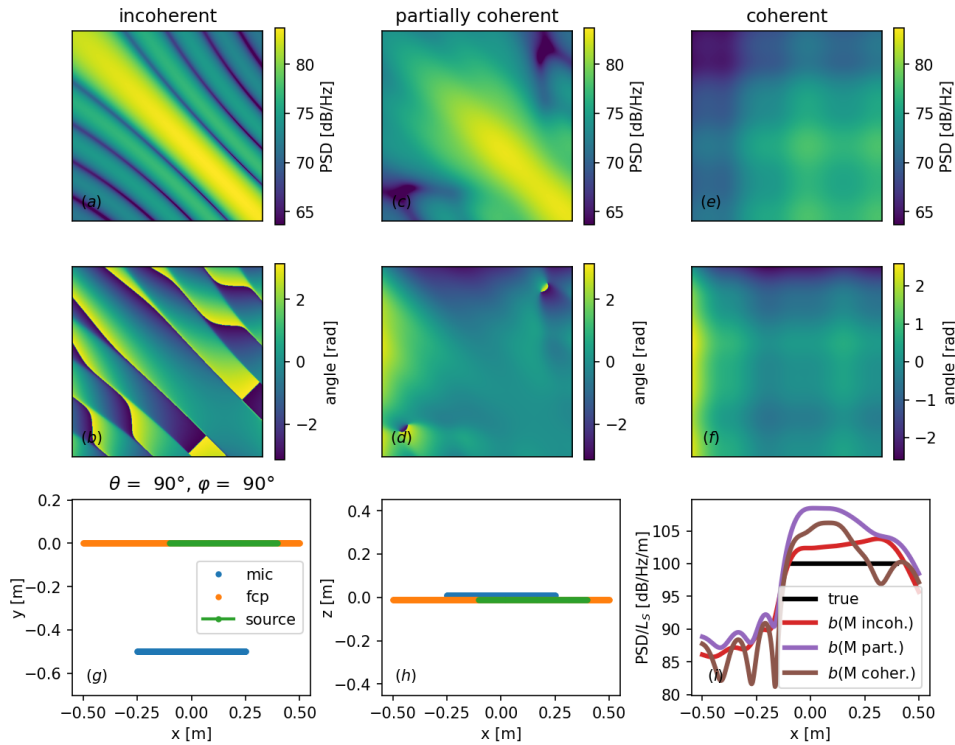


Figure 4.2: The Figure shows a comparison of (a), (b) an incoherent, (c), (d) a partially coherent, and (e), (f) totally coherent monopole line-source with $l = 0.5$ m, $f = 4096$ Hz, $L_C = 3$, $\text{PSD} = 100$ dB m⁻¹. (a) through (f) show the observed CSMs, (g), (h) show the 3D setup, and (i) shows the CBF results \hat{b} (steering vector III, see Section 4.1) based on these CSMs, assuming compact, incoherent monopole sources (M) for the incoherent (red), partially coherent (purple), and coherent case (brown). Thus, the resulting deviations originate from the mismatch of the propagation assumption and true data.

exact sensor positions, the steering vector, and the source type and source position. Additionally, aliasing at around and above the wavelength that equals the spacing of the microphones occurs.

As shown in Section 2.1.6, distributed sources and dipole sources are of particular interest, as they violate the main assumption of conventional beamforming: spatially compact, incoherent monopole sources. Figure 4.2 shows for a monopole line source how the coherence length affects the CSM, and thus, the estimated source power using conventional beamforming. Note, that the beamforming levels are normalized to dB Hz⁻¹ m⁻¹ using the correct η from eq. 2.1.47. As explained in Section 2.1.6, the integration over the line source is supposed to yield the total power, but the power is displayed over a spatial variable. The problem is that the number of sub-sources and focus points is unequal. This is similar to why a PSD (in Pa² Hz⁻¹) is used over an SPL (in Pa²), as the frequency normalization makes the power independent of the step size between the discrete frequency bins. Thus, the normalization by the length is necessary, which, as shown with eq. 2.1.48, requires the knowledge of the coherence between the sub-sources. Note that this is only a problem concerning the display of the results but not obtaining the results. However, one should keep this issue in mind for the interpretation of distributed sources. The source coherence has a strong influence on the beamforming results. While the conventional beamforming assumptions are not violated for the incoherent case (the line source is simply comprised of spatially compact monopoles), the results for a (partially) coherent line source show that the line source is not reconstructed properly. The coherence between

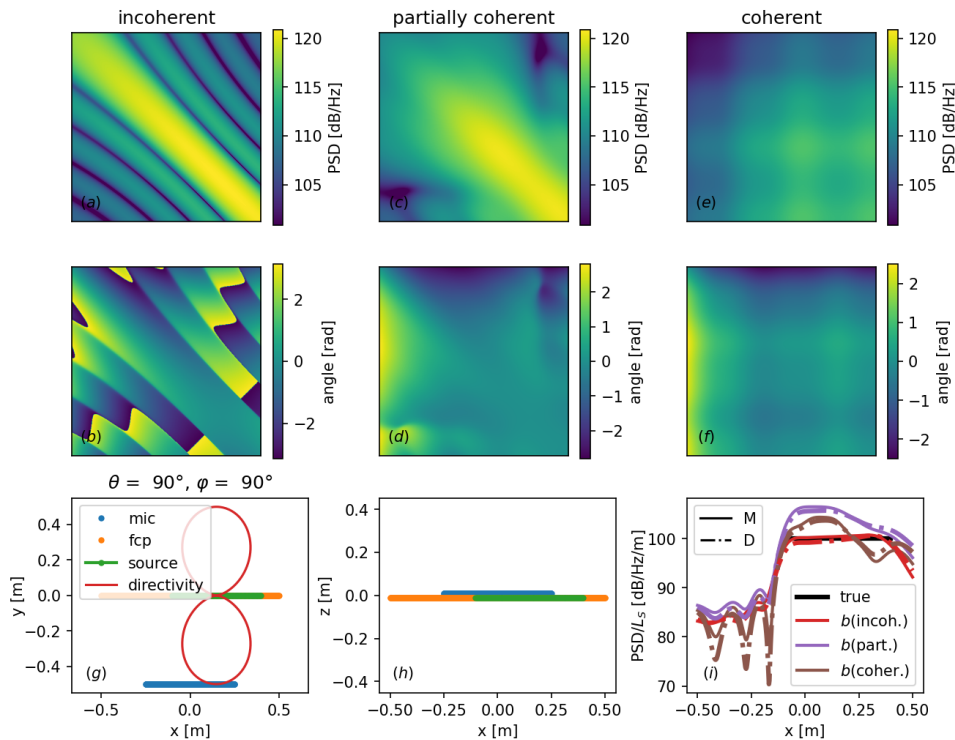


Figure 4.3: The Figure shows a comparison of (a), (b) an incoherent, (c), (d) a partially coherent, and (e), (f) totally coherent dipole line-source with $l = 0.5$ m, $f = 4096$ Hz, $L_C = 3$, PSD = 100 dB m⁻¹. (a) through (f) show the observed CSMs, (g), (h) show the 3D setup, and (i) shows the CBF results (steering vector III, see Section 4.1) based on these CSMs, assuming compact, incoherent monopole sources (solid lines) and compact, incoherent dipole sources with the correct dipole orientation angle (dashed lines).

the sub-sources results in observing a single source that is not well localized. Additionally, the power estimation error is large compared to the incoherent case. Still, the overall detection of a source in the correct area and estimation of the source power shows how robust conventional beamforming is against violations of its assumptions.

Figure 4.3 shows the corresponding result for the same setup from Figure 4.2 for a dipole line source. The monopole beamforming results are additionally normalized by the absolute value of the dipole's Green's function, see eq. 2.1.23 and eq. 2.1.26, which compensates the large frequency-dependent offset in source power compared to the monopole. The result is very similar to the monopole source, even for the beamforming using either a monopole or dipole assumption for the steering vector. The results show that distributed coherent and incoherent sources are observed differently, as the locked phase difference leads to interference in the sound field for the coherent source. Thus, the coherent source is observed as a much more compact source through beamforming with a compact, incoherent monopole assumption, compared to the incoherent source. For the dipole case, the monopole and dipole assumptions yield very similar results since the observed CSM is also very similar. This is because the dipole's main lobe is orientated in the direction of the array, from where it is mostly indistinguishable from a monopole. With an increasing deviation of the dipole's main lobe angle, the results will increasingly differ. In the worst case, at $\theta = 0^\circ$, the dipole will radiate nearly no energy in the directions of the sensors. Thus, its amplitude will be greatly underestimated by conventional beamforming. This means that if the dipole is visible in the conventional beamforming results, its

main lobe must be roughly orientated towards the array, and thus, the results are fairly valid. Otherwise, other sources will dominate the result, and the dipole will not be visible.

The results show that the general reconstruction of distributed, partially coherent dipole sources is qualitatively possible with a compact monopole assumption. When mixing dipole and monopole beamforming results, a drastic over- and underestimation of the source power can be avoided by not calculating the true source power but referencing it to a normalized distance, i.e., $d = 1$ m, so that the frequency dependency in the dipole's Green's function cancels out. Again, this concerns only the display and interpretation of the results rather than their calculation.

4.3 CLEAN-SC

CLEAN-SC is a popular “deconvolution” algorithm for conventional beamforming methods. It is based on the idea that each focal point represents a compact, incoherent source. Thus, any coherence measured between two focal points originates from the PSF. The coherence between two signals is given by

$$\gamma^2 = \frac{|G_{xy}|^2}{G_{xx}G_{yy}}. \quad (4.3.1)$$

CLEAN-SC is based on the idea that the coherence Γ_{jk}^2 between an arbitrary focus point \mathbf{x}_k and all other focus points \mathbf{x}_j can be estimated by steering the CSM to the focus points with

$$\Gamma_{jk}^2 = \frac{|\mathbf{w}_j^* \mathbf{C} \mathbf{w}_k|^2}{(\mathbf{w}_j^* \mathbf{C} \mathbf{w}_j)(\mathbf{w}_k^* \mathbf{C} \mathbf{w}_k)} = \frac{|A_{jk}|^2}{A_{jj}A_{kk}}, \quad (4.3.2)$$

where \mathbf{w} is an arbitrary steering vector [107]. Removing the coherent parts of a source removes the PSF (but also distributed sources) from the map. The advantage over CLEAN-PSF, where the theoretical PSF for a monopole source is subtracted from the beamforming map, is that CLEAN-SC “measures” the PSF. This is performed iteratively with the Algorithm 1, where n is the current iteration, for a maximum number of N iterations, or until a stopping criterion is met [114]. $f \in \mathbf{f}$ is the current frequency, A is the conventional beamforming result for the steering vector \mathbf{w} , and \mathbf{x} is a list of all focus points. \mathbf{C} is the dirty CSM, \mathbf{G} is the CSM of the iteratively identified source, and \mathbf{Q} is the final CLEAN-SC estimation of the “deconvolved” map. For stability, a loop gain $0 < \alpha \leq 1$ is used. The algorithm can be performed with Diagonal Removal (DR) [114] to remove self-noise. Typical stopping criteria for the iterations include a certain dynamic range of the remaining source map compared to the initial maximum or the norm of the remaining CSM.

The method assumes that the global maximum in the beamforming map is the true source position to estimate the source position and strength. While the method is robust towards errors in the localization of the source, one still has to identify the source's main lobe so that the coherence between the estimated source position and all other focus points yields a meaningful result. Thus, a dense focus grid is necessary to achieve satisfying results, especially at short wavelengths, where the spatial resolution is higher than the focus-grid resolution. However, refining the focus points will only solve this problem partially due to the basis mismatch [29]. More advanced methods exist, such as High Resolution HR-CLEAN-SC [116]. However, standard CLEAN-SC will be employed in this thesis due

Algorithm 1 Standard CLEAN-SC.

FUNCTION CLEAN-SC(C, \mathbf{w}, α):

$Q(\mathbf{f}, \mathbf{x}) \leftarrow 0$

for f in \mathbf{f} **do**

$n \leftarrow 0$

$\mathbf{A}_{jj} \leftarrow \mathbf{w}_j^*(f)C(f)\mathbf{w}_j(f)$

while $n \leq N$ **do** ▷ or an other arbitrary stopping criterion is met

$n \leftarrow n + 1$

$k \leftarrow \operatorname{argmax}_j(\mathbf{A}_{jj})$

$A_{kk} \leftarrow \mathbf{A}_{jj}(\mathbf{x}_k)$ ▷ find pos. of max. amplitude

$\mathbf{h} \leftarrow \frac{C(f)\mathbf{w}_k(f)}{A_{kk}}$ ▷ find steering vector to the corresp. loc.

if DR **then**

$\mathbf{H} \leftarrow \mathbf{I} \otimes \mathbf{h}\mathbf{h}^*$ ▷ diag. matrix from steering vector

$\mathbf{h} \leftarrow \frac{1}{1+\mathbf{w}^*\mathbf{H}\mathbf{w}} \left(\frac{C(f)\mathbf{w}}{\mathbf{w}^*C(f)\mathbf{w}} + \mathbf{H}\mathbf{w} \right)$ ▷ iteratively find steering vector if DR

end if

$\mathbf{G} \leftarrow A_{kk}\mathbf{h}\mathbf{h}^*$ ▷ calc. CSM for the identified source

$C(f) \leftarrow C(f) - \alpha\mathbf{G}$ ▷ subtract identified source from dirty CSM

$\mathbf{A}_{jj} \leftarrow \mathbf{A}_{jj} - \alpha\mathbf{w}_j^*(f)\mathbf{G}(f)\mathbf{w}_j(f)$ ▷ subtract clean beam from dirty map

$Q(f, \mathbf{x}_k) \leftarrow Q(f, \mathbf{x}_k) + \alpha A_{kk}$ ▷ add identified source strength to CLEAN-SC output

end while

end for

return $Q(\mathbf{f}, \mathbf{x})$

to its computational efficiency and large datasets.

Since CLEAN-SC will be used as the main method throughout this thesis to evaluate airframe noise, the following results assess how it behaves if the assumptions of spatially compact, incoherent sources are not met. The 1D set-up from Section 2.1.6 will be used to assess this issue, with a 1D focus grid at $-0.5 \text{ m} \leq x \leq 0.5 \text{ m}$ with $N = 500$ focus points at $\Delta y = 0.5 \text{ m}$, and an equidistant array at $-0.25 \text{ m} \leq x \leq 0.25 \text{ m}$ with $M = 100$ microphones. Figure 4.4 shows the result for a spatially compact monopole that meets the CLEAN-SC assumptions. Thus, the source is well reconstructed,

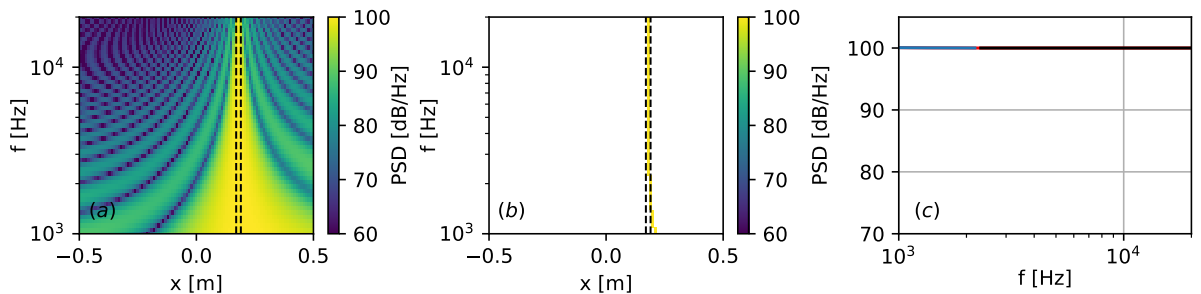


Figure 4.4: Spatially compact source. (a) shows the conventional beamforming solution with steering vector III. The black dashed lines show the outer edges of the true source location, (b) shows the corresponding CLEAN-SC solution. (c) shows the spatially integrated PSD, where the red line shows the integration of the total area, the black line indicates the source area between the black, dashed lines in (a) and (b), and the blue line outside the source area (noise).

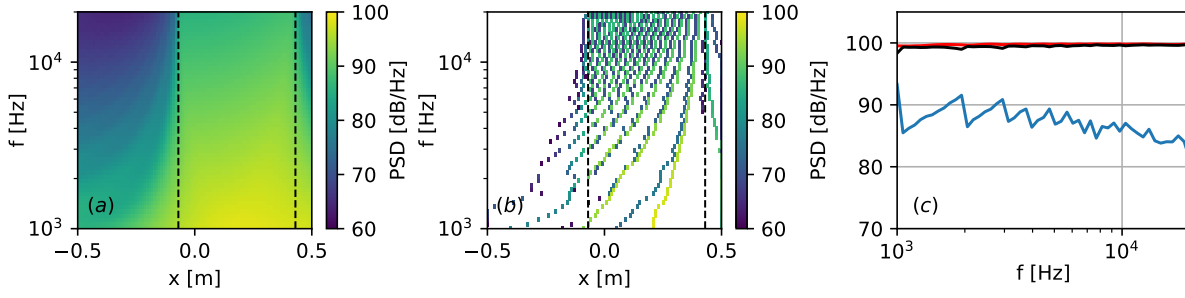


Figure 4.5: Line source with 100 $L_C = 0$ (incoherent) sub-sources according to the description in Figure 4.4 and the setup in Figure 4.2.

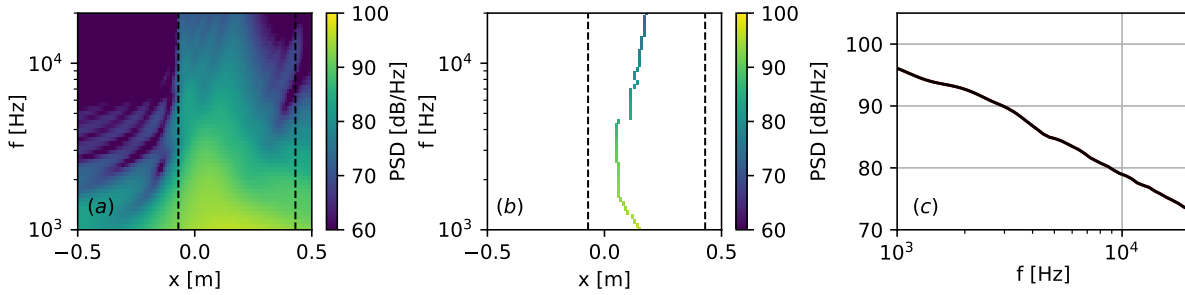


Figure 4.6: Line source with 100 $L_C = \infty$ (coherent) sub-sources according to the description in Figure 4.4 and the setup in Figure 4.2.

except at very low frequencies, where the main lobe cannot be sufficiently resolved spatially.

Figure 4.5 shows the corresponding results for an incoherent line source, presented in Figure 4.2. The line source is constructed from $\hat{N} = 100$ sub-sources, spaced in a $\Delta x = 0.5$ m interval along the focus grid. The amplitude of the line source is $\text{PSD}(f) = 100 \text{ dB Hz}^{-1}$ according to the sub-source scaling presented in Section 2.1.6. The conventional and CLEAN-SC results reconstruct the line source well from medium to high frequencies, where it is spatially well resolved. At lower frequencies, only a few of the sub-sources are reconstructed. The total source spectrum is well estimated.

Figure 4.5 shows the results for a coherent line source, presented in Figure 4.2. The conventional beamforming resolves the spatial location of the source reasonably well. The SPL is underestimated at high frequencies due to the increasing interference from the source at the microphone positions. As a consequence, the right edge of the line source cannot easily be identified. CLEAN-SC reconstructs a single source position at any given frequency, corresponding to its assumptions. Since it assumes incoherent sources, any measured coherence between focus points will be (wrongly) attributed to the PSF. Thus, the SPL is underestimated for distributed, coherent sources, in addition to the underestimation due to the interference at small wavelengths (compared to the size of the source).

Figure 4.5 shows the results for a partially coherent line source with $L_C = 3$, presented in Figure 4.2, with the coherence model presented in Section 2.1.6. Since the coherence model features an exponential coherence decay over increasing frequency, see eq. 2.1.38, the coherence decay counters exactly the power underestimation due to interference, see Figure 4.6 (c). Still, the SPL is underestimated by $\Delta \text{PSD} \approx 4 \text{ dB}$. The spatial estimation lies somewhere between the coherent and the incoherent case.

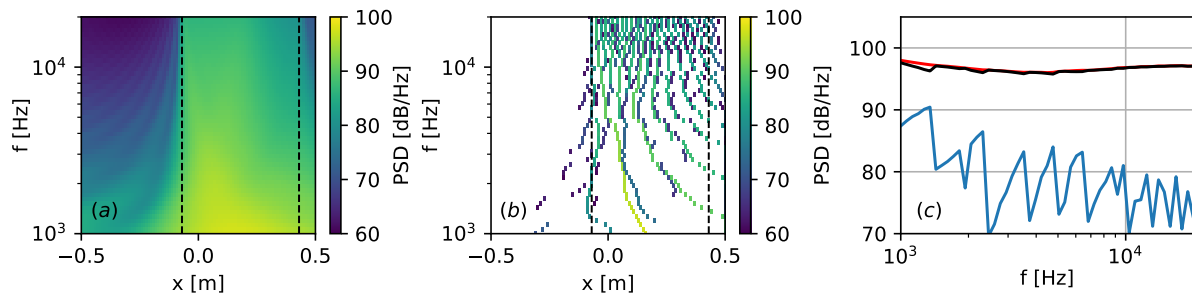


Figure 4.7: Line source with 100 $L_C = 3$ (partially coherent) sub-sources according to the description in Figure 4.4 and the setup in Figure 4.2.

The coherent solution dominates at low frequency due to the long coherence length. At increasing frequency, more sub-sources are estimated at decreasing spatial distances, which corresponds to the coherence model.

In summary, CLEAN-SC will estimate several sources in the area of distributed sources, where the number and density depend on the coherence of the source. The distance between the reconstructed sources increases with an increasing coherence and decreasing frequency. With increasing frequency and increasing coherence, the power is gradually underestimated. However, for real-world sources where we expect the coherence length to shrink with increasing frequency, the effect is countered so that it is reasonable to assume a constant power underestimation over frequency.

Figure 4.8 shows a real-world example of conventional beamforming and CLEAN-SC results of the Embraer model [8] with a traditional display of the map. The Figure shows the over z -integrated third-octave source maps, which show a complex spatial distribution of sources that vary over frequency and Reynolds number. We observe mostly point-like sources along the slat that spatially correlate with the slat tracks. A graphical indication of the source types and their names is shown in Figure 5.3. The locations are mostly consistent over frequency (opposed to the location of coherent, non-compact sources shown in Figure 4.6 and Figure 4.7). This indicates that the CLEAN-SC assumptions are mostly reasonable for the dominant sources at the Embraer wing.

Figure 4.9 shows the corresponding integrated spectra of the full maps presented in Figure 4.8 for DP 2, DP 5, and DP 6, which allow a comparison of the sound emission at increasing Mach number and constant Reynolds number, see Table 3.3 and Section 2.1.2. Figure 4.8 (a) shows the integrated spectra over the Strouhal number, Figure 4.8 (b) over the Helmholtz number, and Figure 4.8 (c) shows the scaled spectra for an M^5 -law, typically proposed for airframe noise [55]. Figure 4.9 and Figure 4.8 are the standard visualization and analysis methods.

4.4 B-CLEAN-SC

This section introduces Broadband-CLEAN-SC (B-CLEAN-SC), based on original work [52], which aims to relax the problems of CLEAN-SC at high and low frequencies by adapting the idea of broadband Global Optimization, see Section 4.5: The processing of multiple frequencies at once, so that the side lobes cancel out, and actual source positions can be identified. This is achieved by introdu-

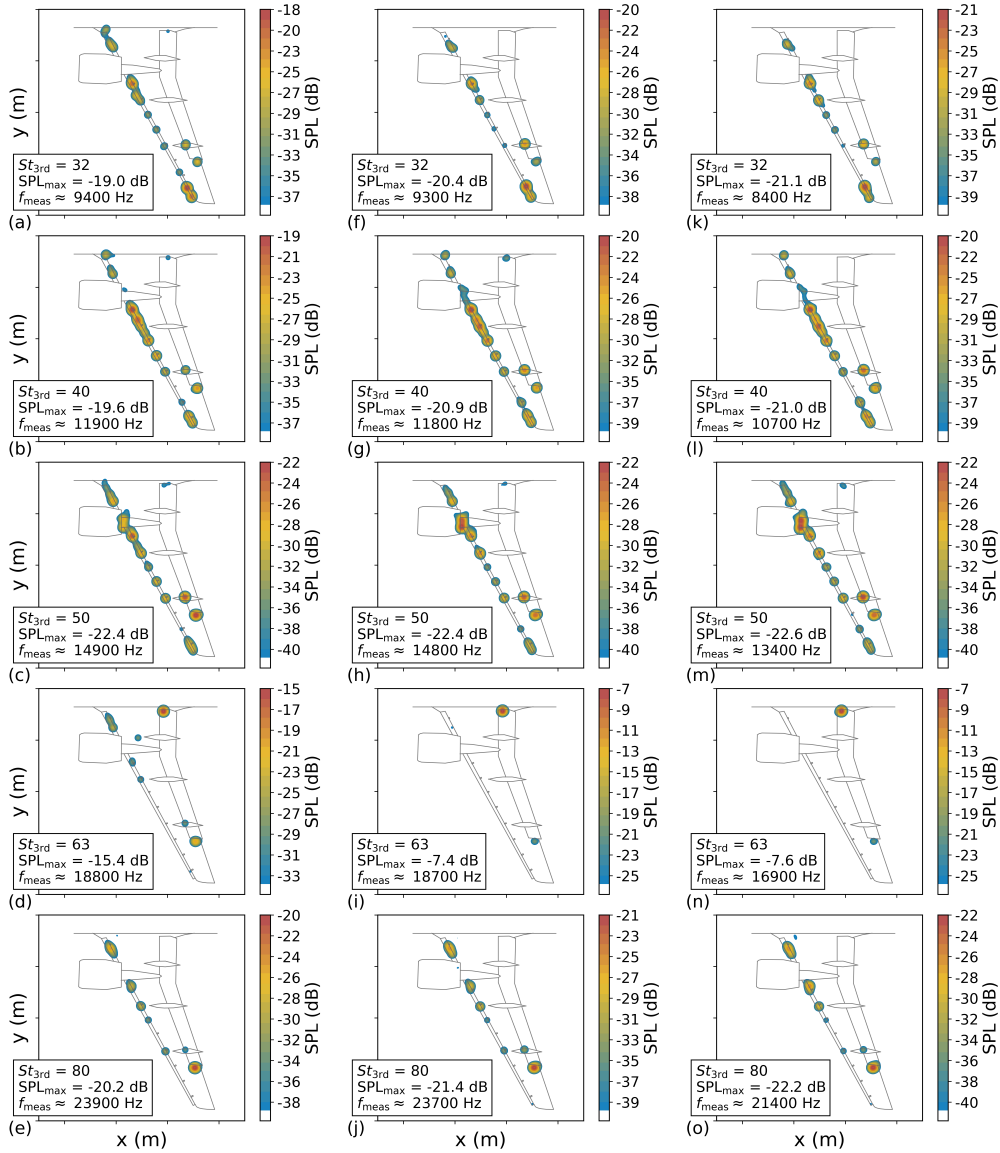


Figure 4.8: Comparison of over x_3 and 3rd octaves integrated source maps for the Embraer DP 1: (a) to (e), DP 2: (f) to (j), and DP 3: (k) to (o), for St_c numbers (a), (f), (k): 32, (b), (g), (l): 40, (c), (h), (m): 50, (d), (i), (n): 63, (e), (j), (o): 80.

cing a simple change to the CLEAN-SC algorithm: Instead of processing each frequency individually, B-CLEAN-SC processes frequency intervals at once (but still obtains smallband solutions). Here, the only difference lies in determining the location from which the source power is sampled. B-CLEAN-SC averages the dirty maps over the frequency interval and uses the location of the maximum averaged source power. It then performs a standard CLEAN-SC iteration for each of the frequencies in the interval with individual source powers per frequency but at the shared location. Thus, the reconstruction at lower frequencies benefits from the resolution at higher frequencies, and the averaging of side- and grating lobes stabilized the process at very high frequencies.

4.4.1 Methodology

The B-CLEAN-SC algorithm is nearly identical to the CLEAN-SC algorithm when CLEAN-SC is performed for all frequencies in parallel with the exception that B-CLEAN-SC performs each iteration

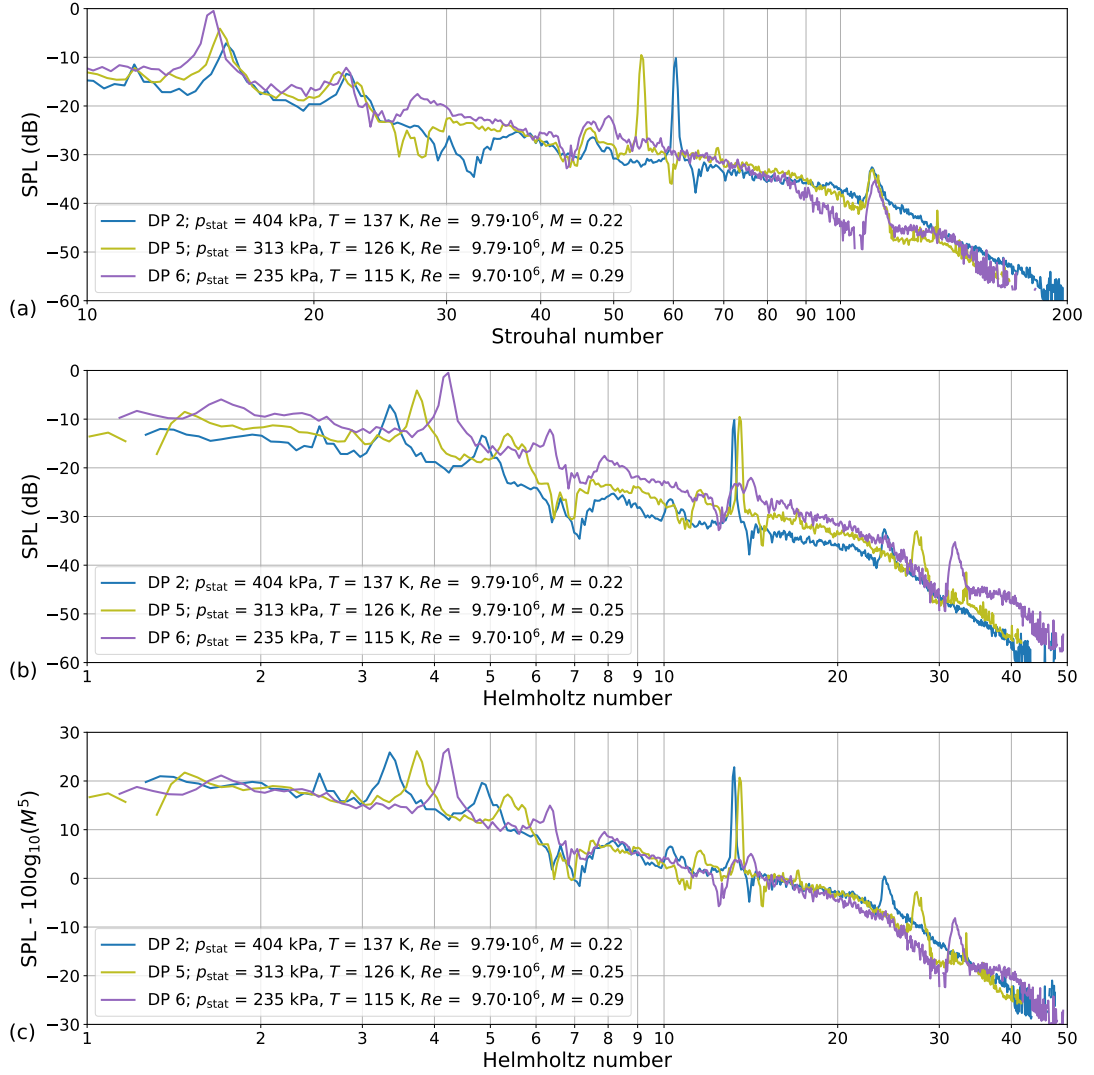


Figure 4.9: Integrated sources for DP 2, DP 5 and DP 6 of the left wing vs (a) Strouhal number and (b) and (c) Helmholtz number. The SPL in (c) is normalized with M^5 .

n at a shared location \mathbf{x}_k for all frequencies (within the processed interval \mathbf{f}). To determine the location, instead of using the maximum of the dirty map $\mathbf{A}_{jj}(f)$ separately for each frequency, the maximum of the over frequency averaged dirty map is used

$$k = \operatorname{argmax}_j \left(\left\langle \frac{\mathbf{A}_{ijj}}{\max_j(\mathbf{A}_{ijj}^0)} \right\rangle_i \right). \quad (4.4.1)$$

Here, \mathbf{A}_{ijj}^0 denotes the original dirty map prior to subtractions. i denotes the index of the frequency $f_i \in \mathbf{f}$, j denotes the index of the focus point \mathbf{x}_j . The subscript of the average operator $\langle \dots \rangle$ or the maximum argument operator indicates the dimension over which they are applied. \mathbf{A}_{ijj}^0 is an estimation for the frequency-dependent amplitude of the overall source power (which typically decreases over frequency for aeroacoustic sources). The normalization by its maximum compensates for this behavior. Eq. 4.4.1 is the only addition to the CLEAN-SC algorithm to obtain B-CLEAN-SC, see Algorithm 2. The algorithm is given for a frequency interval \mathbf{f} . If the frequency interval does not cover the full frequency range, B-CLEAN-SC is performed sequentially for multiple intervals.

Algorithm 2 B-CLEAN-SC for a frequency interval \mathbf{f} .**FUNCTION** B-CLEAN-SC($\mathbf{C}, \mathbf{w}, \alpha$): $\mathbf{Q} \leftarrow \mathbf{0}$ $n \leftarrow 0$ $\mathbf{A}_{ijj}^0 \leftarrow \mathbf{w}_{ij}^* \mathbf{C}_i \mathbf{w}_{ij}$ **while** $n \leq N$ **do** $n \leftarrow n + 1$ $\hat{\mathbf{A}}_{jj} \leftarrow \left\langle \frac{\mathbf{A}_{ijj}}{\max_j(\mathbf{A}_{ijj}^0)} \right\rangle_i$ $k \leftarrow \operatorname{argmax}_j(\hat{\mathbf{A}}_{jj})$ \triangleright change to the CLEAN-SC algorithm $A_{ikk} \leftarrow \mathbf{A}_{ijj}(\mathbf{x}_k)$ $\mathbf{h}_f \leftarrow \frac{\mathbf{C}_i \mathbf{w}_{ik}}{A_{ikk}}$ **if** DR **then** $\mathbf{H}_{ikk} \leftarrow \mathbf{h}_{ik} \mathbf{h}_{ik}^* \mathbf{I}_{kk}$ $\mathbf{h}_{ik} \leftarrow \frac{1}{1 + \mathbf{w}_{ik}^* \mathbf{H}_{ikk} \mathbf{w}_{ik}} \left(\frac{\mathbf{C}_i \mathbf{w}_{ik}}{\mathbf{w}_{ik}^* \mathbf{C}_i \mathbf{w}_{ik}} + \mathbf{H}_{ikk} \mathbf{w}_{ik} \right)$ **end if** $\mathbf{G}_i \leftarrow A_{ikk} \mathbf{h}_i \mathbf{h}_i^*$ $\mathbf{C}_i \leftarrow \mathbf{C}_i - \alpha \mathbf{G}_i$ $\mathbf{A}_{ijj} \leftarrow \mathbf{A}_{ijj} - \alpha \mathbf{w}_{ij}^* \mathbf{G}_i \mathbf{w}_{ij}$ $\mathbf{Q}(f_i, \mathbf{x}_k) \leftarrow \mathbf{Q}(f_i, \mathbf{x}_k) + \alpha A_{ikk}$ **end while****return** $\mathbf{Q}(\mathbf{f}, \mathbf{x})$

Note that the position \mathbf{x}_k is not necessarily located on the main lobe of a dominant source for all frequencies if the sources have a frequency-dependent power. Especially at low frequencies, where the PSF of a dominant source may cover all other sources and dominate the estimated power at their true positions, this would lead to an overestimation of their power and a subtraction of the main lobe when subtracting coherent portions of the map [116]. A low gain factor α is needed to relax this issue so that the number of necessary B-CLEAN-SC iterations increases. Since only the initial calculation of the dirty map is computationally expensive, the extra iterations are not performance-relevant.

4.4.2 CLEAN-SC and B-CLEAN-SC Results

This thesis proposes three evaluation cases. Case 1) is a synthetic 1D example that highlights the differences between standard CLEAN-SC and B-CLEAN-SC. The array is located at $-0.5 \leq x \leq 0.5$, $y = 0$. There are three sources S_i at $x_I = 0$, $x_{II} = 0.1$, $x_{III} = 0.5$, $y = 0.5$. The CSM is calculated at 256 frequencies $f_{\max} = 8192$ Hz, $\Delta f = 32$ Hz. The focus grid is located at $-1 \leq x \leq 1$, $y = 0.5$, $\Delta x = 0.004$ m. The PSD of S_I linearly increases over frequency from $\text{PSD}_I(f_0) = -10$ dB to $\text{PSD}_I(f_{256}) = 0$ dB. The PSD of S_{II} linearly decreases in the same way so that S_{II} dominates at low frequencies and S_I dominates at high frequencies. Additionally, S_{III} is a smallband source that is only present at $3616 \text{ Hz} \leq f \leq 3840 \text{ Hz}$ at -10 dB. For B-CLEAN-SC, the frequencies are processed in intervals of $\Delta f = 2048$ Hz.

Throughout this section, CLEAN-SC is performed with DR, a maximum of $3N_S$ iterations per frequency where N_S is the number of true sources, and a gain factor of $\alpha = 0.9$ per iteration. B-CLEAN-SC is performed with DR, a maximum of $10N_S$ iterations, and $\alpha = 0.1$ per iteration. Beamforming maps are obtained only in 1D for case 1), and 2D for cases 2) and 3) with steering vector formulation

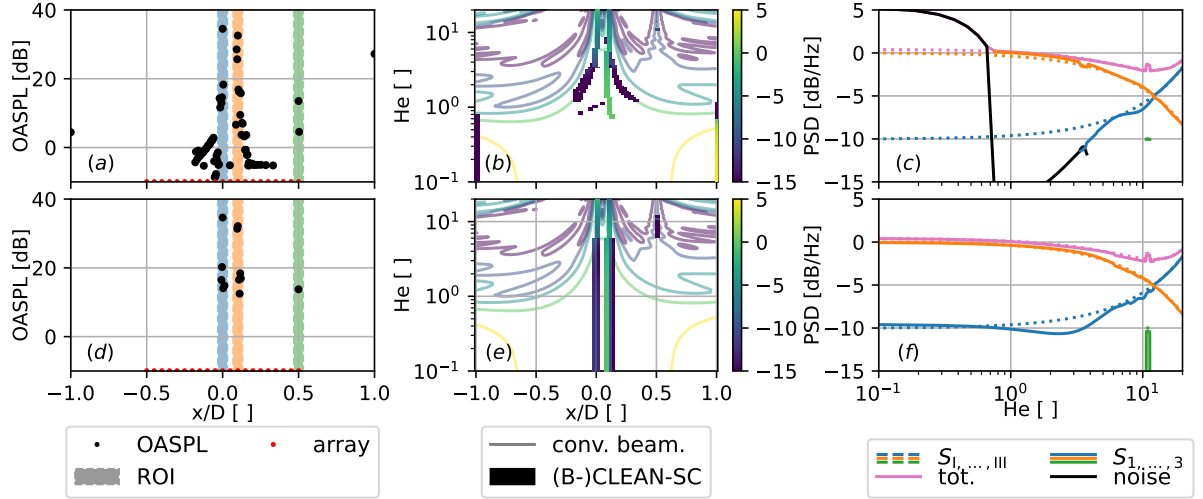


Figure 4.10: Case 1), the top row shows CLEAN-SC, the bottom row B-CLEAN-SC results. (a)&(d) show the OASPL(x/D), integrated over all frequencies. The sensor positions are marked at an arbitrary y -location. The shaded areas represent the ROI. (d)&(e) show the conventional beamforming result and the sparse (B-)CLEAN-SC result, the color indicates the PSD. (e)&(f) show the resulting spectra, integrated from the ROI in (a)&(d). The sources are depicted with different colors: S_1 (blue), S_2 (orange), S_3 (green), and the total integrated power (magenta). (B-)CLEAN-SC results that are not located within any ROI are spatially integrated and classified as noise (black). The ground truth is depicted with dotted lines and Latin numbers, the ROI estimation with full lines and Arabic numbers.

#f	1	2	4	8	16	32	64	128
correct PSD [%]	61.7	62.8	62.5	65.6	66.7	66.7	66.1	64.8
mean error [dB]	2.3	2.2	2.5	2.5	1.3	2.5	3.9	8.9
SNR [dB]	14.5	14.4	14.8	16.4	17.8	18.4	22.6	19.1

Table 4.1: Influence of the frequency interval \mathbf{f} on the resulting error metrics, where $\#\mathbf{f} = 128$ are all frequencies. $\#\mathbf{f} = 1$ corresponds to the CLEAN-SC result in Figure 4.11, and $\#\mathbf{f} = 16$ to the B-CLEAN-SC result, all with DR, $\alpha = 0.1$, $N = 30$.

III [107] instead of 3D to reduce the visual complexity of the results. The results are presented over the Helmholtz number $He = fD/a$, where D is the array's aperture in this case.

Figure 4.10 shows the results of case 1). Figure 4.10 (e)&(f) show the estimated PSD, integrated from the same colored ROI in Figure 4.10 (a)&(d). The black lines represent noise integrated from the area that does not correspond to any ROI, indicating beamforming and deconvolution artifacts. Additionally, a magenta line shows the integration of all sources within the map to estimate the overall sound power. The ground truth is depicted with dotted lines for reference.

CLEAN-SC reconstructs the dominant source S_2 down to $He \geq 0.8$, below which the maximum within the dirty map is estimated with a wrong level along the side lobes and then at the edges of the focal range. For S_1 , the PSD reconstruction works down to $He \geq 4$, below which it underestimates its power and misses the correct location. The smallband source S_3 is reconstructed perfectly. B-CLEAN-SC perfectly estimates the sources' locations. The PSDs are reconstructed throughout the

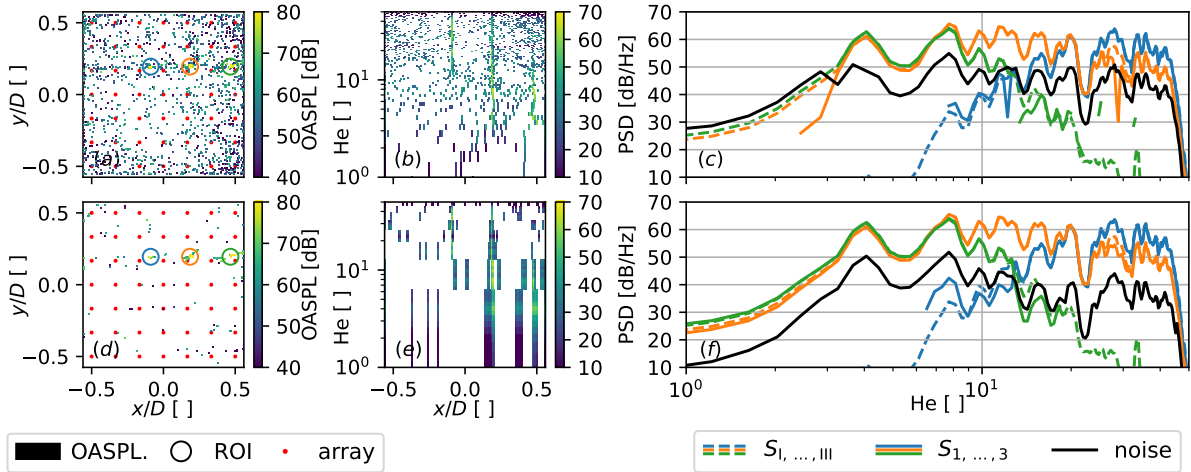


Figure 4.11: Case 2), the top row shows CLEAN-SC and the bottom row B-CLEAN-SC results. (a)&(d) show the OASPL($x/D, y/D$) with colored ROI centered around the true source locations, (b)&(e) show the PSD($x/D, He$) integrated over the y -dimension, (c)&(f) show the ground truth (dotted, Latin numbers) and estimated PSD (solid, Arabic numbers) from the identical colored ROI in (a)&(d). The black line represents noise, integrated from the areas that do not correspond to any ROI.

frequency range, except for S_1 at $He \approx 3$. For B-CLEAN-SC, there is no noise.

Figure 4.11 shows the results for case 2). Figure 4.11 (a)&(d) show that CLEAN-SC results in noisier OASPL maps than B-CLEAN-SC. When integrating the maps over x , Figure 4.11 (b)&(e) show that CLEAN-SC can determine the correct location down to $He \approx 3$. B-CLEAN-SC correctly determines throughout the frequency range. Strong side lobes are reconstructed as “ghost sources” that move closer to the true source position with increasing frequency. Figure 4.11 (c)&(f) shows the spectrum estimation. Source S_1 is estimated well by CLEAN-SC at $He \geq 8$. Source S_2 is estimated well down to $He \approx 1.5$, below which it can no longer be separated from S_3 , estimated well down to $He \geq 2$. Below this frequency, the overall power was estimated well but could not be attributed to a true source position, so it was integrated as noise. Both S_1 and S_3 are reconstructed down a Signal-to-Signal Ratio (SSR) of around $SSR = 30$ dB, which was used as an iteration stopping criterion. B-CLEAN-SC shows similar results, with improved reconstructions of S_2 and S_3 and lower noise levels.

Table 4.1 compares three metrics for exemplary frequency intervals, where $\#(\dots)$ is the number of elements. The relative frequency interval of the PSD that is correct (within a ± 3 dB margin of the ground truth (GT)) is defined for multiple sources S as

$$\text{corr. PSD} = \left\langle \frac{\#_f(-3 \leq |\text{PSD}(S, f) - \text{GT}(S, f)| \leq 3)}{\#_f \text{PSD}(S, f)} \right\rangle_S, \quad (4.4.2)$$

the mean absolute error (for frequencies where the PSD is defined, so that $\text{PSD} \neq -\infty$ dB)

$$\text{mean error} = \langle \langle |\text{PSD}(f) - \text{GT}(f)| \rangle_f \rangle_S, \quad (4.4.3)$$

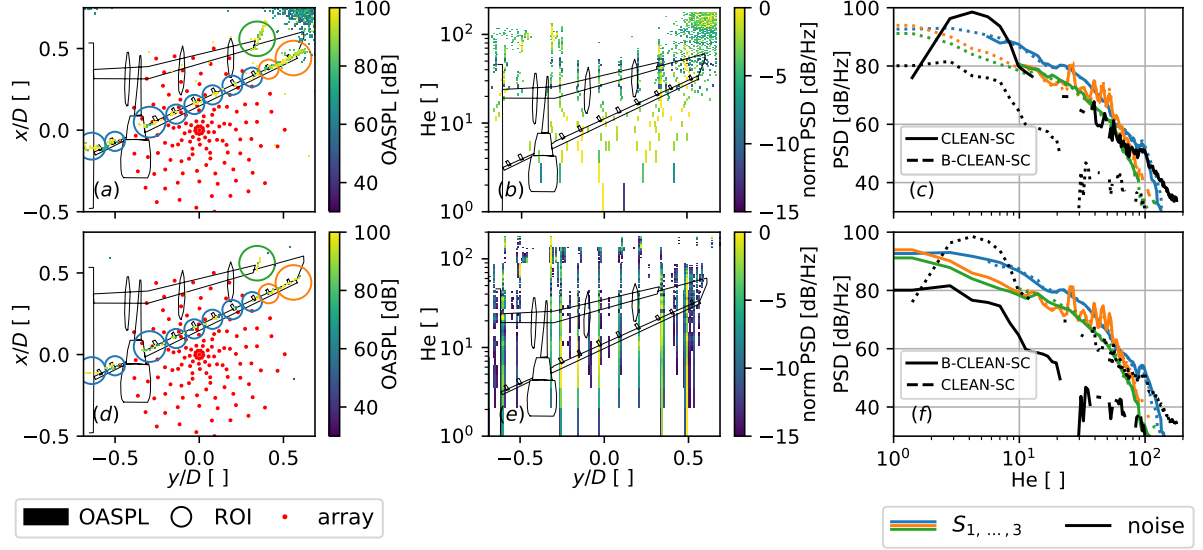


Figure 4.12: Case 3), the top row shows CLEAN-SC and the bottom row B-CLEAN-SC results. (a)&(d) show the OASPL($x/D, y/D$), (b)&(e) show the normalized PSD($y/D, He$) integrated over the x -dimension and normalized per frequency, the model is depicted for reference (but its x -information should be ignored). (c)&(f) show the estimated PSD from the identical colored ROI in (a)&(d). While (c) shows the CLEAN-SC results (solid), the B-CLEAN-SC solution is displayed with dotted lines, and in (f) vice versa for comparison. Black lines indicate noise.

and the SNR is the ratio of the maximum source level to the noise level (for frequencies where both are defined)

$$\text{SNR} = \langle \max_S (\text{PSD}(S, f)) - \text{noise}(f) \rangle_f. \quad (4.4.4)$$

Note that eq. 4.4.3 and eq 4.4.4 are conditional errors since they require a defined PSD estimation. Figure 4.11 (c)&(f) show that this is not always the case, so they must be evaluated as subsidiary results of eq. 4.4.2. For example, the low-frequency CLEAN-SC noise is not captured with the SNR metric, as no signal is present. Table 4.1 shows that B-CLEAN-SC outperforms CLEAN-SC with an increasing frequency interval, with an optimum at $16 \leq \#f \leq 32$. The SNR further improves with an increasing frequency interval, which indicates an improvement in spatial localization, but the spectral estimation deteriorates in return.

Case 3) uses the Dornier 728 data at $\text{Re} = 1.4 \times 10^6$, $\alpha = 1^\circ$, $M = 0.125$, see Section 3.2. This condition is especially challenging because the background noise strongly dominates over the sources, which are weak due to the low Mach number and low angle of attack. The results will be only discussed qualitatively since there exists no ground truth. Figure 4.12 (a)&(d) show the estimated OASPL($x/D, y/D$). The results correspond well to the geometric features of the wing, but CLEAN-SC shows noise in the top right corner, and sources such as the flap side edge are not well localized. Figure 4.12 (b)&(e) show the PSD(y, He), integrated over x and normalized per frequency. Thus, the only sources that can be confused in this depiction are an outboard slat track and the flap side edge at $y \approx 0.3$ m. The model is depicted for reference so that the estimated sources can be attributed to its geometrical features, such as the slat tracks. Note that the x -component of the model is plotted along the frequency axis, but the color map does not include any x -information. The

CLEAN-SC result clearly identifies slat tracks in a frequency range of $10 \leq He \leq 100$. Otherwise, the result mostly shows the inboard Krüger slat, the nacelle area, and the noise for $y/D \geq 0.5$. The source separation fails below $He \leq 10$. The B-CLEAN-SC result shows the same slat tracks as dominant sources. However, they are also reconstructed at low and high frequencies. Additionally, there is nearly no noise for $y/D \geq 0.5$. Additional sources are visible between the slat tracks, typically connected to slat cove tones [48]. Overall, the location of the estimated sources strongly correlates to the geometrical features of the model and is consistent over the whole frequency range.

Based on the analysis of this data [48] ROI are defined that cover the inner (Krüger) slat and the slat tracks (blue), the outer slat (orange), and the flap side edge (green). The ROI is chosen so that the integrated source types are similar [8, 48]. Figure 4.12 (a)&(d) show the (identical) ROI, and Figure 4.12 (c)&(f) show the corresponding PSD. Below $He \leq 10$, CLEAN-SC fails to reconstruct individual sources, resulting in strong noise, additional to the noise $He \geq 40$. B-CLEAN-SC reconstructs the PSD throughout the frequency range with approx. 20 dB less noise. For frequencies where both methods produce a source spectrum, they coincide.

4.5 Global Optimization

This section presents broadband Global Optimization (GO) and is based on original work [53]. Beamforming relies on several assumptions to obtain a solution. The main assumptions generally include one or all of these: spatially compact sources, monopole sources, incoherent sources, and independent sound radiation for each frequency, as well as undisturbed sound propagation through the medium, which are typically violated in real-world scenarios [6, 16, 77, 88].

Recently, gridless methods emerged that have several advantages over grid-based methods. In these gridless methods, the focus points are no longer fixed in space. Thus, the inverse problem becomes nonlinear, but the number of unknown variables is reduced by multiple orders of magnitude in return since fewer focus points are needed. These methods include subspace beamforming [108], machine learning based methods [71], and Covariance Matrix Fitting (CMF) methods [24, 26, 27, 28].

GO is a gridless CMF method, employing a global optimizer such as Differential Evolution [132, 83]. In this method, a synthetic CSM is directly fitted against an observed CSM based on a Mean Squared Error (MSE) energy function that is minimized based on varying the estimated source positions and source strengths. While the method is straightforward, global optimizers are computationally expensive and not guaranteed to find the global minimum [26, 95]. Conversely, the advantage is that CMF methods do not impose any limitations on the model. Thus, including and optimizing parameters often neglected in beamforming methods is possible. This Section includes multipoles in the source model as proof of concept for advanced properties that can be obtained with GO.

Quasi-stationary aeroacoustic sound sources are typically geometry-driven (e.g., leading and trailing edges). Thus, the resulting source locations are constant over frequency [47]. This thesis uses this observation to introduce source objects with multiple properties, such as a location and dipole rotation, which are constant over frequency. This thesis introduces a modified broadband energy function

to GO that allows the CSM-fitting of all frequencies at once, using the source and propagation parameters shared for all frequencies. This thesis shows that the PSF drives the energy, which, depending on the problem, can lead to strong local minima. The proposed broadband energy averages the MSE over all frequencies, equivalent to averaging the PSF and resulting in a much smoother energy function.

4.5.1 Methodology

This subsection uses source objects introduced in Section 2.1.3 and the energy function E for the CSM-fitting. Further, it presents the spectra generation problem from beamforming results and typical solution approaches.

Energy function and optimization

To optimize \mathbf{q} and \mathbf{T} , we need an energy function E to solve eq. 2.1.50, also referred to as a cost function. Von den Hoff et al. [132] suggest the MSE between the measured CSM c_{meas} and the estimated CSM c_{mod} , that is

$$E(f) = \sum_{\hat{i}} \left(|c_{\text{mod},\hat{i}}(f) - c_{\text{meas},\hat{i}}(f)|^2 \right) . \quad (4.5.1)$$

Only elements \hat{i} corresponding to the Vectorized Upper Triangular (VUT) CSM without diagonal should be evaluated to exclude uncorrelated self-noise. Note that according to eq. 2.1.50 c_{mod} is the superposition of the uncorrelated source CSMs so that the energies are added for multiple sources.

Here, the energy function is evaluated for each frequency separately. We will reformulate the energy function so that it is evaluated for all frequencies simultaneously. Since the energy is compared for a varying number of frequencies and microphones, the sum is replaced by an average $\langle \dots \rangle$ over all employed frequencies and upper CSM entries. The average subscript indicates which variable is averaged. An additional normalization for each frequency accounts for different source strengths at different frequencies. The new energy function is

$$E = \left\langle \frac{|c_{\text{mod},\hat{i}}(f_j) - c_{\text{meas},\hat{i}}(f_j)|^2}{\langle |c_{\text{meas},\hat{i}}(f_j)|^2 \rangle_{\hat{i}}} \right\rangle_{\hat{i},j} . \quad (4.5.2)$$

Note that the normalization is based on the measured CSM and thus corresponds to the maximum observed source level per frequency, combined for all sources. Thus, this normalization does not change the relative amplitude levels between several sources at a given frequency. It only changes the combined source levels over frequency so that the energy is weighted equally at each frequency.

We will refer to GO with eq. 4.5.2 for a single frequency (essentially equal to eq. 4.5.1) as standard GO, and eq. 4.5.2 for multiple frequencies as broadband GO. To make the error more robust for real-world applications, and since eq. 2.1.50 is no longer linear, it is also possible to choose the l_1 norm over the l_2 norm (typically chosen to ensure a convex error), which does not prefer single large CSM deviations in the optimization process. A weighted norm, based on the standard deviation of

	N_{true}	datatype	sourcetype	Section	Figures
case 1	1	syn.	monopole	4.5.1	4.13, 4.14, 4.15, 4.16
case 2	2	syn.	monopole	4.5.1	4.17, 4.18, 4.19
case 3	1	syn.	monopole	4.5.2	4.20, 4.21, 4.22
case 4	2	syn.	monopole	4.5.2	4.20, 4.21, 4.22
case 5	3	real	monopole	4.5.2	4.24,4.25,4.26
case 6	2	syn.	multipole	4.5.2	4.27

Table 4.2: Main cases considered in this thesis and their differences, e.g. the number of true sources N_{true} . The cases typically contain sub-cases, where depending on the employed method the properties $N_{\text{est.}}$, broad- and small-band energy, and Mach number are varied.

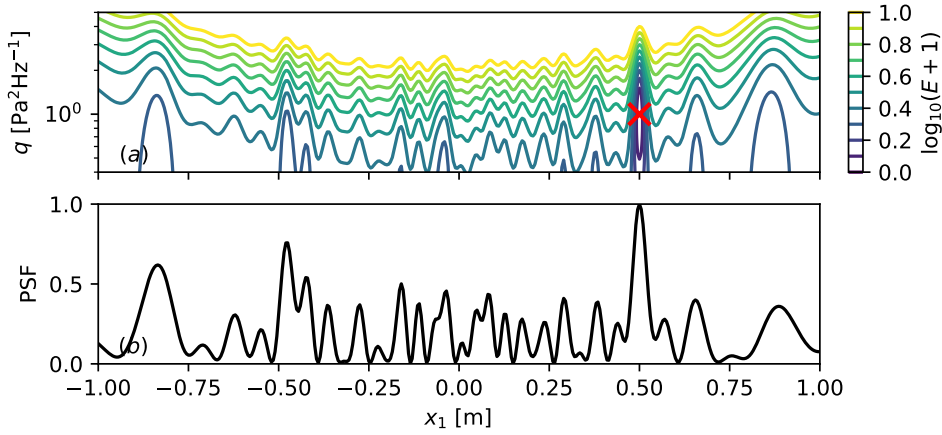


Figure 4.13: Case 1a). (a) shows isocontour lines of the energy for (x_1, q) variations from eq. 4.5.2 for $x_2 = 0.5$ m, $x_3 = 0$ m, and $f = 6144$ Hz. The true source position is marked (red x). (b) shows the corresponding PSF (steering-vector IV [107, 77, 25]) for a source location at $y = [0.5, 0.5, 0]^T$ m.

the CSM Welch averages [106], may further improve the estimation. To limit the several options, we will only analyze the formulation 4.5.2 as a baseline for broadband GO in this thesis.

Energy of a single synthetic monopole

The energy is explored numerically due to the nonlinearity of the propagation operator, the non-convex energy function, and non-uniqueness (the solution is at least permutation invariant). This thesis will contain several different setups summarized in Table 4.2. First, a synthetic monopole at $y = [0.5, 0.5, 0]^T$ m with $q(f) = 1 \text{ Pa}^2 \text{ Hz}^{-1}$ is generated. An equidistant 1D-array at $-0.5 \text{ m} \leq x_1 \leq 0.5 \text{ m}$, $x_2 = 0$ m, $x_3 = 0$ m detects the sound-field with $M = 5$ microphones. The broadband GO energy from eq. 4.5.2 is calculated for a single frequency (equivalent to standard GO, see eq. 4.5.1) as case 1a) at $f = 6144$ Hz, and for multiple frequencies as proposed in this thesis at $2^{10} \text{ Hz} \leq f \leq 2^{15} \text{ Hz}$ with $\Delta f = 1024$ Hz as case 1b). Note, due to the normalization over frequency in eq. 4.5.2, the broad-band energy in case 1b) will be identical for frequency-dependent source amplitudes.

Figure 4.13 (a) shows the case 1a) log-energy for the variation of (q, x_1) for $x_2 = 0.5$ m, $x_3 = 0$ m. The variables not shown in the energy maps (i.e., x_2, x_3) are set correctly so that the energy deviations from zero are only caused by the displayed variables (i.e., x_1, q). The global minimum is at

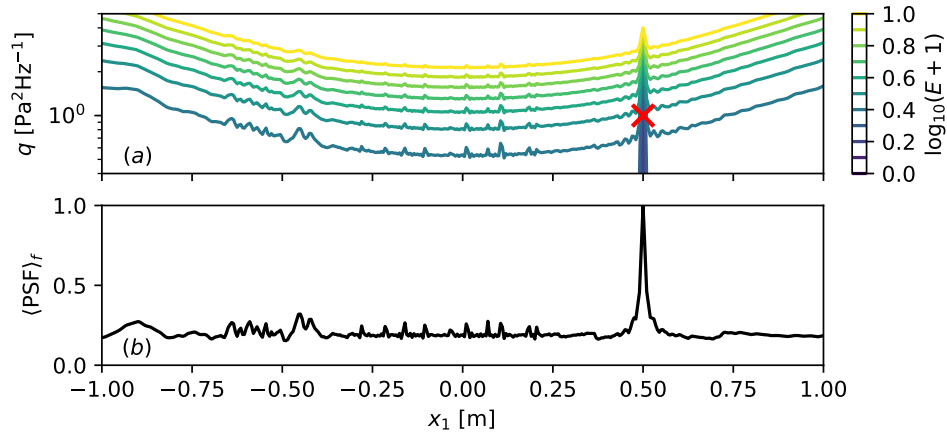


Figure 4.14: Case 1b). (a) shows the energy for (x_1, q) variation from eq. 4.5.2 for $x_2 = 0.5$ m, $x_3 = 0$ m, and $100 \text{ Hz} \leq f \leq 20 \text{ kHz}$, $\Delta f = 100 \text{ Hz}$. (b) shows the corresponding PSF (steering-vector IV [107, 77, 25]), averaged over the frequency, for a source location at $y = [0.5, 0.5, 0]^T$ m.

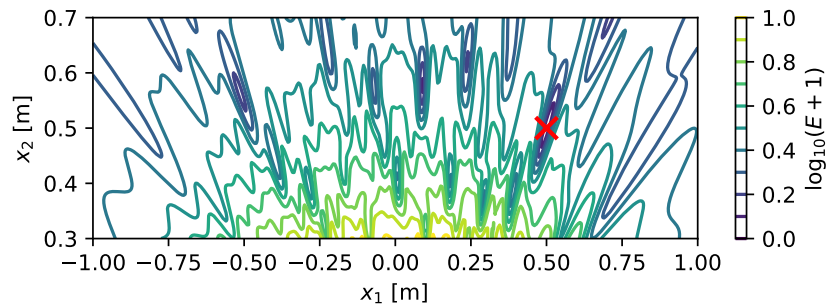


Figure 4.15: Case 1a), energy for (x_1, x_2) variation from eq. 4.5.2 for $x_3 = 0$ m, $q = 1 \text{ Pa}^2$, and $f = 6144 \text{ Hz}$.

$E = 0$, where the variables coincide with the true monopole location and source strength. Multiple local minima are visible for case 1a), so that for a given q , the energy looks like a reciprocal Point Spread Function (PSF) with grating lobes, shown in Figure 4.13 (b). With the averaging over the frequency in case 1b), the PSF and local minima are also averaged, see Figure 4.14 (a) and (b). Thus, the energy becomes mostly smooth.

Figure 4.15 and Figure 4.16 show the corresponding energy of variations of (x_1, x_2) for the correct amplitude. Again, most of the local minima of the single-frequency energy are smoothed for the broadband energy. Additionally, the gradient towards the global minimum is much steeper for the broadband energy. The depicted energy map will increase in smoothness with an increasing number of frequencies (either due to faster sampling rates or larger Welch block sizes, not shown here).

Energy of multiple synthetic monopoles

We will now examine the energy function for a two-source problem. The true sources will be denoted with Roman numbers. The synthetic monopoles are located at $y_I = [0.5, 0.5, 0]^T$ m, $y_{II} = [0.5, 0.6, 0]^T$ m, $q_I(f) = 1 \text{ Pa}^2 \text{ Hz}^{-1}$, $q_{II}(f) = 0.5 \text{ Pa}^2 \text{ Hz}^{-1}$, so that source S_{II} is located slightly behind source S_I . Again, the energy will be calculated for a single frequency $f = 6144 \text{ Hz}$ as case 2a)

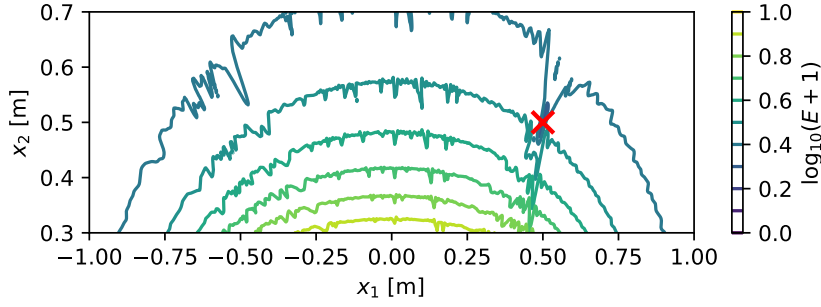


Figure 4.16: Case 1b), energy for (x_1, x_2) variation from eq. 4.5.2 for $x_3 = 0$ m, $q = 1$ Pa², and $2^{10}\text{Hz} \leq f \leq 2^{15}\text{Hz}$.

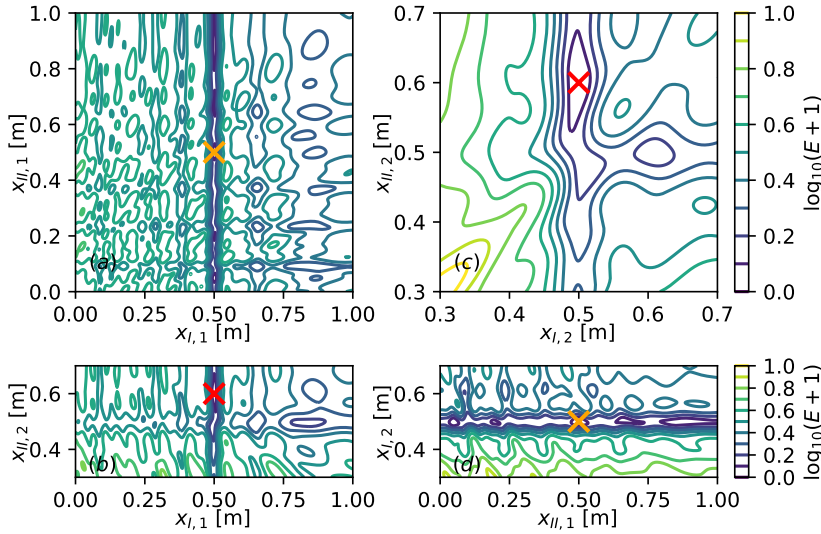


Figure 4.17: Case 2a), slices of the six-dimensional energy, see eq. 4.5.2. All variables for each slice are chosen correctly, except for the shown combinations of (a) $(x_{I,1}, x_{II,1})$, (b) $(x_{I,1}, x_{II,2})$, (c) $(x_{I,2}, x_{II,2})$, (d) $(x_{II,1}, x_{I,2})$. The source positions are marked (x) for S_I (orange), and S_{II} (red).

and multiple frequencies $2^{10}\text{Hz} \leq f \leq 2^{15}\text{Hz}$ with $\Delta f = 1024$ Hz as case 2b). Since the energy space is six-dimensional (three coordinates per source, one amplitude per source, because the amplitude is constant over frequency), only 2D (x_1, x_2) -slices of the energy space are presented. The slices are chosen so that all variables are correct except for the two being displayed.

Figure 4.17 shows the single frequency energy from eq. 4.5.2 for case 2a). The true source positions are marked with an x. For the single frequency energy map (a), (b), and (d), there is a trend of low energy at the correct x_1 positions visible. However, periodically repeating local minima are visible due to the array's PSF at the given frequency. Figure 4.18 shows the corresponding broadband energy for case 2b), which, in comparison, shows a clear global minimum with steep gradients. However, the energy map is not smooth and exhibits minor local minima. Note that these minima appear magnified due to the logarithmic plot of the energy. Figure 4.17 and Figure 4.18 (c) show the variation of x_2 for both sources, for the correct $x_1 = 0.5$. Here, one can see that the main local minimum is caused by the spatial permutation of the sources (when S_I and S_{II} swap their positions), again showing that the problem does not have a unique solution. These results show that the energy function, minimized during the GO CSM-fitting optimization, contains local minima caused by the array's PSF. These

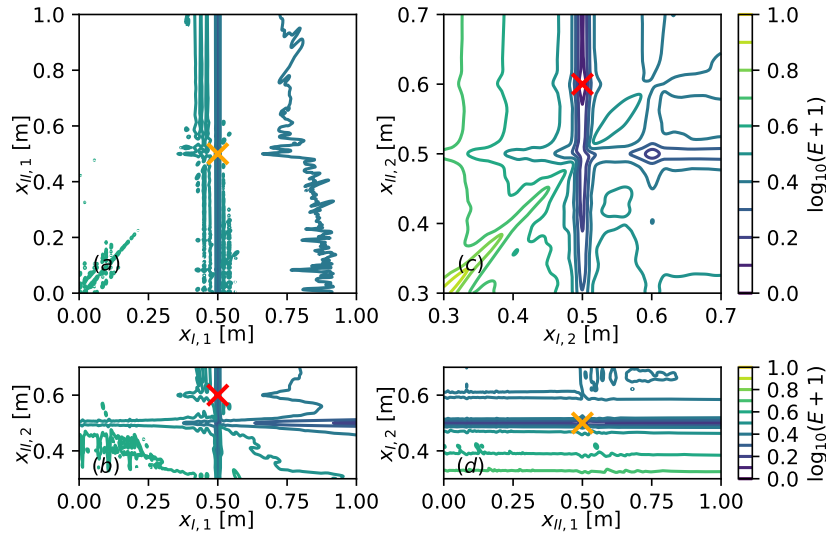


Figure 4.18: Case 2b), slices of the six-dimensional energy, see eq. 4.5.2. All variables for each slice are chosen correctly, except for the shown combinations of (a) $(x_{I,1}, x_{II,1})$, (b) $(x_{I,1}, x_{II,2})$, (c) $(x_{I,2}, x_{II,2})$, (d) $(x_{II,1}, x_{I,2})$. The source positions are marked (x) for S_I (orange), and S_{II} (red).

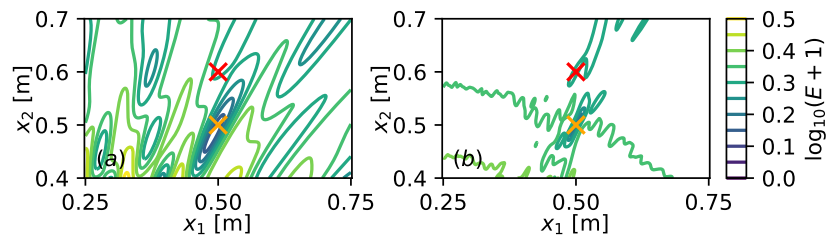


Figure 4.19: Case 2c), (a) smallband energy at $f = 6144$ Hz and (b) broadband energy, with a mismatch of $N_{\text{true}} = 2$, and $N_{\text{est.}} = 1$ for $q = 0.5 \text{ Pa}^2 \text{ Hz}^{-1}$, $x_3 = 0$ m.

minima can be reduced using multiple frequencies at once with the broadband energy formulation in eq. 4.5.2 so that the energy function is mostly smooth.

A question remains if an estimated source is guaranteed to approximate a single true source or if a single estimated source may be located between two real sources, trying to approximate both. This question is of interest since all estimated sources are fitted at once so that the errors of the estimated sources are not independent. While it seems that this is the case from Figure 4.17 and Figure 4.18, where there is no strong local minimum between two true source positions, it is hard to tell, since we only observed slices of the high-dimensional energy function.

This thesis proposes case 2c) to explore this topic further. Case 2c) has a mismatch of the true number of sources $N_{\text{true}} = 2$, and estimated sources $N_{\text{est.}} = 1$. Figure 4.19 (a) shows the resulting single frequency energy, and Figure 4.19 (b) the corresponding broadband energy. The energy is reduced for an estimation of any true source position. However, due to the closer distance of S_I to the array and the decay in amplitude over distance, see eq. 2.1.23, an estimation of S_I reduces the energy significantly more than an estimation of S_{II} . For both energies, the gradient around the source positions leads towards the true positions, and again, there is no local minimum between the

source positions. While this observation might be different for coherent and distributed sources, this means for spatially compact, incoherent monopoles that each estimated source will approximate a single true source. If a local minimum is found for a source, the global minimum for other sources is at the correct location, see Figure 4.17 and Figure 4.18.

A mismatch between the number of true and estimated sources is not problematic, and either an iterative addition of estimated sources [26] until the energy is not reduced anymore or a simple overestimation of sources will be a viable strategy to find all true sources.

Source identification and spectra generation

Another issue for beamforming methods that calculate results independently for each frequency share is that generating a spectrum is not trivial, see Chapter 5. The first challenge is that it is typically unknown how many sources are located within the map, how they are distributed, and in which frequency ranges they can be observed. The second challenge is that true sources are masked by beamforming artifacts, such as side lobes of other sources. The third challenge is generating the correct spectrum from the beamforming map. All single-frequency methods have in common that spectra are obtained by estimating the number and locations of the sources, assigning the source-parts either to a source or rejecting them as noise, and then integrating all source-parts per frequency assigned to a source.

This procedure will be different for the proposed broadband GO method since the source objects already include a full spectrum. However, multiple source objects may be located very close together, either because they approximate a distributed source with multiple point-like source objects or because the solution of GO is not unique. Due to the super-position invariance of the CSM-fitting process, any number of source objects may be located at the exact location, and the true source strength may be arbitrarily distributed between the estimated source objects. This thesis proposes the definition of a minimum spatial distance for these cases, below which source objects will be grouped, and their spectra will be integrated. This can be only performed for spatially compact monopole sources, as more complex properties such as a dipole rotation must be considered when integrating sources.

4.5.2 Results

This section presents standard GO, broadband GO, and CLEAN-SC results with steering vector IV for increasingly complex problems, such as synthetic monopoles, real monopoles, and synthetic dipoles, listed in Table 4.2. Many algorithms exist for GO, which feature a variety of hyper-parameters that can be tuned [83, 132]. Since the main goal is to establish a baseline of broadband GO, hyper-parameter tuning and an exploration of different GO algorithms are out of the scope of this thesis. Thus, Dual annealing [131] with SciPy's standard hyper-parameters is used. L-BFGS-B [131] with SciPy's standard hyper-parameters is used for local optimization.

Global optimization on synthetic monopoles

To evaluate the proposed method, and to compare it to standard GO and CLEAN-SC [114] two examples are proposed. First, case 3) contains a monopole located at $y_I = [0.5, 0.5, 0]^T$ m, with

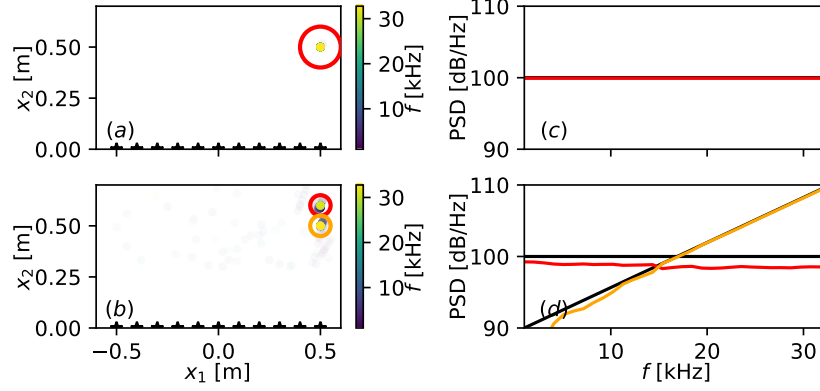


Figure 4.20: CLEAN-SC result for top row case 3), bottom row case 4). (a) and (b) show the spatial distribution of microphones (\star), and of the source-parts (\cdot), their color encodes the corresponding frequency. The opacity indicates the per frequency normalized log-power. (c) and (d) show the integrated spectra, based on the corresponding ROI (o) in (a) and (b). The ground truth PSD is depicted in black.

$Q_I(f) = 100 \text{ dB Hz}^{-1}$, where $Q = 10 \log_{10} (q/4 \times 10^{-10} \text{ Pa}^2)$. Second, case 4) contains two incoherent monopoles with $y_I = [0.5, 0.5, 0]^T \text{ m}$, $Q_I(f) = a_0 f + b_0 \text{ dB Hz}^{-1}$ with $a_0 = 5/7936$ and $b_0 = 2770/31$ so that it increases linearly from $Q_I(2^{10} \text{ Hz}) = 90 \text{ dB Hz}^{-1}$ to $Q_I(2^{15} \text{ Hz}) = 110 \text{ dB Hz}^{-1}$, and $y_{II} = [0.5, 0.6, 0]^T \text{ m}$, $Q_{II} = 100 \text{ dB Hz}^{-1}$. Thus, source S_{II} is located behind source S_I (similar to Section 4.5.1). The array is an equidistant 1D-array at $-0.5 \text{ m} \leq x_1 \leq 0.5 \text{ m}$, $x_2 = 0 \text{ m}$, $x_3 = 0 \text{ m}$ with $M = 11$ microphones. To acquire depth-information with conventional beamforming, steering vector formulation IV [107, 77, 25] and a focus grid $-1 \text{ m} \leq x_1 \leq 1 \text{ m}$, $0.3 \text{ m} \leq x_2 \leq 0.7 \text{ m}$ with $\Delta x_1 = \Delta x_2 = 0.01 \text{ m}$, and $x_3 = 0 \text{ m}$ is chosen.

Figure 4.20 shows the corresponding CLEAN-SC result, top row case 3), bottom row case 4). The first column shows the spatial position of the reconstructed source-parts. A source-part is defined as a single q in a single location and frequency with $q(x, f) > 0 \text{ Pa}^2 \text{ Hz}^{-1}$, that - once integrated through a ROI - provides a source spectrum [47], see Section 4.5.1. The source-parts' color indicates their frequency, and their opacity indicates their log power-level $\log(q + 1)$, normalized for each frequency independently to $[0, 1]$. In Figure 4.20 (a), all source-parts are (correctly) located at the same position. Thus, only one source-part is visible. The ROI are manually defined at the true source locations with case 3) radii $r_I = 0.1 \text{ m}$, and case 4) $r_{II} = 0.05 \text{ m}$ so that the ROI do not overlap. Figure 4.20 shows in the right column the corresponding integrated spectra. Outside of any ROI, source-parts are integrated and labeled as (background) noise. The position and PSD of the single monopole configuration in case 3) are estimated perfectly. For case 4), the dominant source-parts are close to the true source position. However, there is much noise at low frequencies, and the PSD of source S_{II} is underestimated.

GO requires a fixed number of estimated sources, which is typically unknown beforehand. To be able to find and resolve all sources, a simple strategy is to overestimate the number of sources, see Section 4.5.1. Thus, the solution is approached with two sub-cases. First, standard GO is performed with the correct number of estimated sources $N = 1$ as case 3a), then standard GO is performed with an additional estimated source $N = 2$ as case 3b). For case 4) we will underestimate $N_{\text{est.}} = 1$ as

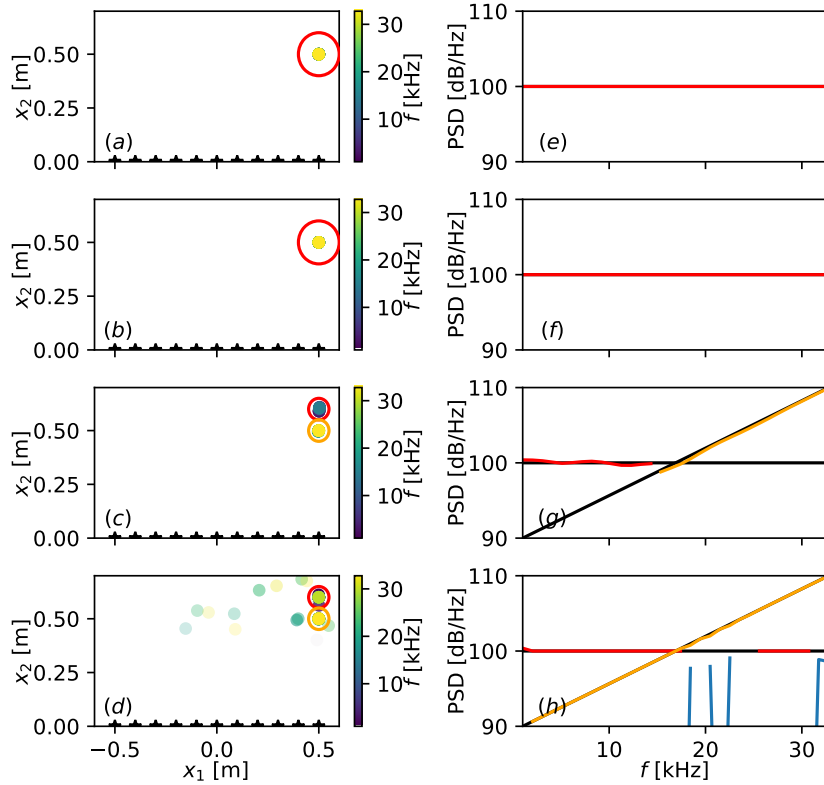


Figure 4.21: Standard GO. First row: case 3a), second row: case 3b), third row: case 4a), fourth row: case 4b). (a), (b), (c), and (d) show the estimated source locations (\cdot), the color displays the corresponding frequency, the opacity the per frequency normalized log-power. (e), (f), (g), and (h) show the PSD estimation (-), integrated from the corresponding ROI (o) in the left row. The ground-truth is depicted in black, sources that do not lie in any ROI are integrated as noise (blue).

case 4a) and overestimate $N_{\text{est.}} = 3$ as case 4b). True sources will be denoted with Roman numbers (e.g. S_I), and estimated sources with Arabic numbers (e.g. S_1).

Figure 4.21 shows the results of standard GO. The left column shows the estimated position of the source-parts, the color encodes their frequency. For cases 3a) and 3b), the source-parts are located mostly in the same (correct) location. For case 4), the source-parts are scattered around the map at medium to high frequencies. A ROI according to the CLEAN-SC result is defined, see Section 4.5.1, since for standard GO a source location is estimated for each frequency separately. The spectra are correctly reconstructed for cases 3a) and 3b). For case 4a), the single estimated source always (correctly) estimates the dominant source. For case 4b), the reconstruction fails for $S_{II}(f \geq 17 \text{ kHz})$, which is likely due to the spatial aliasing and local minima in the energy caused by the side- and grating lobes, see Section 4.5.1. Thus, one can expect the results to gradually improve by increasing the number of global optimization searches [132].

Figure 4.22 shows the result of the proposed broadband GO method. For case 3a) and case 3b), the source location and amplitude are estimated correctly, like for standard GO, and CLEAN-SC. For case 3b), S_2 is arbitrarily positioned with a low PSD and can be neglected. For case 4a) S_1 spatially estimates the source with the highest overall contribution to the CSM (S_I), but at very low

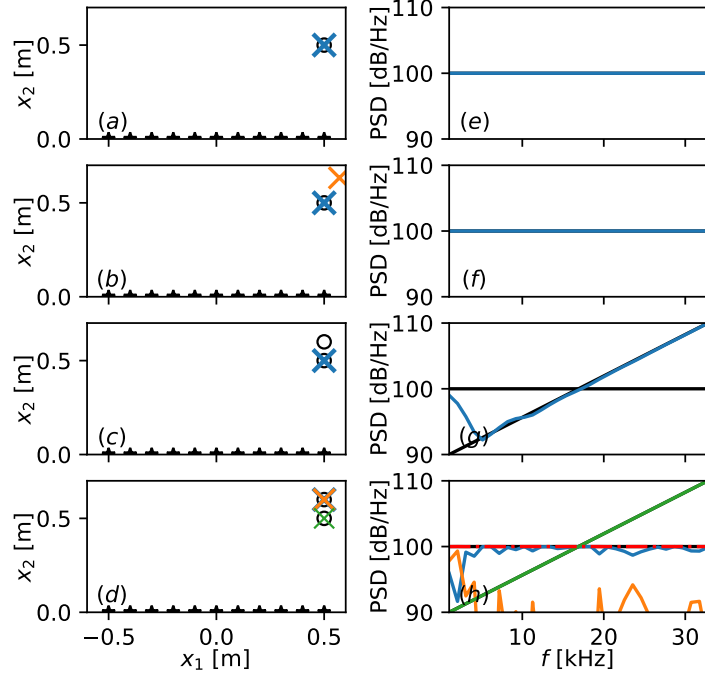


Figure 4.22: Broadband GO. First row: case 3a), second row: case 3b), third row: case 4a), fourth row: case 4b). (a), (b), (c), and (d) show the true source locations (o) and estimated source object locations (x), (e), (f), (g), and (h) show the corresponding PSD estimations (-). The dashed, red line represents the PSD summation of S_1 (blue) and S_2 (orange), which are located at the same spatial position.

frequencies where the array cannot resolve S_I and S_{II} anymore, S_1 estimates S_{II} , which contributes more towards the CSM. For case 4b), S_{II} is estimated with the superposition of S_1 and S_3 , since their position is identical, see Section 4.5.1. The spectral density is arbitrarily distributed between them, but the summation of both spectra reveals that their sum approximates the true PSD. The spectra are reconstructed well throughout the frequency range, and the method outperforms CLEAN-SC and standard GO (for the given number of iterations). The results indicate that overestimating sources is a viable strategy to find and reconstruct all true sources with low errors.

Global optimization on real monopoles

The generic monopole data is used at Mach $M = 0$ as case 5a), see Section 3.1, to evaluate the proposed method on real data.

Conventional beamforming and CLEAN-SC with steering vector formulation IV [107, 77, 25] is performed as a benchmark, see Figure 4.23. The left column depicts the spatial setup and source-parts, their color indicates the frequency, and their opacity indicates the per-frequency normalized SPL. Since the problem is three-dimensional, (a) shows a (x_1, x_2) and (b) shows a (x_1, x_3) projection. There are three ROI defined based on the true source positions with a radius of $r_1 = r_2 = 0.075$ m, $r_3 = 0.3$ m. Due to the low array resolution in x_3 , the ROI are elongated with $r_3 = 4r_{1,2}$. Every source-part within these radii is integrated for the estimated source spectrum, and every source-part not contained in any ROI is integrated and classified as noise. Figure 4.23 (c) shows the corresponding spectra, the estimated ROI spectra are depicted with dashed lines, and the ground truth is

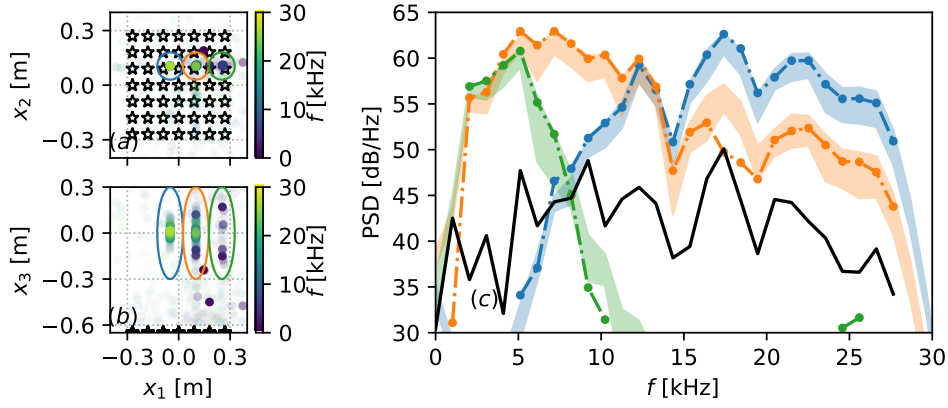


Figure 4.23: CLEAN-SC results for case 5a). (a) and (b) show projections of the spatial distribution of source-parts, their frequency, and normalized amplitude. (c) shows the PSD reconstruction (dotted lines), based on same colored ROI with $r_1 = r_2 = 0.075$ m, $r_3 = 0.3$ m. The ground truth is depicted in the same color with $\pm 1\sigma$ standard deviation.

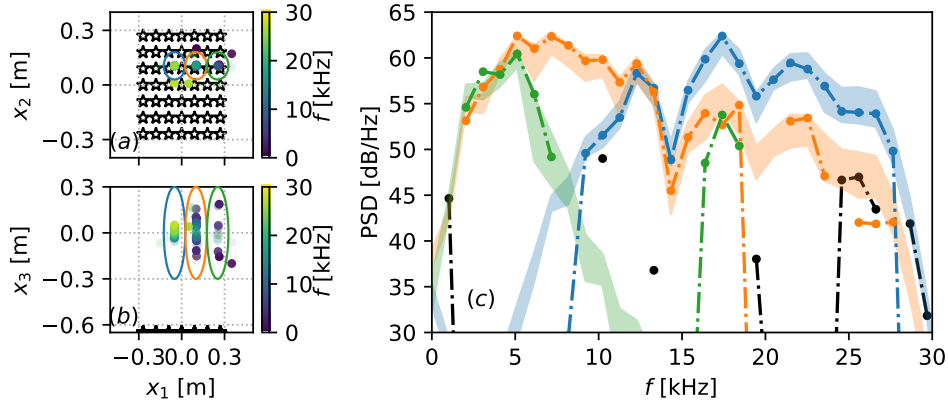


Figure 4.24: Standard GO results for case 5a), three true sources, and $N = 4$. (a) and (b) show projections of the spatial distribution of source-parts, their frequency, and normalized amplitude. (c) shows the PSD reconstruction (dotted lines), based on same colored ROI with $r_1 = r_2 = 0.075$ m, $r_3 = 0.3$ m. The ground truth is depicted in the same color with $\pm 1\sigma$ standard deviation.

depicted as the mean $\pm 1\sigma$ standard deviation. Overall, CLEAN-SC is able to reconstruct the spectra up to a SNR ≈ 30 dB at around $f \approx 10$ kHz. There is an underestimation of the source power of S_2 at $f \approx 17$ kHz. At high frequencies $f \geq 28$ kHz the source reconstruction fails. Additionally, there is much noise at all frequencies that does not correspond to any ROI. It is mainly located at the grating- and side lobe locations [47]. Thus, an optimized array geometry would improve the results.

Figure 4.24 shows the standard GO results for $N = 4$. The space-frequency source-part distribution is very similar to CLEAN-SC. While the reconstruction of S_I at $f \approx 17$ kHz is more accurate, CLEAN-SC outperforms standard GO at low frequencies and low SNR. Generally, the PSD estimation is good for dominant sources. However, the locations of the source-parts are not well estimated, so they are often located in the wrong ROI. It is assumed that the results improve with an optimized array geometry and an increasing number of global searches.

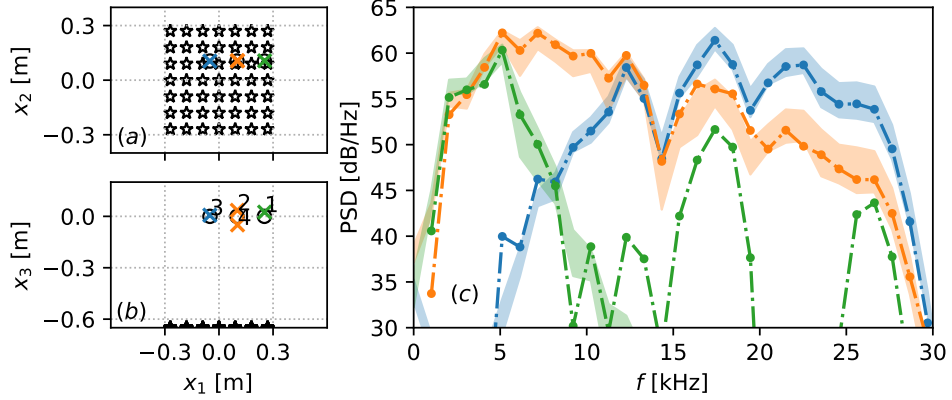


Figure 4.25: Broadband GO result for case 5a), three true sources, and $N_{\text{est.}} = 4$. (a) and (b) show projections of the spatial distribution of the estimated source objects S_i , their ordering is shown in (b). (c) shows the PSD reconstruction (dotted lines), based on the single or integrated source objects (S_{II} is approximated by S_2 and S_4). The ground truth is depicted in the same color with $\pm 1\sigma$ standard deviation.

Figure 4.25 shows the proposed broadband GO result for $N = 4$. In the left column, the estimated source positions are depicted. On the right, the corresponding PSD is depicted. The estimated source object positions (x) are depicted in the same color as the true sources, S_{II} (orange) is estimated by two source objects. Since the ordering of the sources is random, these correspondences were identified based on the spatial distances to the true positions. Note that this assignment problem only arises because of the comparison to the ground truth and does not need to be solved for typical beamforming applications. Similar to the CLEAN-SC result, the sources are well localized in x_1 and x_2 , and S_{II} is slightly distributed in x_3 direction. Figure 4.25 (c) depicts the estimated source spectra by integrating all estimated source objects that correspond to a true source position, which correspond well to the ground source, except for S_{III} which shows two prominent high-frequency bumps.

Overall, the CLEAN-SC and broadband GO results are very similar in terms of SNR, but broadband GO outperforms CLEAN-SC at $f \approx 17$ kHz and high frequencies. The main difference is that the CLEAN-SC result is very noisy, while there are two prominent bumps in the estimated spectrum of S_{III} . The similar shape of the CLEAN-SC noise and GO bumps are likely caused by the before-mentioned monopole assumption violation and reflections, as can also be seen for the same frequencies in Figure 3.2. This inclusion seems to minimize the observed CSM, similar to case 4a) in Figure 4.22 (g), where at low frequencies, the dominant source PSD is estimated instead of the true PSD.

Local optimization on real monopoles

Given that one uses a method like SIND [47] to automatically obtain source positions and spectra from CLEAN-SC maps, this information can be used as initial guesses to transition from Global Optimization to Local Optimization (LO), since the error function is smooth in the amplitude dimension, see Section 4.5.1. The main reason to perform broadband GO or LO after acquiring a CLEAN-SC result would be to include properties in the source object that are neglected by conventional beamforming and CLEAN-SC, such as multipoles. The main reason to perform LO over GO is that GO is computationally very expensive [95, 26].

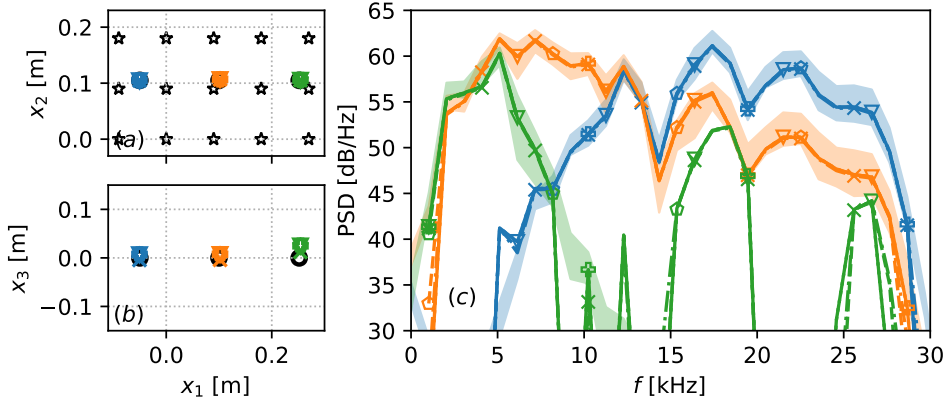


Figure 4.26: Broadband LO result for case 5b). (a) and (b) show spatial projections of the estimated source objects, (c) shows the PSD reconstruction for three true sources at $M = 0.00$ (x, dash dotted line), $M = 0.03$ (∇ , dotted line), $M = 0.06$ (+, dashed line), $M = 0.12$ (\diamond , solid line), $N_{\text{est.}} = 3$, with initial start positions close to the true positions, and $\text{PSD}_{\text{start}} = 50$ dB.

As an example, LO is performed on the generic monopole sources from case 5a), but with $M = [0.00, 0.03, 0.06, 0.12]$ as case 5b). The Amiet open wind tunnel correction [12] is incorporated into the propagation operator for $M > 0$. As initial start values, the true source positions with a random normal error of $\sigma_x = 0.025$ are used and bounded by the optimizer with $\pm 4\sigma_x$. The initial amplitude is $\text{PSD}_{\text{start}} = 50$ dB, and not bounded. Figure 4.26 shows the result of LO. The results are nearly identical to broadband GO, and the Mach number has a neglectable influence on the outcome. This shows that the proposed broadband energy is robust to uncorrelated background noise (i.e., noise from the open wind tunnels). High background-noise situations such as closed wind tunnel measurements are likely to require a noise model [58, 56, 59] either subtracted from the measurement or incorporated in the estimated CSM because the hydrodynamic noise is partially coherent and typically dominates the CSM. The main advantage of LO is that due to the initial guess, the number of true sources is known, which makes the post-processing integration of source objects obsolete, and the optimization process much faster (GO takes approximately 100x longer for the used SciPy implementations [131]). Since the initial source objects are initialized with the error σ_x , the results also show that the broadband energy is smooth enough around the true positions for its gradient to lead towards the global minimum.

Local optimization on synthetic multipoles

As described in the previous section, evaluating complex sources by including parameterized properties in the propagation operator is of interest. One example is a multipole that contains poles of any order, such as a monopole and a dipole, see Section 2.1.4. This is incorporated by super-positioning the estimated, incoherent multipole CSMs in eq. 4.5.2 with

$$c_{\text{mod}} = c_{\text{monop.}} + c_{\text{dip.}} + \dots, \quad (4.5.3)$$

using a shared location and rotation angle for all frequencies and poles in a source object. More complex parameterization may be used here, e.g., allowing for a frequency-dependent multipole rotation, which relaxes the source assumptions but results in more free variables. Thus, it is generally a

var.	x_1	x_2	x_3	pole	$Q(f)$	θ	φ
unit		m			dB Hz ⁻¹	rad	
S_I	0.5	0.5	0.0	monop.	100	-	-
				dip.	60	$\pi/2$	0
S_{II}	0.0	0.5	0.0	monop.	$-\infty$	-	-
				dip.	40	$\pi/2$	$\pi/2$

Table 4.3: Multipole parameters for case 6). The multipoles' amplitudes are constant over frequency.

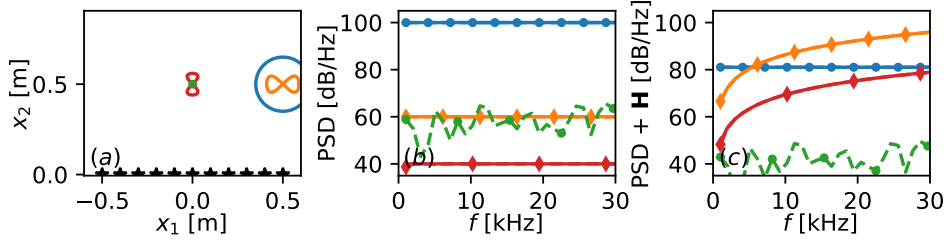


Figure 4.27: Broadband LO result for case 6) with $N_{\text{true}} = 2$ multipole sources, consisting of incoherent monopoles (blue and green), and dipoles (orange and red). (a) shows the true spatial location of the sources. The radius of the source shape is proportional to its strength. (b) shows the broadband LO ($N_{\text{est.}} = 2$) spectral estimation with ground truth (solid) and the estimation (dashed lines) for the monopoles (\cdot) and dipoles (\diamond). (c) shows the perceived PSD at the array location due to the Green's functions eq. 2.1.23 and eq. 2.1.26, which indicates the pole's contribution to the observed CSM.

good idea to include a priori information, such as that a dipole's orientation depends on the object's orientation in the flow and, thus, should be approximately constant over frequency, see Section 2.1. Here, a dipole has two additional variables compared to the monopole, the rotation angle θ , and φ . For $\theta = \varphi = 0$, the dipole's main lobe is orientated in x_3 direction, θ turns the dipole around x_2 , φ around x_3 .

As proof of concept, LO is performed on two synthetic multiples, consisting of monopoles and dipoles, with the parameters given in Table 4.3 with the array setup from Section 4.5.2. The setup is visualized in Figure 4.27 (a). For LO, the initial positional start values are chosen according to the last section with $\sigma_x = 0.025\text{m}$. The start amplitude for the optimizer is $\text{PSD}(f) = 80 \text{ dB Hz}^{-1}$. The start values for the dipole rotation angles φ are random since they cannot be obtained from naive beamforming methods. The rotation angle perpendicular to the array is fixed $\theta = \pi/2$, as it cannot be obtained with a 1D array.

Figure 4.27 shows case 6) results. Figure 4.27 (b) shows the true and estimated pole PSDs. The true and estimated PSDs coincide, except for S_{II} where a monopole amplitude around $Q \approx 60 \text{ dB Hz}^{-1}$ is estimated, whereas the true amplitude is $Q = -\infty \text{ dB Hz}^{-1}$. Note that the SNR of this estimation appears distorted in (b), since the monopole and dipole contribute differently to the total CSM, due to their different Green's functions, see eq. 2.1.23 and eq. 2.1.26. For reference, Figure 4.27 (c) shows the perceived PSD at the array's position $x = [0, 0, 0]^T$, based on the Green's Matrix \mathbf{H} . The SNR is $\text{SNR} \approx 40 \text{ dB}$. The dipoles' rotation angles are estimated with errors below $\epsilon_\varphi < 10^{-5}$ rad.

4.6 Grid-based supervised learning beamforming

This section is based on original research [51] and discusses the use of Artificial Neuronal Networks (ANN) to improve grid-based beamforming. The general approach of deep learning is appealing for wind tunnel experiments since an ANN has to be trained only once for a given array design, which typically stays the same within an experimental campaign. The inference, that is, the processing of the experiments, can then be performed efficiently for all measurements.

For grid-based beamforming, the problem is given in eq. 2.1.50, where the CSM is observed, and the corresponding source distribution is to be estimated. Thus, the task of an ANN in beamforming is to invert the propagation operator. While \mathbf{T}^{-1} is rarely injective and badly conditioned, see Figure 2.1, and the function contains local minima, which will be shown in Section 4.5. Thus, an ANN is not guaranteed to be able to solve this problem. However, the source vector \mathbf{q} is typically sparse. Thus, the ANN may implicitly learn a regulation that improves the performance on source vectors with few real sources.

While ANN research in non-acoustical time-domain beamforming has already advanced significantly, acoustical frequency-domain ANN beamforming is still relatively new. Different architectures have been proposed. On the input side, the ideas can be separated into methods that either use the CSM or conventional beamforming maps. Fully Connected Layers (FCL), Convolutional Layers (CL), and Attention Layers are used for the hidden ANN layers. For the output, either the source distribution is estimated on a grid or gridless. The published research is summed up in Table 4.4 and separated into the different input and output designs.

	gridless	grid-based
CB map	Kujawski et al. [70] Lee et al. [75, 76]	Pinto et al. [101]
CSM	Castellini et al.[23] Kujawski and Sarradj [71]	Ma and Liu [82] Xu et al. [135]

Table 4.4: Overview of the research that has been conducted, separated according to the input and output designs.

4.6.1 Synthetic measurement setup

This thesis uses a simple 1.5D (x, y) -measurement setup, that consists of an equidistant $M = 5$ microphone setup $x = [-0.25 \text{ m}, \dots, 0.25 \text{ m}]^T$, $y = -0.5 \text{ m}$, $z = 0 \text{ m}$ and $N = 15$ focus points $x = [-0.5 \text{ m}, \dots, 0.5 \text{ m}]^T$, $y = 0 \text{ m}$, $z = 0 \text{ m}$. The true source distribution and the corresponding CSM must be known for supervised learning beamforming in the frequency domain. Thus, training data will be generated synthetically for spatially compact monopole sources.

Since ANN architectural design possibilities provide endless combination options, a simple baseline model is proposed, and several parameters are varied. Then, based on the observations, multiple architectures are defined and tested. All architectures are trained on 10^6 training samples for 100 epochs with a 0.9/0.1 validation split, and the error metrics are evaluated on 10^3 test samples.

Note that sources are only located on the focus points (not between them) to prevent aliasing and assignment ambiguities.

4.6.2 Metrics

Three metrics for sparse beamforming maps are defined to evaluate the grid-based ANN results, which are inspired by Lehmann et al. [77], and Herold and Sarradj [61]. For sparse maps, in the sense that the number of non-zero Pa^2 entries is small compared to the number of grid points, the task contains classification, i.e. finding the correct focus points where there exists a source, and regression, i.e., finding the correct source power. Thus, the classification is implicitly based on the regression task. For the classification, a lower threshold is defined (e.g., $L_T = 0$ dB), above which a focus point y is classified as a source S , and below which a focus point is classified as no source $\neg S$. Then, we can define the sensitivity and specificity of the method given the number of True Positives (TP) $S_{\text{true}} \wedge S_{\text{pred.}}$, True Negatives (TN) $\neg S_{\text{true}} \wedge \neg S_{\text{pred.}}$, False Positives (FP) and False Negatives (FN).

$$\text{sensitivity} = \frac{\text{TP}}{\text{TP} + \text{FN}} \quad (4.6.1)$$

$$\text{specificity} = \frac{\text{TN}}{\text{TN} + \text{FP}} \quad (4.6.2)$$

The sensitivity describes how many of the real sources are identified. The specificity describes how many of the no sources are identified. Additionally, an error is needed to estimate for the regression task, i.e., the sound power estimation. We want the error to be relative (in decibels) and independent from the FP and FN classifications. Thus, the Source Strength Deviation (SSD) [77] is used as a Mean Absolute Error (MAE) between the estimated PSD and true PSD for the TP and the average Noise to Signal Ratio (NSR) for the TN.

$$\text{SSD} = \langle |\text{PSD}_{\text{est.}}(y_{\text{TP}}) - \text{PSD}_{\text{true}}(y_{\text{TP}})| \rangle \quad (4.6.3)$$

$$\text{NSR} = \frac{\langle \widehat{\text{PSD}}_{\text{est.}}(y_{\text{TN}}) \rangle}{\max(\widehat{\text{PSD}}_{\text{true}}(y_{S_{\text{true}}}))} \quad (4.6.4)$$

The NSR instead of the typical Signal to Noise Ratio (SNR) is used because, in the best case scenario, the modified PSD (see section 4.6.3 and eq. 4.6.6) of the noise is zero, which can only be used as a numerator (the signal is non-zero by definition). The NSR captures how low the average PSD of an FP is compared to the maximum PSD in the ground truth. We also want to know how close the estimated sources can reconstruct the given CSM. Solving the forward problem in eq. 2.1.50 from the predicted sources to obtain a predicted CSM \mathbf{C}_{pred} , the reconstruction error (RE) is defined by

$$\text{RE} = \langle |\mathbf{C}_{ij,\text{true}} - \mathbf{C}_{ij,\text{pred.}}| \rangle \quad \text{for } i > j \quad (4.6.5)$$

The MAE is used to keep it consistent with the SSD formulation. The RE provides an overall grasp of how well the combined classification and regression task is performed.

In summary, the RE gives a SPL-weighted single metric for both the classification and regression results. The sensitivity and specificity together describe the classification results. The SSD and NSR describe the regression results for TP and FN, thus, based on the classification accuracy.

4.6.3 ANN architectures

For the ANN architectural design different input and output configurations are tested described in the following.

CSM input dimensions

Given that the microphone array is structured so that every inner microphone has $3^D - 1$ neighbors in the D-dimensional array, we can reshape the CSM into an $(M_x \times M_y \times M_z)^2$ tensor. For a 1D-array this is always the case. This allows for two options. First, the upper diagonal of the CSM is reshaped into a row (VUT). Second, the entire CSM is used in tensor form, which contains redundant information but may benefit CNN architectures.

Handling of complex input

Since the CSM is $\mathbf{C} \in \mathbb{C}$, there are three options. Recently, complex-valued neuronal networks were established [18], allowing the complex CSM input. Alternatively, the CSM can be split into their real and imaginary part. Third, the CSM can be split into magnitude and phase. It should be noted that only the first two options are holomorphic mappings, but there is a linear relationship between the absolute CSM and the absolute source power. Suppose the CSM input in tensor form is chosen in combination with a separation of the complex values. In that case, we can either add an additional dimension for the two real-valued CSM parts or use the upper diagonal for the real part and the lower diagonal for the imaginary part.

In- and output layer transformation

Beamforming results are typically evaluated in decibels. However, it is not possible to directly predict the resulting maps in decibels due to the sparseness of the target map. Most of the target values will be $y_{\text{true}} = 0 \text{ Pa}^2 = -\infty \text{ dB}$. First, this thesis proposes a modified SPL formulation with

$$\widehat{\text{SPL}} = 10 \log_{10} \left(\frac{p^2}{p_0^2} + \epsilon \right). \quad (4.6.6)$$

Second, this thesis proposes a natural logarithm with

$$p_{\log}^2 = \log(p^2 + 1). \quad (4.6.7)$$

Third, it is possible to predict y_{true} directly in Pa^2 . The corresponding input CSM will be transformed according to the output layer. The input and output layers are also normalized to $0 \leq |y| \leq 1$, $0 \leq |\mathbf{C}| \leq 1$.

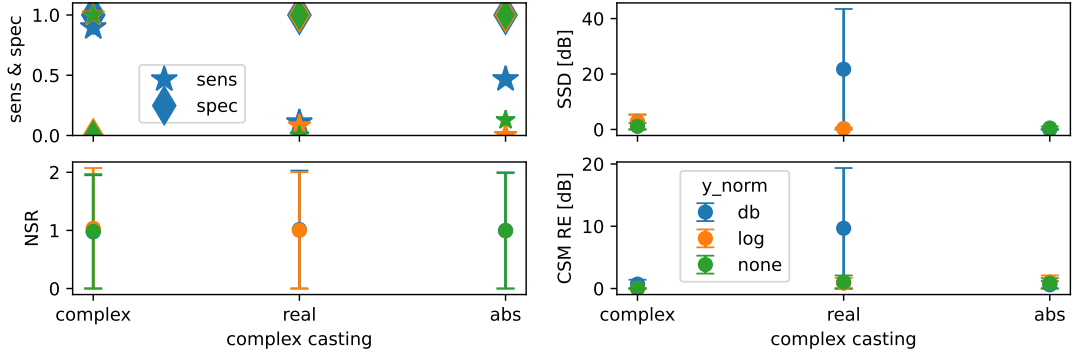


Figure 4.28: Error metrics of section 4.6.2 for the baseline model with variation of the complex input handling (see Section 4.6.3), and the input and output transformation (see Section 4.6.3) for $N_S = 1$ source.

Loss function

The Mean Squared Error is a typical loss function for the regression.

$$\text{MSE} = \langle |y_{\text{true}} - y_{\text{pred}}|^2 \rangle \quad (4.6.8)$$

However, since the output vector is very sparse, we can add a weighting function w to prefer the correct SPL at focus points that feature a true source

$$\text{wMSE} = \langle w |y_{\text{true}} - y_{\text{pred}}|^2 \rangle \quad (4.6.9)$$

For the total number of focus points that have a true source N_S and the total number of focus points that do not have a source $N_{\neg S}$, the weight then is

$$w = \begin{cases} 1/N_S & \text{for } y_{\text{true}} \in S \\ 1/N_{\neg S} & \text{for } y_{\text{true}} \in \neg S \end{cases}. \quad (4.6.10)$$

Optionally, to prevent the sparse output vector, we can use a Fourier Transformation to predict the SPL as a wavenumber. According to the handling of the complex values of the CSM, we can either use a fully complex ANN or split the complex numbers into real and imaginary parts. Adding an additional dimension for a CNN allows the use of convolutions separately on the real and imaginary parts throughout the network.

Baseline Model

The baseline model is a simple, fully connected (FC) network with Rectified Linear Units (ReLU), three Hidden Layers (HL), and 256 Neurons Per Layer (NPL) with an MSE loss. We use $M = 5$ microphones and $N = 15$ focus points. On each grid, there is only $N_{\text{true}} = 1$ true spatially compact monopole source with $50 \text{ dB} \leq \text{SPL} \leq 100 \text{ dB}$ and the threshold for the source classification is set to $L_T = 30 \text{ dB}$.

Figure 4.28 shows the performance of the baseline model for a variation of the handling of complex numbers and normalization for $N_S = 1$ source, and Figure 4.29 for $N_S = 5$ sources. For the compared

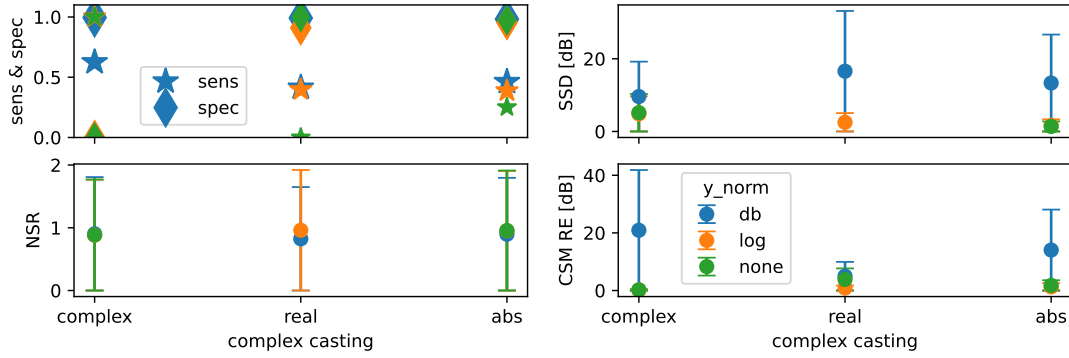


Figure 4.29: Error metrics of section 4.6.2 for the baseline model with variation of the complex input handling (see Section 4.6.3), and the input and output transformation (see Section 4.6.3) for $N_S = 5$ sources.

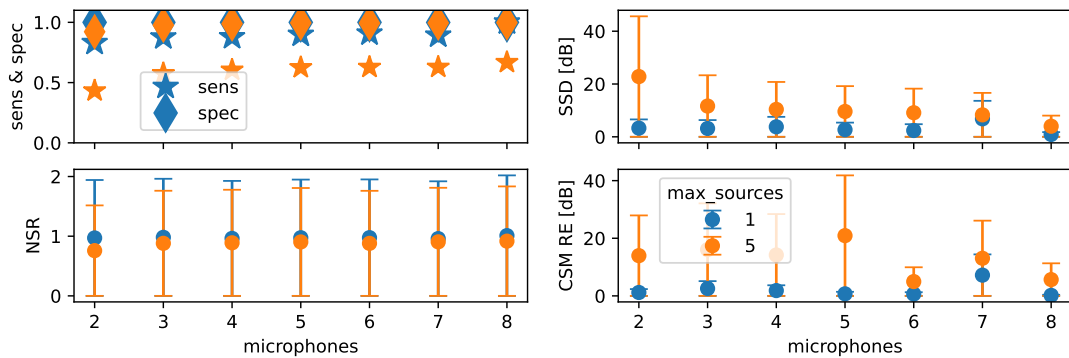


Figure 4.30: Error metrics of section 4.6.2 for the complex baseline model with dB transformation and an increasing number of microphones.

configurations, the complex ANN with the modified dB-transformation according to eq 4.6.6 outperforms the other configurations. The combination of a low CSM RE and an NSR close to unity means that in some instances, the ANN predicted the correct source strength on a wrong but close to the true focus point. Figure 4.29 shows the same setups for $N_S = 5$ sources. Again, the complex ANN in combination with the dB transformation outperforms the other models on the classification task. The other transformation methods are more precise for the regression task. The low CSM RE on the other models combined with the low classification accuracy shows that the models cannot produce sparse results. E.g., the complex ANN with no transformation predicts a source (that is $\text{SPL} \geq 30$ dB) on each focus point, but overall, the predicted pressure distribution is quite reasonable. Since we are both interested in the regression and classification, we will focus on the complex ANN in combination with the dB transformation in the following.

Section 2.1.7 discussed the uniqueness of the solution, given the number of microphones and focus points. We expect that the results of a model depend on whether the problem is ill-posed or over-determined. Figure 4.30 shows the corresponding results for an increasing number of microphones. Given the $N = 15$ focus points, the problem has a unique solution for $M = 7$ microphones. For $N_S = 1$, the ANN achieves good results for the over-determined case at $M = 8$, with a strongly increasing error for the unique case and further degrading results for under-determined cases. Interestingly, for $N_S = 5$, the results are much worse, also for the over-determined case. At $M = 7$, we can see an increased CSM RE, which might be connected to the bad conditioning of the propagation

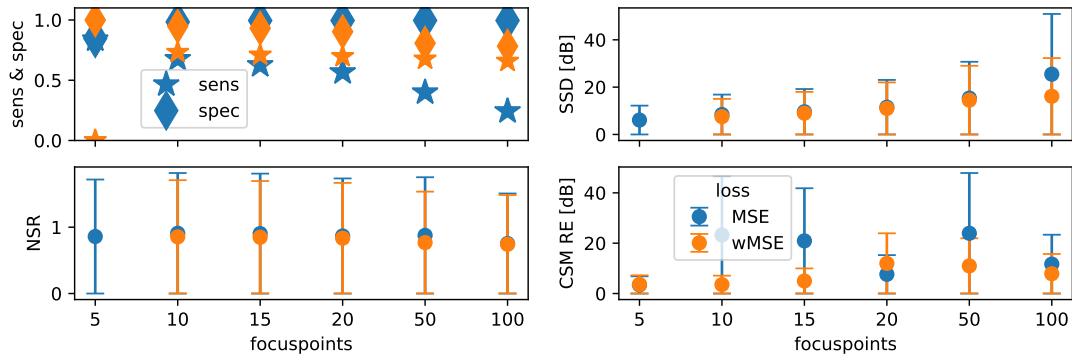


Figure 4.31: Error metrics of section 4.6.2 for the complex baseline model with dB transformation, the MSE and wMSE at an increasing number of focus points.

matrix, see Figure 2.1. While the ANN does not achieve good results for the injective setups, the results for the underdetermined cases with $M < 7$ are impressive (even for $M = 2$ and $N_S = 5$, where the ANN receives only a single complex input, the ANN correctly classifies around 50% of the sources).

Finally, the proposed loss functions are evaluated for the base model, see Section 4.6.3. Figure 4.31 shows the results for the MSE and wMSE for a variation of the number of focus points at $M = 5$, $N_S = 5$. The wMSE outperforms the regular MSE in all cases (except for $M = 5$ where all focus points are weighted with zero for $N_S = 5$).

Combining a wMSE for the loss function and a complex-valued ANN with dB transformation yields the most promising results. Based on this observation, different ANN architectures are evaluated in the following.

4.6.4 Results

This Section compares different ANN architectures. The architectures will be separated into the CSM input, the ANN encoder, the ANN decoder, and the output. For the input, a CSM row structure and tensor structure are compared; for the encoder, a fully connected (FC) and convolutional layers (CL) are used; for the decoder, FC and CL are used, and the output will be predicted on the focus points (FP), and the wavenumber domain (WN) (with an MSE loss). The number of hidden layers of the encoder (EHL) and decoder (DHL) is stated for an FC network (which does not have an encoder-decoder structure), the total number of HL is listed in EHL, see Table 4.5. Since the number of input and output neurons differ based on the given architecture, the numbers of hidden convolutional layers with a (3)-kernel and a (1)-stride also differ. For the tensor input the CSM is 2D, and the convolution kernel is (3×3) with a (1×1) -stride.

Figure 4.32 shows the resulting metrics for the model architectures from Table 4.5. All models perform similarly except for the Baseline model that predicts the complex wavenumber vector. The Auto Encoder 2 model has a slight advantage in terms of SSD and CSM RE, which makes it the best model overall.

model	CSM shape	encoder	EHL	decoder	DHL	output	loss
Base 1	row	FC	3	FC		FP	wMSE
Base 2	row	FC	3	FC		WN	MSE
EC 1	row	CL	3	FC	3	FP	wMSE
EC 2	tensor	CL	2	FC	3	FP	wMSE
DC	row	FC	3	CL	5	FP	wMSE
AE 1	row	CL	3	CL	5	FP	wMSE
AE 2	tensor	CL	2	CL	7	FP	wMSE

Table 4.5: ANN architectures for benchmark.

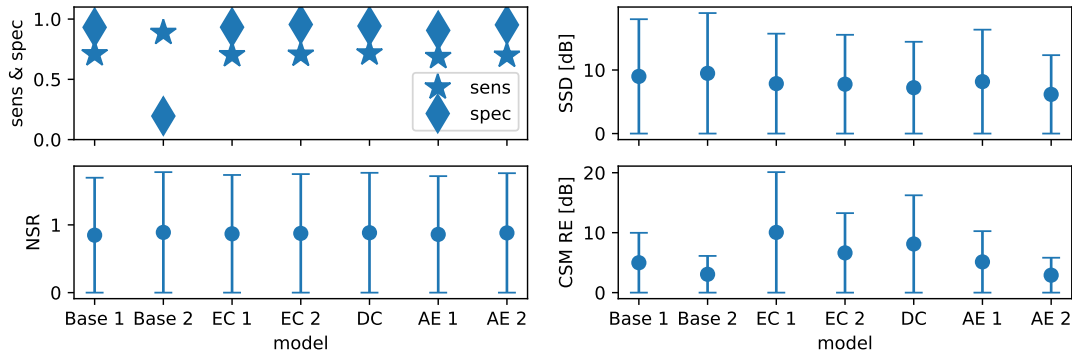


Figure 4.32: Error metrics of section 4.6.2 for the different model architectures from Table 4.5.

4.7 Permutation invariant, gridless ANN beamforming

Recently, gridless beamforming methods emerged that use creative approaches to address the central challenge: The number of sources is unknown, and the sources are permutation invariant. Lee et al. [75, 76] solved this issue using a hybrid, three-step approach, where they first predicted a grid-based beamforming map. Second, they deconvolved the map (still grid-based). Third, they used small map snippets around the peaks in the deconvolved map and serially predicted the gridless source positions from there. Castellini et al. [23] used a straightforward approach where a predefined number of output sources are ordered from the highest to lowest source strength, and the source strengths are predicted relative to the dominating source. The classification problem is solved implicitly, simply by regarding the source amplitudes. Kujawski and Sarradj [71] solve this challenge by predicting a predefined number of gridless output sources. The sources are then clustered with K-Means to solve the permutation assignment problem and prediction of the number of sources. Thus, a true source can be approximated with multiple estimated sources. All of the presented literature discusses the detection of compact monopoles at single frequencies in (nearly) noise-free environments. Further, they predict sources on planes parallel to the array in nearly noise-free environments for sources with similar source strengths.

This section proposes a novel gridless architecture for beamforming with ANN to overcome the inherent challenges of the grid-based approach. The approach is similar to GO, see Section 4.5, where source objects are predicted. The source objects have several properties, such as a spectrum and their location, to be estimated. Since their location is no longer fixed in space, the source objects are no longer ordered, i.e., a vector of source objects, but instead a permutation invariant set of source

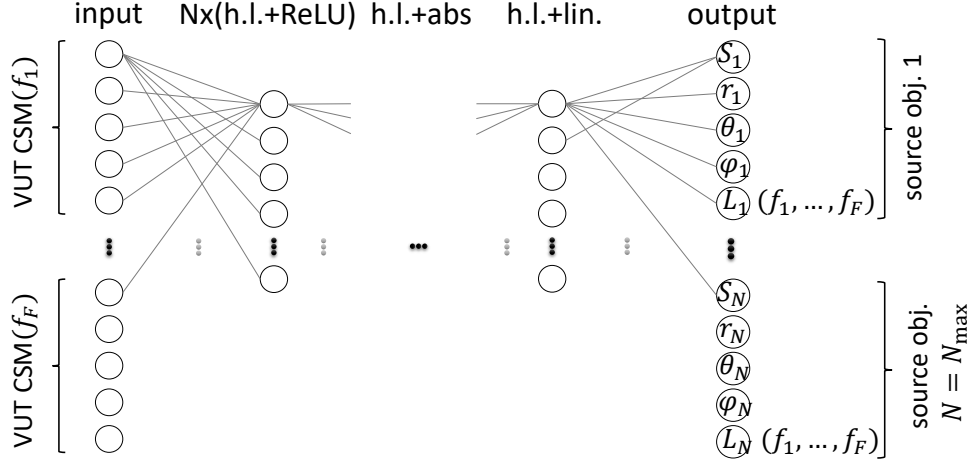


Figure 4.33: Sketch of the proposed ANN architecture. The input is the complex-valued, VUT CSM, normalized according to Section 4.7.1. There follow $N = 3$ complex hidden dense layers with a complex ReLU activation function. A complex dense layer with an absolute-value activation function follows to obtain positive, real values, and a final real-valued hidden layer without an activation function follows to obtain any real output value. For the classification variables, a sigmoid function for binary cross-entropy is employed. The output is the (unsorted) set of the real-valued N_{\max} source-objects, each member containing the $[S, r, \theta, \varphi, (L_1, \dots, L_F)]$ -vector, normalized according to Section 4.7.1.

objects. This section presents a permutation invariant structure and loss for ANN and corresponding metrics to evaluate the results, based on tensor-to-set learning [137, 74, 81, 22].

4.7.1 Architecture

A simple complex valued [18] dense network ANN architecture will be employed since the main focus of this approach is the permutation invariant loss of the estimated source objects. The ANN consists of the input layer of size $[F(M^2 - M)/2]$, three complex valued hidden layers with 256 neurons each, and a real-valued output layer.

The output of the ANN is the desired source objects. A source object for a monopole contains a classification variable s , that is, either $s = 0$ ($-S$) if the source does not exist, or $s = 1$ (S) if the source exists, which is a binary classification problem. This way, the ANN is designed to identify up to N_{\max} sources, but also less. Additionally, a source object contains regression variables such as the source location and power. For the location, spherical (or polar in 2D) coordinates r, θ, φ are chosen with respect to the array's geometric mean due to the large range a source can be located at, and since it is well known that for distant sources the problem typically reduces to a direction of arrival problem. For the strength estimation, the source object contains a Power Spectral Density (PSD) of dimension F . This results in a source object of size of $[4 + F]$, and a total number of output neurons for y_{pred} of $[(4 + F)N_{\max}]$.

Normalization

For acoustic applications, one is typically interested in relative errors (such as a decibel difference) and not the absolute error in Pa^2 . Thus, the source level is predicted logarithmically with

$$p_{\text{true}} = \log(p^2) . \quad (4.7.1)$$

The same holds for the radius

$$r_{\text{true}} = \log(r^2) , \quad (4.7.2)$$

which accounts for the squared decay in level. Since the CSM and the resulting source level describe the same physical property in Pa^2 , the VUT CSM should be treated accordingly

$$c_{\text{input}} = \log(c^2) . \quad (4.7.3)$$

Afterward, the source object regression variables are scaled to $[0, 1]$ to be equally weighted in an error norm.

Permutation invariant loss

The introduced method is a vector-to-set problem, and a set is permutation invariant. Thus, the loss is designed to be permutation invariant as well. Also, since the ANN has a fixed number of output neurons, i.e., a fixed number of maximum sources, the problem consists of a regression error for the source location and source strength and a classification error. A regression error can only be obtained for S_{true} , i.e., if the source exists. Thus, the regression error for $\neg S_{\text{true}}$ will be set to zero. For the classification error, the binary cross-entropy B is chosen. For the regression, the MAE is chosen. The loss is defined as

$$\text{loss} = \alpha B(y_{\text{true}}, y_{\text{pred}}) + (1 - \alpha) \text{MAE}(y_{\text{true}}, y_{\text{pred}}) \delta(S_{\text{true}}) \quad (4.7.4)$$

with

$$\delta(S_{\text{true}}) = \begin{cases} 0 & \text{for } \neg S_{\text{true}} \\ 1 & \text{for } S_{\text{true}} \end{cases} \quad (4.7.5)$$

and

$$\text{MAE}(y_{\text{true}}, y_{\text{pred}}) = \frac{\text{MAE}_r + \text{MAE}_\theta + \text{MAE}_\varphi + \text{MAE}_L}{4} \quad (4.7.6)$$

where α is a weighting coefficient. For this thesis, $\alpha = 0.01$ is used. Preliminary investigations show that this weight has no impact on the results. However, the training is accelerated for low α due to the different orders of magnitude of the regression and classification errors.

The permutation invariant loss (for one sample) works as follows:

- Reshape the output vector y_{pred} into a tensor of shape $[N_{\text{max}}, 4 + F]$
- Calculate all $N_{\text{max}}!$ permutations for y_{pred}
- Calculate the loss between y_{true} and $y_{\text{pred,perm}}$, see eq. 4.7.4

- Set the regression loss $\text{MAE}(y_{\text{true}}, y_{\text{pred,perm}})$ to zero for $y_{\text{true}}(s) = 0$, see eq. 4.7.5 (otherwise it is undefined, as there is no ground truth)
- find the minimum loss over all permutations

This algorithm is also performed to match the predicted source objects with the true test set. While this matching is not computationally efficient with $O(N!)$, one can solve this via bipartite matching such as the Hungarian algorithm, which scales with $O(N^3)$ and, thus, is faster for $N \geq 7$.

Evaluation metrics can be obtained directly from the source object variables, as opposed to the grid-based approach, where the classification is approached implicitly via the source power. Two extreme cases are considered to put errors into perspective. First, a CSM contains $i = 1, \dots, N_{\text{max}}$ source objects, with a dominant source PSD_j

$$\text{PSD}_j \gg \text{PSD}_i \quad \text{for } i \neq j. \quad (4.7.7)$$

Here, the ratio between the source strengths is defined as the Signal to total Signal Ratio (SSR)

$$\text{SSR}_j = \text{PSD}_j - \sum_i \text{PSD}_i = (-\infty, 0] \text{ dB}. \quad (4.7.8)$$

In the case of a single dominant source, the $\text{SSR} = 0 \text{ dB}$. The second extreme case is a source with a low power compared to the dominant source or is located far away from the array $r \rightarrow \infty$ so that $\text{SSR} \rightarrow -\infty \text{ dB}$. From an acoustic standpoint, errors made at large SSR are worse than errors made for weaker sources. Thus, errors should be evaluated with respect to the SSR.

Suppose more than one frequency is employed at the same time. In that case, a separate SSR exists for each frequency so that a classification and positional variable has multiple $\text{SSR}(f)$. Here, the total SSR from the OASPL is used with

$$\text{SSR}_j = \sum_f \text{PSD}_{j,f} - \sum_i \sum_f \text{PSD}_{i,f} = (-\infty, 0] \text{ dB}. \quad (4.7.9)$$

4.7.2 Evaluation metrics

The true SSR can only be obtained for existing true sources. These are True Positives (TP) $S_{\text{true}} \wedge S_{\text{pred.}}$, and False Negatives (FN) $S_{\text{true}} \wedge \neg S_{\text{pred.}}$, but not for True Negatives (TN) $\neg S_{\text{true}} \wedge \neg S_{\text{pred.}}$, False Positives (FP) $\neg S_{\text{true}} \wedge S_{\text{pred.}}$. No true SSR can be obtained for FP and TN since they have an undefined true source strength. Deduced from the extreme cases, one may argue that a TN source has a (normalized) SSR of $\text{SSR} \rightarrow -\infty \text{ dB}$ (it can be very far away or have a neglectable source strength). For the FN, one can estimate an SSR based on the predicted source strength $\text{PSD}_{j,\text{pred.}}$ and the true source strengths $\text{PSD}_{i,\text{true}}$

$$\text{SSR}_{j,\text{pred.}} = \text{PSD}_{j,\text{pred.}} - \sum_i (\text{PSD}_i) = (-\infty, \infty) \text{ dB}. \quad (4.7.10)$$

The predicted SSR for FP may exceed zero decibels since it may exceed the true source strength, which would be considered a worst-case scenario. Evaluation metrics based on TN are excluded since

their SSR is undefined, which yields for the classification the sensitivity, False Discovery Rate (FDR), and F_1 -score

$$\text{sensitivity} = \frac{TP}{TP + FN}, \quad (4.7.11)$$

$$\text{FDR} = \frac{FP}{FP + TP}, \quad (4.7.12)$$

$$F_1 = \frac{2TP}{2TP + FP + FN}. \quad (4.7.13)$$

The FPR is given based on the estimated SSR

$$\text{FDR}(\text{SSR}) = \frac{FP(\text{SSR}_{\text{est.}})}{FP(\text{SSR}_{\text{est.}}) + TP(\text{SSR}_{\text{true}})}, \quad (4.7.14)$$

and the F_1 -score respectively. The sensitivity shows the impact of the SSR on the ability to detect sources. The FDR shows how many sources are wrongly estimated and, via the SSR, how much source power is wrongly introduced into the total configuration. The F_1 -score shows how well the model performs overall. The classification variable is mapped to $[0,1]$ during the training using the sigmoid activation function. During the evaluation of the classification metrics, the variable is rounded so that the estimated source exists for $s \geq 0.5$.

As described above, one can only obtain regression errors for true sources. These contain TP and FN classifications and can be evaluated separately for them. Since the classification and regression errors are independently evaluated in the loss, the regression variables will be predicted independently of the classification, i.e., also for $\neg S$. Thus, for FP, the SSR can be evaluated without ground truth as a regression metric with eq. 4.7.10. If $\text{SSR} \ll 0$, the FP has little impact on the result, for $\text{SSR} \geq 0$, the FP has a large, undesired impact on the result.

The regression metrics are the mean absolute error of the Source Strength Deviation (SSD)

$$\text{SSD} = |\text{PSD}_{\text{pred.}} - \text{PSD}_{\text{true}}|. \quad (4.7.15)$$

The angular deviation ε_θ is

$$\varepsilon_\theta = |\theta_{\text{pred.}} - \theta_{\text{true}}|. \quad (4.7.16)$$

Since the sources are distributed over a large range of radii, the relative error ε_r is used

$$\varepsilon_r = \frac{|r_{\text{pred.}} - r_{\text{true}}|}{r_{\text{true}}}. \quad (4.7.17)$$

Finally, the number of correct estimations is evaluated, where a correct estimation means the classification is correct and the regression errors are low. Here, low errors are defined as $\text{SSD} \leq 3 \text{ dB}$, $\varepsilon_\theta \leq 5^\circ$, and $\varepsilon_r \leq 10\%$.

4.7.3 Cases and setup

Three cases are presented to evaluate the approach. The array contains the third row of the generic experiment ($M = 7$, $-0.27 \text{ m} \leq x \leq 0.27 \text{ m}$) so that it simplifies to a 2D problem with θ, r in polar

case	$\langle \text{SSD} \rangle$ [dB]	$\langle \varepsilon_r \rangle$ [%]	$\langle \varepsilon_\theta \rangle$ [°]
1)	0.87 \pm 0.77	2.33 \pm 1.92	1.94 \pm 1.30
2)	6.06 \pm 6.76	25.14 \pm 41.59	17.50 \pm 18.75
3)	9.22 \pm 7.36	14.65 \pm 13.62	10.00 \pm 10.86

Table 4.6: Regression metrics for the cases from all test samples with ground truth, i.e. TP, and FN in case 3)

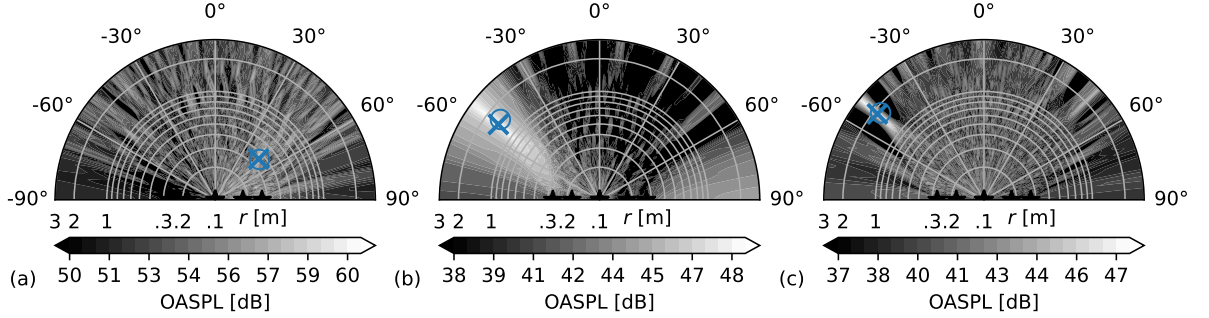


Figure 4.34: Case 1), three random test set results with $N_S = 1$. The true (x) and estimated (o) locations are marked. The underlying colormap shows the OASPL conventional beamforming result with steering vector IV. The microphone positions are marked (\star).

coordinates. The training data is simulated without noise in the frequency domain and contains spatially compact monopoles, according to eq. 2.1.50 and eq. 2.1.23. The PSD of the training data is uniformly random distributed with $20 \text{ dB} \leq \text{PSD} \leq 70 \text{ dB}$. The radius is $0.2 \leq r \leq 2$, and the angle $-\pi/3 \leq \theta \leq \pi/3$. All models are trained for 100 epochs on 10^6 training samples with a 0.9/0.1 training/validation split and are evaluated on 10^4 unseen test samples.

Case 1) contains a single source and the total frequency vector $\mathbf{f} = [1024, 2048, \dots, 32768]$ Hz of the generic experiment. The problem simplifies to a regression problem without permutations so that the general ability to localize a source in polar coordinates using the VUT CSM with the proposed model can be evaluated. Case 2) uses a single frequency $f = 8192$ Hz and several variations of parameters. The base model uses $N_S = 3$ sources and $M = 7$ sensors. Then, the number of sources and sensors is varied to study their influence on the model while keeping the array aperture constant. Further, the use of dropout on the input layer is studied. Finally, the classification variable is added to the problem. Case 3) contains $N_S \leq 3$ sources and the total frequency vector, representing the final architecture.

4.7.4 Results

All cases and models are evaluated on a machine with a Nvidia RTX 2060 graphics card with 6 GB VRAM, 32 GB DDR 3 RAM, Intel i7 4770 processor, and Google TensorFlow. The training takes up to 10 min for each model, including the training data generation.

Table 4.6 shows the regression metrics for all cases from all test samples with ground truth (TP+FN). For case 1), the model accurately predicts the location and source power. Figure 4.34 shows a comparison of the conventional beamforming OASPL with steering vector IV, see Section 4.1, and the

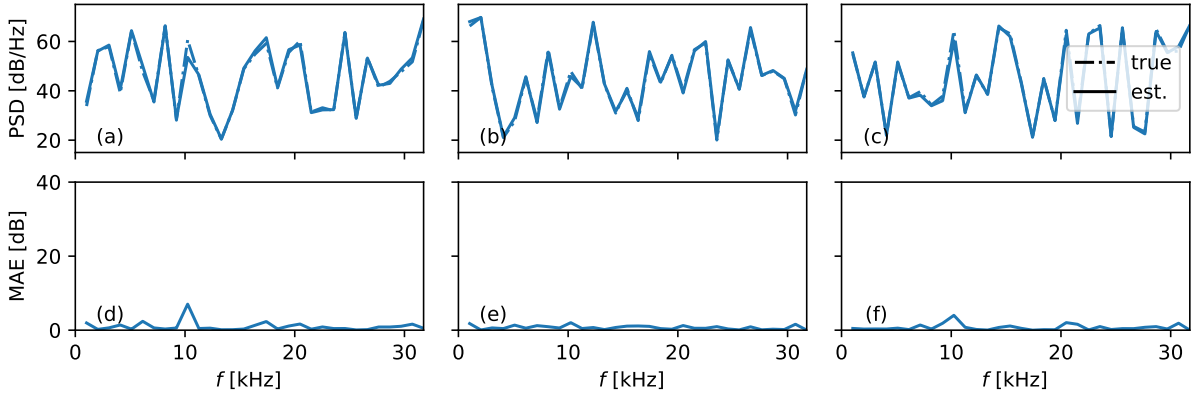


Figure 4.35: Case 1), the corresponding power estimation and SSD for the examples from Figure 4.34. (a) to (c) show the true (dashed) and estimated (solid) source strength, (d) to (f) show the corresponding SSD MAE.

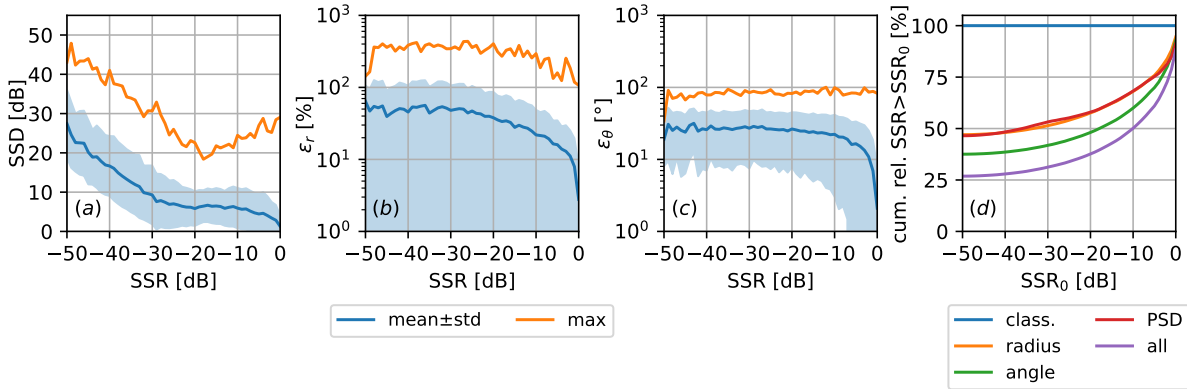


Figure 4.36: Case 2), $N_S = 3, M = 7$, regression metrics over SSR. (a) shows the SSD(SSR), (b) shows $\varepsilon_r(\text{SSR})$, and (c) shows $\varepsilon_\theta(\text{SSR})$. The blue line shows the mean and standard deviation, and the orange line the maximum error occurring in the test set. (d) shows the cumulated relative correct estimations for $\text{SNR} > \text{SNR}_0$.

ANN model for three random examples from the test set. The radius is depicted logarithmically for $r \geq 0.1$ m so that only five of the seven sensors are visible. Figure 4.35 shows the corresponding source powers, which are estimated well throughout the frequency range. The SSD shows no dependency on the frequency. The approach shows that the gridless ANN model is able to estimate the spatial location and source strength of a single source perfectly.

For case 2) the errors increase compared to case 1). Each source has a unique SSR since each source has only a single frequency. Figure 4.36 shows that the errors depend on the SSR of the sources. For the SSD, a local minimum of the error is observed around $\text{SSR} \approx -20$ dB. The local minimum originates from regression-to-the-middle guesses, i.e., if the ANN predicts the average source power to reduce the average error. The same is not observed for the radius and angle. Below $\text{SSR} \approx -30$ dB, the model cannot predict reasonable values, but with increasing SSR the errors decrease. Figure 4.36 (d) shows the number of correct estimation based on the predictions with a low error $\text{SSD} \leq 3$ dB, $\varepsilon_\theta \leq 5^\circ$, and $\varepsilon_r \leq 10\%$. These maximum errors are chosen based on experience so that the deviations from the predictions and the ground truth are reasonable. The number of accurate predictions decreases with decreasing SSR. The number of correct estimations is reduced to a single numerical

N_S	$\langle \text{SSD} \rangle$ [dB]	$\langle \varepsilon_r \rangle$ [%]	$\langle \varepsilon_\theta \rangle$ [°]	corr. est. [%]
1	0.56 ± 0.39	1.43 ± 1.49	1.31 ± 1.03	99.04
2	3.17 ± 4.31	20.68 ± 39.93	14.31 ± 17.44	63.23
3	6.06 ± 6.76	25.14 ± 41.59	17.50 ± 18.75	51.11
4	6.94 ± 7.08	24.50 ± 39.17	16.56 ± 17.85	49.20
5	8.28 ± 7.37	24.65 ± 37.39	16.79 ± 17.30	40.20
6	8.88 ± 7.44	23.44 ± 34.51	16.38 ± 16.86	35.10

Table 4.7: Regression metrics for case 2) $M = 7$, and number of correct estimations for sources $\text{SSR} \geq -10$ dB for a variation of the number of sources N_S .

M	$\langle \text{SSD} \rangle$ [dB]	$\langle \varepsilon_r \rangle$ [%]	$\langle \varepsilon_\theta \rangle$ [°]	corr. est. [%]
2	10.50 ± 7.67	35.38 ± 45.44	24.16 ± 18.43	0.54
3	8.34 ± 7.40	32.88 ± 42.80	20.69 ± 18.44	13.70
4	6.30 ± 6.83	37.36 ± 65.49	17.96 ± 18.41	39.91
5	6.31 ± 6.81	35.50 ± 65.18	17.63 ± 18.57	45.00
7	6.06 ± 6.76	25.14 ± 41.59	17.50 ± 18.75	51.11
11	5.85 ± 6.54	30.18 ± 56.48	16.38 ± 19.09	55.60
15	5.77 ± 6.43	26.14 ± 43.22	15.93 ± 19.35	57.37
31	5.24 ± 5.93	24.84 ± 40.99	13.61 ± 17.62	62.09

Table 4.8: Regression metrics for case 2) $N_S = 3$, and number of correct estimations for sources $\text{SSR} \geq -10$ dB for a variation of the number of microphones M .

value for comparison. Due to the typical decrease with decreasing SSR, it is evaluated for sources with $\text{SSR} \geq -10$ dB. Table 4.7 shows that the errors increase with an increasing number of sources and that the number of correct estimations at $\text{SSR} \geq -10$ dB decays logarithmically. Table 4.8 shows that the errors decrease with an increasing number of microphones, and the correct number of estimations increases. Figure 4.37 shows the logarithmic relationship between the number of correct estimations and the number of microphones and sources. The results show that the dynamic range of the proposed architecture strongly depends on the number of sources and microphones, similar to conventional beamforming. Due to this behavior, it is likely that the performance also strongly depends on the array geometry, such as the aperture and microphone spacing.

Table 4.9 shows that the dropout corresponds to fewer microphones so that the errors increase proportionally. A dropout of 20% for $M = 7$ microphones results in 18 vs. 21 active input neurons and decreases the number of correct estimations by 5%. This may be a reasonable trade-off if many

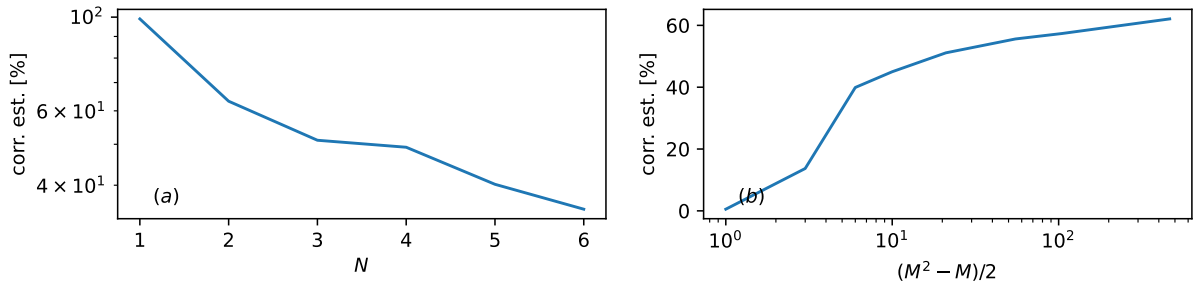


Figure 4.37: Case 2), (a) shows the number of correct estimations for sources $\text{SSR} \geq -10$ dB over a variation of the number of sources N_S , (b) shows the number of correct estimations over a variation of the number of microphones M .

dropout [%]	$\langle \text{SSD} \rangle$ [dB]	$\langle \varepsilon_r \rangle$ [%]	$\langle \varepsilon_\theta \rangle$ [°]	corr. est. [%]
0	6.06 \pm 6.76	25.14 \pm 41.59	17.50 \pm 18.75	51.11
20	6.33 \pm 6.92	26.50 \pm 42.37	18.15 \pm 19.01	45.76
40	7.13 \pm 7.14	28.99 \pm 44.42	19.19 \pm 19.06	36.59

Table 4.9: Regression metrics for case 2) $M = 7$, $N_S = 3$, and number of correct estimations for sources $\text{SSR} \geq -10$ dB for a variation of a dropout on the input layer.

	$\langle \text{SSD} \rangle$ [dB]	$\langle \varepsilon_r \rangle$ [%]	$\langle \varepsilon_\theta \rangle$ [°]	corr. est. [%]
$N_S = 3$	6.06 \pm 6.76	25.14 \pm 41.59	17.50 \pm 18.75	51.11
$N_S \leq 3$	2.93 \pm 4.12	15.98 \pm 25.00	14.29 \pm 17.24	48.87
$N_S \leq 5$	3.82 \pm 4.40	18.62 \pm 22.85	17.15 \pm 16.87	34.61

Table 4.10: Regression metrics for case 2) $M = 7$, and number of correct estimations for sources $\text{SSR} \geq -10$ dB with and without classification.

microphones are used since the dropout will be beneficial to avoid over-fitting and can be used to generate multiple estimations since dropout needs to be active during inference as well for regression tasks. Thus, the generation of different estimations for a single problem can be used to decrease the statistical likelihood of predicting arbitrary results with large errors, which seems to happen in Figure 4.36, where the maximum error is large.

Table 4.10 shows the results for introducing the classification problem so that the number of true sources is no longer fixed. Since for $N_S \leq 3$ the average number of sources per sample is only $\langle N_S \rangle = 2$, results are also given for $N_S \leq 5$ where $\langle N_S \rangle = 3$. The classification reduces both the average errors and the number of correct estimations. This may be because the distribution of occurring SSR in the data changes. For example, while the average number of sources is equal $\langle N_S \rangle = 3$ for $N_S \leq 5$, a fifth of the samples have only a single source, so that the $\text{SSR} = 0$ dB, which the model predicts perfectly, see Table 4.7. However, the classification task and the samples where $N_S \leq 3$ introduce an additional challenge so that the number of correct estimations is reduced.

For case 3) the average SSD is larger compared to case 2) (also for the variation of case 2) with $N_S \leq 3$), but the spatial estimation is improved. The spatial estimation improvement corresponds to the B-CLEAN-SC and GO results: Obtaining a broadband solution allows for the separation of main and side lobes, and the resolution of medium frequencies compensates for the difficulty at low and high frequencies. Note that the small-band solution with $f = 8192$ Hz in case 2) is considered an

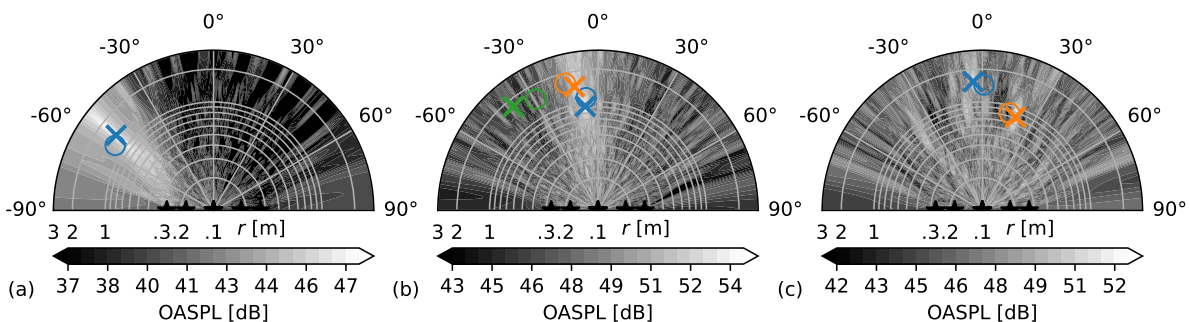


Figure 4.38: Case 3), three random test set results with $N_S \leq 3$.

	$\langle \text{SSD} \rangle$ [dB]	$\langle \varepsilon_r \rangle$ [%]	$\langle \varepsilon_\theta \rangle$ [°]	$\langle \text{SSR} \rangle$ [dB]
TP+FN	9.22 \pm 7.36	14.65 \pm 13.62	10.00 \pm 10.86	
TP	9.16 \pm 7.34	14.56 \pm 13.55	9.81 \pm 10.66	
FN	11.39 \pm 7.61	17.97 \pm 15.64	17.06 \pm 14.94	
FP				-12.67 \pm 7.45

Table 4.11: Case 3), regression metrics, separated for TP, and FN. Additionally, the SSR for FP is shown.

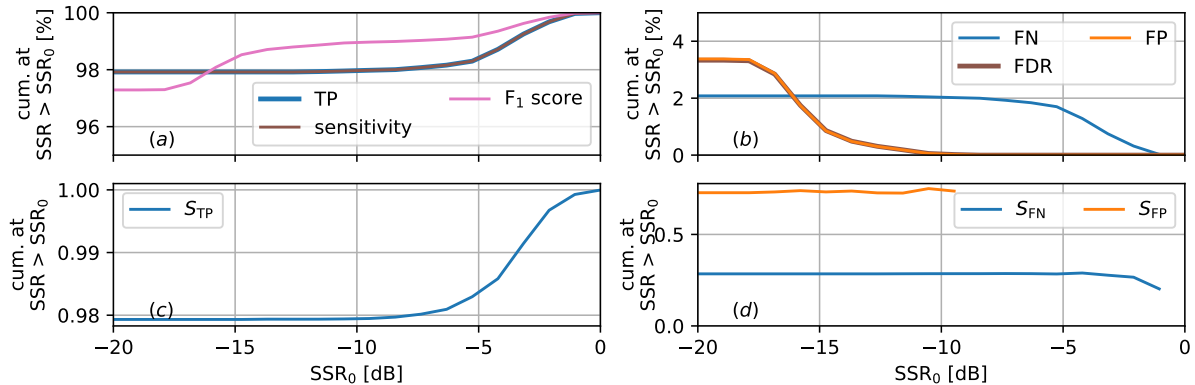


Figure 4.39: Case 3), classification metrics over SSR. (a) shows the accumulated, relative occurrence of TP, the F₁-score, and sensitivity for SSR > SSR₀. (b) shows the corresponding FN, FP and FDR, with an overall sensitivity = 0.98, F₁ = 0.97, FDR = 0.03. (c) and (d) show the corresponding averaged classification confidence, i.e. the estimated S without rounding, accumulated for SSR > SSR₀. The overall averaged values are $S_{\text{TP}} = 0.98$, $S_{\text{FN}} = 0.28$, and $S_{\text{FP}} = 0.73$.

optimal medium frequency. The second reason for the improved localization and larger SSD is that each source has multiple SSRs, so statistically, each source is dominant for at least one frequency. Thus, using an SSR is no longer as meaningful as for the single frequency case 2). In the same way, sources have more often low SSR for some frequencies so that the overall SSD increases. Figure 4.38 shows exemplary results for case 3). The classification is correct for all examples so that the number of estimated sources matches the number of true sources. Further, the estimated source locations correspond well to the true source locations. The underlying OASPL shows that with conventional beamforming, it would be difficult to identify non-dominant sources, as opposed to the ANN solution.

As discussed in Section 4.7.2, regression metrics can be obtained for TP, FP, and FN separately. Thus, it is of interest if they differ. Table 4.11 shows that TP errors are lower than FN. However, they are not arbitrarily large, so the proposed architecture performs the classification and regression task explicitly and separately. The SSR of FP is below SSR < -10 dB so that they introduce only little unwanted energy into the estimation. This is important so wrongly predicted FP sources do not dominate the overall result.

Figure 4.39 shows the classification results for case 3) over the SSR, i.e., the total number of sources per sample. Here, the total SSR (integrated over all frequencies) is used, see eq. 4.7.9. Figure 4.39 (a) and (b) show how many samples are classified correctly (independently of the predicted location and strength). At large SSR, nearly all test samples are classified correctly. Below SSR ≤ -5 dB around 2% are FN, and below SSR ≤ -10 dB up to 3.5% are FP. This shows that with a decreasing SSR,

first samples are more likely to be FN, and with a further decreasing SSR, FP occurs. At an average of -13 dB, see Table 4.11, the influence of the FP on the overall prediction is low. Figure 4.39 (c) and (d) show the averaged classification confidence at the given SSR. At large SSR, the confidence of true positives approaches unity. With decreasing SSR, it decreases down to 0.98. The first FN appear at $SSR \leq -1$ dB with a classification confidence of approx. 0.3, the first FP at $SSR \leq -10$ dB.

5 Regions Of Interest

This chapter is based on original work [47, 48, 8] and discusses source identification and how spectra are obtained from beamforming results.

Beamforming measurements usually result in 2D or 3D beamforming maps for each observed frequency. They are often varied over Mach number M , angle of attack of the flow α , and geometrical parameters of the observed model. The level of the beamforming map entries indicates a sound source emission power, usually described by the $\text{PSD}(\mathbf{x}, f, M, \dots)$ for each frequency f and each focus point \mathbf{x} , but can also result from background noise, spurious noise sources, and beamforming artifacts. Additionally, the localization can be disturbed by sound reflections, scattering, and refraction. Consequently, the resulting beamforming maps must be analyzed to extract the desired source information. For this process, it is useful to integrate the high dimensional $\text{PSD}(\mathbf{x}, f)$ over spatial regions of the map to obtain a low-dimensional $\text{PSD}(f)$ that can be properly displayed in 2D. Ideally, the process only includes the locations of the respective source of interest while rejecting locations of other sound sources. This is aggravated by the fact that the source location may vary over the frequency and Mach number due to the flow-dependent nature of the sources themselves or due to the aforementioned scattering and refraction within the sound propagation from the source to the array microphones.

A common way to handle this source identification is the spatial integration of resulting beamforming maps over so-called Regions Of Interest (ROI). This results in low-dimensional data such as spectra [86], which human experts can interpret. Three approaches exist for the manual definition of ROIs. First, the whole beamforming map is integrated into a single spectrum, which is then analyzed for prominent features, such as tones or peaks, as shown in Figure 4.9. Then, the 2D beamforming map, as shown in Figure 4.8, at these frequencies or frequency bands is observed to determine the origin of these sources, and ROIs are defined to account for these. Second, the beamforming maps are observed at a variety of chosen frequency intervals, such as octaves, and ROIs are defined based on the consistent appearance of sources at multiple frequencies, intuition, and experience. Third, ROIs are defined based on the studied geometry, e.g., leading and trailing edges of a wing, as shown in Figure 5.1. A challenge for these methods is the distinction between beamforming artifacts and real sources; the correct separation of close and overlapping sources; the detection of sources with a low PSD and small-band sources; and the detection of sources that appear only at some of the measurement variations described above, e.g., they only appear at one angle of attack. Therefore, the definition of the ROI may not only depend on the wind tunnel model but on the array resolution as well as the signal-to-noise ratio and the methods used to process the beamforming maps [87]. A wrong or insufficient ROI definition results in degraded or wrong spectra, which is especially problematic since most of the following aeroacoustic analysis is based on these.

For aeroacoustic measurements, the expert performs the important task of defining ROIs manually. It typically takes hours to days, depending on the complexity of the beamforming maps, the studied model, and the number of different configurations (e.g., some sources only appear at specific angles

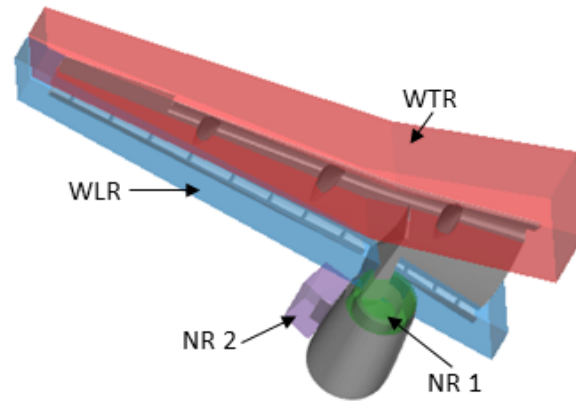


Figure 5.1: Representation of subgrid volumes on the model for the Wing Leading Region (WLR), the Wing Trailing Region (WTR) and two sub-volumes for the Nacelle Region (NR).

of attack or flow configurations). For highly complex models and configurations, such as the presented Do728 and A320 experiments, individual sources and ROI have only been defined and analyzed exemplarily, such as the strake [4].

While the introduced broadband GO and gridless ANN methods solve this problem during the beamforming step by directly predicting source objects, these methods are still only validated on generic problems. Even though conventional beamforming is very limited in terms of resolution and dynamic range, it is still primarily used in wind tunnel experiments in combination with deconvolution methods [4, 7, 8]. The reason for this is the low SNR which is often below $\langle \text{SNR} \rangle_f \leq -10$ dB [19] (the noise exceeds the sources by more than 10 dB), that it does not require prior knowledge of the source configurations and distributions, that it is robust and fast. Thus, this chapter focuses on methods that can be deployed after the use of various existing state-of-the-art imaging techniques in the frequency domain, such as conventional beamforming in combination with CLEAN-SC or DAMAS. The main advantage is that the underlying beamforming methods can be improved while the presented post-processing methods are still applicable. The methods are evaluated on CLEAN-SC results of the generic dataset, the Do728, A320, and Embraer model.

5.1 Manual ROI definition

Typically, ROI are manually defined based on experience and a priori knowledge of the expected sound sources. As an example, the result of manual ROI will be shown for the Embraer. Figure 5.1 shows the manually defined ROI for the Wing Leading Region (WLR), for the Wing Trailing Region (WTR), and two sub-volumes for the Nacelle Region (NR I and NR II).

Figure 5.2 shows the resulting ROI spectra. One can argue that for many aeroacoustic analyses, these spectra are sufficient. However, when trying to perform an in-depth analysis to extract the aeroacoustic source mechanism, these spectra are insufficient, see Section 2.1.2. Figure 4.9 showed the self-similarity analysis of the spatially integrated source maps. Subfigures (a) and (b) show that a Strouhal-like scaling is appropriate for some frequency ranges. For others, a Helmholtz-like scaling is appropriate. However, no perfect self-similarity is observed. Further, a different Mach power

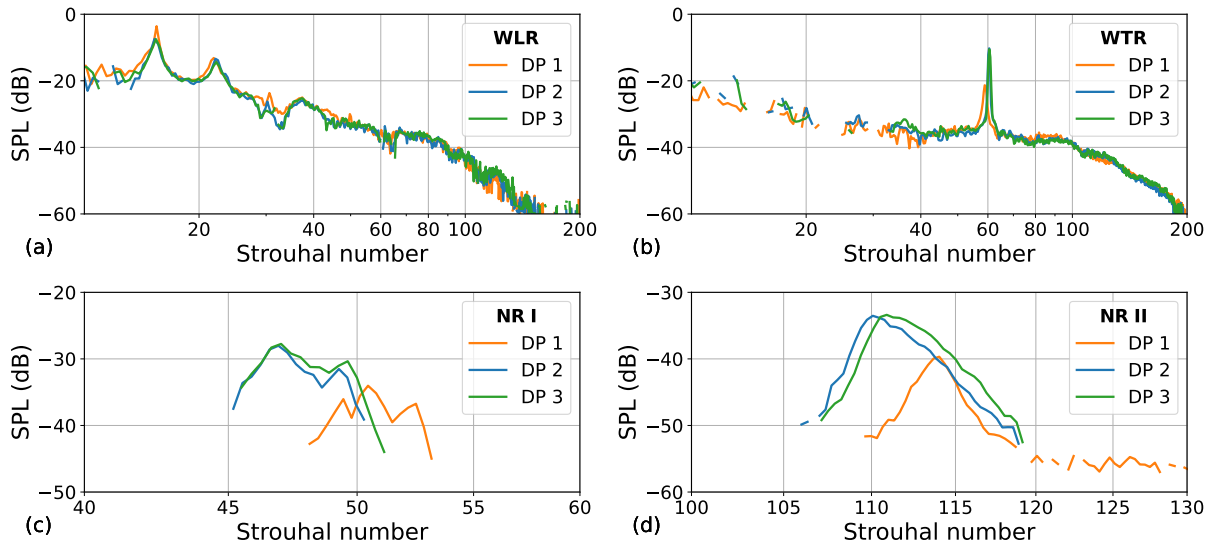


Figure 5.2: Integrated sources of the subgrid volumes (a) WLR, (b) WTR, (c) NR I and (d) NR II vs Strouhal number for DP 1, DP 2 and DP 3.

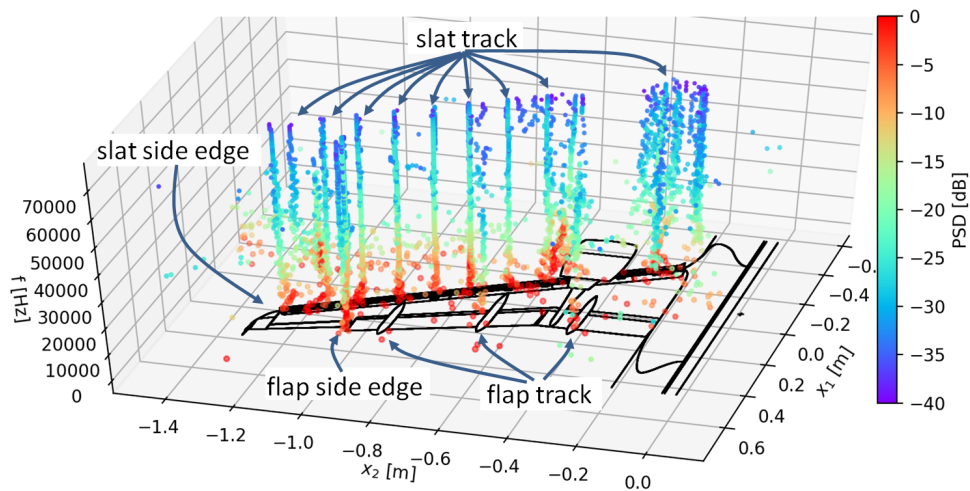


Figure 5.3: A320, CLEAN-SC result on 2D-plane using conventional beamforming, the z-axis displays the frequency. The color represents the normalized PSD in decibel at $M = 0.2$, $\alpha = 3^\circ$.

scaling is observed for different frequency ranges. While for low to medium frequencies, a M^5 -scaling seems appropriate, as the aeroacoustic literature suggests, this exponent does not scale the tonal components of the spectra. Further, the ROI spectra in Figure 5.2 still contain broadband and tonal components with different scaling behavior.

This exemplary result emphasizes that for an in-depth source analysis, ROI for individual sources must be defined to observe their individual spectra. A priori information about the source locations should be neglected, as they contradict the idea of beamforming: Integrating large areas can lead to integrating different source types and may result in accidentally ignoring sources in unexpected regions.

5.2 Source identification results

A general problem concerning beamforming is that the localization of acoustic sources is difficult at long wavelengths. Furthermore, imaging artifacts may occur due to the sparse spatial distribution of the microphone array. These artifacts result from background noise, the array's PSF, and aliasing or insufficient Welch estimations [87].

This section proposes two ideas on identifying sources from beamforming maps contaminated with noise and obtaining their spectrum. The ideas are based on the sparsity of beamforming maps, in the sense that the quantity of zero elements ($\text{PSD} = 0 \text{ Pa}^2 \text{ Hz}^{-1}$) is large compared to the non-zero elements in the maps ($\text{PSD} \geq 0 \text{ Pa}^2 \text{ Hz}^{-1}$). This can be achieved using inverse beamforming methods or conventional beamforming [87] in combination with what is known in the aeroacoustic beamforming community as “deconvolution”, such as CLEAN-SC [114] or DAMAS [16].

Conventional beamforming with diagonal removal [87] in combination with CLEAN-SC is used over DAMAS because of the huge number of computed beamforming maps and the high spatial resolution of the maps. CLEAN-SC results in a sparse representation of the estimated sound power, see Section 4.3, which allows us to analyze the spatial distributions of non-zero elements in space and frequency. For terminology, every non-zero element in the map is called a “source-part” s since they represent full sources once integrated over space and frequency. Thus, the resulting sparse beamforming maps can be reduced to a list of n source-part vectors $s_i = [\mathbf{x}_i, f_i, \alpha_i, M_i, \text{PSD}_i]$, with $i = 1, \dots, I$.

Figure 5.3 displays the source-parts of the CLEAN-SC result on a 2D-focus grid for the A320. On the z-axis, the frequency is displayed, and the color represents the normalized PSD. We can identify multiple vertical pillars of source-parts s which, spatially integrated, represent a source spectrum $\text{PSD}(f)$. However, we also observe pillars that suddenly split with increasing frequency (e.g., at the flap side edge) or dense point clouds that are spatially scattered around (e.g., the inner slat). A source-part pillar that splits with increasing frequency can either be caused by a complex aeroacoustic mechanism or the limitations of beamforming and CLEAN-SC. It is expected to observe this behavior for frequencies around the Rayleigh Criterion f_R below which two separate sources cannot be spatially resolved. This frequency is in the range of $5 \text{ kHz} \leq f_R \leq 6 \text{ kHz}$ for the Do728 and $8 \text{ kHz} \leq f_R \leq 16 \text{ kHz}$ based on the oval array apertures and the distance between the high-frequency pillars. Since the frequencies at which the pillars separate coincide with the Rayleigh frequencies f_R , this behavior is probably caused by the latter. Unfortunately, beamforming and deconvolution methods do not provide any information on which source-parts (in space and frequency) are generated by the same turbulence-induced aeroacoustic source-mechanism.

Figure 5.4 displays the source-parts of the CLEAN-SC result on a 2D-focus grid for the Do728 similarly. However, the delta PSD from the mean per frequency is displayed with

$$\Delta \text{PSD}(f) = \text{PSD}(f) - \langle \text{PSD}(f) \rangle_f. \quad (5.2.1)$$

This way, the frequency-dependent decrease in SPL is compensated, and one can observe dominant sources per frequency. One can observe that in some frequency regions, the inboard slat is domin-

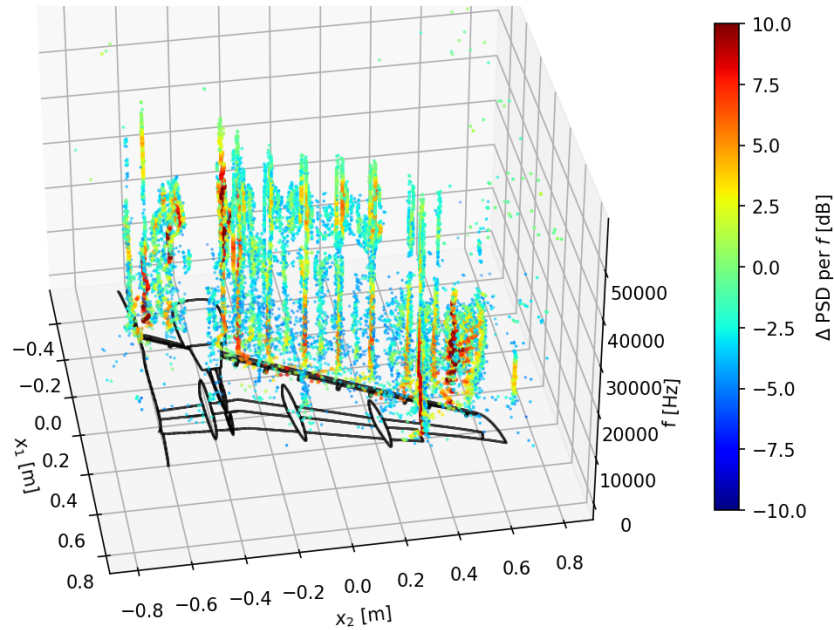


Figure 5.4: Do728, CLEAN-SC result on 2D-plane using conventional beamforming. The color represents the per frequency normalized PSD in decibel at $Re = 1.4 \times 10^6$, $M = 0.125$, $\alpha = 1^\circ$.

ant, the nacelle region, the outboard slat between the last two slat tracks, as well as the flap side edge.

As shown in the previous subsection, large spatial ROIs were defined manually as integration areas to obtain spectra [113] such as the whole slat and flap region. This partly contradicts the beamforming idea, as we often do not know where sources are located and whether all source-parts within the integration region belong to the same source. The following section introduces two methods to estimate the existence and positions of individual sources in sparse beamforming maps and how to assign the corresponding source-parts to them correctly.

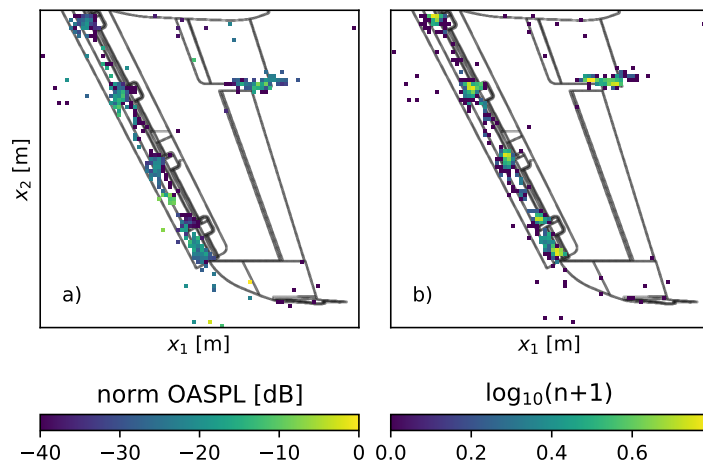


Figure 5.5: A320, section of the CLEAN-SC map at $M = 0.175$, $\alpha = 3^\circ$. (a) shows the normalized OASPL, (b) shows a log-histogram of the n source-parts s per focus point \mathbf{x} .

5.2.1 Source Identification based on spatial Normal Distributions (SIND)

Figure 5.5 (a) shows the normalized Overall Sound Pressure Level (OASPL) for each spatial location \mathbf{x} for the A320. The OASPL is the integration of the source-parts Sound Pressure Level (SPL) over frequency. We observe that the individual slat tracks, which are assumed to be individual sources, cannot be easily distinguished based on the OASPL because the sound carries most energy at long wavelengths. Due to the array resolution, beamforming is not able to localize sources well at these wavelengths (see Figure 5.3). However, ignoring the SPL and simply counting how often a source-part s was reconstructed by CLEAN-SC at every location \mathbf{x} in the entire map over frequency provides a better grasp on individual source distributions, which are shown in the logarithmic histogram in Figure 5.5 (b). Thus, the OASPL(\mathbf{x}) gives an estimation of a source emission power while the histogram(\mathbf{x}) estimates how many frequencies emit sound per location in the source map. In the log-histogram, we observe mostly distinguishable blobs with maxima in their center that probably represent aeroacoustic sources, as the blobs' positions coincide with the location of the slat tracks, the slat side edge, and the flap side edge. These blobs probably originate from point-like sources that are smeared out in the beamforming map due to the Gaussian nature of the turbulence-induced source mechanisms and the scattering and refraction of sound waves in turbulent structures [37].

While the blobs in the log-histogram do resemble normal distributions, statistical tests such as the Shapiro-Wilk or the Anderson-Darling test do not determine that data as normal. This is because of the discrete spatial sampling, the overlapping of sources, and the large population of source-parts. Thus, to verify the normality assumption, the histogram of individual sources is compared to a normal distribution. To do so, a normal distribution is fitted to the log-distribution of source-parts' appearance by minimizing the absolute difference between the source-part's position histogram and the estimated normal distribution using a l_1 -norm. Then, the estimated distribution is compared to the observed data. The normal distribution in 2D is calculated with eq. 5.2.2 [1]. For practical applications, it is recommended to optimize for the normal distribution's amplitude \hat{A} , the standard deviations σ_{x_i} , the distribution rotation θ , and the location $x_{i,0}$ by using a bounded optimization method with equations 5.2.3. The histogram's global maximum determines the starting values for the first source's \hat{A}, \mathbf{x}_0 ; the bounds $\hat{A} \pm \varepsilon_{\hat{A}}, \mathbf{x} \pm \varepsilon_{\mathbf{x}}$ prevent the optimizer from wandering off to a completely different source.

$$\mathcal{N}_{2D} = \hat{A} \exp \left(- (a(x_1 - x_{1,0})^2 + 2b(x_1 - x_{1,0})(x_2 - x_{2,0})) + c(x_2 - x_{2,0})^2 \right) \quad (5.2.2)$$

$$a = \frac{\cos^2 \theta}{2\sigma_{x_1}^2} + \frac{\sin^2 \theta}{2\sigma_{x_2}^2} \quad (5.2.3a)$$

$$b = -\frac{\sin 2\theta}{4\sigma_{x_1}^2} + \frac{\sin 2\theta}{4\sigma_{x_2}^2} \quad (5.2.3b)$$

$$c = \frac{\sin^2 \theta}{2\sigma_{x_1}^2} + \frac{\cos^2 \theta}{2\sigma_{x_2}^2} \quad (5.2.3c)$$

The following Do728 and A320 results are based on 2D beamforming with steering vector formulation III. Figure 5.6 (a) shows the normalized log-distribution of the source-parts (dotted lines) for the Do728 flap side edge region. The histogram shows the summation of all source-part from all beam-

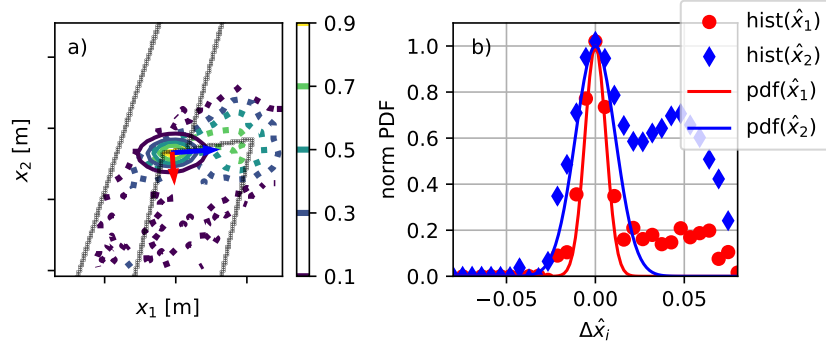


Figure 5.6: Do728, flap side edge region. (a) shows the isocontour lines of the by \hat{A} normalized distribution (dotted lines) and its fitted PDF (full lines). (b) shows the normalized distribution and PDF on its principal axis \hat{x}_1 and \hat{x}_2 which result from the θ -rotation of the fitted distribution and are marked with arrows of the same color in (a).

forming maps in the dataset containing 48 individual measurement configurations. We observe two overlapping blobs in this region, a major one upstream and a minor one downstream. As described above, a 2D normal distribution is fitted to minimize the major source-part blob (full lines) using eq. 5.2.2. Two principal axes \hat{x}_1 and \hat{x}_2 are introduced for which the normal distributions standard deviations σ_{x_i} are independent. They are obtained for each source from the fitted normal distribution's angle θ . Figure 5.6 (b) compares the normalized histogram and fitted distribution along these axes to verify the normality assumption. For terminology, the fitted, amplitude-normalized normal distributions are referred to as the Probability Density Function (PDF) of the source-part distribution of a source. While a PDF in the traditional mathematical sense is defined as a normalized distribution so that its integrated area is unity, here the PDF is normalized so that $0 \leq \text{PDF}(\mathbf{x}) \leq 1$. This means that the integrated area of the defined source-part PDF can be any real number $\mathbb{R} \geq 0$ and that the PDF can be interpreted as the probability of a spatial location \mathbf{x} belonging to a source.

As shown in Figure 5.6, an individual source can be approximated with a normal distribution in the histogram. To find and fit all sources in the beamforming map (e.g., the second source on the right in Figure 5.6), the distance metric d_{S_i} is introduced, see eq. 5.2.4, to measure and minimize the l_1 -norm of the estimated PDF of a source S_i and the histogram. With the set X_{S_i} containing all focus points \mathbf{x}_j , we want to minimize d_{S_i} for all assumed sources $S_i \in \mathcal{S}$ in the beamforming map so that the l_1 -norm of the source-part histogram and the fitted normal distributions achieves a minimum.

$$d_{S_i} = \sum_{\mathbf{x}_j \in X_{S_i}} |\text{hist}(\mathbf{x}_j) - \text{PDF}_{S_i}(\mathbf{x}_j)| \quad (5.2.4)$$

This thesis proposes a greedy algorithm that uses this metric to find all sources by minimizing $d_S = \sum_i d_{S_i}$ by iteration. First, we find the maximum in the source-part histogram; second, we fit a normal distribution that minimizes the histogram, see eq. 5.2.4; third, we subtract the fitted distribution from the histogram and fourth, repeat the process until the remaining histogram-maximum drops below a threshold t_I . This threshold represents a lower significance bound and prevents endless fitting iterations since d_S will decrease with an increasing number of sources that are either irrelevant or fitting artifacts. Thus, the order in which the method identifies sources in the histogram corresponds to their descending magnitude \hat{A}_{S_i} in the histogram. Note that this magnitude \hat{A}_{S_i} does

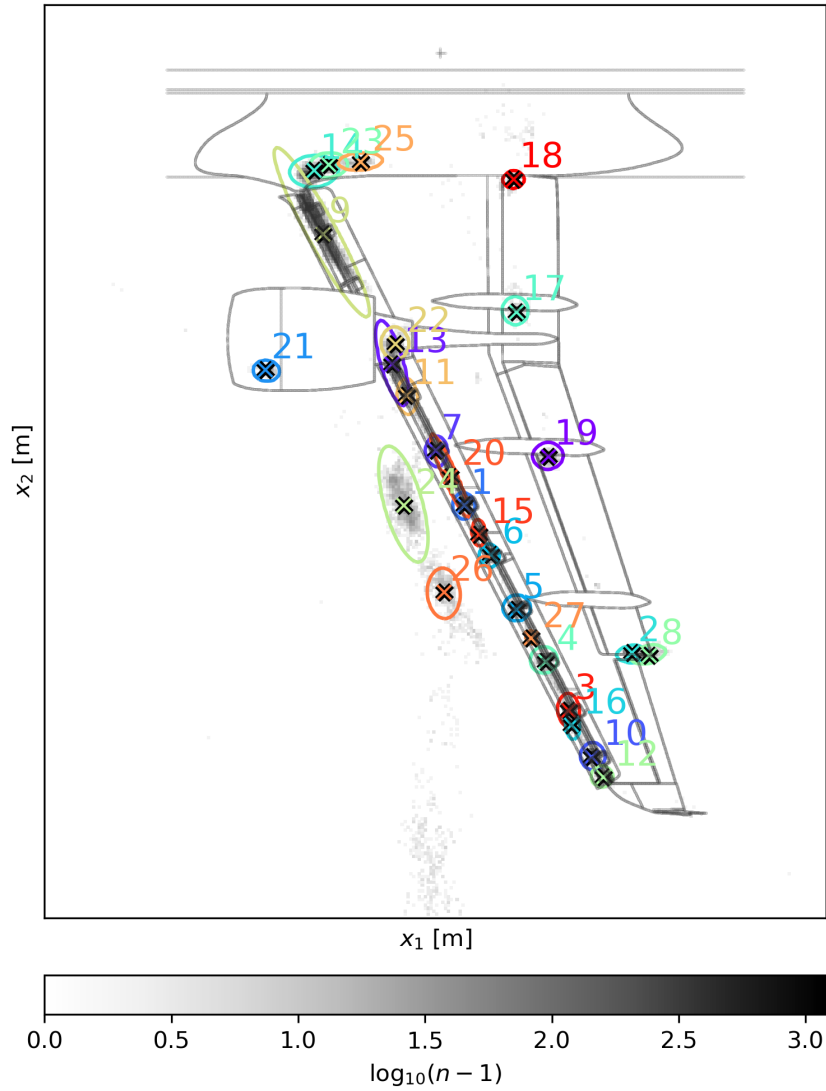


Figure 5.7: A320. The SIND solution for $t_I = 20$ is shown. The source numbers correspond to the order of found sources via the maxima in the histogram n , which is displayed with the underlying colormap. The ellipses around the sources represent the PDF functions at $1 - 3\sigma$.

not explicitly depend on the source-part's PSD and, thus, does not necessarily indicate a dominant source. Instead, a large \hat{A}_{S_i} indicates either a broad-band source, a spatially well-localized source, or a combination of these features. However, since CLEAN-SC works within a certain SNR, a set of source-parts that represent a source implicitly indicate that the source was somewhat relevant within the beamforming map.

This makes this method similar to an iterative GMM. Traditionally, a degree-of-freedom weighted residual such as the Bayesian Information Criterion is used for GMM to determine the optimal number of sources [111]. Since the result of GMM heavily relies on the chosen number of sources, the number of sources must be estimated before clustering, as opposed to the proposed method because it works

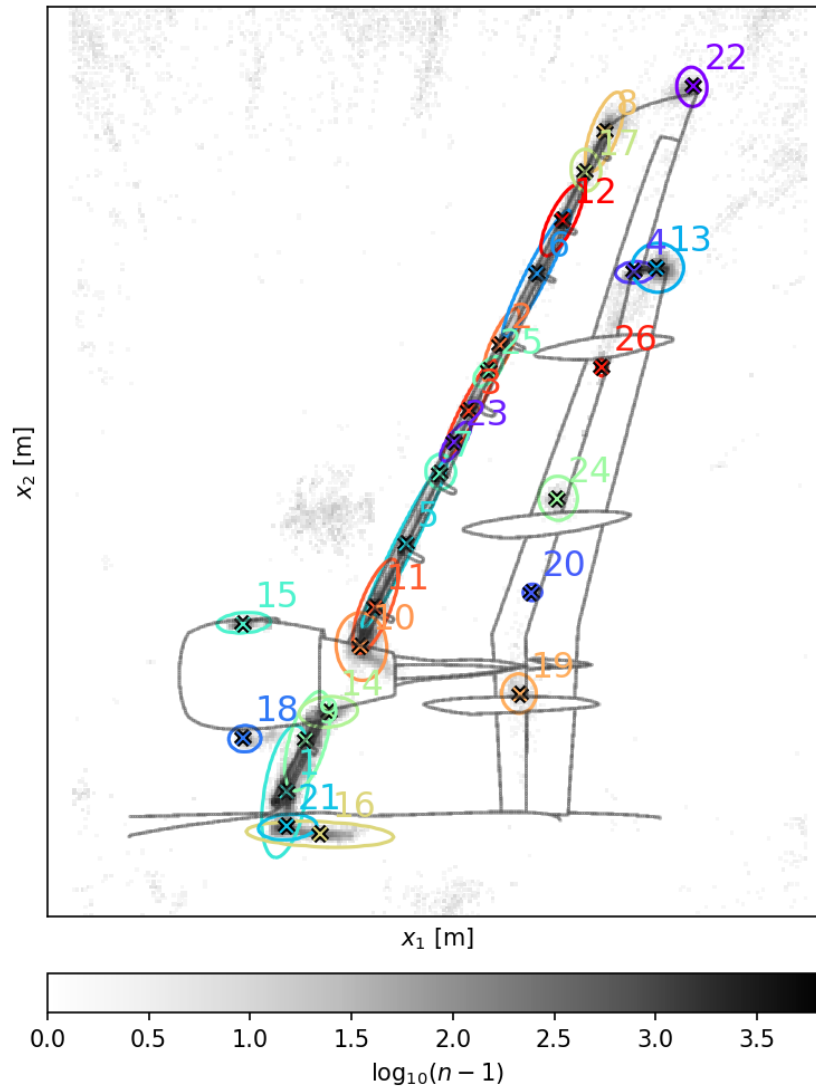


Figure 5.8: Do728. The SIND solution for $t_I = 30$ is shown. The source numbers correspond to the order of found sources via the maxima in the histogram n , which is displayed with the underlying colormap. The ellipses around the sources represent the PDF functions at $1 - 3\sigma$.

iteratively. The number of sources can be estimated after the fitting process is complete. To do so, the fitted normal distributions are integrated, see eq.5.2.2, to obtain an area A_{S_i}

$$A_{S_i} = \int_{x_1} \int_{x_2} \hat{A}PDF_{S_i}(x_1, x_2) dx_2 dx_1 \quad (5.2.5)$$

for each source. This area reflects the impact of the estimated individual sources on the l_1 -norm for d_S . If A_{S_i} drops below a threshold t_A we can reject it as a fitting artifact or negligible source. A_{S_i} of artifacts is orders of magnitude below A_{S_i} of real sources. However, if the threshold t_I is sufficiently large, SIND's iterations often stop before fitting artifacts occur.

Figure 5.7 shows the result of the procedure for the A320 with the selected thresholds given in Table 5.1. No sources are rejected as fitting artifacts ($t_A=0$). The crosses mark the determined centers of the sources. The numbers correspond to the order in which they are identified (descending \hat{A}).

	n	SIND			SIHC	
		t_I	t_A	t_σ	t	t_σ
Do728	10^6	30	0	$1 - 3\sigma$	500	$1 - 3\sigma$
A320	10^4	20	0	$1 - 3\sigma$	105	$1 - 3\sigma$
generic	10^3	20	0	$1 - 3\sigma$	100	$1 - 3\sigma$

Table 5.1: SIND and SIHC parameters for the A320, Do728, and generic dataset and the total number n of source-parts present in the datasets.

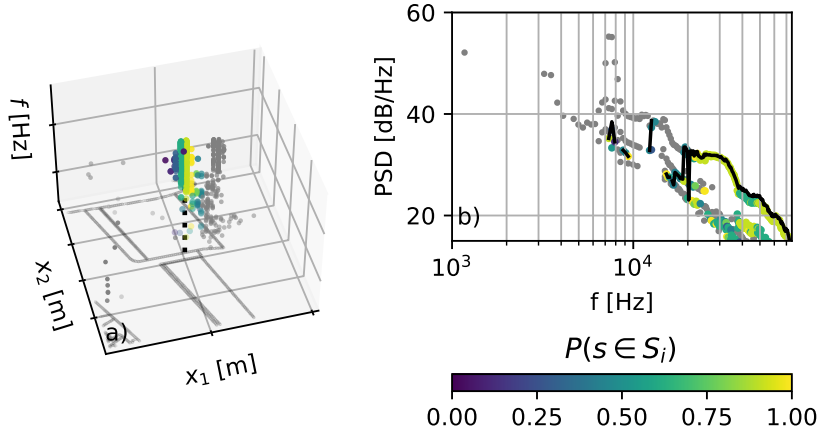


Figure 5.9: (a) shows the source-parts of the A320 upstream flap side edge region (source number 2 in Figure 5.7) at $M = 0.175$, $\alpha = 9^\circ$, (b) shows the same source-parts without the x_i -information. The color represents the source-parts' conditional probability of belonging to the source $P(s \in S_j)$ under the condition that they were assigned to it, gray source-parts were rejected as noise or assigned to another source. The black line represents the integrated spectrum from all source-parts that were assigned to the source.

Figure 5.8 shows the procedure result for the Do728. Then, the probability P of belonging to each source using PDF_{S_i} is calculated for all source-parts. Finally, source-parts with a PDF value below a threshold t_σ are discarded as noise. The remaining source parts are assigned to the source with the highest probability and integrated for each frequency. Thus, each source-part is either assigned to a single source or classified as noise if $P(s \in S) < t_\sigma$. In Figure 5.7 and Figure 5.8, the ellipses around the marked sources represent $\text{PDF}_S(\mathbf{x}) = 1 - 3\sigma$ and thus indicate the spatial locations (ROI) that are assigned to the corresponding sources.

Figure 5.9 shows the method's result in detail for the leading flap side edge (LFSE) source location (see also Figure 5.6 for the Do728 LFSE fit, which shows two source-part distributions in this region) and all source-parts in this region. The source-parts' color encodes their corresponding PDF value. This can be interpreted as the conditional probability that they belong to the assigned source under the condition that they were assigned to it. Gray source-parts were either rejected as noise or assigned to another source, as its PDF (i.e., probability of belonging to this source) was higher in these spatial locations. Figure 5.9 (a) shows the source-part distribution on the 2D focus grid, and the z-axis displays the frequency. Figure 5.9 (b) shows all source-parts from the region depicted in (a), neglecting the x_i -information. In Figure 5.9 (b), we observe multiple horizontal rows of points. They can either have a different shape, which indicates that these are the source-parts from two different sources, or a similar shape with a simple vertical decibel offset. If the latter is observed, these rows

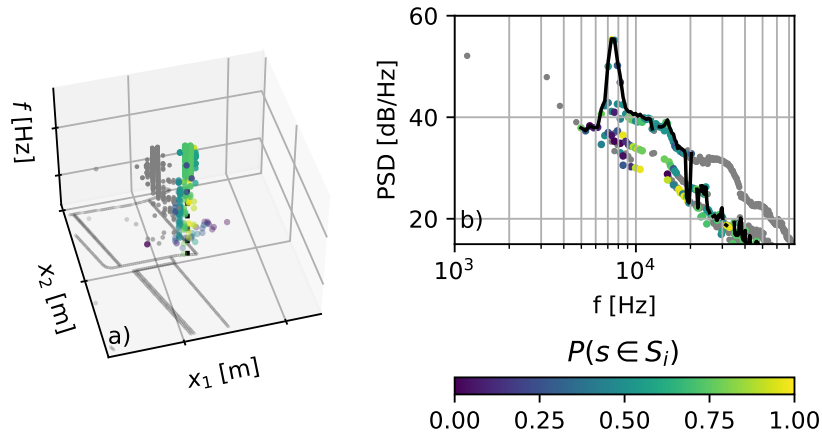


Figure 5.10: The Figure shows the source-parts of the A320 downstream flap side edge region (source number 8 in Figure 5.7) at $M = 0.175$, $\alpha = 9^\circ$, according to the description in Figure 5.9.

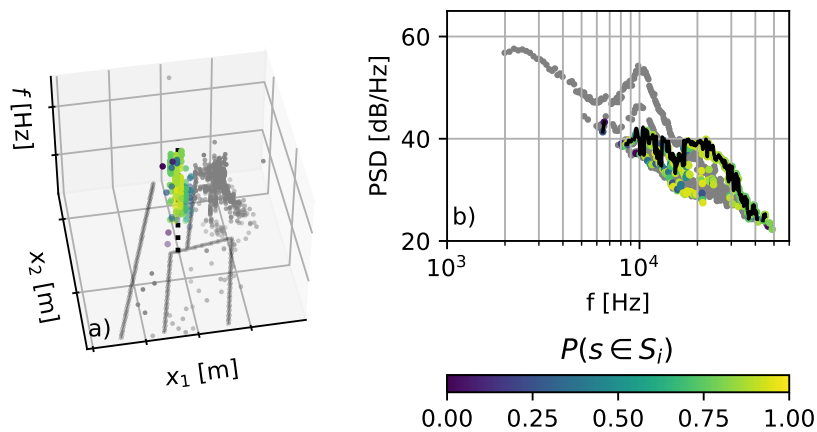


Figure 5.11: (a) shows the source-parts of the Do728 upstream flap side edge region (source number 4 in Figure 5.8) at $M = 0.250$, $\alpha = 6^\circ$, according to the description in Figure 5.9.

at a lower PSD are artifacts from the CLEAN-SC process due to the gain factor, see Section 4.3. If the source-part rows have a different shape and are expected to belong to different source PSDs, the optimal scenario would be if one is assigned to the source with high confidence (color) and the others are rejected (gray).

Figure 5.10 shows the same for the downstream flap side edge region. The top row of source parts in the Figures shows, from low to high frequencies, a tonal peak around $f \approx 6$ kHz, and then three humps at $f \approx 15$ kHz, $f \approx 30$ kHz, and $f \approx 50$ kHz. Most source-parts of the first peak and hump were assigned to the TFSE, the source-parts of the two high-frequency humps were mainly assigned to the LFSE. A detailed analysis of how well this separation is performed is given in section 5.2.3. After integrating all source-parts assigned to the source over the frequency, we obtain the source spectra, indicated by the black line in Figure 5.9 and Figure 5.10. In these examples, the spectra are mostly smooth, but around $f \approx 20$ kHz there are strong artifacts from incorrectly assigned source-parts.

Figure 5.11 and Figure 5.12 show the corresponding results for the Do728 flap side edge. Figure 5.13 shows an exemplary Do728 slat / slat track source. This source will be analyzed in detail in sec-

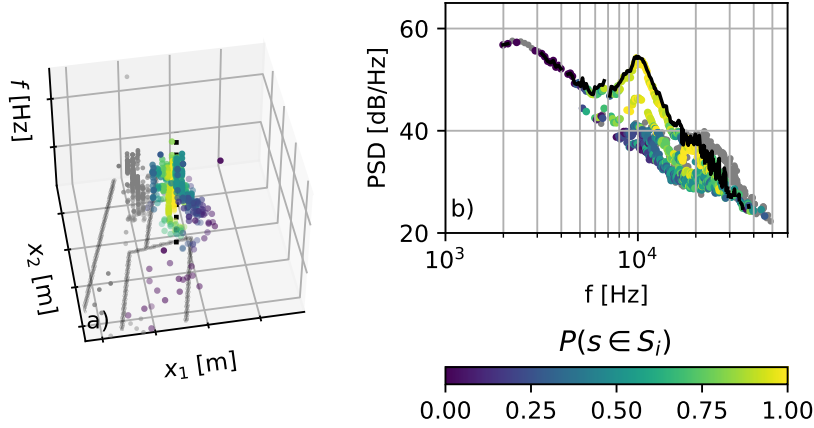


Figure 5.12: (a) shows the source-parts of the Do728 downstream flap side edge region (source number 13 in Figure 5.8) at $M = 0.250$, $\alpha = 6^\circ$, according to the description in Figure 5.9.

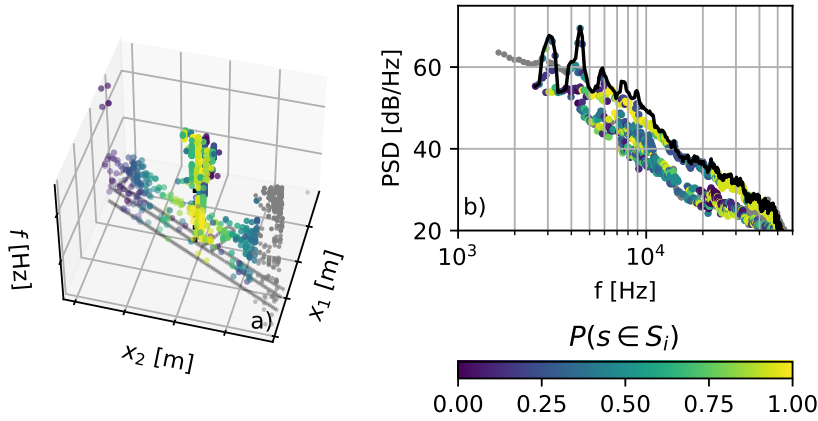


Figure 5.13: (a) shows the source-parts at the DO728 slat track (source number 5 in Figure 5.8) at $M = 0.250$, $\alpha = 1^\circ$, according to the description in Figure 5.9.

tion 5.2.3 since it is presumably a complex spatial superposition of a line source (slat) and a point source (slat track).

SIND assumes that the source positions do not fundamentally change in the beamforming map over M or α (considering a focus grid that rotates and moves with α) so that the source-parts of different measurement configurations can be stacked and fitted at once to obtain global source positions and distributions, as shown in the results above. However, beamforming can suffer from the approximation of Greens Functions in complex medium flows to calculate the sound propagation from the source position to the microphone array or errors in the position of the focal plane [87]. The first results in a shift or stretch of the beamforming maps, the second results in a source that moves through the map with increasing angle α because of the projection error (the strakes of the Do728 in Figure 5.8 show this behavior). The first problem can be fixed by aligning the beamforming maps before fitting the normal distributions. To do so, the source-part histogram of each configuration is calculated individually. Then, a histogram is chosen as a reference. All remaining histogram positions are then linearly modified with

$$\mathcal{F}(x_i) = a_i x_i + b_i \quad (5.2.6)$$

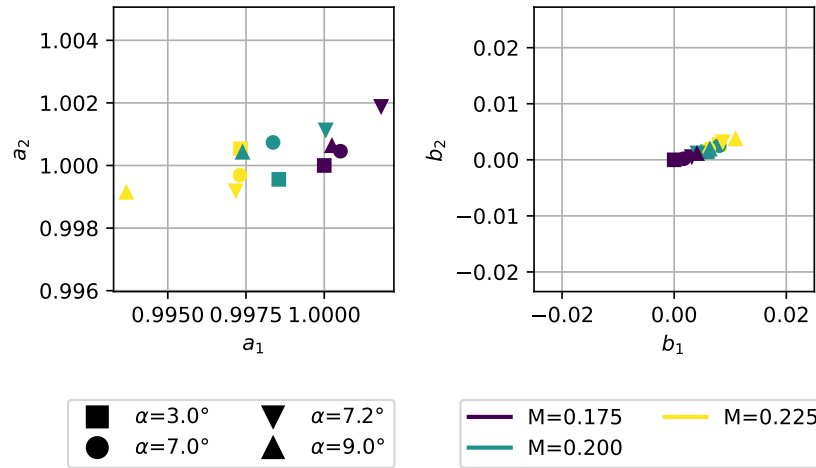


Figure 5.14: A320, beamforming map alignment stretch a_i and shift parameters b_i for the source-part positions x_i relative to the reference beamforming map at $M_1 = 0.175$, $\alpha_1 = 3^\circ$.

to achieve a maximum spatial correlation with the reference histogram using standard optimization methods, using nonlinear interpolation due to the discrete spatial sampling of the data. Eq. 5.2.6 is then used to modify the source-parts' positions x_i before calculating the global histogram. Figure 5.14 shows the obtained parameters a_i, b_i for the A320. While the stretch factors a_i are small, the shift factors b_i show a clear trend. The beamforming maps shift slightly with increasing angle of attack and substantially with increasing Mach number downstream (more than $b_1 \geq 2\Delta x_1$).

5.2.2 Source Identification based on Hierarchical Clustering (SIHC)

A second approach to identifying sources and assigning the corresponding source-parts is clustering methods, which can automatically group source-parts in a multidimensional space. Since we do not know the number of expected clusters (sources) and their distribution beforehand, this thesis employs HDBSCAN [21, 84], see Section 2.3. Similar to SIND, HDBSCAN requires a threshold t below which a cluster is rejected as noise. The threshold significantly affects the resulting clusters and must be determined with the expert in the loop. The source-parts are clustered based on their normalized location \mathbf{x}_i , normalized Strouhal number St_i and Mach scaled, normalized PSD level (all normalized to the range $[0, 1]$), thus in 6D-space. When clustering source-parts of maps at different Mach numbers at the same time, it is recommended using a Mach scaled PSD, see. eq. 2.1.20 with $n \approx 5$ and a normalized frequency like the Strouhal or Helmholtz number. This scaling ensures that the source-parts of sources at different Mach numbers are roughly at the exact location in the frequency and PSD-level space, as aeroacoustic noise generally scales around this Mach exponent [55], see Section 2.1.1.

Figure 5.15 shows the result of HDBSCAN for the A320 at $t = 105$ and Figure 5.16 for the Do728 at $t = 500$, see Table 5.1. The crosses mark the cluster midpoints of the corresponding source-parts, displayed in the same color. Gray source-parts are rejected as noise as their confidence of belonging to any source is below $t_\sigma = 1 - 3\sigma$. The color intensity displays the classification confidence. Figure 5.17 shows the resulting integrated spectra from the A320 flap side edge region in comparison to the SIND method, Figure 5.18 shows the same for the Do728. Figure 5.19 shows the same slat track source from the SIND solution in Figure 5.13 as well as the upper part of the corresponding

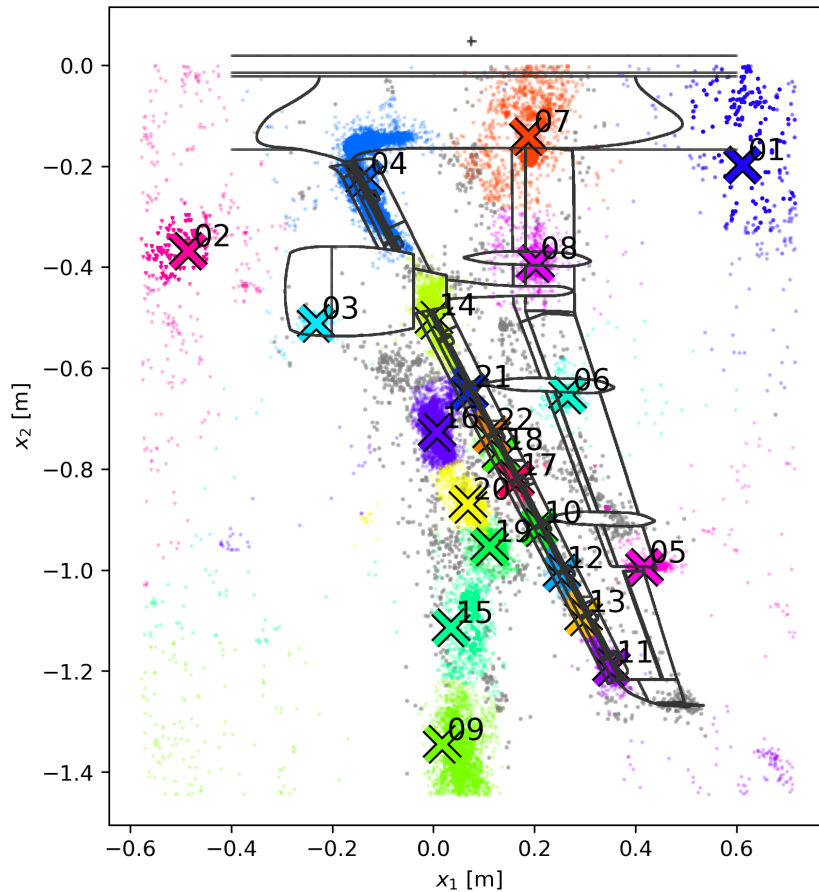


Figure 5.15: A320. Resulting clusters from HDBSCAN at $t = 105$, using an Euclidean distance metric. The cluster midpoints are marked, the corresponding source-parts are displayed in the same color. The color intensity displays the probability of belonging to the cluster. Gray source-parts were rejected as noise.

slat for the SIHC solution.

5.2.3 Comparison of SIND and SIHC

To assess the quality of the ROIs, both methods are compared to each other and sources from the literature. Both methods yield comparable ROIs and can identify the prominent source locations such as the flap side edge, slat tracks, wingtip, or strakes that are indicated by the blobs in the corresponding histograms in Figure 5.7 and Figure 5.8. SIND often separates individual sources in dense and overlapping source regions that are clustered together by SIHC, especially at the inner slat or the flap side edge region. SIHC finds additional source regions that are not well localized and spread over the map, especially sources that are not located on the wing, such as what are assumed to be wind tunnel noise reflections. We observe that SIND and SIHC often find comparable sub- or super-sources in the sense that some sources detected in SIND correspond to multiple sources detected by SIHC or vice-versa, e.g., the flap side edge in Figure 5.17 and Figure 5.18 or the slat / track in Figure 5.19 for the Do728. To assess the quality and legitimacy of the ROI separation, a self-similarity analysis is performed. Thus, the spectra levels are power scaled with eq. 2.1.20 and displayed over Strouhal and Helmholtz numbers. While a single self-similarity across the whole spec-

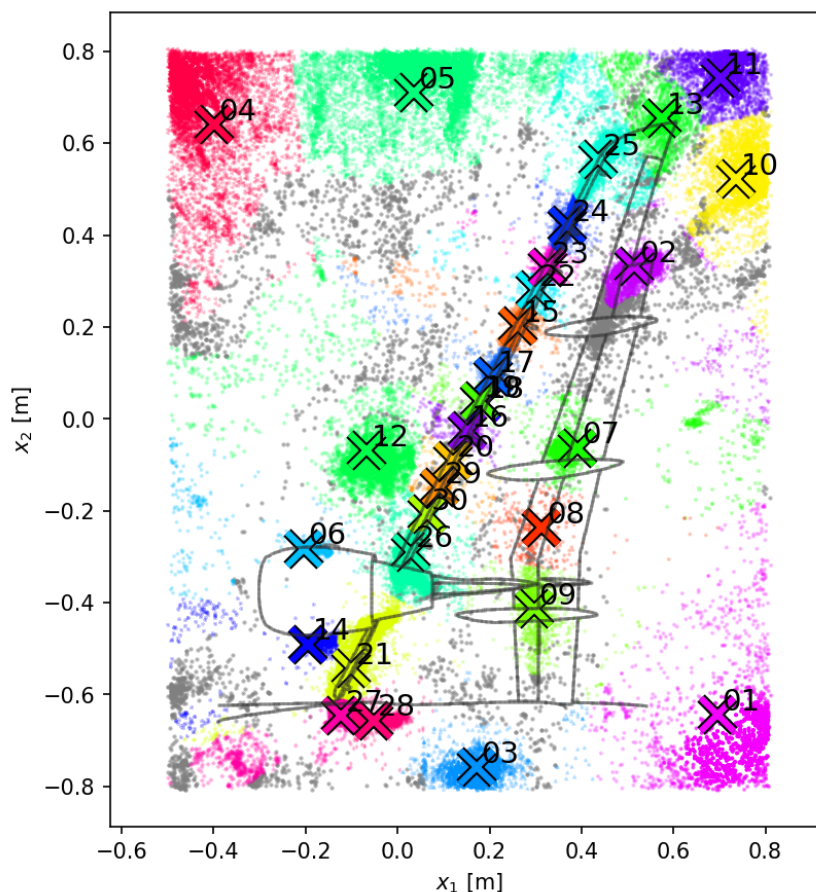


Figure 5.16: Do728. Resulting clusters from HDBSCAN at $t = 500$, using an euclidean distance metric. The cluster midpoints are marked, the corresponding source-parts are displayed in the same color. The color intensity displays the probability of belonging to the cluster. Gray source-parts were rejected as noise.

trum does not necessarily imply that the whole spectrum is generated by the same mechanism, a self-similarity over multiple combinations of the frequency, Helmholtz and Strouhal number in different frequency intervals doubtlessly shows that there exist multiple source mechanisms [93].

For the A320 flap side edge, a self-similarity analysis shows that the up- and downstream separation of SIND is reasonable, see Figure 5.20 and Figure 5.21. While the low-frequency peak scales over the Strouhal number, the high-frequency humps scale over the Helmholtz number, which suggests different aeroacoustic source mechanisms and justifies the spatial separation. Dobrzynski points out that the complex acoustical behavior of the flap side edge is a combination of trailing-edge noise, noise of a primary suction side vortex, a secondary suction side vortex, their mixing, and accelerated free turbulence in the vortex flow [31], which supports this result. We explicitly see in Figure 5.21 that the smaller, high-frequency hump is also self-similar over the Strouhal number, which indicates that it is assigned to the correct source. The analysis of the Do728 flap side edge shows the same self-similarities (not shown). While SIND and SIHC separate most slat and slat tracks, SIHC reconstructs more smooth spectra than SIND by correctly identifying the corresponding source-parts. Figure 5.13 shows that the low-frequency slat tones are not well localized and scattered around the slat area, which matches Dobrzynski's hypothesis that these tones result from model-scale low Reynolds numbers and are generated by coherent laminar flow separation at the slat cove and, thus,

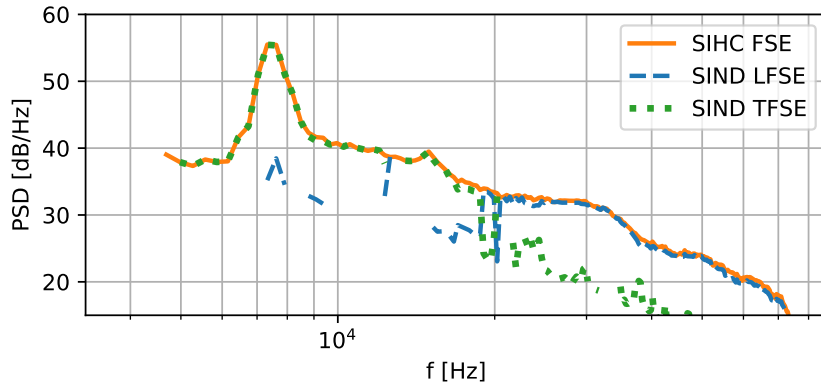


Figure 5.17: Comparison of the resulting source spectra from the SIND and SIHC method at $M = 0.175$, $\alpha = 9^\circ$ for the A320 flap side edge (FSE), respectively leading flap side edge (LFSE) and trailing flap side edge (TFSE).

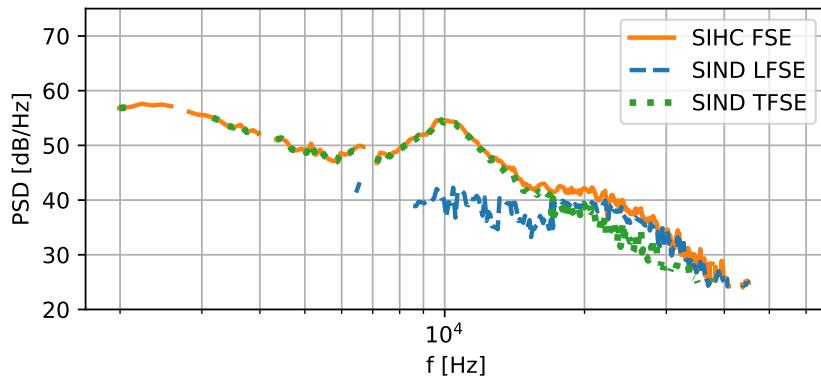


Figure 5.18: Comparison of the resulting source spectra from the SIND and SIHC method at $M = 0.125$, $\alpha = 7^\circ$ for the Do728 flap side edge (FSE), respectively leading flap side edge (LFSE) and trailing flap side edge (TFSE).

are line sources [33, 31]. By distribution assumption, SIND assumes point-like sources, which cannot properly detect these line sources. Even if so, SIND only assigns the source-parts based on their spatial distribution to the sources, but these sources spatially overlap. SIHC, on the other hand, not only separates the Strouhal number scaling slat tones, see Figure 5.22, from the Helmholtz number scaling slat track source, see Figure 5.23, it assigns the source-parts mostly correct in terms of self-

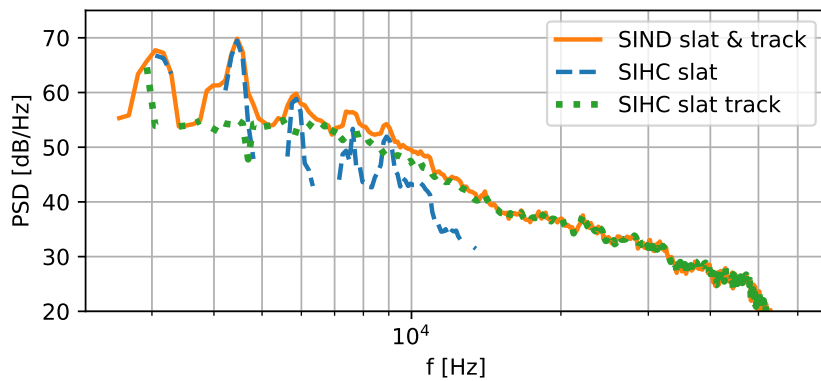


Figure 5.19: Comparison of the resulting source spectra from the SIND and SIHC method at $M = 0.250$, $\alpha = 1^\circ$ for the Do728 slat, the slat track and the combined SIND ROI.

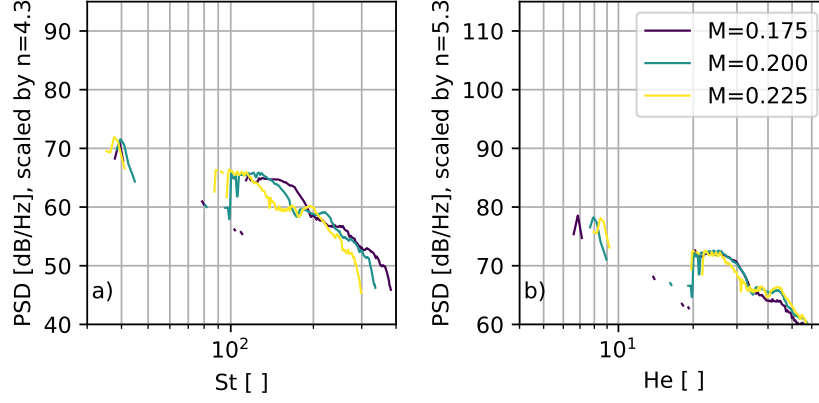


Figure 5.20: The A320 spectra of the SIND leading flap side edge source (number 2 in Figure 5.7) at $\alpha = 9^\circ$ over (a) Strouhal number and (b) Helmholtz number. The spectra are Mach scaled with the scaling exponent n , see eq. 2.1.20.

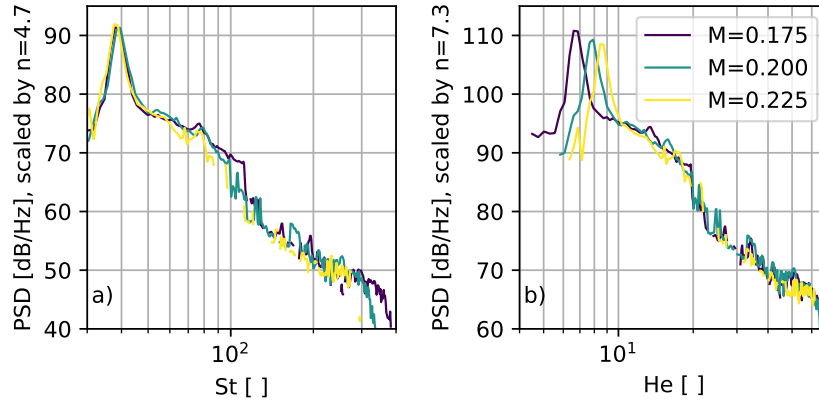


Figure 5.21: The A320 spectra of the SIND trailing flap side edge source (number 8 in Figure 5.7) at $\alpha = 9^\circ$ over (a) Strouhal number and (b) Helmholtz number. The spectra are Mach scaled with the scaling exponent n , see eq. 2.1.20.

similar behavior to the corresponding source spectra. This is possible due to the additional frequency and SPL information, which helps to identify the correct cluster members.

Performance-wise SIHC's computation time scales around $\mathcal{O}(n \log n)$ for the number n of source-parts [84]. Since SIND does not cluster the points directly, the computation time is independent of the number of points, which is a huge advantage for large datasets. The total number of source-parts in the Do728 dataset is around $n = 10^6$, which SIND processes within seconds and SIHC within an hour on a standard laptop. Both methods process the A320 dataset within seconds, which contains around $n = 10^4$ source-parts.

5.2.4 SIND 3D

SIND and SIHC can be performed for 3D beamforming maps. For SIND, the solution for the 3D case can be derived from the multiplication of a 3D normal distribution with at least two different rotation matrices. For practical applications, it is recommended to use all three rotation matrices. This adds an additional rotation angle to the optimization process but yields more stable and better

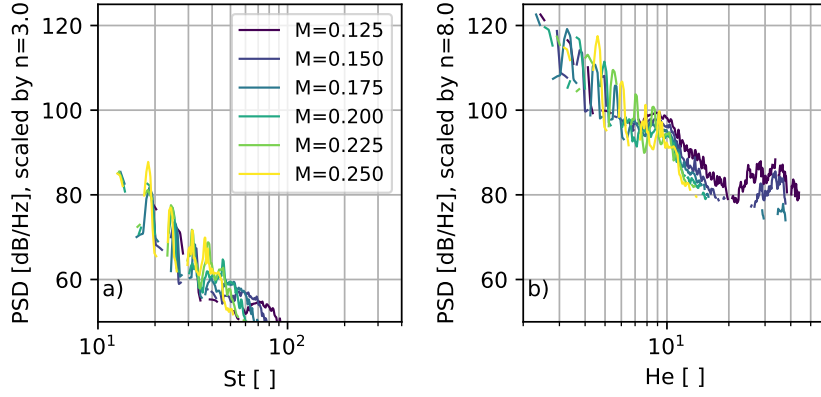


Figure 5.22: The Do728 spectra of the SIHC slat source (number 20 in Figure 5.16) at $\alpha = 1^\circ$ over (a) Strouhal number and (b) Helmholtz number. The spectra are Mach scaled with the scaling exponent n , see eq. 2.1.20.

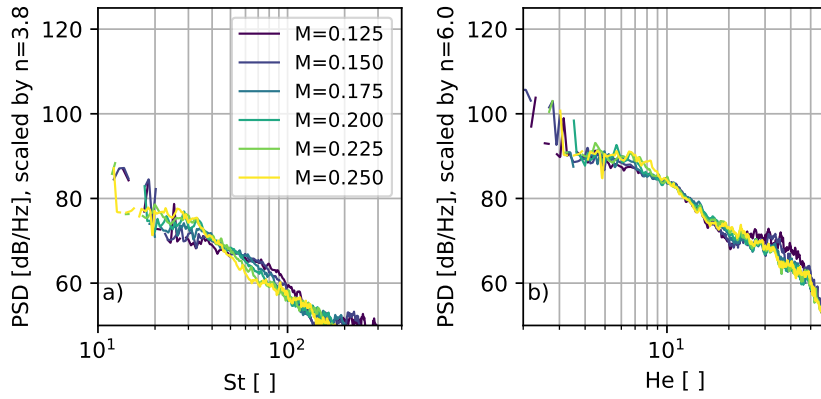


Figure 5.23: The Do728 spectra of the SIHC slat track source (number 29 in Figure 5.16) at $\alpha = 1^\circ$ over (a) Strouhal number and (b) Helmholtz number. The spectra are Mach scaled with the scaling exponent n , see eq. 2.1.20.

results than only two rotations since the l_1 -norm is not convex, and the rotation is non-commutative. With the rotations $R_{x_1}(\alpha)$, $R_{x_2}(\beta)$, and $R_{x_3}(\gamma)$ the 3D normal distribution is

$$\mathcal{N}_{3D} = \hat{A} \exp \left(- (a(x_1 - x_{1,0})^2 + 2b(x_1 - x_{1,0})(x_2 - x_{2,0}) + 2c(x_1 - x_{1,0})(x_3 - x_{3,0}) + d(x_2 - x_{2,0})^2 + 2e(x_2 - x_{2,0})(x_3 - x_{3,0}) + f(x_3 - x_{3,0})^2) \right) \quad (5.2.7)$$

$$a = \frac{\cos^2(\alpha) \cos^2(\beta)}{\sigma_{x_1}^2} + \frac{(\cos(\alpha) \sin(\beta) \sin(\gamma) - \sin(\alpha) \cos(\gamma))^2}{\sigma_{x_2}^2} + \frac{(\cos(\alpha) \sin(\beta) \cos(\gamma) + \sin(\alpha) \sin(\gamma))^2}{\sigma_{x_3}^2} \quad (5.2.8a)$$

$$\begin{aligned}
b = & \frac{\cos(\alpha) \sin(\alpha) \cos^2(\beta)}{\sigma_{x_1}^2} \\
& + \frac{(\cos(\alpha) \sin(\beta) \sin(\gamma) - \sin(\alpha) \cos(\gamma))(\sin(\alpha) \sin(\beta) \sin(\gamma) + \cos(\alpha) \cos(\gamma))}{\sigma_{x_2}^2} \\
& + \frac{(\sin(\alpha) \sin(\beta) \cos(\gamma) - \cos(\alpha) \sin(\gamma))(\cos(\alpha) \sin(\beta) \cos(\gamma) + \sin(\alpha) \sin(\gamma))}{\sigma_{x_3}^2}
\end{aligned} \tag{5.2.8b}$$

$$\begin{aligned}
c = & -\frac{\cos(\alpha) \cos(\beta) \sin(\beta)}{\sigma_{x_1}^2} + \frac{\cos(\beta) \sin(\gamma)(\cos(\alpha) \sin(\beta) \sin(\gamma) - \sin(\alpha) \cos(\gamma))}{\sigma_{x_2}^2} \\
& + \frac{\cos(\beta) \cos(\gamma)(\cos(\alpha) \sin(\beta) \cos(\gamma) + \sin(\alpha) \sin(\gamma))}{\sigma_{x_3}^2}
\end{aligned} \tag{5.2.8c}$$

$$\begin{aligned}
d = & \frac{\sin^2(\alpha) \cos^2(\beta)}{\sigma_{x_1}^2} + \frac{(\sin(\alpha) \sin(\beta) \sin(\gamma) + \cos(\alpha) \cos(\gamma))^2}{\sigma_{x_2}^2} \\
& + \frac{(\sin(\alpha) \sin(\beta) \cos(\gamma) - \cos(\alpha) \sin(\gamma))^2}{\sigma_{x_3}^2}
\end{aligned} \tag{5.2.8d}$$

$$\begin{aligned}
e = & -\frac{\sin(\alpha) \sin(\beta) \cos(\beta)}{\sigma_{x_1}^2} + \frac{\cos(\beta) \sin(\gamma)(\sin(\alpha) \sin(\beta) \sin(\gamma) + \cos(\alpha) \cos(\gamma))}{\sigma_{x_2}^2} \\
& + \frac{\cos(\beta) \cos(\gamma)(\sin(\alpha) \sin(\beta) \cos(\gamma) - \cos(\alpha) \sin(\gamma))}{\sigma_{x_3}^2}
\end{aligned} \tag{5.2.8e}$$

$$f = \frac{\sin^2(\beta)}{\sigma_{x_1}^2} + \frac{\cos^2(\beta) \sin^2(\gamma)}{\sigma_{x_2}^2} + \frac{\cos^2(\beta) \cos^2(\gamma)}{\sigma_{x_3}^2} \tag{5.2.8f}$$

Figure 5.24 shows the 3D histogram of the source-parts of the 3D CLEAN-SC beamforming result with steering vector formulation IV. Here, we observe that the source distribution is convoluted with the array's PSF since the sources form ovals in the direction of the array. The main advantage of the 3D result is that sources overlapping in the 2D result can now be spatially well separated, such as in the nacelle region. Also, since sources that are not in the plane of focus are projected onto the focus plain with the use of steering vector formulation III, which is not the case with formulation IV, which results in less noise and artifacts (e.g., sources 1, 2, 9, 15, 26, 19, and 20 in Figure 5.15 and sources 1, 3, 4, 5, 10, 11, and 12 in Figure 5.16 which are not located on the wing).

Figure 5.25 shows an exemplary result of an by SIND 3D identified slat track source. The true source (normalized) distribution is shown with dashed lines. The fitted normal distribution is shown with full lines. They show a good agreement, considering that multiple sources are present on the slat.

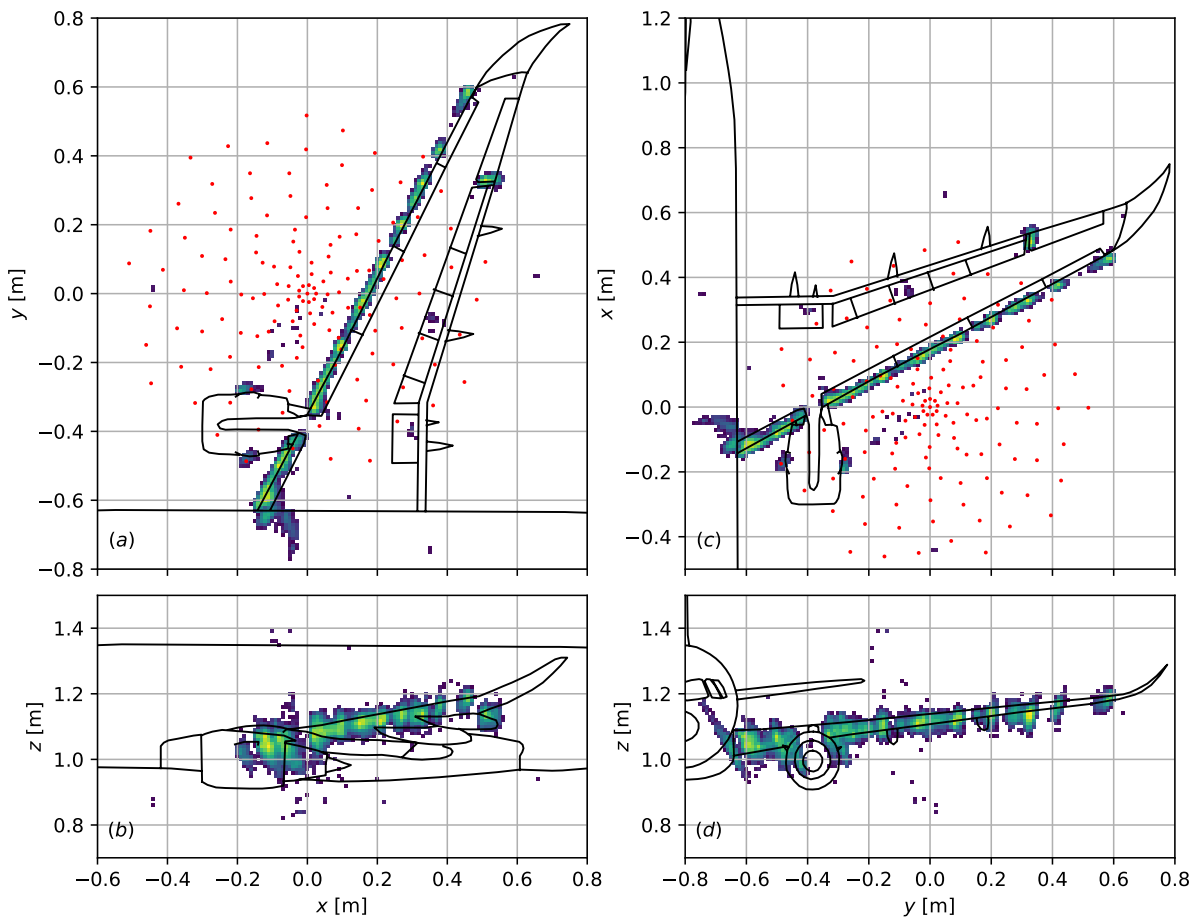


Figure 5.24: Do728 histogram of source-parts at $Re = 1.4 \times 10^6, \alpha = 7^\circ$, all Mach numbers. The histogram is integrated over the dimension not shown. The array is depicted in red for reference and is located at $z = 0$ m.

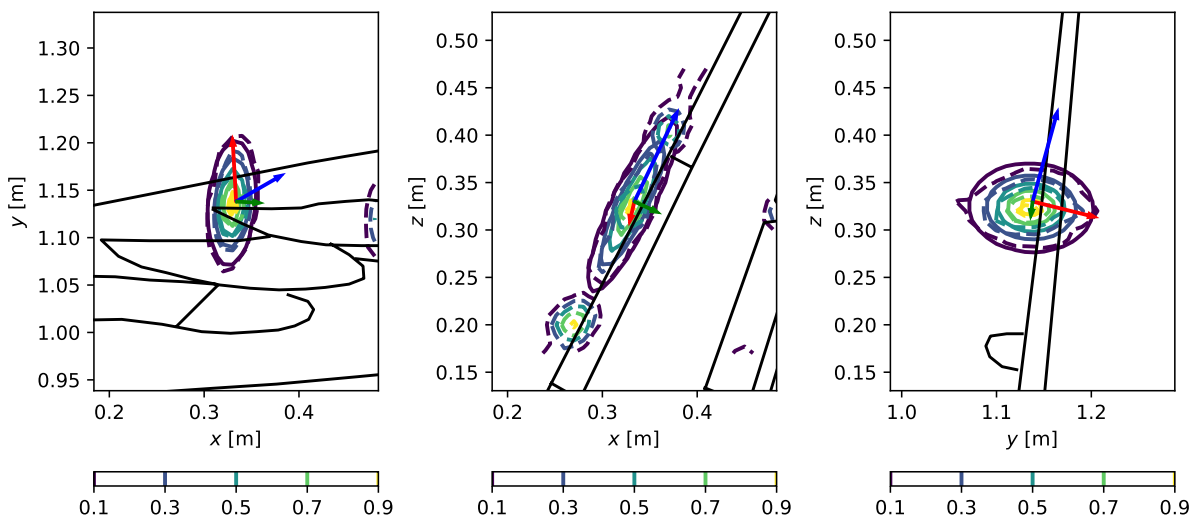


Figure 5.25: SIND 3D solution on an exemplary slat track source of the Do278 according to the description in Figure 5.6. The subfigures show projections of the 3D distribution. The main component of the fitted distribution are indicated with colored arrows.

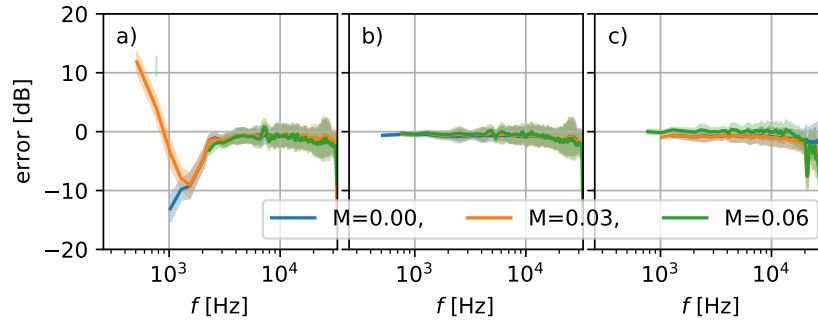


Figure 5.26: Figure shows the error $\varepsilon = \text{PSD}_{\text{CLEAN-SC}} - \text{PSD}_{\text{true}}$, see eq. 3.1.2, for each Mach number for (a) S_1 , (b) S_2 , and (c) S_3 . The shaded area depicts the standard deviation of the ground truth sound power over all microphones.

5.3 Method errors

As stated in the sections above, it is not possible to quantitatively estimate the methods' errors on the real-world datasets due to the lack of a ground truth. Thus, the generic dataset from Section 3.1 is used to validate the 2D methods to estimate how well the source spectra are reconstructed and how well the source positions are estimated.

Conventional beamforming and CLEAN-SC are performed on the individual source CSMs. This allows us to estimate how well the individual source powers obtained by CLEAN-SC correspond to the ground truth. To obtain CLEAN-SC reference spectra from the beamforming maps, all source-parts within a spatial radius $r = 0.1$ m of the true source positions are integrated. Additionally, these source-parts' positions are averaged to obtain a source position estimation of the CLEAN-SC process. Figure 5.26 shows the error $\varepsilon = \text{PSD}_{\text{CLEAN-SC}} - \text{PSD}_{\text{true}}$ for each individual source and all Mach numbers. The standard deviation depicts the variance over the microphone averaged ground-truth, see eq. 3.1.2. A cut-on frequency can be observed, below which CLEAN-SC cannot reconstruct the sound source correctly. For source S_I , below $f < 1.5$ kHz, the beamforming results over- or under-predict the PSD. The reason for this might be the low SNR at these frequency intervals. The Mach and frequency averaged position errors $|\varphi|$ and Mach and frequency averaged spectra errors $|\varepsilon|$ of the CLEAN-SC process are given in Table 5.2 for the individual source maps. Multiple averages are computed at once, including all individual errors $\langle |\varepsilon(S, M, f)| \rangle_{M, f}$ and not sequentially, i.e., $\langle \langle |\varepsilon(S, M, f)| \rangle_f \rangle_M$, because the errors contain a different quantity of frequency bins for different sources and Mach numbers. The position errors are given as angular errors with respect to the microphone array center instead of Δx_i since beamforming localization usually depends on the distance of the focal plane. For comparison, the focus point resolution is $\Delta x_i = 0.005$ m $\approx 0.44^\circ$ in the center of the focus grid. The total errors are additionally averaged over all three sources.

Then, a source-separation problem is created by superpositioning the three individual source CSMs for each Mach number and performing conventional beamforming in combination with CLEAN-SC, see Figure 5.27. The performance of SIND and SIHC is evaluated on their ability to detect the dominant sources correctly and by comparing the reconstructed spectra to the ground truth.

		SIND	SIHC	CLEAN-SC
S_1	$ \varphi [^\circ]$	0.48 ± 0.01	0.46 ± 0.02	0.61 ± 0.32
	$ \varepsilon [\text{dB}]$	1.62 ± 2.35	1.64 ± 2.71	1.59 ± 1.72
S_2	$ \varphi [^\circ]$	0.28 ± 0.06	0.28 ± 0.06	0.45 ± 0.92
	$ \varepsilon [\text{dB}]$	2.19 ± 3.00	2.19 ± 3.00	1.13 ± 1.16
S_3	$ \varphi [^\circ]$	0.28 ± 0.11	0.43 ± 0.20	0.28 ± 0.10
	$ \varepsilon [\text{dB}]$	2.73 ± 7.34	3.45 ± 7.88	2.47 ± 2.97
total	$ \varphi [^\circ]$	0.35 ± 0.09	0.39 ± 0.08	0.45 ± 1.13
	$ \varepsilon [\text{dB}]$	2.03 ± 3.66	2.14 ± 3.99	1.73 ± 2.16
f_r		65.6 %	66.8 %	96.8 %

Table 5.2: Absolute positional errors $|\varphi|$ in degree, absolute spectrum reconstruction errors $|\varepsilon|$ in decibel, and relative reconstructed spectrum frequency interval $0 \leq f_r \leq 1$ of SIND and SIHC performance and the integration of the individual CLEAN-SC source-maps.

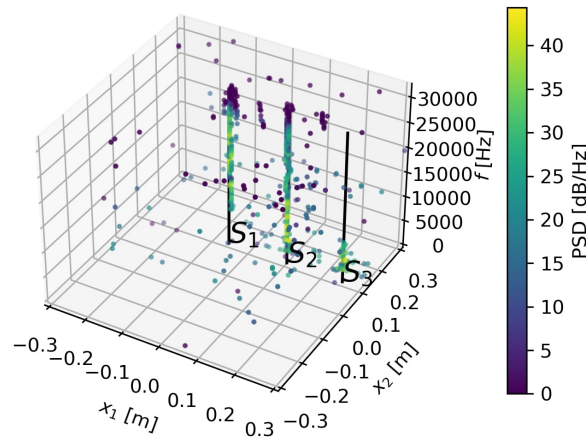


Figure 5.27: CLEAN-SC result of the superpositioned, denoised CSMs at $M_3 = 0.06$. The true positions are marked with black lines.

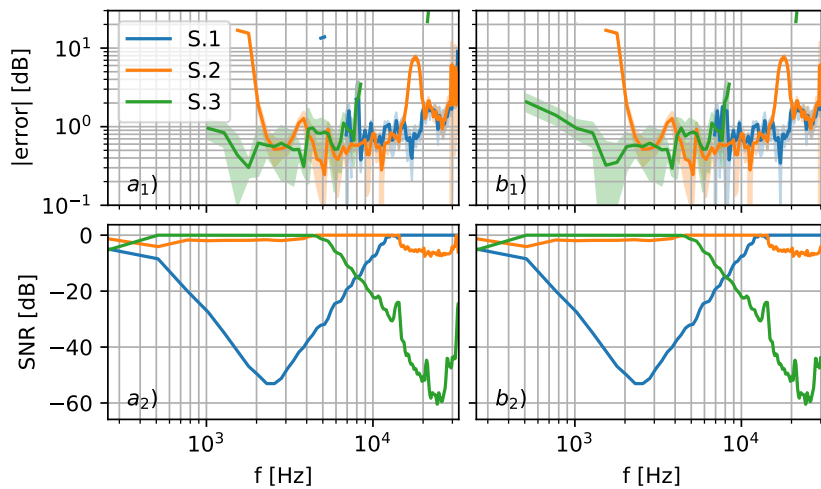


Figure 5.28: The top row (1) shows the Mach-averaged absolute error $|\varepsilon| = |\langle \text{PSD}_{\text{method}} \rangle_M - \text{PSD}_{\text{reference}}|$ for each source in (a) for SIND and (b) for SIHC. The shaded area depicts the corresponding standard deviation. The bottom row (2) shows the corresponding Signal To Noise ratios, see eq. 5.3.1.

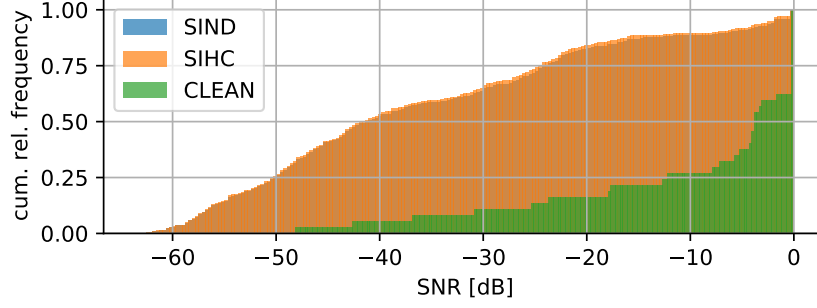


Figure 5.29: A cumulative histogram of the spectra SNR from all sources and Mach numbers, see eq. 5.3.1, that were not reconstructed $\text{SNR}(\text{PSD}(f) = -\infty \text{dB})$.

Both methods identify the three dominant monopole sources with the parameters given in Table 5.1. Figure 5.28, top row, shows the resulting absolute source power reconstruction error $|\varepsilon|$ for SIND and SIHC, and Table 5.2 lists the frequency and Mach averaged reconstruction errors and averaged position errors $|\varphi|$. For the localization, both methods perform similarly on all sources with an estimation error smaller than two focus points. For the reconstruction of the corresponding spectra, both methods perform identically on source S_{II} , similar on source S_I , and different in terms of reconstructing the low frequencies on source S_{III} , with SIHC performing slightly better.

For evaluating the PSD reconstruction error in detail, two points will be considered. First, we often prefer a correct spectrum for high SNRs over minor deviations at low SNRs in real-world applications. In this context, the SNR is the difference between the true single source's PSD and the summed PSD of all sources (also later referred to as the Signal to Signal Ratio) is

$$\text{SNR}_{S_i}(f, M) = \text{PSD}_{S_i} - \sum_{S_i} 10 \log_{10} \left(10^{\frac{\text{PSD}_{S_i}}{10}} \right). \quad (5.3.1)$$

Figure 5.28, bottom row, shows the corresponding SNRs, see eq. 5.3.1. The SNR can also be interpreted as the per frequency normalized true source spectra from eq. 3.1.2. We observe that at frequencies above $f \geq 1$ kHz the spectra reconstruction failed or resulted in significant errors when the SNR was low ($\text{SNR} \leq -15$ dB). Since at high frequencies, the beamforming map and resulting source-parts are well localized, see Figure 5.27, and SIND and SIHC performed somewhat similar, see Figure 5.28, these errors are mainly produced by the beamforming process itself. Also, the relative frequency interval $0 \leq f_r \leq 1$ of a valid spectrum reconstruction is essential but not captured in the average error $|\varepsilon|$. The relative interval is defined by the ratio of reconstructed frequency bins to the total number of frequency bins in a spectrum. A value of $f_r = 1$ indicates that a spectrum is reconstructed at each frequency bin, and a value of $f_r = 0$ indicates an empty spectrum with no information. The Mach averaged relative frequency interval is given in Table 5.2. Both methods perform similarly and reconstruct approximately $f_r = 2/3$, while the individual CLEAN-SC references contain nearly full spectra. However, the CLEAN-SC reference was obtained from the individual source-maps (no CSM superposition) and thus the SNR was $\text{SNR} = 0$ dB (for high frequencies that were above the wind tunnel noise-floor). Figure 5.29 shows the corresponding SNR of the parts of the source spectra that were not reconstructed in a cumulative histogram. Thus, for each given SNR on the x-axis, the cumulative relative frequency shows how much percent of the failed reconstructions are

below this SNR (e.g., 50 % of the failed reconstructions are below $\text{SNR} \leq -40$ dB and 75 % are below $\text{SNR} \leq -25$ dB). Both methods perform nearly identically on the generic dataset. The CLEAN-SC reference confirms that the failed reconstructions are mainly due to the CLEAN-SC process.

6 Expert Decision Support System

This chapter presents an Expert Decision Support System for the analysis of aeroacoustic data and is based on original work [46, 47, 48].

The main goal of this thesis is to provide a method of automatically identifying sources and analyzing their behavior. Currently, supervised machine learning often outperforms other methods given enough training data. However, wind tunnel experiments are expensive, the results are typically confidential, and the results cannot be easily classified, even by experts. An additional challenge is that supervised machine learning can only classify into known categories (or detect novelty). At the same time, wind tunnel experiments are typically performed to detect irregularities and unknown sources. The results strongly depend on the wind tunnel facility, the used microphones and the setup, the model, and the use case. An additional constraint is that the results of such a source identification must be reproducible and comprehensible to the expert. Thus, only unsupervised learning is considered, emphasizing comprehensibility and knowledge generation in the form of an Expert Decision Support System (EDSS).

Figure 6.1 compares the proposed EDSS process to a standard manual source analysis process for beamforming maps $\text{PSD}(\mathbf{x}, f_i, M_j, \alpha_a, \text{Re}_e)$, which typically includes spatial variables \mathbf{x} , multiple frequencies or frequency intervals f_i , angles of attack α_a , Mach numbers M_j , and Reynolds numbers Re_e . In the manual process, multiple ROI $R_r(\mathbf{x})$ are defined and spatially integrated to derive acoustic spectra $\text{PSD}(R_r, f_i, M_j, \alpha_a, \text{Re}_e)$. This first step is already challenging since the ROIs must only contain the individual sources to obtain individual source spectra, which can only be verified using the resulting spectra. This often requires several iterations, as described in the following. After definition, the ROI spectra are analyzed, often requiring expert knowledge and intuition. Based on the analysis, the ROIs are then redefined (e.g., if two separate sources are detected within a ROI). Based on the spectra at different Mach numbers, expert knowledge, intuition, and meta-information (e.g., the source is located at a trailing edge and, thus, must be trailing edge noise) aeroacoustic properties are derived, and the source type is then identified or vice versa. The main challenge for this process is the high dimensionality of the properties $P_k(R_r, f_i, M_j, \alpha_a, \text{Re}_e)$ and the requirement for an iterative approach.

In comparison, the EDSS aims at automating most of these tasks. First, the ROI definition $R(\mathbf{x})$ and spectra generation was shown to have the capacity to be automated [47], see Chapter 5. The EDSS then defines a source S_{rae} for each ROI R_r , at each angle of attack α_a , and at each Reynolds number Re_e . This results in multiple sources $S_{rae}(\text{PSD}(f_i, M_j))$, for which aeroacoustic features $F_k(S_{rae})$ are then calculated. Finally, the sources are clustered based on the k -dimensional feature space with the process $\hat{c}(F_k)$, which results in a cluster prediction for each source $C_c(S_{rae})$. This provides c -dimensional prediction information (each source is assigned to a cluster). Also, additional information about the similarity of source groups based on their cluster-averaged features is provided. The source types can then be identified manually based on the expert's knowledge and the low-dimensional information provided by the EDSS.

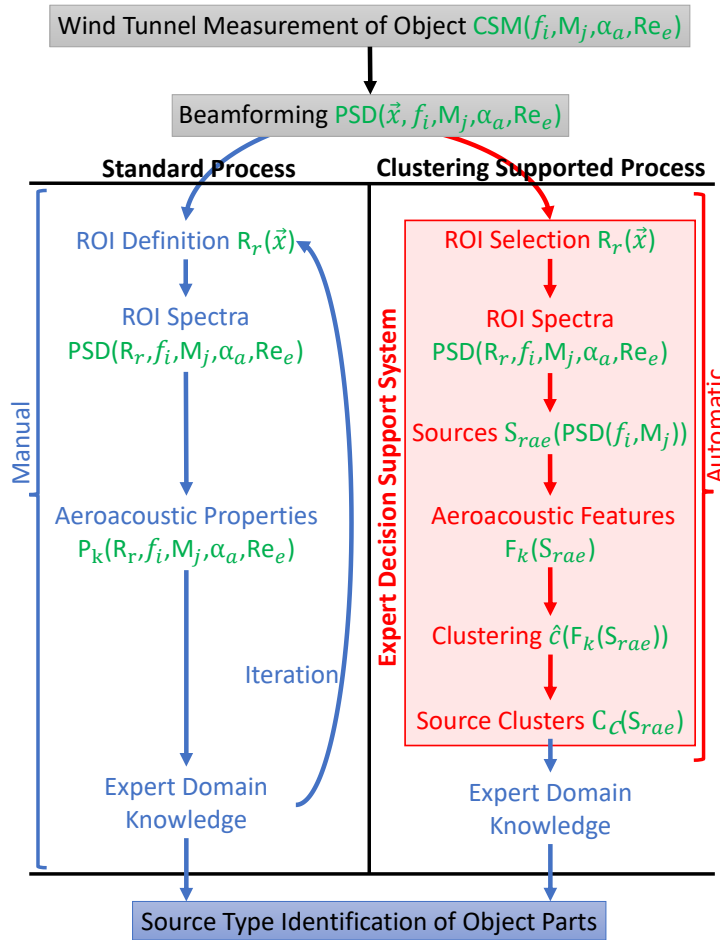


Figure 6.1: Comparison of the evaluation process of wind tunnel beamforming measurements. Left: a standard process using manual analysis. Right: the proposed Expert Decision Support System. Manual processing steps are displayed in blue, while automatic steps are displayed in red. The resulting variables of each step are displayed in green. The indices indicate the dimensionality of these variables.

6.1 Quasi-stationary, self-similar sources

For the proposal of an EDSS, we need to clarify what a source is and for which variations of parameters we consider that it is still the same source. The proposed EDSS is based on the assumption of self-similarity, see Section 2.1.2. Thus, only small, subsonic Mach number variations are considered. All variations except for the Mach number, such as the angle of attack α , Reynolds number, or changes in geometry may alter the dominant source mechanism abruptly (e.g., slat tones and flow separation in airframe noise may appear). This thesis treats these variations as potentially different source mechanisms and, thus, different sources.

Since we are interested in clustering the sources according to their underlying physical mechanisms rather than clustering them by their dominance, we need to analyze the scaling behavior over Mach number and the similarity laws [66] rather than absolute levels at specific Mach numbers. Therefore, this thesis defines the properties of a source as follows. First, a source is connected to a spatial region $R(\mathbf{x})$. Second, when a source is observed at different Mach numbers, it is still the same source. Third, a source may be observed for small variations of the Reynolds number due to the change in the Mach

	(a)	(b)	(c)	(d)	(e)	(f)	(g)
m	0.90	0.00	0.75	0.00	1.09	0.00	0.71
n	4.44	5.47	3.43	4.23	4.43	4.09	3.43
α [°]	3	5	9	9	3	5	9
$\langle \text{Re} \rangle_M [1 \times 10^6]$	1.4	1.4	1.4	1.4	1.4	10.6	1.4
	(h)	(i)	(j)	(k)	(l)	(m)	(n)
m	0.00	0.94	0.00	1.00	0.00	0.66	0.00
n	3.87	3.68	5.47	3.26	6.07	3.59	5.26
α [°]	10	3	5	10	3	9	1
$\langle \text{Re} \rangle_M [1 \times 10^6]$	2.5	10.6	1.4	10.6	1.4	1.8	1.4

Table 6.1: Generalized frequency exponents m , Mach scaling exponents n , angles of attack α , and Mach averaged Reynolds numbers $\langle \text{Re} \rangle_M$ for the displayed sources in Fig. 6.2.

number. A significant variation of the Reynolds number due to changes in temperature or pressure results in a different source. Fourth, any change in the angle of attack results in a different source. Based on this definition, a sound source's PSD, obtained from the spatially integrated ROI, possesses the free variables PSD (f, M) at a fixed $\langle \text{Re} \rangle_M$ and α . For example, a ROI $R(\mathbf{x})$ that was identified by SIND within the Do728 beamforming maps is treated as a unique source for each angle of attack and Reynolds number (which results in $8\alpha \times 5\langle \text{Re} \rangle_M = 40$ individual sources for any identified spatial ROI), each represented by six spectra at different Mach numbers $M = [0.125, \dots, 0.250]$. We can derive the acoustic properties not only from the individual spectra but from the changes over Mach number or as an average property of the spectra since multiple spectra of different Mach numbers are assigned to one source. This has the advantage that the Mach-normalized features of different datasets are comparable despite their measurement at different Mach numbers. Additionally, the averaging reduces the uncertainty of the feature estimation.

6.2 Manual source identification

First, this thesis identifies source types manually. It presents labels for the sources in the Do728 and A320 datasets based on their spectra and self-similarity so that they can be visualized and analyzed and the EDSS results can be quantified. The labels for the manually identified source types are mainly chosen based on the sources' spatial location. The source spectra are also compared to each other to identify sub and super-categories. To make this process transparent to the reader, Figure 6.2 presents exemplary Do728 spectra for the most common categories. The sources in the left column are displayed over the modified Strouhal number, and sources in the right column are displayed over the Helmholtz number. The manual source type identification and label choices may be ambiguous, contain errors, and misinterpretations. Also, the source groups and corresponding labels cannot be held as ground truth since they have not been obtained by independent researchers.

- The slat cove features Strouhal number scaling peaks with overtones that decay in level and prominence with increasing frequency, see Figure 6.2 a). They are mainly located at or between the slat tracks, see Figure 6.12 source locations 2, 4, 8, 9, 17, 20, 21, and 28.

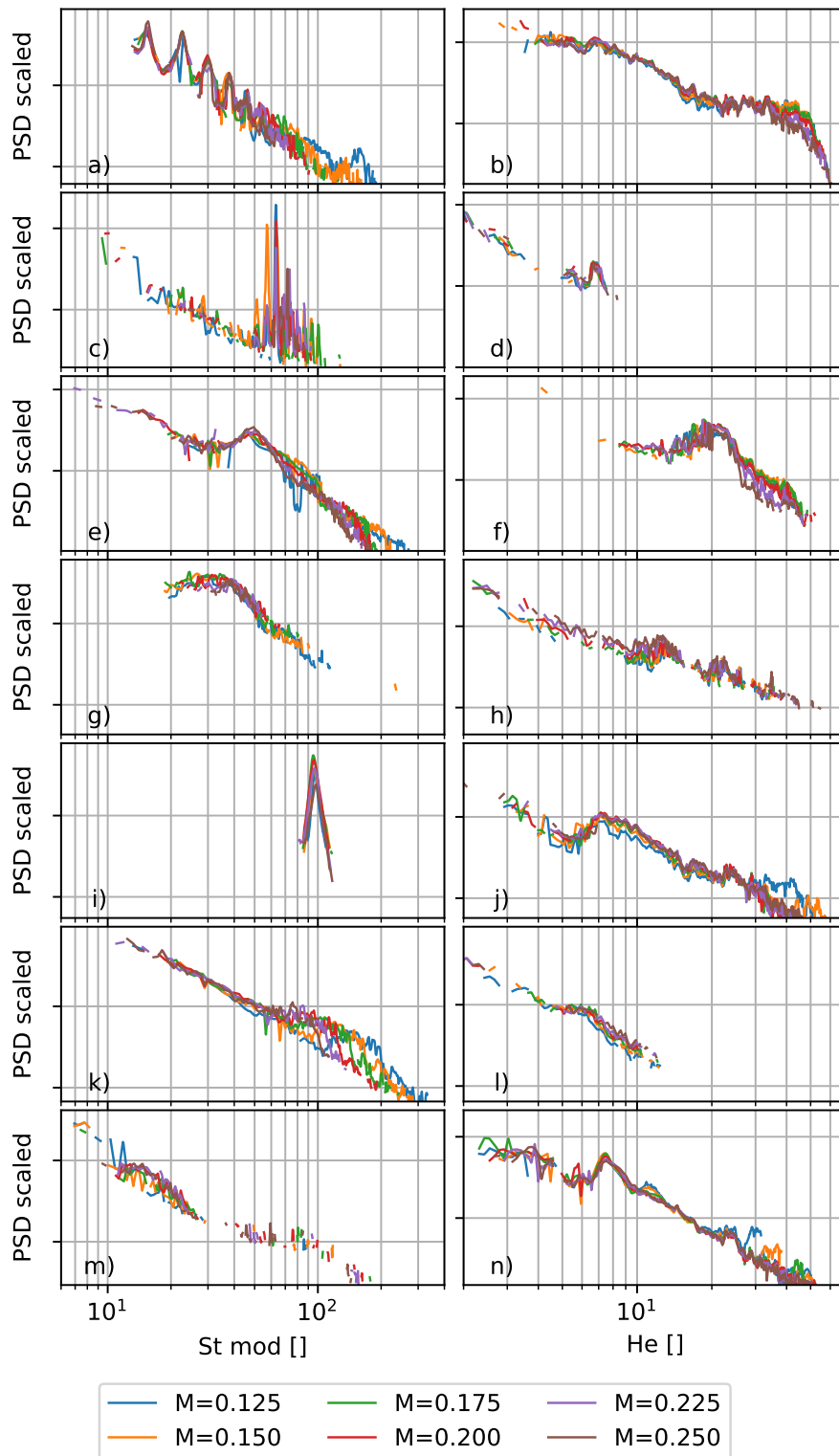


Figure 6.2: Do728, normalized spectra of the typical source types: (a) slat, (b) slat track, (c) slat tone, (d) flap tone, (e) trailing flap side edge, (f) leading flap side edge, (g) strake at low Reynolds number and high angle of attack, (h) wind tunnel, (i) strake tone at high Reynolds number and low angle of attack, (j) outer nacelle, (k) slat edge, (l) flap track, (m) wing tip, and (n) slat resonance. The horizontal grid lines depict $\Delta 20 \text{ dB}$. The frequency modification exponents m , the Mach scaling exponents n , and the corresponding angles of attack α and Reynolds numbers are given in Table 6.1.

- The slat tracks scale over Helmholtz number, see Figure 6.2 *b*). At high frequencies they often exhibit a Helmholtz scaling hump that is Mach number dependent. In Figure 6.12 they are at the source locations 2, 3, 4, 7, 8, 9, 11, and 16.
- The slat tones feature extremely dominant Strouhal number scaling small-band tones, see Figure 6.2 *c*). They are mainly located at the slat positions, see Figure 6.12 locations 4, 7, 9, 11, 16, 21, 22, 25, and 28.
- The flap (track) tones feature a small Helmholtz scaling tone and are a sub-category of the flap track, see Figure 6.2 *d*). In Figure 6.12 they are at the locations 23, 29, and 32.
- The trailing flap side edges (TFSE), Figure 6.12 at location 12, feature a prominent Strouhal scaling peak, see Figure 6.2 *e*).
- The leading flap side edges (LFSE), Figure 6.12 at location 6, feature a smaller Helmholtz scaling peak, see Figure 6.2 *f*). At increasing Reynolds numbers, a second Helmholtz number scaling peak emerges.
- The strakes feature a Strouhal number scaling hump, see Figure 6.2 *g*). It increases in intensity with increasing angle of attack and disappears with increasing Reynolds number. In Figure 6.12 they are at the locations 18, and 26.
- The wind tunnel noise, Figure 6.12 at location 31, scales over Helmholtz number, see Figure 6.2 *h*). It appears next to the wing and is considered as a spurious noise source in this measurement [4].
- The strake tone, Figure 6.12 at location 18, is a dominant Strouhal scaling tone, see Figure 6.2 *i*). It appears only at high Reynolds numbers and low angles of attack and decreases in intensity with increasing angle of attack. It is a sub-category of the strake.
- The outer nacelle area, Figure 6.12 source location 13, features a broadband hump that scales over Helmholtz number, see Figure 6.2 *j*).
- The slat edge is located close to the wing tip, Figure 6.12 position 10, and its noise scales over Strouhal number, see Figure 6.2 *k*). The spectrum level decays over frequency and features an additional, low-level Helmholtz scaling hump at high frequencies. It is a sub-category of the slat track.
- The flap tracks feature a low-level Helmholtz number scaling hump, see Figure 6.2 *l*). They are located in Figure 6.12 at locations 23, 29, and 32.
- The wing tip, Figure 6.12 source location 27, features a Strouhal number scaling hump, see Figure 6.2 *l*), that increases in intensity with increasing angle of attack. The spectra are often contaminated with wind tunnel noise.
- The Krüger slat resonances exhibits strong, Helmholtz number scaling peaks and are a sub-category of the slat track, see Figure 6.2 *n*). In Figure 6.12 they are at the slat tracks 1, and 5.

The fuselage (Figure 6.12 location 19), nacelle track (appearing only at very high Reynolds numbers at location 30 in Figure 6.12, scaling over Helmholtz number with a very high Mach power exponent $n \approx 7.02$), inner slat gap (Helmholtz scaling hump, similar to the LFSE, location 15 in Figure 6.12), and flap gap (location 24 in Figure 6.12) are identified and named based on their spatial appearance.

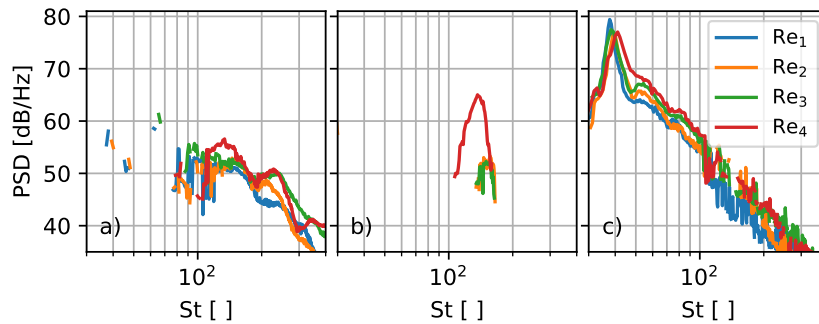


Figure 6.3: A320. The figure shows the Reynolds number effect on the source types (a) leading flap side edge at $\alpha = 7^\circ$, $M = 0.175$, (b) high Strouhal number scaling tone at $\alpha = 9^\circ$, $M = 0.200$, located on the slat and flap, and (c) trailing flap side edge at $\alpha = 7^\circ$, $M = 0.200$.

Noise occurring at the flap gap was caused by loose tape on the model during the measurement. Additionally, the category slat / slat track is introduced to account for various spectra that are located on the slat or slat tracks but are ambiguous, e.g., the slat / slat track shown in Figure 6.10, containing some Strouhal number scaling low-frequency peaks, and some Helmholtz number scaling high frequencies.

The manual source type identification in the A320 dataset is more challenging than for the Do728. The smaller microphone array results in less reliable spectra, especially at low frequencies, and due to the small variation in Mach number, the correct scaling behavior and scaling exponent are difficult to identify. Additionally, the typical spectra do not consistently correlate with the spatial appearance of the sources, e.g., the spectra are different for different flap tracks. Finally, the sources are strongly affected by the large range of Reynolds numbers, which often result in sources transitioning from one mechanism to another, see Figure 6.3. Thus, there are multiple sources that we assign the same label but that feature different spectra (e.g., the fuselage, the slat tracks, and leading flap side edge, see Figure 6.2), and vice versa. However, many of the sources are similar to the one found in the Do728 dataset (e.g., LFSE, TFSE, strake, strake tone, slat, slat resonance, slat tone). In addition to the Do728 source types, there exist multiple A320 sources on the slat and flap that feature a high Strouhal number scaling tone (high St tone) that increases in intensity with increasing Reynolds number like the strake tone, see Figure 6.3 (b).

6.3 Source identification results

This section presents exemplary source identification results based on 3D conventional beamforming with steering vector IV, SIND 3D, see Section 5.2.4, for the Do728, A320, and Embraer models. The source types were identified manually based on their spatial location and spectral features, and the results from Section 6.2. They will give the reader an impression of which sources dominate the airframe sound radiation and how they behave regarding scaling and self-similarity, see Section 2.1.2.

6.3.1 Do728

Figure 6.4 shows the 3D SIND result for the Do728 at $\alpha = 3^\circ$. Figure 6.4 (a) and (b) shows the spatial source distribution. All main sources are located on the wing. The sources were labeled based on Section 6.2 and the clustering results that will be presented in Section 6.6. Figure 6.4 (c) shows for $M = 0.2$ the contributions of the source types to the total sound emission, integrated from all focus points. At low frequencies $St \leq 30$, tonal components from the slat cove dominate the sound emission. At medium frequencies $30 \leq St \leq 250$ the slat tracks dominate with broadband noise. Above $St \geq 250$ the inboard Krüger slats dominate the sound emission. However, the spectra are noisy and degenerated from the beamforming and CLEAN-SC process. Figure 6.4 (d) shows the resulting similarity spectra, referenced to $M_0 = 0.2$, with 1σ standard deviation with the scaling parameters given in Table 6.2. If the standard deviation is low, self-similarity holds. We observe that this is not the case for the Krüger slat and the high-frequency content of the slat cove. For the Helmholtz-scaling Krüger slat, we observe a true Mach-dependency $\hat{f} \geq 10$. Below $\hat{f} \leq 10$ the Krüger slat scales at $M^{6.1}$, which indicates a dipole, see Section 2.1.2. Note again that while the absolute level of the sources may be over- or underestimated due to the monopole assumption for a dipole source, see Section 2.1.6, the relative increase due to the increased Mach number does not change. Thus, the scaling exponent holds, even for dipole sources, but may incorporate other effects such as convective amplification or a change in directivity over Mach number (e.g., jet noise). For the Strouhal-scaling slat cove the large standard deviation results from the fact, that the high frequency source spectrum is driven by a Helmholtz number scaling mechanism, see Figure 6.10. Thus, the 2D beamforming and SIND method was not able to separate the overlapping two source mechanisms (slat cove and slat track) into separate spectra. The slat cove scales at $M^{4.1}$ over the Strouhal number, which indicates a monopole, see Section 2.1.2. The slat tracks which contain two Helmholtz-scaling broadband humps. Another prominent source is the Helmholtz-scaling Leading Flap Side Edge (LFSE). Here, we observe a monopole behavior. The Trailing Flap Side Edge scales over the Strouhal number with $m > 1$, which indicates a locally accelerated flow. At this angle of attack, the strakes and the wing tip do not contribute towards the sound emission, except for the tip of the outer strake, which produces a major and a minor Strouhal-scaling tone. It scales perfectly over the Strouhal number, as it is located in the undisturbed free-flow.

Figure 6.5 shows the corresponding results at $\alpha = 7^\circ$. Some source types on the slat have changed. Slat tones are now present, and the outer slat edge exhibits a strong source. Additional strake sources and the wing tip appeared. In return, the slat cove sources disappeared. The dominating Strouhal-scaling slat tones were presented in Figure 6.9 in detail and show that the strength of the individual tones vary with Mach number, so self-similarity only holds partially.

6.3.2 A320

Figure 6.6 and Figure 6.7 show the corresponding A320 results, with the self-similarity parameters given in Table 6.3. The beamforming result and ROI are also calculated in 3D, but due to a lack of a 3D model only the (x, y) -projection is displayed. Due to the low spatial resolution and small variety in measure Mach numbers, the parameters of some source types show strong deviations with respect to the angle of attack and the Do728. Also, compared to the Do728, the same source types show similar

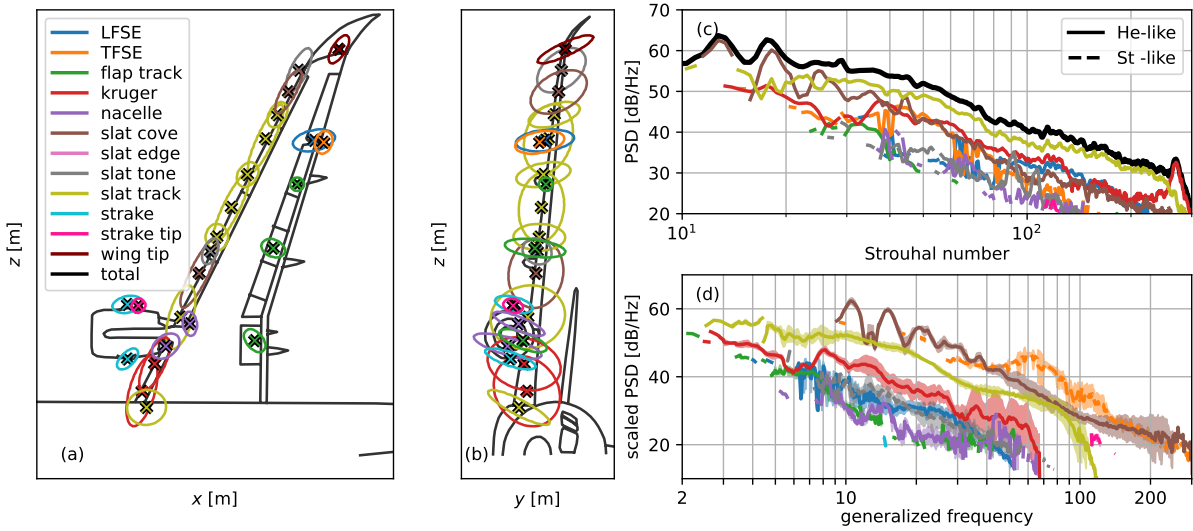


Figure 6.4: Do728 sources at $Re = 1.4 \times 10^6$, $\alpha = 3^\circ$. The Figure shows source type based 3D-ROI in (a) and (b). Identical colors depict the same source type, for which the integrated spectra are shown in (c) at $M = 0.2$. The total integrated SPL from all focus points is depicted in black. (d) shows the averaged spectra with 1σ standard deviation of all Mach numbers. The SPL is scaled according to eq. 2.1.20 with $M_0 = 0.2$, and displayed over the generalized frequency, see eq. 2.1.19. Helmholtz-like scaling spectra are depicted with solid lines, Strouhal-like scaling spectra are depicted with dotted lines. The corresponding scaling exponents are given in Table 6.2.

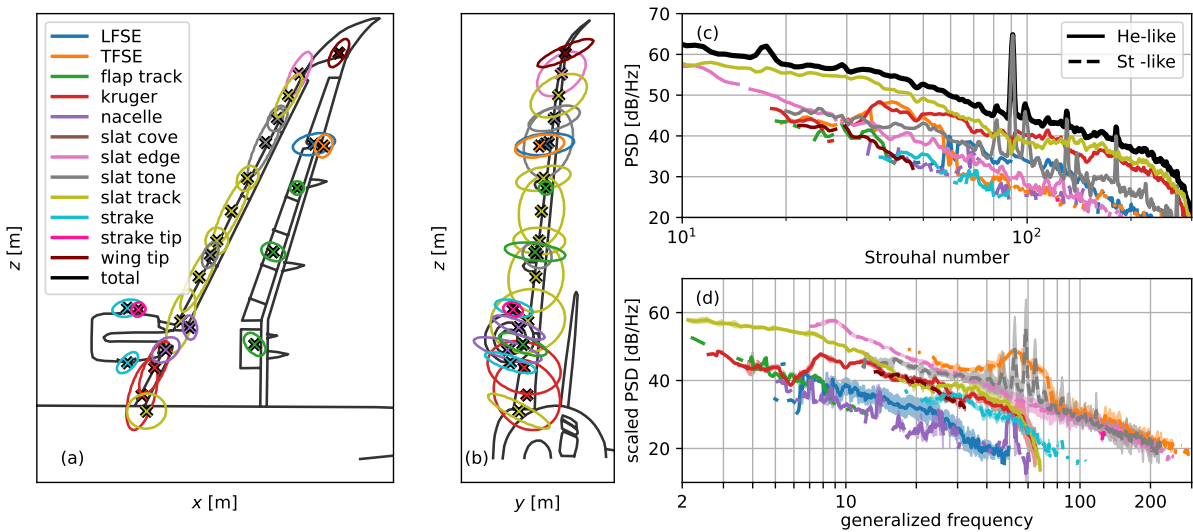


Figure 6.5: Do728 sources at $Re = 1.4 \times 10^6$, $\alpha = 7^\circ$, according to the description in Figure 6.4. The corresponding scaling-exponents are given in Table 6.2.

	LFSE	TFSE	flap track	Kröger	nacelle	slat cove	slat edge	slat tone	slat track	strake	strake tip	wing tip
$m(3^\circ)$	0.00	1.23	0.04	0.05	0.05	0.89	-	0.21	0.34	-	1.00	-
$m(7^\circ)$	0.00	1.17	0.05	0.03	0.00	-	0.88	0.73	0.05	0.73	1.00	0.74
$n(3^\circ)$	4.2	3.1	5.7	6.3	4.0	4.1	-	4.2	4.3	-	4.2	-
$n(7^\circ)$	2.9	3.5	6.1	4.4	5.1	-	3.6	4.1	5.4	2.4	5.7	4.6

Table 6.2: Do728 modification exponent m for the generalized frequency \hat{f} , and Mach power-scaling exponent n for the source types displayed in Figure 6.4 and Figure 6.5.

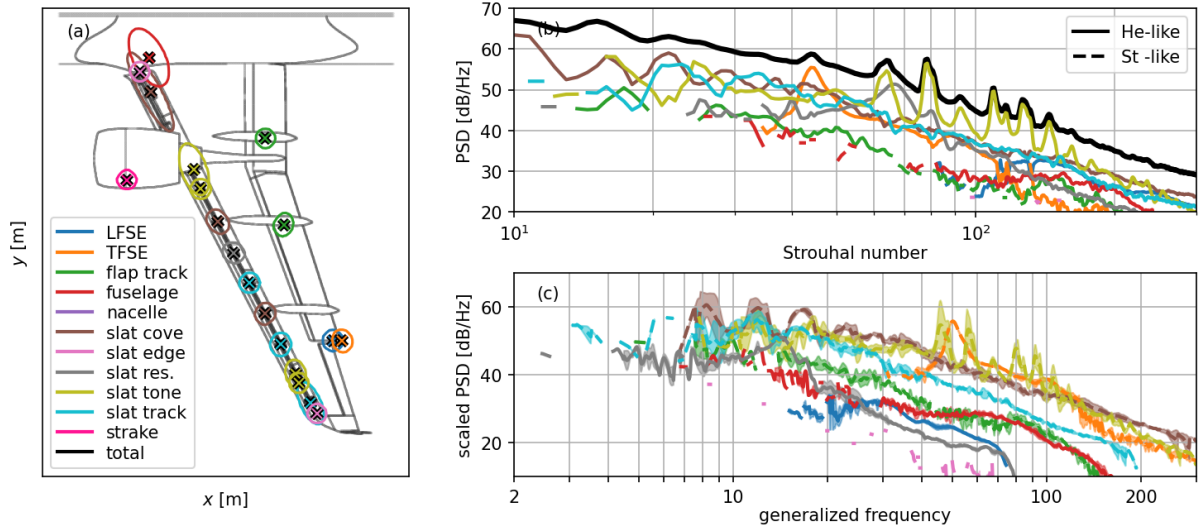


Figure 6.6: A320 sources at $Re = 1.4 \times 10^6$, $\alpha = 3^\circ$, according to the description in Figure 6.6. The corresponding scaling-exponents are given in Table 6.3.

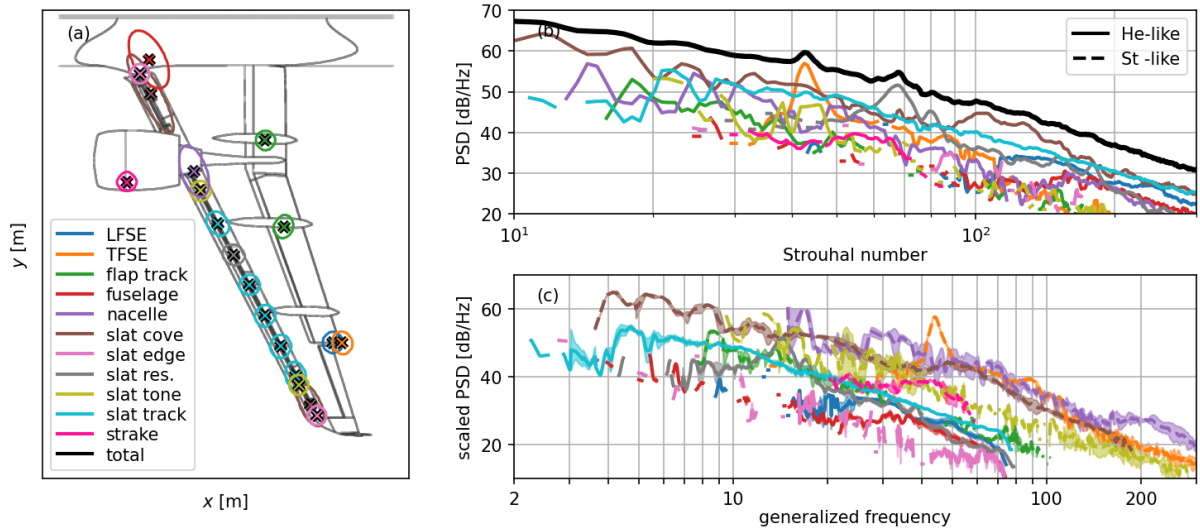


Figure 6.7: A320 sources at $Re = 1.4 \times 10^6$, $\alpha = 7^\circ$, according to the description in Figure 6.7. The corresponding scaling-exponents are given in Table 6.3.

generalized frequency modification exponents, but overall higher Mach scaling exponents. Prominent examples are both the LFSE and TFSE. For both wings the power scaling exponents decreases with increasing angle of attack. While the reason for these elevated scaling exponents is unknown, they

	LFSE	TFSE	flap track	fuse-lage	na-celle	slat cove	slat edge	slat res.	slat tone	slat track	strake
$m(3^\circ)$	0.00	1.08	0.63	-	0.53	0.84	0.00	0.03	0.81	0.55	-
$m(7^\circ)$	0.00	1.02	0.55	0.00	1.09	0.54	0.00	0.03	0.80	0.02	0.78
$n(3^\circ)$	5.0	4.3	3.3	5.8	0.9	6.4	3.8	5.4	3.2	4.6	-
$n(7^\circ)$	4.6	4.1	5.8	6.3	4.0	6.3	0.0	4.7	6.0	5.3	3.2

Table 6.3: Do728 modification exponent m for the generalized frequency \hat{f} , and Mach power-scaling exponent n for the source types displayed in Figure 6.6 and Figure 6.7.

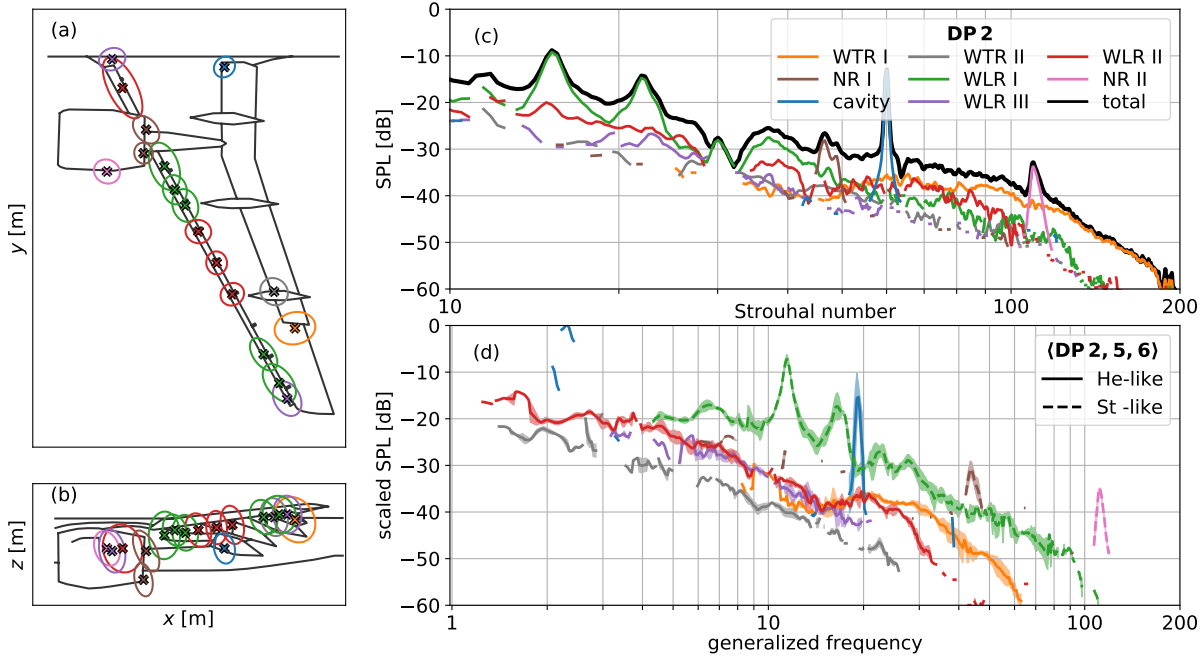


Figure 6.8: The Figure shows source type based 3D-ROI in (a) and (b). Identical colors depict the same source type, for which the integrated spectra of the exemplary DP 2 are shown in (c). The total integrated SPL from all focus-points is depicted in black. (d) shows the averaged spectra with 1σ standard deviation of DP 2, 5 and 6. The SPL is scaled according to eq. 2.1.20 with $M_0 = 0.220$, and displayed over the generalized frequency, see eq. 2.1.19. Helmholtz-like scaling spectra are depicted with solid lines, Strouhal-like scaling spectra are depicted with dotted lines. The corresponding scaling-exponents are given in Table 6.4.

	WTR I	WTR II	NR I	NR II	cavity	WLR I	WLR II	WLR III
m	0.26	0.03	0.96	1.01	0.25	0.81	0.22	0.28
n	2.26	6.14	6.40	-1.63	-10.52	3.89	4.86	3.64

Table 6.4: Modification exponent m for the generalized frequency \hat{f} , and Mach power-scaling exponent n for the source types displayed in Figure 6.8.

are subject to some uncertainty due to the small Mach number range obtained in the experiment and the degraded spectra due to the array aperture.

6.3.3 Embraer model

Figure 6.8 shows the corresponding Embraer results. The identified locations coincide with the main sources of the Do728 and A320. We observe that the WLR I sources dominate the SPL at low Strouhal number $10 \leq St \leq 30$, the NR I and cavity show a prominent peak around $St \approx 45$, the NR II shows a prominent peak around $St \approx 110$, and above $St \geq 120$ the SPL is dominated by broad-band noise from the WTR I. Interestingly, for all three models, the inner wing trailing regions are silent or cannot be reconstructed by CLEAN-SC due to the limited dynamic range. A major difference is the WTR I source, where there are two distinct (leading and trailing edge) sources on the Do728 and A320 [47, 48, 17] but only one (presumably leading, based on the aeroacoustic behavior) source on the Embraer. The positions of the sources remain approximately the same for the variation

of the Reynolds number, Mach number, and the slotted and closed test section.

6.4 Feature engineering

We require a set of features that describe the aeroacoustic properties of a source for clustering. For optimal clustering results and interpretability of the results, we require a feature-set that meets the following conditions:

- All features together must unambiguously describe a source or its mechanism.
- A feature must describe a basic property of a source and must provide additional information.
- The calculation of a feature must be automatable and robust.
- A feature must be represented by a single numerical value.
- A feature must correspond to a physical property.

In real-world applications, it is typically not possible to fulfill these requirements completely. Additionally, it can only be analyzed how well the introduced features meet these requirements in the context of the observed sources. In the following, this thesis identifies aeroacoustic properties and breaks them down to numerical features in the subsequent sections. A complete list of the features is given in Table 6.5.

Broadband self-similarity

An essential property of any aeroacoustic source is the self-similarity or scaling behavior over increasing Mach number, see Section 2.1.2, indicated by the Strouhal and Helmholtz number, see eq. 2.1.16 and eq. 2.1.17. Suppose a source is self-similar over a frequency type (here, the absolute frequency, the Helmholtz number, and the Strouhal number are referred to as frequency types). In that case, there is a linear dependency between the PSD levels over frequency at different Mach numbers. Thus, the self-similarity is based on the Pearson correlation coefficients $\rho_{jj'}$ between all spectra at different Mach numbers M_j and $M_{j'}$.

$$\rho_{jj'} = \frac{\sum_i^I [(PSD(M_j, f_i)) - \langle PSD(M_j, f_i) \rangle_i] \times [(PSD(M_{j'}, f_i)) - \langle PSD(M_{j'}, f_i) \rangle_i]}{[\sigma_i(PSD(M_j, f_i))\sigma_i(PSD(M_{j'}, f_i))]} \quad (6.4.1)$$

Note that for the calculation of eq. 6.4.1 using the Strouhal or Helmholtz number, the spectra have to be interpolated on the same Strouhal or Helmholtz number vectors for different Mach numbers. For the results presented in this thesis, a linear interpolation on a logarithmic Strouhal and Helmholtz number vector with 12 bins per octave is used. This way, each frequency bin corresponds to a relative interval. Since the correlation matrix is symmetric and the diagonal entries are unity, the

property	feature	var.	eq.	log	range
self-similarity	scal. over St number	scal(St)	6.4.4	no	[0, 1]
	scal. over He number	scal(He)	6.4.4	no	[0, 1]
	freq. norm. exp.	m^*	6.4.7	no	[0, ∞ [
power-scaling	M scal(St)	n_{St}	2.1.20	no	[0, ∞ [
	M scal(He)	n_{He}	2.1.20	no	[0, ∞ [
tonality	number of tones	\hat{P}_n	6.4.10	yes	[0, ∞ [
	tone St shape	k_{St}	6.4.11	yes	[0, ∞ [
	tone St scale	θ_{St}	6.4.11	yes	[0, ∞ [
	tone St loc	l_{St}	6.4.11	yes	[0, ∞ [
	tone width shape	k_w	6.4.11	yes	[0, ∞ [
	tone width scale	θ_w	6.4.11	yes	[0, ∞ [
	tone width loc	l_w	6.4.11	yes	[0, ∞ [
	tone prom shape	k_p	6.4.11	yes	[0, ∞ [
	tone prom scale	θ_p	6.4.11	yes	[0, ∞ [
	tone prom loc	l_p	6.4.11	no	[0, ∞ [
	scal. over St number	scal _p (St)	6.4.14	no	[0, 1]
	scal. over He number	scal _p (He)	6.4.14	no	[0, 1]
	tone intensity	prop _p	6.4.15	no	[0, 1]
source loc.	source movement	Δl	6.4.16	no	[0, ∞ [
spatial dist.	source compactness	A	6.4.17	no	[0, ∞ [
	source shape	R_σ	6.4.18	yes	[0, ∞ [
spectrum shape	regression slope	\hat{s}	6.4.19	yes	[0, ∞ [
	regression r^2 -value	r^2	6.4.21	no	[0, 1]
	avg. St number	\bar{St}	6.4.23	yes	[0, ∞ [
	std. St number	St_σ	6.4.24	yes	[0, ∞ [
	PSD _{max} St number	St_{Lmax}	6.4.25	yes	[0, ∞ [

Table 6.5: Table of all aeroacoustic properties, their corresponding features, their variables, equations, if they are used logarithmically with $\log(|v| + 1)$, and their (log) value range.

Mach average $\overline{\text{corr}}$ and standard deviation corr_σ of the correlation coefficients is determined using the upper triangular matrix $j > j'$ with $J = \#_j(M_j)$.

$$\overline{\text{corr}} = \frac{2}{J(J-2)} \sum_{j>j'} \rho_{jj'} \quad (6.4.2)$$

$$\text{corr}_\sigma = \sqrt{\frac{2}{J(J-2)} \sum_{j>j'} (\rho_{jj'} - \overline{\text{corr}})^2} \quad (6.4.3)$$

Most aeroacoustic spectra decay in SPL over frequency due to the corresponding turbulent energy decay. If this decay is stronger than local structures or peaks in the spectra, this can result in elevated correlations for frequency types over which the spectra are not self-similar. However, the correlation matrix $\rho_{jj'}$ often exhibits a substantial variance. Thus, a mean correlation $\overline{\text{corr}}$ is not an optimal definition for the self-similarity. It can be improved by considering its standard deviation corr_σ and the mean p-value \bar{p} . The p-values are averaged as shown in eq. 6.4.2 and represent the reliability of the correlation estimation. Due to the beamforming process in combination with CLEAN-SC, the discrete spectra often contain missing values. If we drop the corresponding frequencies f where $\text{PSD}(M, f) = -\infty \text{dB Hz}^{-1}$ before the calculation, the standard deviation, and the p-value will

increase drastically due to the decreasing sample size when the spectra are not self-similar. Using these properties, this thesis introduces the final broadband self-similarity (scal) with

$$\text{scal} = (\overline{\text{corr}} - \text{corr}_\sigma)(1 - \bar{p}), \quad (6.4.4)$$

which can be calculated over all frequency types separately. This definition strongly penalizes a high p-value and a large correlation variance.

Frequency normalization exponent

As stated in Section 2.1.2, a source scales over the Strouhal or the Helmholtz number. However, we observe in the presented data that spectra that are supposed to scale over the Strouhal number are often not perfectly aligned as depicted in Figure 6.1 (a). In this rare case of multiple cryogenic measurement conditions, the experiments allow us to observe spectra at constant absolute Reynolds number over increasing Mach number (at decreasing temperatures and increasing pressure). Using spectra at different Mach numbers from different Reynolds configurations so that the absolute Reynolds number is kept constant, most sources show a true Strouhal scaling, but not all, see Figure 6.8. Thus, increasing the Reynolds number over the Mach number at constant pressure and temperature may cause some sources to decrease or increase the Strouhal number's dependency on the Mach number. Additionally, some sources show an altered Mach number dependency even at constant Reynolds number over increasing Mach number.

To overcome this issue, this thesis proposes a modified normalized frequency \hat{f} that compensates for this altered Mach dependency by introducing the generalized frequency normalization exponent m in eq. 2.1.19. This normalized frequency is a generalization of the Helmholtz number (for $m = 0$) and the Strouhal number (for $m = 1$). For convenience, we will speak of a modified Strouhal number if $m \geq 0.5$. To obtain the generalized frequency normalization exponent, we optimize the collapse of the spectra by maximizing its broadband self-similarity (see Section 6.4). Figure 6.9 shows the comparison of the (a) normal Strouhal number and (b) the modified Strouhal number with $m = 0.72$. Figure 6.9 (c) shows the mean spectra correlation $\overline{\text{corr}}$ (black line), and its standard deviation corr_σ (gray area) over the modification exponent m . The blue line is the mean p-value \bar{p} , indicating the reliability of the correlation estimation. The optimal value m^* (shown with the red x) is achieved at the global maximum of the self-similarity, see equation 6.4.4.

$$m^* = \underset{m \in [0, \infty[}{\text{argmax}}(\text{scal}(m)) \quad (6.4.5)$$

In the example of these slat tones, the increase in Reynolds number results in a weaker Mach dependency of the normalized frequency than a regular Strouhal number.

The following acoustic properties are derived from spectra at different Mach numbers, which can be displayed over the Strouhal number, the Helmholtz number, or the introduced modified normalized frequency. Since aeroacoustic experts are used to analyze spectra displayed over Strouhal and Helmholtz numbers, all features are calculated separately over both Helmholtz and modified Strouhal numbers. If a spectrum is dominated by a Helmholtz number scaling mechanism, the frequency modification exponent will result in values $m \approx 0$. To present spectra over both Helmholtz and

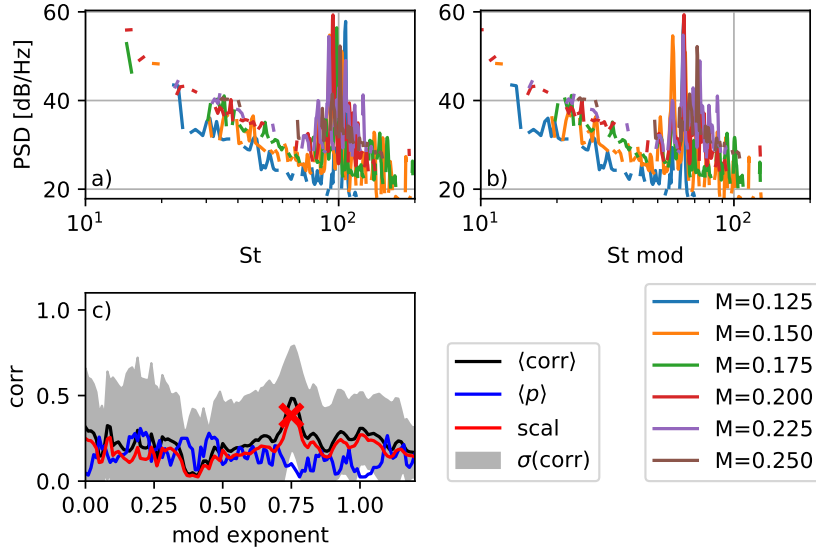


Figure 6.9: Do728, $Re = 1.4 \times 10^6$, slat tones at $\alpha = 8^\circ$. Comparison of source spectra at different Mach numbers over (a) normal Strouhal number and (b) modified Strouhal number, see eq. 2.1.19, with $m = 0.74$. (c) shows the mean and standard deviation σ of the Pearson correlation coefficient of the source spectra at different Mach numbers over the variation of the modification exponent, the mean p -value, and the resulting self-similarity (scal), see Section 6.4. The modification exponent $m = 0.74$ achieves the optimal self-similarity, marked with an x .

(modified) Strouhal numbers, we have to find a local maximum of the self-similarity function around $m_{St} \approx 1$ to account for spectra that include minor, Strouhal number scaling mechanisms. To do so, a standard peak detection is performed over the self-similarity function $scal(m)$ to find a local maximum $\tilde{m} \geq 0.5$ with a peak prominence $\hat{P}_p \geq 0.1$. If none is detected and $m^* < 0.5$, we set $m_{St} = 1$ to obtain a Strouhal number.

$$\tilde{m} = \underset{\substack{m \in [0.5, \infty[\\ \max(\hat{P}_p) \geq 0.1}}{\text{peak}} (scal(m)) \quad (6.4.6)$$

$$m_{St} = \begin{cases} m^* & \text{if } m^* > 0.5 \\ \tilde{m} & \text{if } m^* \leq 0.5 \\ 1 & \text{else} \end{cases} \quad (6.4.7)$$

Sound power scaling

The power of aeroacoustic noise generally increases with increasing Mach number, captured by the Mach power exponent n in eq. 2.1.20. A regression on the OASPL or peak levels of eq. 2.1.20 is typically used to determine the scaling exponent. This does not work for spectra from CLEAN-SC maps since the microphone array aperture in combination with deconvolution acts like a high-pass filter at an absolute frequency. This is problematic when scaling over the Strouhal number (and Helmholtz number at different temperatures and pressures). It effectively creates a Mach-dependent low-cut filter, which, in combination with a typical SPL decrease over frequency for aeroacoustic

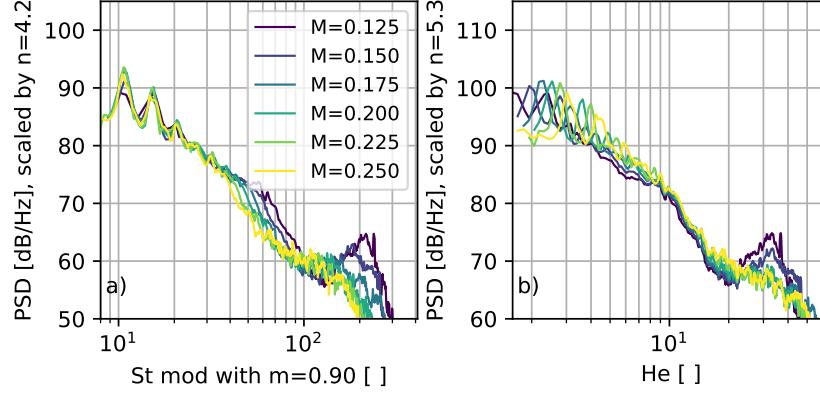


Figure 6.10: Do728 slat / slat track source at $Re = 1.4 \times 10^6$, $\alpha = 3^\circ$. Comparison of the power scaling over modified Strouhal ($m = 0.9$) and Helmholtz number to collapse the PSDs with eq. 2.1.20. The scaling exponents are $n_{St} = 4.2$, $n_{He} = 5.3$, $n_{OASPL} = 6.3$.

sources, results in a wrong OASPL and, thus, a scaling exponent. Instead, the mean distance between all power scaled spectra $\widehat{PSD}(f_i, M_j)$ is minimized bin-wise over frequency with a standard bounded minimization algorithm. The spectra's standard deviation σ at every discrete frequency is employed to calculate the distance between multiple spectra simultaneously. Since parts of a spectrum with a high SPL are often considered more important for the scaling, we can weight the standard deviations at every frequency with the Mach averaged spectrum power $\langle PSD(f_i, M_j) \rangle_{M_j}^\kappa$. The hyperparameter κ of this weight determines how much we want to prefer the scaling of high levels. Thus, we minimize

$$\min_{0 \leq n < \infty} \left\langle \sigma_j(PSD(f_i, M_j) - n 10 \log_{10}(M_j)) \langle PSD(f_i, M_j) \rangle_j^\kappa \right\rangle_i, \quad (6.4.8)$$

with $n, \kappa \in \mathbb{R} \geq 0$. At least spectra at three different Mach numbers should be used to calculate a reliable power scaling exponent. A large variation in Mach number also increases the scaling's reliability. Figure 6.10 shows the resulting power scaling for a slat / slat track source and $\kappa = 10$ over modified Strouhal and Helmholtz numbers. Note the different scaling behavior over Strouhal and Helmholtz numbers for the low and high-frequency part of the spectrum and that the OASPL scaling n_{OASPL} obtained by a linear regression neither matches the Helmholtz nor the Strouhal scaling exponent correctly, as described above. Figure 6.2 displays more examples of scaled PSDs with $\kappa = 10$, used for all results presented in this thesis, yielding reasonable and robust results for the partially degenerate spectra.

Tonality

Accounting for the tonal behavior of the sources results in less straightforward feature descriptions since the number of tonal peaks varies from source to source and within a source for different Mach numbers. However, their properties must be captured by a finite amount of features, see section 6.4. These properties are the peak-width intervals \widehat{P}_w , peak prominences \widehat{P}_p , peak frequencies \widehat{P}_f , and the number of peaks \widehat{P}_n . First, a standard automated peak detection on the spectra results in a set of peak prominences $P_p(M_j)$, peak widths $P_w(M_j)$, and peak frequencies $P_f(M_j)$ for every Mach

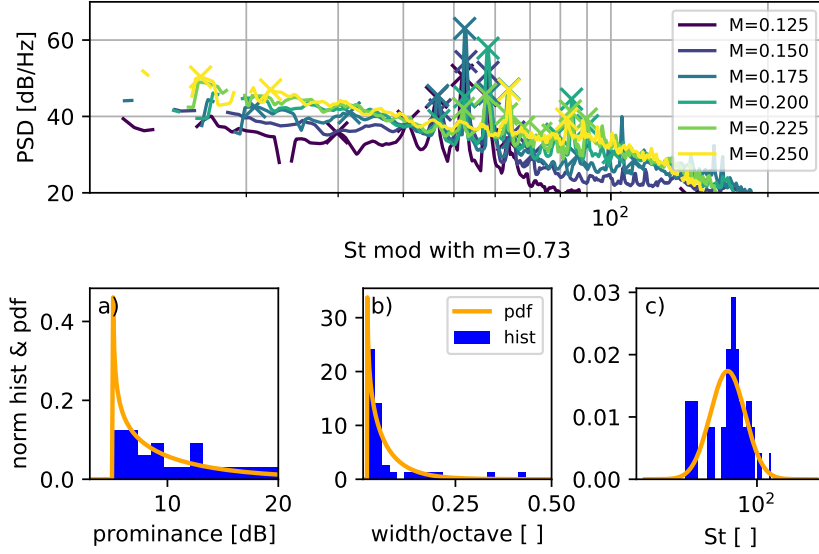


Figure 6.11: Do728, $Re = 1.4 \times 10^6$, slat tones at $\alpha = 8^\circ$. Top, the spectra and the automatically detected peaks, depicted with an x . Bottom, a normalized histogram and the fitted PDF of the (a) peaks prominence, (b) peak width, and (c) peak Strouhal number.

number M_j . Additionally, sets of frequency bins $P_{\hat{f}}(M_j)$ are defined that include all frequency bins that lie within the peak width intervals $P_w(M_j)$.

$$P_{\hat{f}}(M_j) = \{f_i | s.t. f_i \text{ belongs to a peak for } M_j\} \quad (6.4.9)$$

The number of peaks \hat{P}_n is defined as the Mach averaged number of elements in the sets.

$$\hat{P}_n = \langle |P_p(M_j)| \rangle_j \quad (6.4.10)$$

As stated in section 6.4, we have to break down the properties of the peaks to single value features. This can be achieved by describing the distribution of the peaks' properties instead of using the individual peaks' properties directly. Naturally, peaks with lower prominence appear more often than peaks with very high prominence in P_p . This assumption is also used for the peak width in P_w . This behavior can be modeled using a gamma distribution [1]. With the gamma function $\Gamma(k)$, the Probability Density Function (PDF) γ of the gamma distribution over a variable v with a shape k , scale θ and location l is

$$\gamma(v, k, \theta, l) = \frac{(v - l)^{k-1} \exp(-\frac{v-l}{\theta})}{\theta^k \Gamma(k)} \quad \text{for } v, k, \theta, l \geq 0. \quad (6.4.11)$$

For the peak frequency locations in $P_{\hat{f}}$ a log-normal distribution fits most of the sources best. The distributions of these properties have unknown shape (standard deviation), scale (distribution median), and location (distribution offset) parameters, which can be approximated from any number of samples greater than one by fitting the gamma or log-normal distribution to the data with standard fitting methods. The shape, scale, and location for each peak width, peak prominence, and peak frequency are used as comparable feature values, independent of the number of tones in the PSDs and the number of different Mach numbers. Figure 6.11 shows the peak detection and the corresponding distributions for all Mach numbers of a Do728 slat tone source. A lower threshold of 3 dB

for the peak prominence prevents the algorithm from detecting many irrelevant low-level peaks that dominate the distributions. If only one or fewer tones are detected, the feature values are set to zero (no distribution can be obtained).

The ratio of how many peaks overlap at every detected peak frequency interval is used to determine how well the prominent peaks scale over Strouhal or Helmholtz number (scal_p). Working with logarithmically spaced, discrete frequencies f_i , I sets E_i are introduced, each containing up to J Mach numbers for which the frequency bin of the corresponding spectrum lies within a peak interval. \hat{I} is a single set, that contains the frequency indices i for which at least one spectrum features a peak.

$$E_i = \{M_j \mid \text{so that } f_i \in P_{\hat{f}}(M_j)\} \quad (6.4.12)$$

$$\hat{I} = \{i \mid \exists M_j \text{ so that } f_i \in P_{\hat{f}}(M_j)\} \quad (6.4.13)$$

The resulting scaling of the tones is then the ratio of spectra that share a peak at the same frequency to the total number of spectra at different Mach numbers J , averaged over all frequency bins i for which at least one peak was detected is

$$\text{scal}_p = \frac{1}{|\hat{I}|} \sum_{i \in \hat{I}} \frac{|E_i| - 1}{J - 1}. \quad (6.4.14)$$

The minus ones ensure a soft feature value $0 \leq \text{scal}_p \leq 1$ for the modified Strouhal and Helmholtz number, since each E_i contains at least one element. Finally, the tonal intensity prop_p is defined as the Mach averaged ratio of tonal SPL to total SPL. It expresses how much percent of the energy in the spectra is caused by tones.

$$\text{prop}_p = \left\langle \frac{\sum_{f_i \in P_w(M_j)} \text{PSD}(f_i, M_j)}{\sum_i \text{PSD}(f_i, M_j)} \right\rangle_j \quad (6.4.15)$$

Source location dependency on the Mach number

The spatial location of some aeroacoustic sources may change with the Mach number. An example of a moving source would be a flow detachment, at which the sound-generating eddies move further downstream with increasing Mach number or jet noise, while cavity noise would remain at the exact location. Figure 6.12 (a) shows the variation of source positions on the Do728 with increasing Mach number. Here, the positional change of the source with increasing Mach number is defined as the source movement Δl , that is, the mean movement of the local source position \mathbf{x} , normalized by the change in Mach number, shown in Figure 6.12 (b). A limitation of this feature is that it assumes the monotonous movement of the source in one direction with the Mach number.

$$\Delta l = \left\langle \frac{|\mathbf{x}_j - \mathbf{x}_{j-1}|}{M_j - M_{j-1}} \right\rangle_j \quad \text{for } j \geq 2 \quad (6.4.16)$$

Spatial source distribution

Aeroacoustic sources can be spatially distributed, such as line or volume sources. The sources' spatial PDFs obtained with SIND can be used to describe this behavior. SIND approximates the spatial

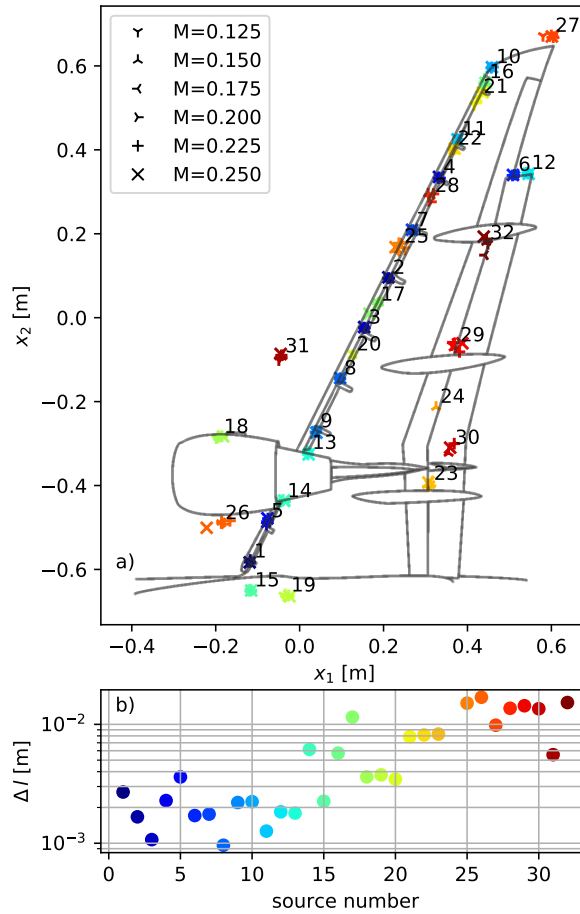


Figure 6.12: Do728. (a) shows the source positions at $Re = 1.4 \times 10^6$, $\alpha = 10^\circ$ (if the source is present at this configuration) for the given Mach numbers. (b) shows the mean movement of the sources calculated with eq. 6.4.16.

source distributions with 2D normal distributions, described by the standard deviations σ_{x_i} . Here, the integrated, normalized PDF area A represents the spatial compactness of the source.

$$\begin{aligned}
 A &= \int_{x_1} \int_{x_2} \frac{\text{PDF}(x_1, x_2)}{\|\text{PDF}(x_1, x_2)\|_\infty} dx_2 dx_1 \\
 &= 2\pi\sigma_{x_1}\sigma_{x_2}
 \end{aligned} \tag{6.4.17}$$

The ratio of the PDFs standard deviations σ_{x_i} is an indicator for line sources with

$$R_\sigma = \max\left(\frac{\sigma_{x_1}}{\sigma_{x_2}}, \frac{\sigma_{x_2}}{\sigma_{x_1}}\right) - 1. \tag{6.4.18}$$

Thus, $R_\sigma \approx 0$ indicates a point or sphere-like source while an increasing R_σ indicates a line source.

Spectrum shape

A linear regression $L(f)$ for $\text{PSD}(f)$ captures the general shape of the spectrum, which consists of two values: the interception i_0 of the line at $f = 0$ Hz and the slope \hat{s}

$$L(f) = \hat{s}f + i_0. \tag{6.4.19}$$

The interception is an absolute value, varies with the Mach number, and is discarded. The slope is the increase or decrease of the PSD level over the frequency. Additionally, the regression's r^2 -value describes how well the linear regression explains the spectrum. A low r^2 value indicates that the linear regression is not capturing the movement in the spectrum well. Thus, it is an indication of the waviness of the spectra. With the error e of the regression model

$$e_{ij} = \text{PSD}(f_i, M_j) - L(f_i, M_j) \quad (6.4.20)$$

the Mach-averaged r^2 value is then calculated with

$$r^2 = \left\langle 1 - \frac{\sum_i e_{ij}}{\sum_i (\text{PSD}_{ij} - \langle \text{PSD}_{ij} \rangle_i)^2} \right\rangle_j \quad (6.4.21)$$

Similar to the spatial source distribution, a source distribution over frequency is defined. Since we work on sparse spectra that are not defined on all frequency bins, the mean \bar{f} and standard deviation f_σ of the frequencies can be used for which the source PSD is real-valued to capture the source's radiation frequency interval. With the sets Q_j that contain the real-valued frequency bins f_i for the spectra at Mach number M_j

$$Q_j = \{f_i \mid \text{such that } \text{PSD}(f_i, M_j) \in \mathbb{R}\} \quad (6.4.22)$$

$$\bar{f} = \frac{1}{J} \sum_j \left(\frac{1}{|Q_j|} \sum_{f \in Q_j} f \right) \quad (6.4.23)$$

$$f_\sigma = \sqrt{\frac{1}{J} \sum_j \left(\frac{1}{|Q_j|} \sum_{f \in Q_j} (f - \bar{f})^2 \right)} \quad (6.4.24)$$

Finally, the frequency $f_{L\max}$ for which the PSD level has a maximum is defined with

$$f_{L\max} = \langle \text{argmax}_i (\text{PSD}(f_i, M_j)) \rangle_j. \quad (6.4.25)$$

6.5 Feature results

Figure 6.13 presents the distributions of exemplary features for exemplary source types and compares them for the Do728 and A320 datasets. The horizontal lines within the distributions display the 0.25, 0.50, and 0.75 percentiles. The exemplary source types were chosen because they were manually identified in Section 6.2 with great confidence based on their spectral features in Figure 6.2, and they showed interesting acoustical properties. The features were chosen to cover the variety of aeroacoustic properties introduced in Section 6.4.

Figure 6.13 shows the self-similarity over (a) the modified Strouhal number, and (b) the Helmholtz number, see Section 6.4. Based on the exemplary source spectra in Figure 6.2 and the aeroacoustic literature, the slat track, slat resonance, and leading flap side edge strongly scale over the Helmholtz number and the slat tone, strake, trailing flap side edge, slat and strake tone to strongly scale over the (modified) Strouhal number. For the slat tracks the feature does not achieve satisfying results since it wrongly predicts a strong self-similarity over the Strouhal number for both datasets. This is

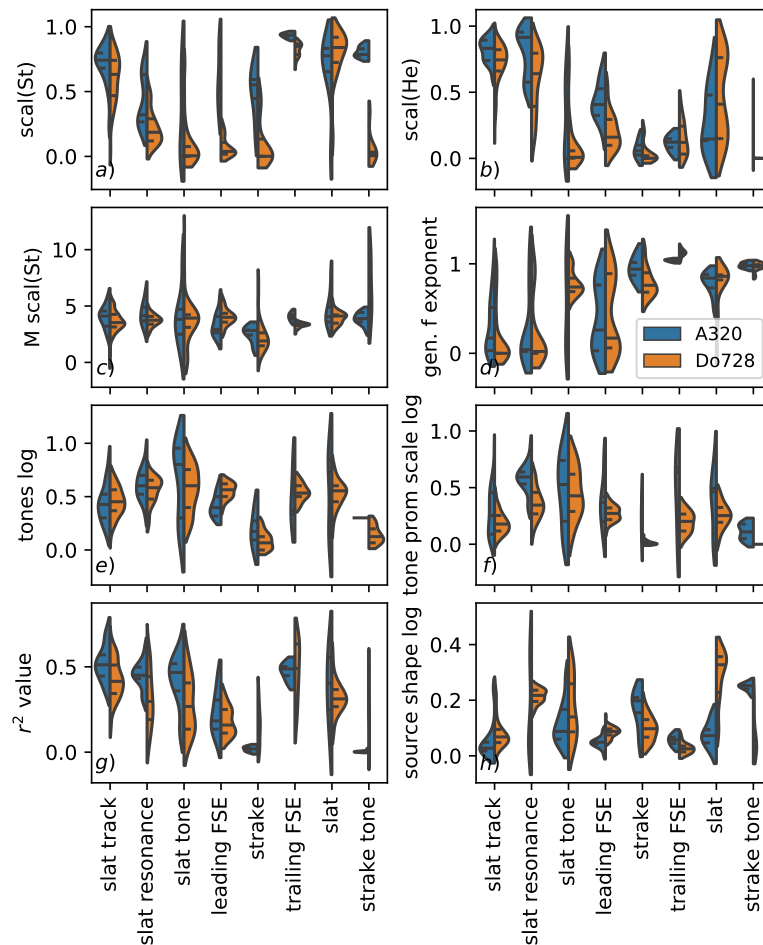


Figure 6.13: Violin plot comparison of the A320 (blue) Do728 (orange) for exemplary source types and exemplary features from Table 6.5. (a) shows the broadband self-similarity over the modified Strouhal number, see Section 6.4. (b) shows the broadband self-similarity over the Helmholtz number. (c) shows the Mach power scaling over the modified Strouhal number, see Section 6.4. (d) shows the generalized frequency modification exponent, see Section 6.4. (e) shows the logarithmic number of tones, and (f) shows the gamma distribution's logarithmic scale of the tone prominence, see Section 6.4. (g) shows the r^2 -value of the linear regression of the spectrum, see Section 6.4, and (h) shows the logarithmic spatial source shape, see Section 6.4.

because of the strong decay in SPL over frequency, which dominates the correlation stronger than the local spectral features such as tonal peaks or humps. For the Do728 strake tones, a low Strouhal self-similarity is wrongly predicted. This is due to the inclusion of the p -value in eq. 6.4.4, which becomes large for small-band sources. For the A320 slat tone and LFSE the feature is not robust and results in a large range of values. The expected self-similarity over the Helmholtz number is well captured in Figure 6.13 (b). This is also true for Strouhal number scaling slat sources with additional Helmholtz scaling high-frequency content, see Figure 6.3 (a) at $100 \leq St \leq 200$.

Figure 6.13 (c) shows the Mach power scaling over the modified Strouhal number. Similar power scalings around $M \text{ scal}(St) \approx 3.73$ (averaged over the displayed source types) are observed. This is expected as aeroacoustic noise is known to scale within a small range (e.g., M^4 for monopoles, M^6 for dipoles, and M^8 for quadrupoles), depending on the source mechanism. However, the variance

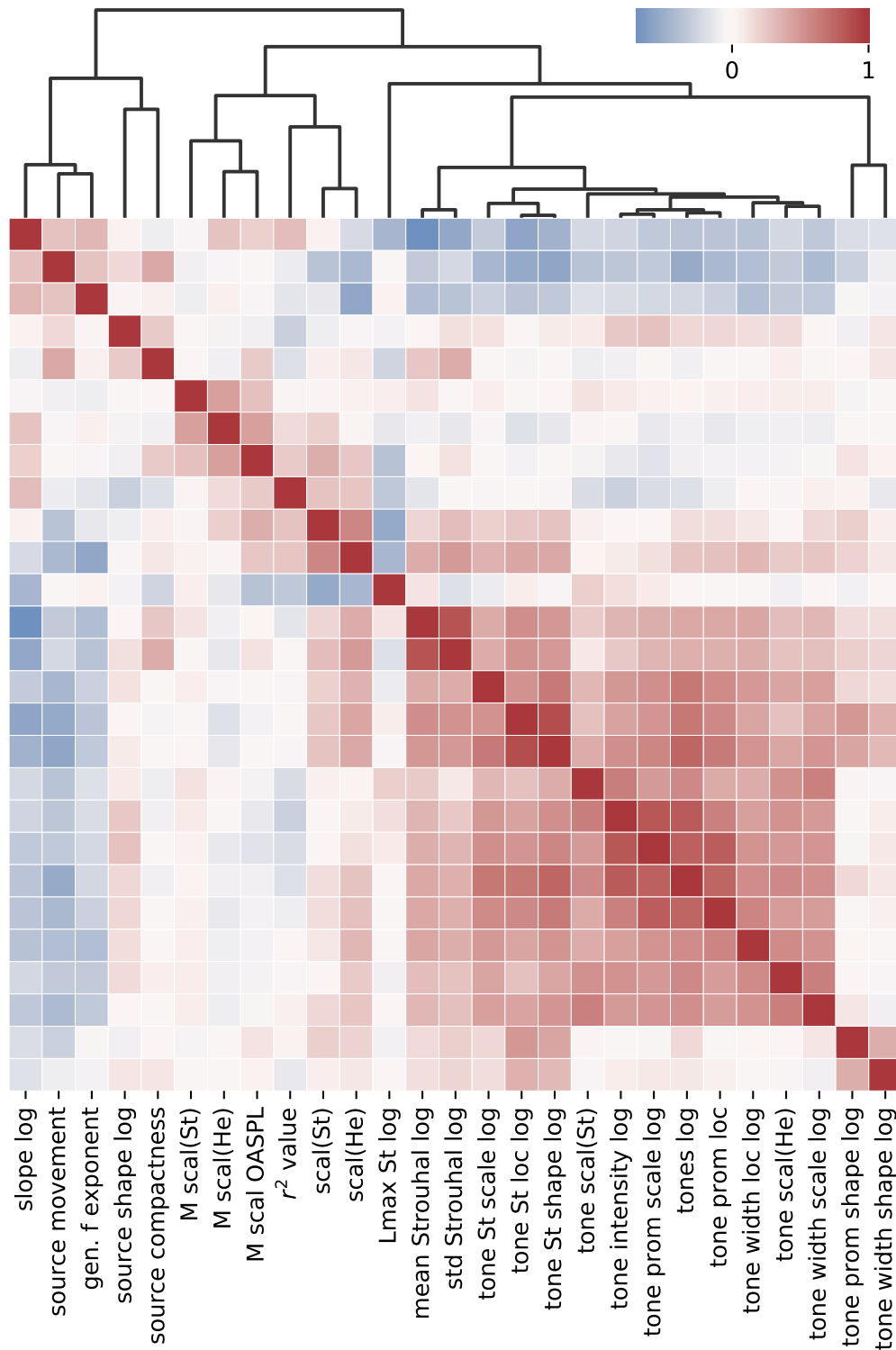


Figure 6.14: Symmetric heatmap of all Do728 feature Pearson correlation coefficients and their hierarchy based on hierarchical clustering with a correlation distance metric (top).

within the source types often exceeds the variance between the source types. Also, as seen for the trailing flap side edge the Mach scaling can differ for the same source type for different datasets. At this point, it is not clear if this is caused by the assumptions of the method (e.g., ignoring the source directivity) or by the different model geometries.

Figure 6.13 (d) shows the generalized frequency normalization exponent m , see Section 6.4. Most of the slat tracks and slat resonances show an exponent around $m \approx 0$. This indicates a Helmholtz scaling and corresponds to the presented self-similarities. For both datasets, there are two groups of LFSE, one that features $m \approx 0$, and one that features $m \approx 1$. For the Do728 strakes, a mean exponent $m \approx 0.79$ is observed, for the A320 strakes $m \approx 0.95$. For the Do728 TFSE $m \approx 1.13$ is observed, for the A320 $m \approx 1.06$. For the Do728 slat $m \approx 0.78$ is observed, for the A320 $m \approx 0.72$.

Figure 6.13 (e) shows the Mach averaged occurrence of tones (logarithmic), see Section 6.4. Some source types feature few tones, i.e., the strake and strake tone, some source types feature many tones, i.e., the slat tones. Figure 6.13 (f) shows the corresponding scale parameter of the tone prominence distribution (logarithmic). A large scale feature indicates that the distribution is spread out, including tones with small and large prominence. A small scale parameter indicates that all tones have a similar prominence. Both datasets show similar distributions for the features. Generally, the features correspond to our expectations. However, the gamma distribution approximation fails for sources that contain only one prominent tone, such as the Do728 strake tone sources.

Figure 6.13 (g) shows the spectrum shape r^2 based on a linear regression, see Section 6.4. For the Do728, the distributions of the strake, the TFSE, and the strake tone are spread out compared to the A320 distribution. Overall, they show similar trends. The feature mainly highlights the fact that many aeroacoustic sources are broad-band sources with a linear decay in SPL over logarithmic frequency and correctly identifies small-band sources such as the strake and strake tone.

Figure 6.13 (h) shows the source shape (logarithmic). A value close to zero indicates a point source and an increasing value indicates a line source. The results directly depend on the output of SIND, which correctly identified the slat track, LFSE, strake, and TFSE as point-like sources. The Do728 slat was correctly identified as a line-like source. However, the A320 slats were wrongly identified as point-like sources. While SIND yielded overall comprehensible results, on some occasions, sources were wrongly spatially separated or combined. E.g., the slat tones sometimes appear on slat track positions and, thus, are identified as point-like sources, while they should be line-like sources [33].

Figure 6.14 shows a Pearson correlation coefficient heatmap for the Do728 feature space. On the top, a feature hierarchy is displayed based on hierarchical clustering with a correlation distance metric based on the Unweighted Pair Group Method with Arithmetic mean algorithm. This hierarchy shows which features are similar based on the displayed correlations to all other features. The heatmap and hierarchy show that many of the introduced features correlate strongly, especially features that were introduced together to cover an aeroacoustic property such as tonality or self-similarity. The feature hierarchy shows that these features originate from the same branch. From left to right, the first major branch includes the linear regression's slope (\log), the source movement, the generalized frequency exponent, and the source compactness. The first three features correlate negatively with the features that correspond to the tonality and form a sub-branch. The second main branch on the right contains all other features. Its left sub-branch contains the Mach scaling over the Strouhal and Helmholtz number, as well as the linear regression's r^2 -value, and the self-similarity (scal) over Strouhal and Helmholtz number. The other branch contains all features that describe the frequency content of the

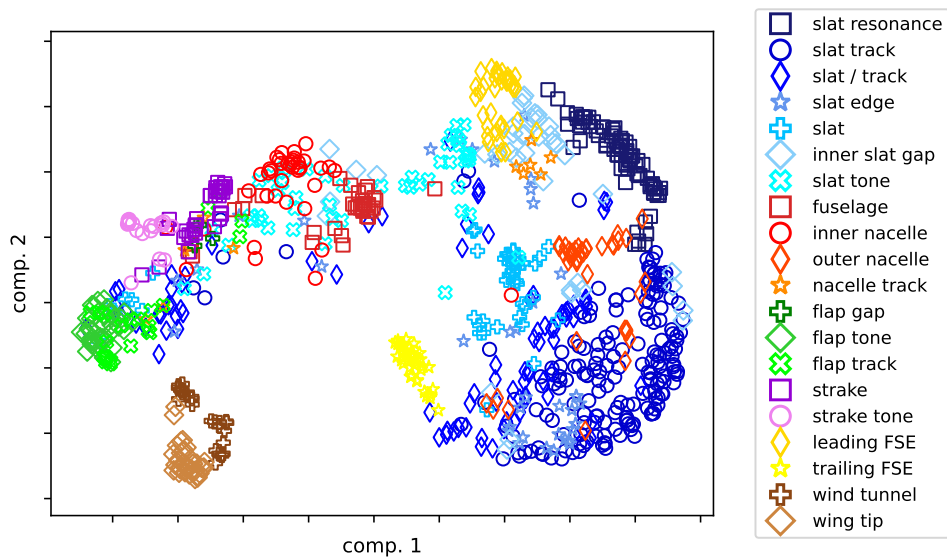


Figure 6.15: Do728. UMAP [85] components for $n_{\text{components}} = 2$, $n_{\text{neighbors}} = 90$ ($\approx 10\%$ of the dataset), and a correlation distance metric for the presented feature space.

spectrum ($St_{L_{\max}}$, mean and std Strouhal numbers) and its strongly correlated tonality features.

Figure 6.15 shows a Uniform Manifold Approximation and Projection for Dimension Reduction [85] (UMAP) of the Do728 sources. The colors and symbols both represent the manual labels. UMAP estimates a manifold that locally (and to some extent globally) preserves the data structure in a low-dimensional space, based on which the data can be displayed in low-dimensional space. UMAP requires a distance metric, such as a spatial metric (e.g., Mahalanobis, Minkowski), or a similarity metric (e.g., cosine, correlation). All mentioned metrics yield similar results for the presented feature space. Figure 6.15 shows a 2D feature space projection, in which we can observe how similar source types are in the introduced feature space and how well the introduced feature space separates the proposed source types. The slat track and slat edge sources are similar and gradually transition to slat / track sources, and then to slat sources. These groups are not well separated, which corresponds to the manual classification in Section 6.2, since the spectra often smoothly transition from one shape to another and show great variance. The slat tone sources are not captured well in the feature space, since they are manually identified with very high confidence but do not form a well-separated group. Other source types, such as the wing tip and the trailing flap side edge are well captured in the feature space and show little variance.

The figure shows that sources of the same manually introduced source type are close to each other in the introduced feature space. The ability of UMAP to form separable source-type groups highlights two results. First, the introduced feature space captures sufficient aeroacoustic information for the presented sources under the condition that the labeling is correct. Thus, groups of multiple sources are formed in the UMAP based on the feature space. Second, the labeling is sufficiently good under the condition that the feature space correctly captures the sources' aeroacoustic behavior. Thus, the groups mainly contain unique source types. Since the source types were identified manually based on the source spectra and not on the introduced feature values, see Section 6.2, this indicates that the label choices are reasonable.

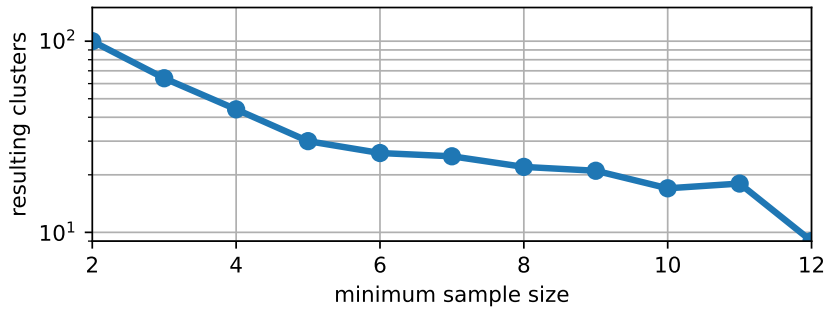


Figure 6.16: Do728, resulting cluster number based on the minimum sample size N_s for HDBSCAN.

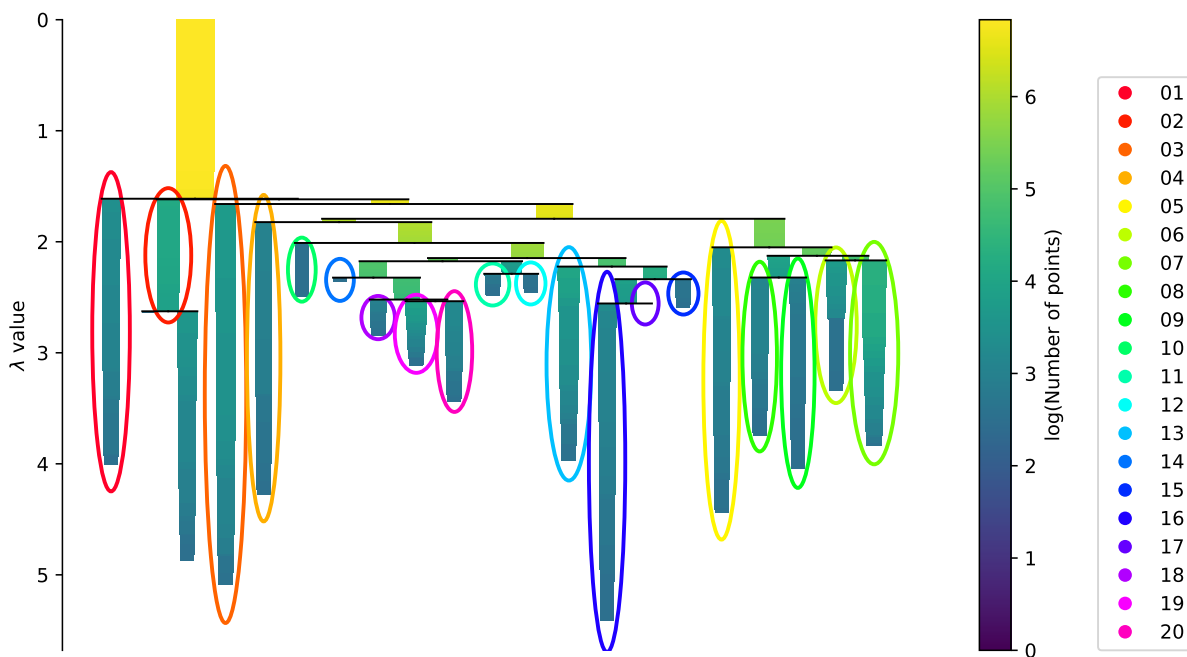


Figure 6.17: Do728, cluster tree for $N_s = 11$. The chosen clusters are marked with colored ellipses.

6.6 Source-type clustering

This section presents unsupervised clustering of the aeroacoustic spectra based on the presented features. The advantage of unsupervised over supervised learning is that no ground truth is necessary. Instead of classifying sources into predetermined classes, unsupervised learning groups the presented data into by the expert previously unknown clusters. The main aim is to aid the expert in the manual classification of the sources and the following analysis and gain a deeper insight into the sources and their aeroacoustic behavior.

6.6.1 Methodology

For clustering HDBSCAN [21, 84] is selected due to its soft clustering support without prior knowledge about the number of clusters, i.e., an expectation of the number of different source types, see Section 2.3. Here, the clustering probability can also be interpreted as the clustering confidence. Since the distances between sources in a high dimensional feature space become alike [3], the feature space must be reduced prior to the distance-based clustering. The most prominent dimensionality reduction technique is Principal Component Analysis, which orthogonalizes the feature space and sorts

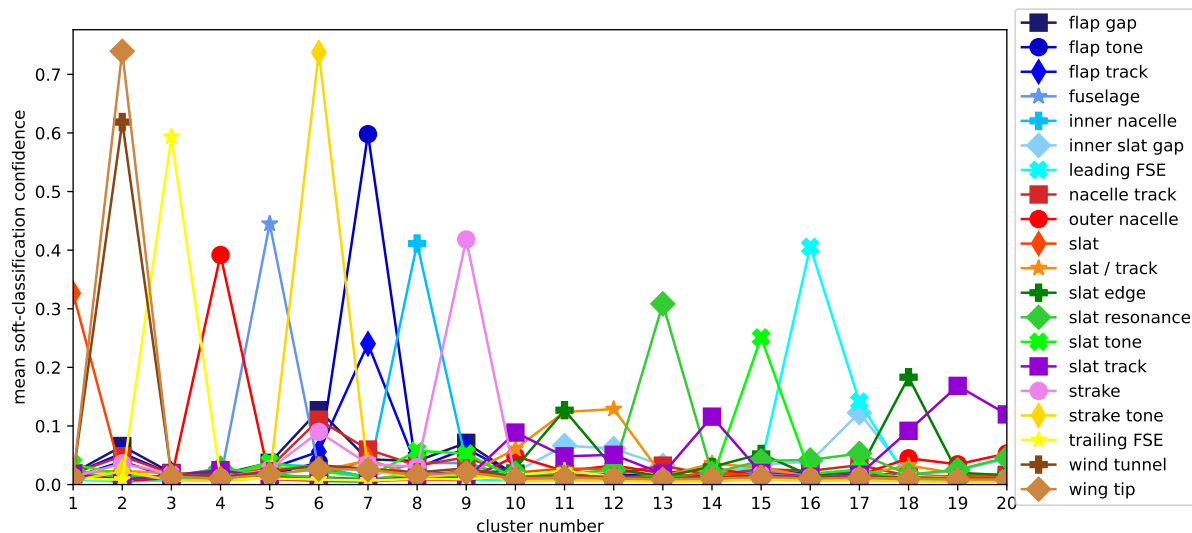


Figure 6.18: Do728, mean clustering confidence per label and cluster.

the dimensions based on their explained variance. Then, dimensions with little statistical variance can be discarded. For the presented method, a Kernel Principal Component Analysis (KPCA) [112] with a Radial Basis Function (RBF) as a kernel is employed. The KPCA uses a nonlinear convolution kernel, which allows the PCA to embed the feature space in a nonlinear manifold. For dimensionality reduction, $2\sigma \approx 95\%$ of the explained variance is retained by discarding the KPCA dimensions with the least variance. Before using a PCA or KPCA, the feature space must be normalized to zero mean and unity variance. This normalization assumes that the features are normally distributed. However, most of the features F are distributed exponentially and are transformed to a log-space prior to the KPCA with $\log_{10}(F + 1)$, see Table 6.5. Thus, the feature space is partially transformed into a log-space, normalized, orthogonalized, and reduced to 95% explained variance using a KPCA and then clustered using HDBSCAN.

HDBSCAN requires a minimum sample size, determining how many source members a cluster must have. Smaller clusters are discarded as noise. We can determine a reasonable sample size by examining the resulting cluster numbers. With an increasing sample size, the resulting number of clusters first drops massively and then decreases only slightly. Figure 6.16 demonstrates this for the Do728 dataset. We pick the sample size after which the total quantity of clusters n_{clusters} only decreases slightly, in this case around $N_s = 7$. This is sometimes called the “elbow-method” or “knee-method” [128]. It is noteworthy that picking a bad sample size may result in sub-clusters (splitting a cluster) or super-clusters (merging clusters), but the overall results remain comparable. Thus, it can be helpful to start with a large sample size to obtain a few clusters that are manageable to analyze manually and then transition towards smaller sample sizes. The methodology for this EDSS is called “Clustering sources based on their aeroacoustic features” (CRAFT).

6.6.2 Results

The results presented are based on the Do728 and A320 datasets, obtained from 2D CLEAN-SC beamforming maps, see Section 4.3, with steering vector III and DR, see Section 4.1, 2D SIND, see Section 5.2.1, and CRAFT. Figure 6.17 shows an exemplary HDBSCAN cluster tree for the Do728

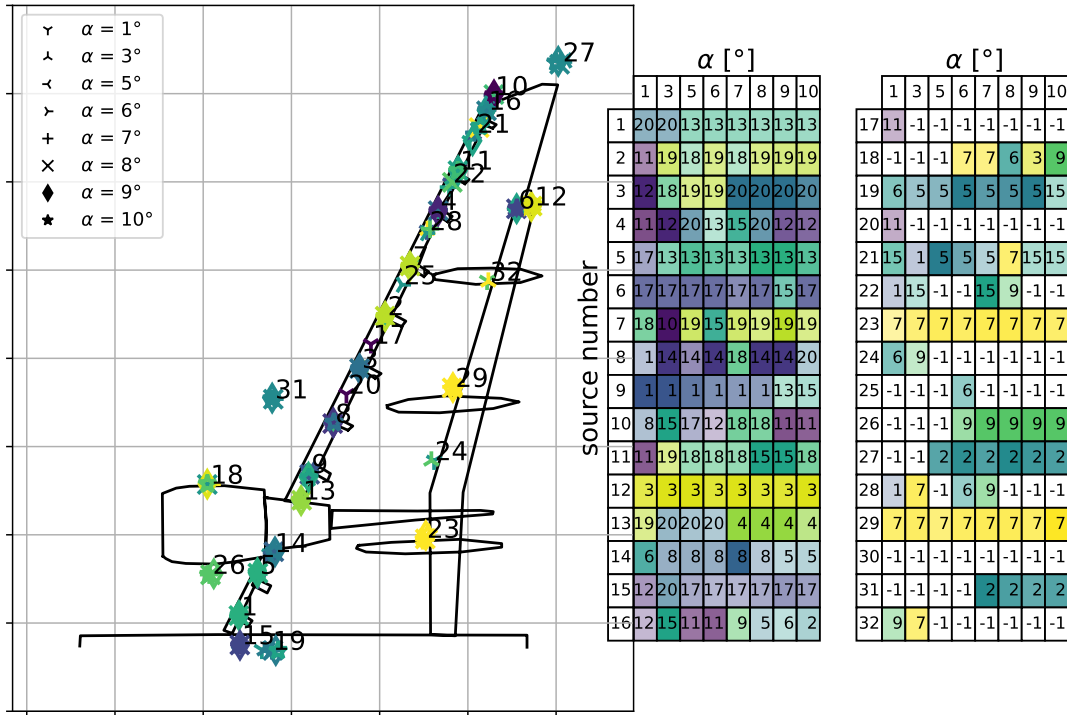


Figure 6.19: Do728, clustering result at $Re = 1.4 \times 10^6$. For each source location the predictions are given for each angle of attack in the corresponding table. Each cluster number is assigned a corresponding color for visual support. The color opacity indicates the clustering confidence. If the cluster number is -1, the source does not exist at this angle of attack.

data and 20 clusters. On the vertical axis, the λ value shows the distance between the sources in the feature space, and on the horizontal axis, the thickness of the bars (and color) indicates the number of cluster members. The ellipses show the selected clusters by HDBSCAN. If clusters are located on the same branches, they are sub-clusters of a super-cluster. Larger values of the minimum sample size will lead to the formation of super-clusters, while smaller values will increase the number of sub-clusters.

Since HDBSCAN estimates the PDF of each cluster in the high-dimensional feature space, it allows the calculation of the probability of each source belonging to each cluster. Thus, we can manually define how sources should be clustered based on the resulting PDF. Given that this thesis proposed

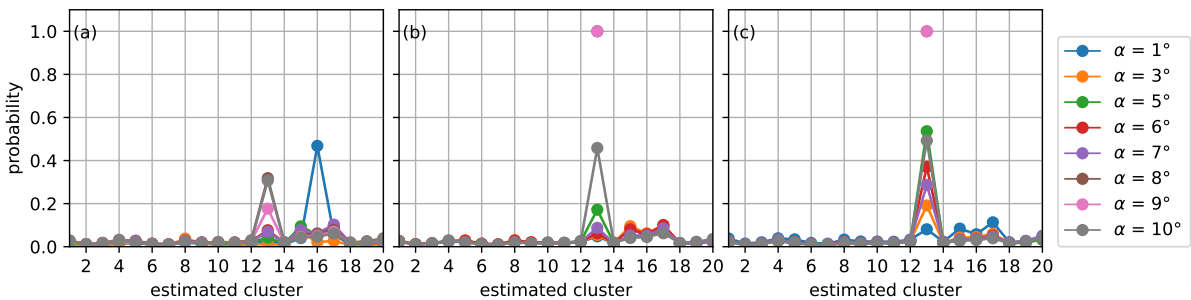


Figure 6.20: Do728, soft cluster confidences of source five 5 in Figure 6.19 (Krüger slat) for (a) $Re = 10.6 \times 10^6$, (b) $Re = 2.5 \times 10^6$, (c) $Re = 1.4 \times 10^6$.

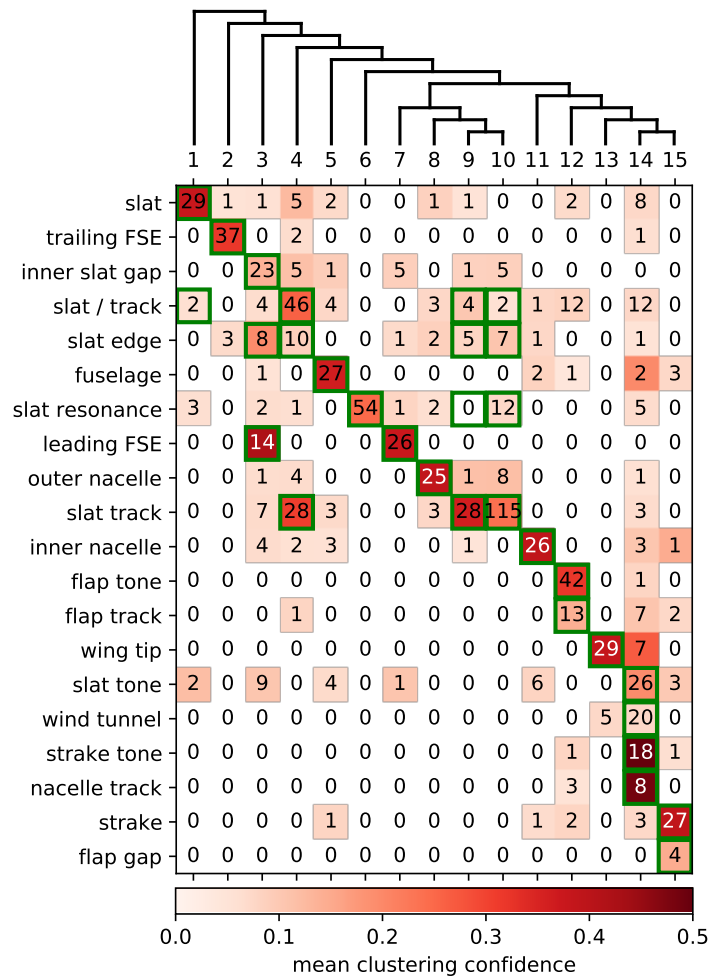


Figure 6.21: Do728, confusion matrix of the occurrences of our manually identified source types in CRAFT's determined clusters. The color intensity displays the mean clustering confidence. Cluster choices this thesis considers correct are marked with a green box. The tree above the clusters displays their hierarchy.

manual labels for the sources, we can compare the resulting clusters to the manual labels (typically not the case, as we cluster the sources to identify and label the sources, not vice versa). Figure 6.18 shows the resulting clustering confidence, averaged over all label members. Most clusters correspond to the manual labels.

For the final Do720 clustering results a minimum sample size of seven was used for HDBSCAN. CRAFT determined fifteen source clusters. Figure 6.21 shows a confusion matrix of the manually determined labels, see Section 6.2, and the clustering results. The matrix shows how often a source from a manually determined category was clustered into the corresponding clusters. Given that the manual source type identification is correct, a perfect clustering would result in a cluster group for every manual label, and all corresponding sources would be clustered within their corresponding group. Thus, a perfect clustering would achieve a square confusion matrix with all results on the diagonal. The underlying color in the confusion matrix depicts the mean clustering confidence. Since most clusters correlate to the manual labels (they are mostly located on the diagonal axis), our definition of correct clustering results (which are marked with a green box in the confusion matrix)

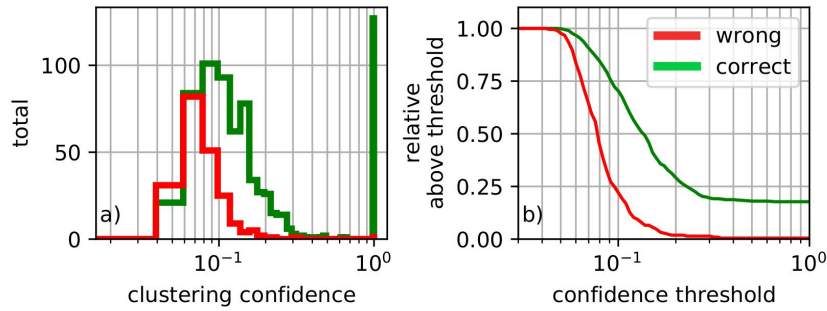


Figure 6.22: Do728, (a) shows a histogram of the total wrong and correct cluster choices over their clustering confidence. (b) shows the relative number of cluster choices above the confidence threshold t_C on the x -axis.

will be based on its comparison to the manual labels.

To identify the clusters corresponding to the manual labels, we will take the occurrences of source types per cluster, their estimated confidence, their similarity to other source types, and the cluster hierarchy into account. Thus, cluster number one is assigned to the slat sources. Here, slat sources that are assigned to cluster one are considered as correct clustering results, slat sources assigned to other clusters are considered as wrong clustering results. A slat resonance, which was categorized as cluster number nine or ten (which consists mainly of slat tracks) instead of cluster number six (which consists solely of slat resonances), is considered correct since it is a sub-type of a slat track source. All sub-categories clustered with their super-categories are considered correct, but not vice versa. Thus, slat tracks that are clustered in group six (slat resonances, a sub-category of slat tracks) are considered wrong. Slat and slat tracks that fall in cluster four (slat / slat track) and vice versa are considered correct, which is a super-category of these ambiguous sources. Cluster numbers three, four, fourteen, and fifteen comprise multiple source types. As long as the corresponding source types were assigned to the cluster containing most sources, they are considered correct. The slat tracks occupy the two clusters, nine and ten, with high clustering confidence, which are considered equally correct, as the clusters are both branches of a super-cluster. The leading flap side edge occupies both cluster numbers three and seven with high confidence. Thus, both clusters are considered as correct. All other clustering results are considered as wrong.

The following clustering assessment is based on the thesis' manual source labeling and manual definition of correct confusion matrix entries. In total, 213 out of 928 Do728 source predictions (22.95 %) are considered wrong and 715 (77.04 %) are considered correct. Figure 6.22 (a) shows the number of clustering choices at the given clustering confidence. The correct and wrong clustering choices decrease with increasing confidence. Figure 6.22 (b) shows the relative number of wrong and correct clustering choices that lie above the confidence threshold t_C . We observe that the wrong clustering results decrease much more rapidly than the correct clustering results. As an example, if the clustering results with confidence below $t_C = 0.1$ are discarded, only a prediction for 59.26 % of the sources is retained, but the clustering accuracy increases to 91.45 %.

Figure 6.23 shows the confusion matrix of our manually identified source types and the clustering results for the A320. The correct clusters are determined as stated above for the Do728. In particular,

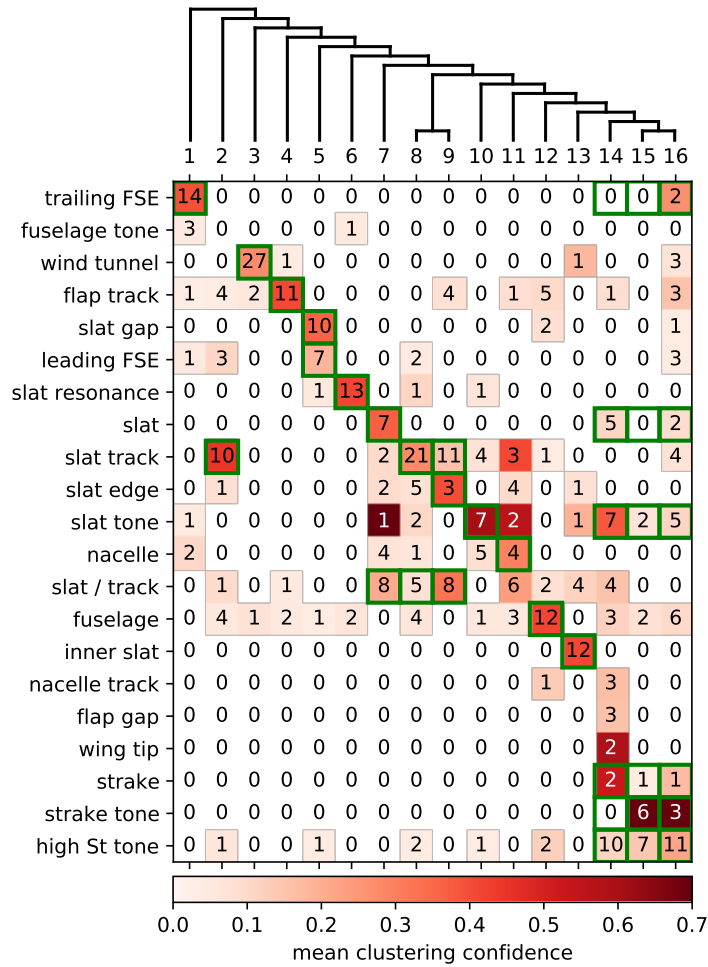


Figure 6.23: A320, confusion matrix of the occurrences of our manually identified source types in CRAFT's determined clusters. The color intensity displays the mean clustering confidence. Cluster choices this thesis considers correct are marked with a green box. The tree above the clusters displays their hierarchy.

the super-cluster 14, 15, and 16 represent Strouhal number scaling tones. Thus, the clustering results for the nacelle track, flap gap, and wing tip are considered as wrong. The super-cluster 7, 8, and 9 represent slat / tracks, with sub-cluster 7 including the slats and sub-clusters 8, and 9 including the slat tracks and the slat edge. In total, 154 out of 408 source predictions (37.75%) are wrong and 254 (62.25%) are correct. As shown for the Do728 results, if the clustering choices with confidence below $t_C = 0.1$ are discarded, only a prediction for 51.47% of the sources is retained, but the clustering accuracy increases to 74.29%.

7 Discussion

The subsequent sections discuss the results presented in the previous chapters for beamforming, Regions Of Interest, the Expert Decision Support System, and the implications on aeroacoustics.

7.1 Beamforming

Beamforming in noisy environments proved to be a valuable tool to suppress noise and estimate the source power and source distribution in an area of interest. The accuracy and limitation depend on the method and its assumptions, discussed in the following.

7.1.1 Conventional beamforming

Conventional beamforming proved to be a robust algorithm in the presence of strong background noise. It yields systematic errors when the compact, incoherent monopole assumption is violated, but the resulting spatial and power estimations are still reasonable approximations of the ground truth. Conventional beamforming uses a normalized Green's function to estimate the sound radiation, which cannot be correct in estimating the source's power and locations. Thus, two (out of four) steering vector formulations are used.

Formulation III yields the correct source power estimation but not the correct source position and formulation IV yields the correct positions but not the correct power estimation due to how sources are projected on the source map. If the steering grid does not cover the sources, formulation III estimates distributed, blurred sources. This contaminates the locations where true sources are located. At the same time, it is forgiving towards slight errors in the focal plane. They result in a source power estimation error. For 3D focus grids, formulation III cannot be combined with CLEAN-SC since sources estimated further away appear louder due to the steering vector distance normalization. Effectively, CLEAN-SC always estimates the source positions at the focal plane furthest away from the array.

Formulation IV suppresses sources not located in the focal plane strongly compared to formulation III. Thus, the source maps are less contaminated with background noise, reflections, and source projections. In return, errors in the focal plane lead to drastic underestimations in the source power. In the worst case, a source is not detected. Thus, formulation IV must be used with 3D focus grids spanning the entire wing.

If the array is small compared to the focus distance and compared to the model itself, a 2D grid with formulation III is appropriate. Otherwise, formulation IV and a 3D focus grid is advantageous.

7.1.2 CLEAN-SC and B-CLEAN-SC

Given the discussed steering vector limitations, CLEAN-SC yields the correct estimation for incoherent monopole sources as intended. When CLEAN-SC's assumptions, such as compactness and incoherence, are violated, the source power and spatial distribution are wrongly estimated. Fully coherent, distributed sources are wrongly estimated in a single location. Further, CLEAN-SC is limited by the resolution of conventional beamforming, which cannot resolve sources below the Raleigh frequency limit that depends on the array's aperture. Aliasing occurs above a frequency that depends on the sensor spacing, so sources are often estimated at the locations of side and grating lobes.

B-CLEAN-SC overcomes the spatial estimation issue by assuming that source locations do not change over frequency. CLEAN-SC results in arbitrary errors at low frequencies in combination with steering vector III. B-CLEAN-SC fixed this by averaging frequency intervals of dirty maps to improve the source location estimation. This works, as the locations of side and grating lobes change with frequency so that they cancel out during the averaging, whereas true source locations add. Additionally, the source location at low frequencies below the Rayleigh resolution limit is determined based on higher frequencies, where the source positions can still be resolved. B-CLEAN-SC also works for sources with a frequency-dependent spectrum and smallband sources. Here, the initial location estimation is only guaranteed to be simultaneously on the dominant source for some frequencies. Thus, B-CLEAN-SC is prone to "confuse" the power contribution of these sources. A low iteration gain factor must be used to relax this issue. Additionally, using frequency intervals instead of the whole spectrum further relaxes this issue.

B-CLEAN-SC can correctly determine the location and power of the sources at low frequencies in an open wind tunnel experiment and a lower overall noise level compared to CLEAN-SC. B-CLEAN-SC spatial and spectral accuracy depends on the used frequency interval and showed an optimum at 1/4 of the total frequency interval, after which spatial accuracy is traded for a deteriorating spectral estimation. One can account for this by defining frequency-dependent intervals so that the intervals are large at low and high frequencies and small at medium frequencies, where B-CLEAN-SC then effectively transitions to standard CLEAN-SC. A lower gain factor further relaxes this issue but increases the number of iterations. The number of iterations is not performance-relevant since the computationally costly part of the algorithm is only the initial calculation of the steering matrix and initial dirty map.

The Do728 data showed that B-CLEAN-SC works well on wind tunnel data. B-CLEAN-SC estimated consistent source locations throughout the frequency range, compared to CLEAN-SC, which identified sources mainly at medium frequencies. B-CLEAN-SC's spatial estimations are presumably correct due to their consistency and correlation to geometric features such as slat tracks and the flap side edge. Further, B-CLEAN-SC suppresses noise effectively compared to CLEAN-SC. The ROI spectra showed identical results for both methods at medium frequencies where CLEAN-SC identified sources. However, the estimated frequency range was limited compared to B-CLEAN-SC. CLEAN-SC strongly overestimated the source power at low frequencies because of the distance scaling issue of steering vector III, which was also observed for the synthetic example.

The popularity of CLEAN-SC lies in its robustness and computational efficiency. Larger arrays and high-resolution focus domains are likely to increase the computational effort and mitigate many of CLEAN-SC's shortcomings, such as the spatial resolution at low frequencies, further manifesting its leading position in industrial applications. B-CLEAN-SC and other computationally efficient derivatives, such as HR-CLEAN-SC, have the potential to be used in large-scale industrial applications. It is unlikely that they will be replaced by advanced but computationally expensive methods such as GO or machine learning beamforming soon. Instead, these methods should be treated as subsidiary methods for specific use cases where complex acoustic properties, such as coherent, distributed multipole sources, are of primary interest.

7.1.3 Global Optimization

generalized frequency Global Optimization is an established, non-linear imaging method, different from grid-based methods. Conventional beamforming is a linear transformation, and due to the steering vector problem, one cannot obtain a correct solution for the amplitudes and locations. Grid-based inverse beamforming potentially solves this issue but suffers from the basis mismatch problem, so sparsity has to be enforced artificially using regularization. GO offers a different solution since the introduced propagation matrix is no longer fixed and can include any number of parameters, such as the speed of sound, dipole source rotations, and other model properties, which can all be subject to the optimization process. Optimizing any parameter in the source or propagation model is possible, making the method suitable for incorporating the previously mentioned neglected properties.

A solution is obtained by minimizing the observed and estimated CSM error. The established error metric is the MSE of the observed and estimated CSM, which is proportional to the inverse PSF of the sources. Therefore, the method suffers from similar problems as conventional beamforming and CLEAN-SC at low and high frequencies and estimates sources at local minima (side-lobes). This thesis introduced a new energy function with parameters shared over the frequency, such as the source locations. This model assumption is based on the observations throughout this thesis that a source position is reasonably constant over large frequency intervals. This assumption increases the ratio of equations to unknowns in the GO problem and smooths out the PSF and, thus, the energy. A smooth energy function is essential since global optimizers are slow compared to local optimizers, especially if the number of variables and their domain are large. While the proposed broadband GO method outperformed CLEAN-SC and standard GO with nearly perfect results for the generic dataset, the method is computationally expensive compared to CLEAN-SC.

Since the broadband energy function is somewhat smooth, Local Optimization offers a computationally less demanding solution to the problem. The optimization results are nearly identical, given a reasonable initial spatial estimation. An initial spatial estimation can be determined with CLEAN-SC and SIND. As discussed above, it makes sense to use GO and LO as subsidiary methods to investigate complex acoustic properties neglected by CLEAN-SC. Exemplary results for a synthetic multipole showed that LO identifies the pole rotation, location, and source strength well. Thus, the presented method is a viable candidate for these complex phenomena.

GO, and LO require a predetermination of the number of sources, which is unknown prior to beamforming. A simple method is to overestimate the number of sources in the domain. Then, multiple estimated sources approximate a true source, or spare estimated sources are randomly scattered around the domain with zero source strength. The energy for multiple sources suggested that underestimating the number of sources will not lead to an estimated source approximating multiple true sources. Thus, it may also be a computationally efficient strategy to solve GO and LO iteratively for multiple sources.

Another challenge is the stability of the GO and LO results. Suppose one optimizes parameters such as a dipole rotation or distributed source coherence with an underlying model. In that case, one will obtain a result that estimates these parameters, even if the model does not fit the data. Thus, the optimization loss should be evaluated with the results to estimate how well the results actually approximate the data.

The results introduce further complexity to the interpretation due to increased parameters. Partially coherent, distributed multipole sources can no longer be integrated but must be evaluated individually and manually, and the literature currently proposes no guideline for such an endeavor.

7.1.4 Grid-based ANN beamforming

This thesis evaluated grid-based ANN beamforming. Various researchers simultaneously proposed this method during the period of the thesis. The elegance of supervised learning methods in aeroacoustic testing is that the setup does not change during experiments, so the training must be only performed once before the experiment, and results can be produced efficiently during the experiment in situ. While the method quickly advanced in terms of ANN sizes and focus grid resolution, it proved difficult to interpret the results since there did not exist a rigorous definition of metrics that assess the result's quality.

This thesis introduced several metrics that enable an interpretation of the sparse results that comprise classification and regression errors. Here, the classification can only be assessed implicitly based on the estimated source strength. The thesis surveyed different architectures and proposed several input and output designs, of which a complex-valued ANN in combination with a logarithmic normalization performed best. The under-performance of the absolute number casting may be because the mapping is not holomorphic. The increasing sparseness on an increasingly dense focus grid was partially overcome using a weighted loss, but the results still degraded with increasing focus point resolution.

The architecture inherits all downsides of grid-based imaging methods, as it is difficult to handle multiple source types at once, suffers from aliasing, and does not scale well for real-world focus grid sizes. The ANN is supposed to learn the inverse, ill-conditioned propagation operator, a sub-optimal task for ANNs. It also suffers from the problematic mapping from distributed sources on focus points and spatial aliasing. Furthermore, the result is a high-dimensional map in which real sources and their spectra must be identified. Due to the above reasons, this thesis sees limited use cases for grid-based ANN beamforming and recommends transitioning to gridless methods.

7.1.5 Gridless ANN beamforming

Gridless ANN beamforming results in a set of unordered predicted sources and, thus, requires a permutation invariant error. GO is permutation invariant because it solves the forward problem, i.e., GO estimates a CSM based on the predicted sources and uses a MSE between the observed and estimated CSM. However, the loss has local minima. Further, the existence of sources is determined implicitly by their estimated power, similar to the grid-based ANN approach. Thus, this approach should be avoided. Instead, this thesis proposed to predict the set of sources directly. This is known as a tensor-to-set problem and uses a two-step loss function. First, a set member matching must be performed, and then the best match loss is calculated. Here, the loss itself is used to calculate the best match. For multiple source objects, the sets can be efficiently matched using the Hungarian sorting algorithm; for a few sources, calculating all permutations is computationally more efficient. The architecture allows directly including and learning properties, such as an explicitly formulated classification variable. Hence, the classification is no longer implicitly assessed based on the source power like in the grid-based approaches.

The proposed approach fixes the inherent problems of grid-based approaches, such as the discretized mapping of distributed sources and detecting real sources from the resulting beamforming maps. The estimation of a single monopole in a large domain showed that the architecture can accurately estimate its location and spectrum, unlike the grid-based approach. The approach included distance estimation, a difficult problem for beamforming methods due to the limited spatial resolution. Preliminary tests showed that the estimation can be arbitrarily improved with further model training.

The architecture could accurately predict multiple sources' existence, location, and power, but the results showed a significant dependency on the SSR. This dependency was influenced by the total number of sources and microphones, similar to conventional beamforming. The accuracy increased logarithmically with increasing sensors, compared to conventional beamforming, which improves with the inverse square root of microphones. The proposed model showed that the general approach of a permutation invariant loss with a combined explicit regression and classification metric is viable.

The only comparable publication in this field is by Kujawski and Sarradj [71] with accurate spatial resolution and source power estimations for up to ten sources. However, only a maximum $SSR_{\max} = 10$ dB was used (instead of 50 dB for this thesis), with a Rayleigh distribution of the source strength (instead of a uniform distribution for the PSD). Further, sources are located on a plane parallel to the array (instead of perpendicular). Thus, this thesis's problem is drastically more complex to solve with beamforming.

Dropout was introduced in the architecture to make it robust towards overfitting and ensure that all frequencies are used to learn the source location. Since a regression task is performed, dropout must be used not only during training but also during the inference. Dropout effectively results in fewer sensors during the prediction and, thus, a lower dynamic range. Since modern arrays use many microphones, dropout offers a unique solution to the "black box" machine learning problem. The problem is that machine learning models can predict arbitrary results under unpredictable circumstances. Dropout allows the generation of multiple results for different active sensor pairings. Since

the inference is computationally fast, many different results can be generated to obtain statistically sound predictions and reduce the risk of observing an outlier prediction, e.g., caused by a defect sensor.

At this point, it must still be determined why the ANN only works within a limited dynamic range. Due to the limited SSR in Kujawski and Sarradj's work, it is unclear if the model could resolve sources at a lower SSR. They use a subspace approach, decomposing the CSM into its eigenvalues and eigenvectors before beamforming. This might be a viable approach for noise-free environments so that the sources are separated prior to ANN beamforming with conventional machine precision. However, in noisy environments such as closed wind tunnels, the eigenvalues are dominated by flow noise, so subspace methods generally do not work. Further, it is unclear why an architecture should predict multiple sources at once if the subspace approach separates the total CSM into individual source CSMs that can be processed sequentially.

Since the proposed model is small, it may be possible to improve further the dynamic range with advanced architectures such as transformers, as successfully employed by Kujawski and Sarradj, and throughout the machine learning community for other tasks. Compared to Kujawski and Sarradj's model, the proposed architecture trains fast (10 min versus 60 h).

Like generalized frequency Global Optimization, the proposed approach can be extended to complex sources by adding more regression variables, such as a dipole spectrum and orientation. Additional classification variables can be used with cross-entropy for multi-class classification and mask the loss for the regression variables if the source type is absent.

7.2 Regions Of Interest

This thesis presented two methods to detect sources and extract their spectra from sparse beamforming maps. The methods were developed and evaluated on real-world wind tunnel experiments since aeroacoustic experts only need support identifying sources in maps of complex, ambiguous data. The drawback of this choice is the lack of a ground truth to quantify the results with a related metric. Thus, the results are only discussed qualitatively by comparing them to each other, their consistency, and the literature. Additionally, the results of the generic dataset are discussed quantitatively with known source distribution, location, and emission power.

7.2.1 SIND

SIND assumes that compact acoustic sources appear spatially normally distributed in sparse beamforming maps. Note that while SIND is very similar to GMM, GMM (with an exponential kernel) fails to reproduce the results of SIND. This is because of the high noise level, the arbitrary domain borders (which randomly cut parts of the source distributions), and some distributions that violate the Gaussian assumption (such as line-like sources on the slat). An additional problem poses the manual definition of the number of expected clusters and its strong influence on the cluster outcome.

SIND correctly identified point-like sources such as slat tracks, strakes, flap tracks, or the wing tip. It also identified overlapping sources like the flap side edge or point-like sources embedded in distributed sources such as the nacelle and the slat tracks in the inner slat region. It profits from stacking the histograms of multiple measurements at different Mach numbers and angles of attack to increase the sample size for the histogram, yet fails to recognize sparsely distributed source blobs with no clear midpoint. Wind tunnel noise is a prominent example of this, as this source is projected on different parts of the image with increasing angle of attack due to the mismatched focal plane.

SIND can be efficiently employed on datasets of any size, which makes it a viable candidate for 3D source identification in the future, where larger arrays and increased processing power will result in more detailed, high-resolution beamforming maps. The results on the Embraer model already showed a drastic improvement in resolution over the Do728 and A320 experiments where SIND extracted clean spectra compared to the degenerate Do728 and A320 spectra.

SIND is robust against variations of the introduced thresholds and, thus, is consistent with the expert out of the loop. Furthermore, the introduced change only the selection of the clusters, but not the clusters themselves, as opposed to GMM. The source positions on the two similar airframe models are consistent and correlate to the blobs in the underlying source-part histogram. The correct identification of line-like sources, such as the slat, needs to be improved for this approach. Combined with CLEAN-SC, line-like sources' source-parts do not reassemble normal distributions. SIND tends to wrongly identify these as multiple point-like sources due to its distribution assumption in combination with CLEAN-SC processing. However, the airframe datasets showed that SIND's normal distribution approach was suited for most sources. A second distribution more suited towards fitting line-like sources is of interest for future improvements. Using DAMAS over CLEAN-SC and the analysis of aeroacoustic line sources such as leading and trailing edges might provide a more suited starting point for this endeavor. SIND completely ignores the predicted source-part's power in its current implementation. Since the resulting spectra are expected to be smooth in a mathematical sense, this information could be potentially used additionally to the spatial criterion, as shown with the SIHC method.

7.2.2 SIHC

SIHC does not assume a predefined source distribution. Instead, it learns the underlying source distribution from the presented data using the established clustering algorithm HDBSCAN. This requires the expert in the loop, which means a threshold has to be determined manually to give accurate results. The threshold, the minimum number of source parts for a cluster to form, can be roughly estimated based on the number of frequency bins in a spectrum. Based on the threshold, HDBSCAN can form sub- and super-clusters. Thus, the expert can iteratively obtain a desired clustering result. This thesis presented several novel visualization methods for beamforming and source identification, which can aid the expert in judging if the clustering outcome approximates the true source distribution well.

Because of the additional frequency and SPL information, SIHC has the potential to separate spatially overlapping sources, such as slat tracks and slats. On the one hand, it clustered the inner slat

and the flap side edge to single sources for which the SIND solution is superior. On the other hand, it was able to identify sources containing source-parts that are too far scattered around the map to be identified by SIND, such as spurious noise sources that are not located on the wing. This is an advantage, as these sources originate from the wind tunnel and steering vector III, and an early in situ detection during test measurements can potentially help to find and eliminate them.

7.2.3 Comparison of both methods

Despite the similar identified source regions, SIND's estimation of individual source positions is more refined than the SIHC solution. Both methods identified the individual slat tracks (except for the A320 inner slat), where two slat tracks exist, embedded in a distributed high-frequency noise source belonging to the Krüger slat. Both methods identified the strakes, the wing tip, and the flap tracks on the Do728, but SIHC did not identify the outer flap track on the Do728 and A320. The same is true for SIND and the Embraer model. The source analysis showed that the outer flap track is quiet compared to other sources and is only statistically deduced by SIND when simultaneously analyzing multiple maps at different angles and Mach numbers. Its reconstructed spectrum is very degenerated, so this issue can be attributed to the SNR of the beamforming process and CLEAN-SC.

SIHC also clustered the inner slat region of the Do728 to a single ROI, the nacelle region of the A320, and Do728's outer slat edge of the A320 and Do728. This thesis analyzed the Do728 and A320 flap side edge and a Do728 slat source to evaluate the ROI quality. While the source-parts of the flap side edge form two overlapping normal distributions, SIHC identified a single, combined source. However, the flap side edge is composed of multiple spatially distributed aeroacoustic source mechanisms [65, 31] and showed that its spectrum is driven by at least two, confirmed by independent studies [17]. Thus, the SIND result is superior to the SIHC result. The exemplary Do728 slat source showed that the low Strouhal number scaling tones are a distributed line source superimposed with point-like slat track sources that scale over the Helmholtz number at high frequencies. While SIND identified most of the slat sources as point-like sources between the slat tracks, it could not assign the low-frequency source-parts to the slat located at the slat track positions. Since SIHC has the additional SPL and frequency information of each source-part and had no prior assumption of the source distribution, it could assign the source-parts of overlapping sources to the correct sources in this case. Thus, the SIHC result is superior for the slat sources, especially at low frequencies.

Both methods identify similar ROIs with different advantages and disadvantages to wind tunnel airframe experiments. SIHC works well for small datasets (e.g., a single angle of attack and few Mach variations) with little statistical noise. It is advantageous for exploring the dataset because a single threshold drastically changes the ROI outcome. Generally, density-based clustering methods fail to separate clusters when too much noise is present that connects the clusters, so-called bridge points. Consequently, SIHC yields better results when decreasing the Welch block size, which increases the number of averages and results in less statistical noise but a lower frequency resolution.

SIND works well for noisy datasets with high-resolution spectra (large Welch block sizes) and yields stable results mostly independent of the selected thresholds and profits from large datasets, i.e., sim-

ultaneously clustering multiple parameter variations. Multiple parameter variations ensure that each source is observed multiple times. Thus, the total number of source-parts increases, which allows the detection of sources that are not detectable in single noisy beamforming maps. Since SIND's thresholds only limit the processing time and drop sources after the identification, increasing or decreasing these values will not change the outcome of the remaining sources. This makes the results reproducible and the method robust.

SIHC is well-suited for an iterative process with the expert in the loop that can be fine-tuned to the desired outcome, while SIND requires no tuning to generate stable results and can be employed autonomously. The quality of SIND's results decreases with smaller datasets (fewer measurements) as the number of source-parts decreases. SIHC's results improve as it has to handle less statistical noise and vice versa. In specific cases, when two sources overlap spatially but can be distinguished based on their spectrum, such as slat sources, the SIHC method has a clear advantage over SIND, which naively assigns the source-parts based on their spatial probability alone. While dense source distributions with bridge points are problematic for SIHC, it can detect sparse source distributions without a clear midpoint, which SIND cannot detect (it relies on a well-localized distribution center as a starting point during the iterations). Thus, SIND's results heavily rely on a well-resolved beamforming map but can handle statistical noise due to insufficient CSM averages. SIHC, on the other hand, can, to some degree, correctly assign the source-parts that are far away from their corresponding source due to a low beamforming resolution based on their SPL and frequency information. Thus, it can compensate for the deficiencies of conventional beamforming and CLEAN-SC. However, its results suffer from statistical noise, requiring long measurement times or small block sizes for sufficient CSM block averaging. Combining both methods by first employing SIND to extract the high-density clusters and then performing SIHC on the remaining source-parts is possible.

The ability to identify sources quantitatively and estimate their position accuracy and acoustic power was evaluated on the generic dataset with ground truth. This dataset provides a limited source identification challenge, consisting only of three spatially separated monopole sources. The challenging aspect is the equidistant array spacing, which results in strong side and grating lobes. These are visible in the CLEAN-SC maps at high frequencies. Also, the array resolution provides a separation challenge at low frequencies. These limitations resulted in CLEAN-SC failing to reconstruct the beamforming map at frequencies at low frequencies and estimating the correct PSD at high frequencies.

Both proposed methods identified the three sources in the CLEAN-SC maps with similar spatial accuracy. Out of the total spectrum range, both proposed methods could reconstruct around 2/3 of the spectrum. Most of the failed reconstructions happened at a low SNR. These are caused not by the proposed methods' misidentification of source-parts but by CLEAN-SC's failure to predict correctly deconvolute the beamforming map at low SNR and low frequencies.

Performance-wise, SIND is superior to SIHC and can be employed on datasets of any size. It does not cluster the points directly but estimates only the underlying distribution from a histogram, which can be calculated very efficiently for structured grids used in conventional beamforming. Additionally, both methods provide a confidence estimation for each source-part belonging to all sources. While

the manual definition of ROIs determines if a source-part is part of a source, this information is valuable for an expert in estimating the reliability of the source spectra. Together, both methods cover the automatic source identification and spectrum generation from single, sparse, low-resolution beamforming maps to high-resolution beamforming maps, including multiple parameter variations with speed and accuracy that are unmatched by human experts.

7.3 Expert Decision Support System

This thesis presented the EDSS CRAFT, which clusters sources in a feature space that corresponds to physical properties, to help the expert analyze the data and gain new insights into aeroacoustic source mechanisms.

7.3.1 Manual classification

To evaluate the quality of the features and CRAFT, the thesis author labeled the presented datasets manually. Sources can gradually shift their spectrum shape with an increasing Reynolds number and feature multiple frequency regions with different mechanisms. Thus, this thesis heavily relied on meta-information for the manual source type identification, such as the source position. Since the proposed method was designed to overcome this problem, the resulting metrics should be evaluated cautiously. Also, the labeling was not performed by independent researchers.

To assess the combined quality of the feature space and the manual labels, the dimensionality reduction UMAP was performed, visualizing the data in two dimensions. The distance between the source groups, distribution density, and connections relate well to the manual classification. Also, the source type distribution emphasizes the problem of manually labeling the sources based on their spectra because source types gradually transition from one category to another in the feature space, e.g., slat cove noise that gradually transitions to slat track noise. The projected source distribution showed that the source labels are reasonable since the sources form groups in the projection, and the manual labels correspond well to the location of the members within their group. This shows that both the feature space and the labels are appropriate to describe the sources in the presented dataset.

7.3.2 Aeroacoustic features

CRAFT is built on the assumption that an aeroacoustic source is driven by a mechanism that reveals its nature over the variation of the Mach number. The aeroacoustic self-similarity theory showed how the variation of the Mach number reveals the physical mechanism of a source. The limitation of this very general and strong assumption is that any changes in the source mechanism over the Mach number are neglected. However, the resulting standard deviations from the self-similarity optimization showed at high Helmholtz numbers that sources can exhibit a substantial Mach dependency, not captured by the proposed method. The Embraer data suggests that sources such as a cavity can exhibit a Mach number dependency even at a constant Reynolds number based on their aeroacoustic mechanism, which contradicts the initial EDSS self-similarity assumption. Reasons why some sources show this violation of self-similarity are up to debate and may include resonance effects that are coupled to the flow speed and the thickness of the shear layer depending on the Mach number

when the object is small, such as the strake. These are exceptions to the general observation that self-similarity holds for nearly all observed sources.

Based on this assumption, this thesis proposed various features that are supposed to formalize aeroacoustic properties and are robust towards degraded spectra, typically resulting from CLEAN-SC. This is necessary since the source spectra are often unreliable at low frequencies or contain missing values, as discussed above for conventional beamforming, CLEAN-SC, and the SIND/SIHC methods. This is especially problematic since their dominant source power, which is preferred in many features, occurs at these low frequencies. It is neither claimed that the list of the properties is complete and covers all acoustic phenomena, nor is it claimed that the feature calculation is robust in all data scenarios. Alternative feature definitions may outperform the ones proposed in this thesis. In other scenarios, more features may be necessary to describe time-dependent phenomena, such as rotor noise, jet noise, or landing gear noise, to name a few. However, since the proposed features are based on fundamental aeroacoustic laws, they are assumed to capture the essence of any aeroacoustic spectrum. Since the features were originally designed for the Do728 dataset but worked very well on the A320 and Embraer datasets (which showed similar sources), they are assumed to generalize well on airframe noise experiments.

The thesis proposed a definition of how self-similar the source spectra are over a given frequency type, i.e., the Helmholtz and Strouhal numbers. The feature did not achieve satisfying results for several source types, such as slat noise. The reason for this is the substantial decay in sound power over the frequency of aeroacoustic noise due to its turbulence-induced origin, which dominates the correlation stronger than the local spectral features such as tonal peaks or humps. Additionally, while the slat tones are somewhat self-similar, as the normalized frequency of the tones does not change, their intensity does over Mach number. The increased Mach number acts as an amplitude modulation filter on the spectrum so that self-similarity, as defined, is violated. This behavior is not captured in the proposed definition and degrades the results.

The true Strouhal number definition is insufficient for aeroacoustic source spectra since it does not scale sources well. Thus, this thesis introduced normalized frequency, a generalization of the Strouhal and Helmholtz numbers. This is the first time this phenomenon was described, but it is too complex to be fully covered within the scope of this thesis. More research is necessary to understand the underlying acoustic mechanisms and the implications on wind tunnel measurements. It is presumably caused by local flow acceleration and deceleration around the complex object, so the aeroacoustic mechanism is driven by the local flow instead of the free flow Mach number. This local acceleration itself must be Mach-dependent. Otherwise, it would not alter the scaling exponent. While the presented airframe models are somewhat similar, their detailed geometries are very different. The presented data showed that the trailing flap side edge depends more strongly on the Mach number than a true Strouhal number and that slat cove tones depend weaker on the Mach number for all models. It is of interest for future research if the modification exponent generalizes well for source types, as this thesis' observations suggest.

After obtaining the estimated self-similarity (i.e., Helmholtz-like and Strouhal-like scaling) modification exponent, two approaches can calculate further properties. The first approach is to calculate features based on the best self-similarity estimation, i.e., the Helmholtz or Strouhal numbers. The second approach is to calculate features over both the Strouhal and Helmholtz numbers. The advantage of the first approach is that it reduces feature redundancy and is closer to what the aeroacoustic expert is used to do. However, this thesis showed that aeroacoustic spectra can include multiple mechanisms that exhibit different self-similarities, such as the Do728 and A320 slat tracks. At this point, it is unclear whether this behavior is caused by the insufficient spatial resolution of beamforming and the source identification methods or if it is driven by a complex aeroacoustic mechanism such as jet noise, where the low frequencies are well-known to scale over the Strouhal number, while high frequencies scale over the Helmholtz number due to source coherence and propagation effects such as convective amplification [89, 90, 91, 49]. Note that while this behavior was not observed for the high-resolution Embraer experiment, the occurring Helmholtz scaling frequencies lie outside the frequency range due to the smaller model size. Thus, this thesis employed the second approach and calculated all features for both the Strouhal number and Helmholtz number independently.

This thesis presented a method to determine the power exponent for a separate scaling over the Strouhal and Helmholtz numbers. The literature traditionally proposes to use linear regression on the OASPL, but as discussed above, the aeroacoustic spectra show a substantial decay in power over frequency. Since CLEAN-SC acts at low frequencies like a cut-on filter in absolute frequency, this results in a different cut-on frequency for sources that scale over the Strouhal number. Thus, the relative OASPL is larger at increasing Mach number as the cut-on frequency is lowered. Thus, this method should be avoided for deconvoluted beamforming results. The proposed calculation method is still sensible to degenerated spectra, especially since the assessed Mach number range is typically small but yields stable results for most sources. Since the resulting feature is an exponent, it may vary significantly with little influence on the observed scaling and cause significant variances within source types, which can exceed the variances between different source types. Generally, many Mach numbers and a large Mach number range are beneficial to assess the self-similarity of the spectra. However, the Embraer results showed that high-resolution arrays and reliable spectra result in reliable power exponents, where the standard deviation between the scaled spectra is very low, even for a few Mach numbers.

A definition for the tonality of the spectra was introduced, resulting in several features. The tonality features are highly correlated and belong to the same branch of the feature hierarchy. At this point, it is unclear if fewer features with less correlation can capture the tonal behavior. Also, the features are based on the statistical properties of the tones and yield unstable results if only one strong tone exists, such as for the trailing flap side edge and strake.

This thesis introduced a method to detect if sources spatially move with increasing Mach number if they are point-like or line-like. The results suggest that the source movement feature currently estimates the position uncertainty instead of the true movement of sources (e.g., downstream moving vortex detachments). The source movement, shape, and compactness are mostly correlated and belong to the same branch in the feature hierarchy. This suggests that they are subjected to an

underlying, yet unknown, phenomenon. When comparing different datasets, the variance due to the different array resolutions typically exceeds the variance between the source types. Thus, these features should only be used to compare sources within one dataset.

Overall, the feature results showed that they strongly depend on the quality of the spectra. An interesting effect is that, while self-similarity holds for most sources, a continuous change of the self-similarity parameters was observed over increasing angle of attack and increasing Reynolds number. While the latter may be related to actual changes in the sources' aeroacoustic properties, a change in the angle of attack should not alter a source's self-similarity. The change in the generalized frequency exponent may be caused by a further accelerated flow due to the change in the angle of attack, but the reason for an altered Mach power exponent is unknown. A possible explanation might be a change of the source's directivity with increasing Mach number due to the aforementioned source coherence and convective amplification since beamforming estimates the sound power of a source from a small angular range (technically, the average sound intensity within the array's area is estimated and not the sound power).

7.3.3 Clustering

This thesis used HDBSCAN to cluster the sources without any prior assumption of the expected number of source types or source distributions in the feature space. For the Do728, the resulting clusters related well to the manual classification. This is a promising result since the feature space not only captures enough information to separate most of the source types, but the variance between the different source types is also greater than the variance of a phenomenon that is not of interest (e.g., sources could be clustered based on their loudness and not based on their physical mechanism). Since the manual source classification was often ambiguous and not all clusters related to the labels, the exact accuracy of CRAFT and the reason for the wrong cluster choices is up for debate. The quantitative evaluation of the Do728 clustering was based on the introduced confusion matrixes and, thus, dependent on the manual determination of correct cluster estimations. The accuracy for the Do728 is 77.04%. The clustering accuracy was improved to 91.45% using a lower confidence threshold $t_C \geq 0.1$ by ignoring predictions below the threshold. This shows that wrong clusters are often chosen with low confidence so that the expert can use high-confidence clusterings as a guideline for the different source types and their representative spectra.

The usefulness of the chosen clusters can only be evaluated qualitatively based on their consistency, ability to separate source mechanisms from each other, and ability to identify sources with a spatially misleading location. Regarding the Do728 slat region, CRAFT showed that typical slat sources (slat cove and slat tones) distinctly differ from slat track sources based on the cluster hierarchy. Occasionally, slat tones appeared with decreasing probability towards high Reynolds numbers. Often, they occurred at the slat positions but at different angles of attack (slat noise appeared mainly at low angles of attack). CRAFT was able to separate these slat-related phenomena very well.

In comparison, multiple source types were clustered into a single cluster (typically the last cluster). Decreasing the sample size for HDBSCAN results in a separation of these sources eventually, but also in numerous sub-clusters for the other source types, especially the slat / track sources. The

reason for this is the substantial mismatch of expected members per cluster. While there are ten slat tracks on the Do728, only one strake is present, which is silent at most angles of attack. The expert should keep this in mind when evaluating the clustering results, especially for clusters further down the hierarchy branches.

Additionally, the clustering probability of HDBSCAN can be used to study the sources further. The clustering probability can be used to identify ambiguous sources and sources that are prominent examples of a cluster. If sources showed an ambiguous behavior so that the probability for more than one cluster was dominant, both clusters would be typically correct clustering choices based on the aeroacoustic behavior. An example is the Krüger slat, which showed an elevated probability of belonging to the clusters associated with the slat resonance (at the Krüger slat), but also the leading flap side edge (which features strong Helmholtz number scaling tones), the slat tones (Strouhal number scaling tones), and a cluster that includes both slat resonances and the slat gap (also driven by Helmholtz number scaling tones).

For the A320, CRAFT's clusters did loosely correlate to the manually classified source types, and thus, the accuracy of the result is more challenging to evaluate. Readers are encouraged to interpret the confusion matrix results based on their experience. The evaluation based on the proposed confusion matrix resulted in an accuracy of 61.52%. The lower clustering accuracy can be attributed to the larger feature variance compared to the Do728 sources. This is mainly caused by the worse spectra quality due to the smaller microphone array employed for the measurements, fewer Mach numbers, and smaller Mach number range.

Generally, the clustering results strongly depended on the feature quality, which depends on the spectra quality. Thus, dominant sources within the dataset were clustered with much more confidence than weak sources. Prominent examples are the flap side edge and the Krüger slat, which were clustered correctly with high confidence. While the 3D beamforming results showed improvements in spatial accuracy and source spectra reconstruction over the 2D results, the array resolution limits its application for the Do728 and A320 datasets. Due to the intensive manual work of classifying the sources and clustering results, the EDSS was not reperformed on the 3D beamforming data, compared to the original publication [48]. For the Embraer experiment no clustering result or additional results over the original publication [8] were presented, due the confidentiality of the data.

7.4 Aeroacoustics

This section discusses the implications of the thesis' results on aeroacoustics. Note that the Do728 and A320 results are obtained for a Reynolds number that increases with an increasing Mach number, while the results of the Embraer model were obtained at a constant Reynolds number. This allows us to separate the effects of a change in Mach number and Reynolds number.

The first observation is that the prominent sources are nearly identical for all three models. The dominant sources are the Krüger slat tracks, the outer slat track next to the nacelle, the vicinity between the slat and the nacelle, the slat between the outer slat tracks, the flap side edge, and with a

strong overall contribution, the slat tracks. Lesser contributions yielded the wing tip, a source next to the slat on the fuselage, and the flap tracks. At increasing angles of attack, the strakes also become a dominant source.

The continuous location of the sources over the frequency indicates that the sources are spatially compact. An exception is the slat between the slat tracks, particularly between the outer slat tracks, related to the low Strouhal-scaling slat cove tones since it shows a continuous distribution similar to the one presented for the synthetic line source model. The B-CLEAN-SC result supports further evidence since B-CLEAN-SC's algorithm tries to enforce spatially compact sources, but the estimated outer slat area is still distributed.

This thesis presented various sources and their similarity spectra. They comprise different aeroacoustic mechanisms with different scaling behaviors, Mach power scaling, and spectral features. Comparing the source types between the models, the strake shows $m = 0.79$ for the Do728, $m = 0.95$ for the A320, $m = 0.78$ for the Do728 slat cove, and $m = 0.72$ for the A320. However, these are obtained at increasing Reynolds numbers over increasing Mach numbers and show a dependency on the angle of attack. For the Do728 and A320, it remains unclear to which degree the increased Reynolds number or Mach number causes the modification exponent. The deviation of the Embraer strake modification exponent $m = 1.01$ from the other models suggests that it is caused by the increase in Reynolds number and not by the increase in Mach number. The small deviation of the Embraer slat cove modification exponent $m = 0.81$ from the other models suggests that the increase in Mach number mostly causes it.

The slat cove tones are caused by Rossiter modes [62], where the peak frequencies depend on the convective Mach number at the cove, which might have a non-linear relationship with the free-flow Mach number. For cavity noise, a slight increase in the Helmholtz number over the Mach number is described in the literature [45] for Rossiter modes, matching the experimental observations. A similar increase in frequency with increasing Mach number is observed for the slat tracks, slat edges, and flap side edges. The Embraer flap side edge source probably corresponds to a leading flap side edge on the Do728 and A320 based on the Helmholtz-like scaling behavior and spectral shape. Trailing flap side edge noise is not present on the Embraer wing. Note that due to the small (31%) and few variations in Mach number in the Embraer dataset, low modification exponents are subject to some uncertainty and may not indicate a deviation of a true Helmholtz number. Thus, the flap side edge, cavity, slat tracks, and slat edges should be regarded as a true Helmholtz-like scaling. For the nacelle region and strake, a true Strouhal scaling is observed, which indicates an acoustic mechanism depending on the free-stream Mach number.

For the power scaling of aeroacoustic noise, the literature proposes M^5 for low frequencies [55] based on 2D source-mechanisms [54], and M^6 for high frequencies because of the dipole character of sources [55]. This yielded a reasonable overall scaling for the broadband SPL of the Embraer model. However, the sources that dominate the total broadband level, and roughly follow a M^5 -law are the slat track sources. Williams [133] proposes that sharp geometrical edges cause these sources and also follow a M^5 -law. Further investigations are necessary to clarify which theory is better supported

by the data. This should be studied using reconstruction algorithms that preserve spatially extended sources such as DAMAS. The slat cove tones strongly depend on the angle of attack [127] and dominate the total SPL at lower frequencies and low angles of attack. However, their power scaling is lower than the slat track broadband sources. This means they will be masked if present at higher Mach numbers, which may explain why we do not experience such tonal noise in real aircraft noise.

The Embraer flap tracks and nacelle scaling exponents exceed M^6 , which might indicate the dipole source mechanism. However, their source power contributes little to the total power at the observed Mach numbers. Hence, the scaling exponents are subject to the uncertainty introduced by CLEAN-SC due to the limited SNR. Similar scaling exponents for the Do728 and A320 are observed for the flap tracks, while the sources at the nacelle are of different origins.

Negative scaling exponents were observed for sources such as the Embraer cavity and the strake, indicating that their power decreases with increasing Mach number. The cavity phenomenon might be due to a growing misalignment of the convective Mach number and the cavity resonance frequency. For the strake, the absolute frequency of the tonal peak increases with increasing Mach number so that the dominant wavelength shrinks compared to the shear layer, which was shown to decrease the source power and lead to spectral broadening [69]. The Do728 showed that strake noise can be composed of two parts, one originating upstream and one originating downstream at its tip, with different scaling behaviors. However, the spatial resolution and SNR of this experiment are too low to obtain reliable spectra to study this phenomenon further.

8 Summary

This chapter provides a summary of the discussed methodologies, such as conventional beamforming, CLEAN-SC, B-CLEAN-SC, GO, and LO, supervised learning beamforming, identifications of sources and ROI, and the employment of an EDSS for automated feature calculation, and clustering of the sources, their results and main findings, and key points from the discussion.

8.1 Beamforming

This thesis showed how conventional beamforming and CLEAN-SC compare against proposed methods custom-tailored to broadband sources. Results were presented for synthetic compact monopoles, dipoles, and partially coherent line sources. Experimental results were presented for a streamlined speaker in an open wind tunnel and a Dornier 728, Airbus 320, and Embraer model in closed wind tunnels.

8.1.1 Conventional beamforming

Conventional beamforming results depend on the steering vector, a normalized Green's function, of which four formulations are typically considered. D. Ernst's steering vector generalization showed that they can either be used to obtain the correct source location or the correct source strength, but never both. While this is an inherent problem to the linear transformation and naïve approach of conventional beamforming, the method is fast and robust towards violations of the spatially compact, incoherent monopole at the same time. While violating the method's assumptions increases the localization and power estimation error, the result is often still sufficient to identify and analyze the source's behavior.

8.1.2 CLEAN-SC

CLEAN-SC is designed to identify spatially compact, incoherent monopole sources. It is robust towards distributed, coherent sources. While the positional estimation of the source suffers from totally coherent sources, partially coherent sources are reconstructed as a point cloud that reassembles the true source distribution fairly well, depending on the frequency and array setup. Depending on the wavelength, a coherent distributed source will create an interference pattern in the resulting sound field, leading to an underestimation of the source strength with increasing frequency. With decreasing frequency, the source appears more and more compact compared to the wavelength so that the error of the estimated power is reduced.

The quality of the CLEAN-SC result strongly depends on the conventional beamforming result, which in return depends mainly on the experimental setup, that is, how many sensors are used, how large the array's aperture is, and the distance between the model and array. Due to the increasing distance to the array, center side lobes at the edges of the focus domain can exceed the main lobe with steering vector \mathbf{III} for 2D planar beamforming and are reconstructed at the wrong position. Further, sources not located within the focus domain still spill their side lobes into the domain, which then

are estimated as sources. This is a problem in closed wind tunnel sections, where the walls are reflective, and strong sources of interference exist. These effects are mostly mitigated with steering vector formulation IV, a 3D focus domain, and a large array so that beamforming is assessed in the near-field of the array, as presented for the Embraer experiment.

8.1.3 B-CLEAN-SC

This thesis introduced B-CLEAN-SC, a variation of CLEAN-SC specifically tailored to broadband sources. B-CLEAN-SC assumes that the location of broadband sources is constant over frequency intervals. For synthetic and experimental wind tunnel data, B-CLEAN-SC outperformed CLEAN-SC at low frequencies. For experimental real data, B-CLEAN-SC also reduced noise throughout the frequency range. On wind tunnel data of a Dornier 728, both methods showed that the source location assumption is valid, improves the spatial estimation of sources, and reduces noise.

The algorithmic difference between CLEAN-SC and B-CLEAN-SC is small. B-CLEAN-SC processes multiple frequencies simultaneously and uses one additional operation per iteration compared to CLEAN-SC. As it requires a lower gain factor, the number of iterations increases inverse proportionally to the gain factor to meet a convergence criterion, which is not performance-relevant. The necessary memory scales linearly with the number of employed frequencies within the interval compared to standard CLEAN-SC, which is not an issue in terms of today's computational capacities. This makes B-CLEAN-SC a viable method for little computational effort but improved results at low and high frequencies.

8.1.4 Global Optimization

This thesis introduced the gridless Global and Local Optimization for acoustic broadband sources, with parameters like the spatial location or source orientation shared for all frequencies. The advantage over the single-frequency optimization process is the increased ratio of equations to unknown variables, the smoothing of local minima in the energy function, which results from the array's point spread function, and the simple process of extracting the source positions and spectra from the results.

While the approach outperformed methods such as CLEAN-SC and standard GO on synthetic data, the results were similar for the generic monopole experiment, with the proposed methods having an advantage in low- and high-frequency regions, similar to B-CLEAN-SC. The main difference is the handling of noise and the violation of the monopole assumption due to the speaker. While CLEAN-SC results in strong noise scattered around the map, GO includes these violations in the estimated source spectra, which results in an error in the predicted sound power. Thus, naïve beamformers seem to be more forgiving towards violated assumptions, but GO provides the remaining energy to indicate the violation's severity.

One challenge for broadband Global Optimization is correctly determining the number of source objects. It was shown that an overestimation is a valid approach to finding all sources or to accounting for properties not included in the Green's functions, such as reflections or distributed sources. Then, multiple source objects approximate a single source. However, they can be identified based on their

spatial distance and integrated much simpler than CLEAN-SC or standard Global Optimization results.

GO is computationally expensive, and global optimizers are not guaranteed to find the global minimum. However, the problem reduces to Local Optimization by using reasonable initial locations and multiple frequencies, which reduces local minima in the energy function. A reason to perform Local or Global Optimization after obtaining reasonable initial values might be to identify source properties neglected by grid-based beamformers, such as multipoles and distributed sources. The thesis proposed a synthetic multipole problem, which was estimated with low errors.

8.1.5 Supervised learning beamforming

This thesis analyzed the capabilities of neuronal networks for beamforming using supervised machine learning. Typical challenges that arise from the standard method, which maps the CSM to a focus point vector, like conventional beamforming, are, first and foremost, the complex input and CSM tensor dimensions and the sparsity of the resulting output vector. Several proposed evaluation metrics showed that a weighted loss and a vectorized upper triangular matrix of the CSM are promising components for a successful machine learning model. At the same time, the neuronal network learns the inverse of the propagation operator, which is ill-conditioned and rarely invertible, which leads to unsatisfactory results.

This thesis proposed a novel gridless architecture similar to GO. Instead of predicting sources on a fixed grid, few source objects are predicted, including their spatial location and spectrum. The advantage of this method is that the output vector is small (a few sources times the number of properties, e.g., source power and source location) compared to the grid-based approach (typically several thousand grid points for 2D grids and several million points for 3D grids). The architecture demonstrated a high classification accuracy, a low positional error, and a low spectrum estimation error for dominant sources on a problem with up to three sources. The error increased with decreasing source strength. Weak sources were insufficiently estimated below a ratio of approx. 10 dB compared to the dominant source. Thus, the permutation invariant loss with an explicit classification and regression metric works in general, but the results suffer from low Signal to total Signal Ratios (SSR), compared to CLEAN-SC and Global optimization where typically SSR of approx. 30 dB can be achieved.

8.2 Regions Of Interest

Identifying sources manually, defining ROI, and extracting their spectrum from beamforming maps is difficult and time-consuming. This thesis presented the two methods SIND and SIHC, which automatically detect aeroacoustic sources in deconvolved beamforming maps. They identify underlying source distributions and, thus, allow for the automatic determination of ROI. These are the first automated approaches to identify sources and generate corresponding spectra from sparse beamforming maps without prior information about the source locations and the number of sources. Both

methods cover various real-world scenario use cases, from single measurements with sparse source distributions to high-dimensional datasets with parameter variations, and can be combined.

The resulting ROI and spectra for exemplary sources showed that SIND is superior in separating dense, overlapping source regions, while SIHC is superior in assigning the source-parts to the correct sources. This results in an improved reconstruction of spectra at low frequencies, typically scattered around the whole map due to the shortcomings of conventional beamforming and CLEAN-SC. A three-dimensional implementation of SIND in combination with steering vector IV showed improved abilities to separate sources since the 3D source distributions are no longer projected on a 2D plane, so the sources show less overlapping. Thus, a 3D domain of interest is advantageous if the array's resolution is sufficient. The elegance of SIND and SIHC is that they can be performed on any sparse beamforming map. Thus, the underlying beamforming methods can be improved (e.g., with HR-CLEAN-SC, B-CLEAN-SC, or DAMAS) without changing the source identification process.

8.3 Expert Decision Support System

This thesis presented the Expert Decision Support System Clustering source based on Aeroacoustic Features (CRAFT), which aims to identify and analyze acoustic sources from beamforming maps automatically. CRAFT uses clustering to group multiple sources based on their aeroacoustic properties to reveal underlying physical mechanisms and guide the acoustic expert in identifying and analyzing the sources correctly. The general assumption of CRAFT is that the physical mechanism of a source can be determined by the change of its properties over the Mach number, also referred to as self-similarity. Thus, measurements at multiple flow speeds are required. The results showed that self-similarity holds for nearly all airframe sources, except for slat tones and the Krüger slat resonance.

This thesis introduced a feature set that expresses aeroacoustic properties as a combination of single numerical values. This reduces the complex acoustic properties to a data space that both machine and expert can understand. The features are independent or averaged over the spectra at different Mach numbers, which enables CRAFT to compare and cluster sources from different experiments, typically obtained at different Mach numbers. The features directly correspond to meaningful physical properties. The results for the different experiments showed that the features are robust towards degenerate spectra, but their estimation improves with improved spectra quality.

Exemplary source spectra and corresponding manual labeling of the sources were presented to evaluate the data further. The manual labeling of the sources is often ambiguous due to degenerated spectra, multiple source mechanisms, or Reynolds number-dependent trends. Despite the ambiguous manual source type identification, the source types formed distinguishable distributions in the introduced feature space, which was visualized with a Uniform Manifold Approximation and Projection for Dimension Reduction. Thus, the feature space captures enough variance between the proposed source types, and the manual labeling corresponds to the observed feature variance.

The established Hierarchical Density Based Clustering for Applications with Noise algorithm was used to group the sources in the introduced feature space, which did not include meta-information

such as the source position, the angle of attack, or the Reynolds number. Thus, the clustering result was purely based on the aeroacoustic properties of the sources. The estimated clusters corresponded mostly to the manually identified source types, were consistent between the datasets, and provided the necessary information to identify sources that behaved atypically for their spatial locations. For example, it allowed the correct identification of the different source types located on a single slat position at different angles of attack, such as slat cove tones. The clustering also provides a confidence estimation. Sources are mostly clustered wrongly by CRAFT at low confidence, while the clustering at high confidence is mostly correct. Experts can discard predictions below a confidence threshold, increasing the prediction accuracy.

8.4 Aeroacoustics

The acoustic analogies propose mainly dipole and quadrupole sources that scale around M^6 to M^8 . In contrast, dipole line sources scale at M^5 and monopoles at M^4 . Sources scaling over the Strouhal number can be attributed to free-flow effects and turbulence-induced noise, whereas sources over the Helmholtz number indicate resonance phenomena and propagation effects such as spatially distributed source coherence and radiation modes. The scaling theory is based on the assumption of self-similarity, which assumes that the observed phenomenon changes continuously over the flow speed variation. However, a normalization of the observed phenomenon reveals that the underlying mechanism has not changed.

Self-similarity holds for nearly all observed acoustic airframe phenomena. Exceptions are the strake on the Do728, the cavity on the Embraer model, slat tones on the Do728 and A320, and the Krüger slat on the Do728 at low angles of attack. The self-similarity analysis showed that sources either scale over the Helmholtz number or around the Strouhal number. Some sources, such as the slat cove-induced tonal noise at low frequencies, are self-similar over a by M^m , $m \approx 0.8$ normalized frequency, which indicates that the phenomenon depends on a convective Mach number that is slower than the free flow Mach number, matching the Rossiter modes theory. Other sources, such as the trailing flap side edge, show an increased Mach number dependency, such as the trailing flap side edge with $m \approx 1.2$ for the Do728, which indicates a locally accelerated local flow. This observation was described for the first time in the literature, presumably because sources are typically evaluated isolated in generic experiments where the local Mach number is assessed or because of the lack of capabilities to investigate a large number of sources systematically.

The power scaling exponent of the sources showed deviations over the different experiments for similar source mechanisms. These can be attributed to the small sampled Mach number range and the degenerate spectra, but also possible aeroacoustic mechanisms. The continuous shift of the exponent over parameters such as the angle of attack and Reynolds number indicate the influences of an underlying phenomenon. A possible explanation might be that beamforming observes the sources only at a small angular range so that convective amplification and source directivity are neglected but may have an unpredictable influence on the scaling. To address this issue, further testing with larger arrays from which subarrays are sampled to derive a source directivity is necessary.

8.5 Thesis conclusion

This thesis introduced the necessary tools to advance broadband beamforming, either with conventional optimization methods such as Global and Local Optimization or statistical optimization and machine learning means. Since conventional beamforming and deconvolution methods such as CLEAN-SC are still regarded as state-of-the-art for wind tunnel applications, this thesis provides with B-CLEAN-SC, SIND, and SIHC Clustering the necessary tools to identify sources in sparse beamforming maps and extract their corresponding spectra.

For decades, the analysis and comparison of the resulting spectra depended on the often implicit knowledge of the aeroacoustic expert. This thesis introduced features that capture that implicit knowledge of aeroacoustic properties in explicit formulas, which are robust towards degenerate spectra, typically resulting from beamforming and deconvolution methods. The result is a machine-readable high-dimensional feature space independent of the observed model and the employed Mach numbers. Thus, different experiments are comparable by both experts and machines, and experts can interpret the physically meaningful features. The introduced Expert Decision Support System allowed for the first time to analyze complete datasets with hundreds of configurations and thousands of individual sources. It was able to determine meaningful source clusters that relate well to manually determined categories and proved fast and reliable during experiments for the in situ detection of spurious noise sources.

Bibliography

- [1] Milton Abramowitz. *Handbook of Mathematical Functions, With Formulas, Graphs, and Mathematical Tables*. Dover Publications, Inc., 1974.
- [2] T. Adali, P. J. Schreier, and L. L. Scharf. Complex-valued signal processing: The proper way to deal with impropriety. *IEEE Transactions on Signal Processing*, 59(11):5101–5125, nov 2011. doi:10.1109/tsp.2011.2162954.
- [3] Charu C. Aggarwal, Alexander Hinneburg, and Daniel A. Keim. On the surprising behavior of distance metrics in high dimensional space. In Jan Van den Bussche and Victor Vianu, editors, *Database Theory — ICDT 2001*, pages 420–434. Springer Berlin Heidelberg, 2001. doi:10.1007/3-540-44503-X_27.
- [4] T. Ahlefeldt. Aeroacoustic measurements of a scaled half-model at high reynolds numbers. *AIAA J.*, 51(12):2783–2791, 2013. doi:10.2514/1.J052345.
- [5] T. Ahlefeldt. Microphone array measurement in european transonic wind tunnel at flight Reynolds numbers. *AIAA J.*, 55(1):28–48, 2017. doi:10.2514/1.J055262.
- [6] T. Ahlefeldt, L. Koop, A. Lauterbach, and C. Spehr. Advances in microphone array measurements in a cryogenic wind tunnel. In *Berlin Beamforming Conference*, February 2010. URL: www.bebec.eu/fileadmin/bebec/downloads/bebec-2010/papers/BeBeC-2010-03.pdf?origin=publication_detail.
- [7] Thomas Ahlefeldt. Microphone array measurement in european transonic wind tunnel at flight reynolds numbers. *AIAA Journal*, pages 1–13, oct 2016. doi:10.2514/1.j055262.
- [8] Thomas Ahlefeldt, Daniel Ernst, Armin Goudarzi, Hans-Georg Raumer, and Carsten Spehr. Aeroacoustic testing on a full aircraft model at high reynolds numbers in the european transonic windtunnel. *Journal of Sound and Vibration*, 2023. doi:10.1016/j.jsv.2023.117926.
- [9] Thomas Ahlefeldt, Stefan Haxter, Carsten Spehr, Daniel Ernst, and Tobias Kleindienst. Road to acquisition: Preparing a MEMS microphone array for measurement of fuselage surface pressure fluctuations. *Micromachines*, 12(8):961, aug 2021. doi:10.3390/mi12080961.
- [10] Thomas Ahlefeldt and Lars Koop. Microphone-array measurements in a cryogenic wind tunnel. *AIAA Journal*, 48(7):1470–1479, jul 2010. doi:10.2514/1.j050083.
- [11] Thomas Ahlefeldt and Jürgen Quest. High-reynolds number aeroacoustic testing under pressurised cryogenic conditions in PETW. In *50th AIAA Aerospace Sciences Meeting including the New Horizons Forum and Aerospace Exposition*. American Institute of Aeronautics and Astronautics, jan 2012. doi:10.2514/6.2012-107.
- [12] Roj K. Amiet. Correction of open-jet wind-tunnel measurements for shear layer refraction. In *Aeroacoustics: Acoustic Wave Propagation; Aircraft Noise Prediction; Aeroacoustic Instrumentation*, pages 259–280. American Institute of Aeronautics and Astronautics, jan 1976. doi:10.2514/5.9781600865206.0259.0280.
- [13] Mihael Ankerst, Markus M. Breunig, Hans-Peter Kriegel, and Jörg Sander. OPTICS. *ACM SIGMOD Record*, 28(2):49–60, jun 1999. doi:10.1145/304181.304187.
- [14] Jérôme Antoni. A bayesian approach to sound source reconstruction: Optimal basis, regularization, and focusing. *The Journal of the Acoustical Society of America*, 131(4):2873–2890, 2012. doi:10.1121/1.3685484.

- [15] Simon Arridge, Peter Maass, Ozan Öktem, and Carola-Bibiane Schönlieb. Solving inverse problems using data-driven models. *Acta Numerica*, 28:1–174, may 2019. doi:10.1017/s0962492919000059.
- [16] C. J. Bahr, W. M. Humphreys, D. Ernst, T. Ahlefeldt, C. Spehr, A. Pereira, Q. Leclère, C. Picard, R. Porteous, D. Moreau, J. R. Fischer, and C. J. Doolan. A comparison of microphone phased array methods applied to the study of airframe noise in wind-tunnel testing. In *23rd AIAA/CEAS Aeroacoustics Conference*, 2017. doi:10.2514/6.2017-3718.
- [17] Baohong Bai, Dakai Lin, and Xiaodong Li. Identification of flap side-edge two-source mechanism based on phased arrays. *AIAA J.*, 60(1):249–260, 2022. doi:10.2514/1.J060377.
- [18] J. Agustin Barrachina. Complex-valued neural networks (cvnn). *Zenodo*, January 2021. doi:10.5281/zenodo.4452131.
- [19] Daniel Blacodon. Array processing for noisy data: Application for open and closed wind-tunnels. *AIAA Journal*, 49(1):55–66, 2011. doi:10.2514/1.J050006.
- [20] Daniel Blacodon and Georges Elias. Level estimation of extended acoustic sources using a parametric method. *Journal of Aircraft*, 41(6):1360–1369, 2004. doi:10.2514/1.3053.
- [21] Ricardo J. G. B. Campello, Davoud Moulavi, and Joerg Sander. Density-based clustering based on hierarchical density estimates. In *Advances in Knowledge Discovery and Data Mining*. Springer Berlin Heidelberg, 2013. doi:10.1007/978-3-642-37456-2_14.
- [22] Nicolas Carion, Francisco Massa, Gabriel Synnaeve, Nicolas Usunier, Alexander Kirillov, and Sergey Zagoruyko. End-to-end object detection with transformers, 2020. doi:10.48550/ARXIV.2005.12872.
- [23] Paolo Castellini, Nicola Giulietti, Nicola Falcionelli, Aldo Franco Dragoni, and Paolo Chiariotti. A neural network based microphone array approach to grid-less noise source localization. *Applied Acoustics*, 177:107947, jun 2021. doi:10.1016/j.apacoust.2021.107947.
- [24] Gilles Chardon. Gridless beamforming: Theoretical analysis of one source case, and sparsity based methods for multiple sources. In *Berlin Beamforming Conference*, 2022. URL: www.bebec.eu/fileadmin/bebec/downloads/bebec-2022/papers/BeBeC-2022-D13.pdf.
- [25] Gilles Chardon. Theoretical analysis of beamforming steering vector formulations for acoustic source localization. *Journal of Sound and Vibration*, 517:116544, 2022. doi:10.1016/j.jsv.2021.116544.
- [26] Gilles Chardon. Gridless covariance matrix fitting methods for three dimensional acoustical source localization. *Journal of Sound and Vibration*, 551:117608, 2023. doi:<https://doi.org/10.1016/j.jsv.2023.117608>.
- [27] Gilles Chardon and Ulysse Boureau. Gridless three-dimensional compressive beamforming with the sliding frank-wolfe algorithm. *The Journal of the Acoustical Society of America*, 150(4):3139–3148, 2021. doi:10.1121/10.0006790.
- [28] Gilles Chardon, José Picheral, and François Ollivier. Theoretical analysis of the damas algorithm and efficient implementation of the covariance matrix fitting method for large-scale problems. *Journal of Sound and Vibration*, 508:116208, 2021. doi:<https://doi.org/10.1016/j.jsv.2021.116208>.
- [29] Yuejie Chi, Louis L. Scharf, Ali Pezeshki, and A. Robert Calderbank. Sensitivity to basis mismatch in compressed sensing. *IEEE Transactions on Signal Processing*, 59(5):2182–2195, may 2011. doi:10.1109/tsp.2011.2112650.

- [30] Jan Delfs. Basics of aeroacoustics, 2017. Accessed: 2023-07-27. URL: www.dlr.de/as/en/Portaldata/5/Resources/dokumente/abteilungen/abt_ta/2018/Notes_Basics_of_Aeroacoustics_Delfs.pdf.
- [31] W. Dobrzynski. Almost 40 years of airframe noise research: What did we achieve? *J. Aircr.*, 47(2):353–367, 2010. doi:10.2514/1.44457.
- [32] Werner Dobrzynski, Roland Ewert, Michael Pott-Pollenske, Michaela Herr, and Jan Delfs. Research at DLR towards airframe noise prediction and reduction. *Aerosp. Sci. Technol.*, 12(1):80–90, jan 2008. doi:10.1016/j.ast.2007.10.014.
- [33] Werner Dobrzynski and Michael Pott-Pollenske. Slat noise source studies for farfield noise prediction. In *7th AIAA/CEAS Aeroacoustics Conference and Exhibit*, volume 5805, 05 2001. doi:10.2514/6.2001-2158.
- [34] Bin Dong, Jérôme Antoni, Antonio Pereira, and Walter Kellermann. Blind separation of incoherent and spatially disjoint sound sources. *Journal of Sound and Vibration*, 383:414–445, 2016. doi:<https://doi.org/10.1016/j.jsv.2016.07.018>.
- [35] Bin Dong, Jérôme Antoni, and Erliang Zhang. Blind separation of sound sources from the principle of least spatial entropy. *Journal of Sound and Vibration*, 333(9):2643–2668, 2014. doi:10.1016/j.jsv.2013.12.011.
- [36] Robert P. Dougherty. Beamforming in acoustic testing. In *Aeroacoustic Measurements*, pages 62–97. Springer Berlin Heidelberg, 2002. doi:10.1007/978-3-662-05058-3_2.
- [37] Daniel Ernst. *Akustischer Kohärenzverlust in offenen Windkanälen aufgrund der turbulenten Scherschicht*. PhD thesis, Technische Universität Berlin, 2020. doi:10.14279/DEPOSITONCE-9712.
- [38] Daniel Ernst, Carsten Spehr, and Tobias Berkefeld. Decorrelation of acoustic wave propagation through the shear layer in open jet wind tunnel. In *21st AIAA/CEAS Aeroacoustics Conference*. American Institute of Aeronautics and Astronautics (AIAA), jun 2015. doi:10.2514/6.2015-2976.
- [39] F. Farassat, Mark Dunn, Ana Tinetti, and Douglas Nark. Open rotor noise prediction methods at nasa langley: A technology review. In *15th AIAA/CEAS Aeroacoustics Conference (30th AIAA Aeroacoustics Conference)*, 2009. doi:10.2514/6.2009-3133.
- [40] J. E. Ffowcs Williams and L. H. Hall. Aerodynamic sound generation by turbulent flow in the vicinity of a scattering half plane. *J. Fluid Mech.*, 40(4):657–670, 1970. doi:10.1017/S0022112070000368.
- [41] Antonio Filippone. Aircraft noise prediction. *Prog. Aerosp. Sci.*, 68:27–63, jul 2014. doi:10.1016/j.paerosci.2014.02.001.
- [42] World Health Organization. Regional Office for Europe. *Burden of disease from environmental noise: quantification of healthy life years lost in Europe*. World Health Organization. Regional Office for Europe, 2011. URL: <https://apps.who.int/iris/handle/10665/326424>.
- [43] H. P. Franz. The half-model technique in the wind tunnel and its employment in the development of the airbus family. *NASA Technical Reports*, 1982.
- [44] Stefan Funke, Alexander Skorpel, and Ulf Michel. An extended formulation of the SODIX method with application to aeroengine broadband noise. In *18th AIAA/CEAS Aeroacoustics Conference (33rd AIAA Aeroacoustics Conference)*. American Institute of Aeronautics and Astronautics, jun 2012. doi:10.2514/6.2012-2276.

- [45] Xavier Gloerfelt. Cavity noise. In *VKI lectures: Aerodynamic Noise from Wall-Bounded Flows*. Von Karman Institute, 2009.
- [46] A. Goudarzi, C. Spehr, and S. Herbold. Expert decision support system for aeroacoustic classification from deconvolved beamforming maps. In *AIAA Aviation*, 2020. doi:10.2514/6.2020-2610.
- [47] A. Goudarzi, C. Spehr, and S. Herbold. Automatic source localization and spectra generation from sparse beamforming maps. *J. Acoust. Soc. Am.*, 150(3):1866–1882, 2021. doi:10.1121/10.0005885.
- [48] A. Goudarzi, C. Spehr, and S. Herbold. Expert decision support system for aeroacoustic source type identification using clustering. *J. Acoust. Soc. Am.*, 151(2):1259–1276, 2022. doi:10.1121/10.0009322.
- [49] Armin Goudarzi. Temperature effects on aeroacoustics of a subsonic jet flow from an open pipe. Technical University of Berlin, 2018. doi:10.13140/RG.2.2.29429.42725.
- [50] Armin Goudarzi. Coherence based reflection coefficient estimation. In *DAGA - 46. Jahrestagung für Akustik*, 2020. URL: https://pub.dega-akustik.de/DAGA_2020/data/articles/000179.pdf.
- [51] Armin Goudarzi. Frequency domain beamforming using neuronal networks. In *Berlin Beamforming Conference*, 2022. URL: www.bebec.eu/fileadmin/bebec/downloads/bebec-2022/papers/BeBeC-2022-S02.pdf.
- [52] Armin Goudarzi. B-CLEAN-SC: CLEAN-SC for broadband sources. *JASA Express Letters*, 3(9):094804, 09 2023. doi:10.1121/10.0020992.
- [53] Armin Goudarzi. Global, and local optimization beamforming for broadband sources. *arXiv*, 2023. arXiv:2211.04921, doi:10.48550/arXiv.2211.04921.
- [54] Y. Guo. Slat noise modeling and prediction. *JSV*, 331(15):3567–3586, 2012. doi:10.1016/j.jsv.2012.03.016.
- [55] Y. P. Guo and M. C. Joshi. Noise characteristics of aircraft high lift systems. *AIAA J.*, 41(7):1247–1256, 2003. doi:10.2514/2.2093.
- [56] S. Haxter and C. Spehr. Infinite beamforming: Wavenumber decomposition of surface pressure fluctuations. In *Berlin Beamforming Conference*, February 2014. URL: www.bebec.eu/fileadmin/bebec/downloads/bebec-2014/papers/BeBeC-2014-04.pdf.
- [57] Stefan Haxter, Jens Brouwer, Jörn Sesterhenn, and Carsten Spehr. Obtaining phase velocity of turbulent boundary layer pressure fluctuations at high subsonic mach number from wind tunnel data affected by strong background noise. *Journal of Sound and Vibration*, 402:85 – 103, 2017. doi:10.1016/j.jsv.2017.05.011.
- [58] Stefan Haxter and Carsten Spehr. Two-dimensional evaluation of turbulent boundary layer pressure fluctuations at cruise flight conditions. In *18th AIAA/CEAS Aeroacoustics Conference (33rd AIAA Aeroacoustics Conference)*. American Institute of Aeronautics and Astronautics (AIAA), jun 2012. doi:10.2514/6.2012-2139.
- [59] Stefan Haxter and Carsten Spehr. Comparison of model predictions for coherence length to in-flight measurements at cruise conditions. *Journal of Sound and Vibration*, dec 2016. doi:10.1016/j.jsv.2016.10.038.
- [60] William Herkes and Robert Stoker. Wind tunnel measurements of the airframe noise of a high-speed civil transport. In *36th AIAA Aerospace Sciences Meeting and Exhibit*. American Institute of Aeronautics and Astronautics, jan 1998. doi:10.2514/6.1998-472.

- [61] Gert Herold and Ennes Sarradj. Performance analysis of microphone array methods. *Journal of Sound and Vibration*, 401:152–168, aug 2017. doi:10.1016/j.jsv.2017.04.030.
- [62] F. H.T. Himeno, D. S. Souza, F. R. Amaral, D. Rodríguez, and M. A.F. Medeiros. SPOD analysis of noise-generating rossiter modes in a slat with and without a bulb seal. *J. Fluid Mech.*, 915:A67, 2021. doi:10.1017/jfm.2021.93.
- [63] Thorsten Hohage, Hans-Georg Raumer, and Carsten Spehr. Uniqueness of an inverse source problem in experimental aeroacoustics. *Inverse Problems*, 36(7):075012, jul 2020. doi:10.1088/1361-6420/ab8484.
- [64] Kurt Hornik, Maxwell Stinchcombe, and Halbert White. Multilayer feedforward networks are universal approximators. *Neural Networks*, 2(5):359–366, jan 1989. doi:10.1016/0893-6080(89)90020-8.
- [65] M. S. Howe. On the generation of side-edge flap noise. *Journal of Sound and Vibration*, 80(4):555 – 573, 1982. doi:10.1016/0022-460X(82)90498-9.
- [66] M. S. Howe. *Hydrodynamics and Sound*. Cambridge University Press, 2007.
- [67] H.H. Hubbard. *Aeroacoustics of Flight Vehicles: Theory and Practice. Volume 1: Noise Sources*. Defense Technical Information Center, 1991. URL: <https://ntrs.nasa.gov/api/citations/19920001380/downloads/19920001380.pdf>.
- [68] Michael Kingan, Vincent Blandeau, Brian Tester, Phillip Joseph, and Anthony Parry. Relative importance of open rotor tone and broadband noise sources. In *17th AIAA/CEAS Aeroacoustics Conference (32nd AIAA Aeroacoustics Conference)*, 2011. doi:10.2514/6.2011-2763.
- [69] Stefan Kroeber, Marius Hellmold, and Lars Koop. Experimental investigation of spectral broadening of sound waves by wind tunnel shear layers. In *19th AIAA/CEAS Aeroacoustics Conference*. American Institute of Aeronautics and Astronautics, may 2013. doi:10.2514/6.2013-2255.
- [70] Adam Kujawski, Gert Herold, and Ennes Sarradj. A deep learning method for grid-free localization and quantification of sound sources. *The Journal of the Acoustical Society of America*, 146(3):EL225–EL231, sep 2019. doi:10.1121/1.5126020.
- [71] Adam Kujawski and Ennes Sarradj. Fast grid-free strength mapping of multiple sound sources from microphone array data using a transformer architecture. *The Journal of the Acoustical Society of America*, 152(5):2543–2556, nov 2022. doi:10.1121/10.0015005.
- [72] A. Lauterbach, K. Ehrenfried, S. Kröber, T. Ahlefeldt, and S. Loose. Microphone array measurements on high-speed trains in wind tunnels. In *Berlin Beamforming Conference*, February 2010. URL: www.bebec.eu/fileadmin/bebec/downloads/bebec-2010/papers/BeBeC-2010-01.pdf.
- [73] Q Leclère, A Pereira, C Bailly, J Antoni, and C Picard. A unified formalism for acoustic imaging based on microphone array measurements. *International Journal of Aeroacoustics*, 16(4-5):431–456, jul 2017. doi:10.1177/1475472x17718883.
- [74] Juho Lee, Yoonho Lee, Jungtaek Kim, Adam R. Kosiorek, Seungjin Choi, and Yee Whye Teh. Set transformer: A framework for attention-based permutation-invariant neural networks. In *International Conference on Machine Learning*. arXiv, 2018. doi:10.48550/ARXIV.1810.00825.
- [75] Soo Young Lee, Jiho Chang, and Seungchul Lee. Deep learning-based method for multiple sound source localization with high resolution and accuracy. *Mechanical Systems and Signal Processing*, 161:107959, dec 2021. doi:10.1016/j.ymsp.2021.107959.

- [76] Soo Young Lee, Jiho Chang, and Seungchul Lee. Deep learning-enabled high-resolution and fast sound source localization in spherical microphone array system. *IEEE Transactions on Instrumentation and Measurement*, 71:1–12, 2022. doi:10.1109/tim.2022.3161693.
- [77] Marius Lehmann, Daniel Ernst, Marc Schneider, Carsten Spehr, and Markus Lummer. Beamforming for measurements under disturbed propagation conditions using numerically calculated green's functions. *Journal of Sound and Vibration*, 520:116638, mar 2022. doi:10.1016/j.jsv.2021.116638.
- [78] Gaetano Licitra, Francesco Artuso, Marco Bernardini, Antonino Moro, Francesco Fidecaro, and Luca Fredianelli. Acoustic beamforming algorithms and their applications in environmental noise. *Current Pollution Reports*, 9(3):486–509, may 2023. doi:10.1007/s40726-023-00264-9.
- [79] M. J. Lighthill and M. H. A. Newman. On sound generated aerodynamically i. General theory. *Proc. Math. Phys. Eng. Sci. P ROY SOC A-MATH PHY*, 211(1107):564–587, 1952. doi:10.1098/rspa.1952.0060.
- [80] Michael James Lighthill. On sound generated aerodynamically II. turbulence as a source of sound. *Proceedings of the Royal Society of London. Series A. Mathematical and Physical Sciences*, 222(1148):1–32, feb 1954. doi:10.1098/rspa.1954.0049.
- [81] Francesco Locatello, Dirk Weissenborn, Thomas Unterthiner, Aravindh Mahendran, Georg Heigold, Jakob Uszkoreit, Alexey Dosovitskiy, and Thomas Kipf. Object-centric learning with slot attention, 2020. doi:10.48550/ARXIV.2006.15055.
- [82] Wei Ma and Xun Liu. Phased microphone array for sound source localization with deep learning. *Aerospace Systems*, 2(2):71–81, may 2019. doi:10.1007/s42401-019-00026-w.
- [83] Anwar M. N. Malgoezar, Mirjam Snellen, Roberto Merino-Martinez, Dick G. Simons, and Pieter Sijtsma. On the use of global optimization methods for acoustic source mapping. *The Journal of the Acoustical Society of America*, 141(1):453–465, jan 2017. doi:10.1121/1.4973915.
- [84] Leland McInnes, John Healy, and Steve Astels. hdbscan: Hierarchical density based clustering. *The Journal of Open Source Software*, 2(11), mar 2017. doi:10.21105/joss.00205.
- [85] Leland McInnes, John Healy, and James Melville. Umap: Uniform manifold approximation and projection for dimension reduction, 2020. arXiv:1802.03426.
- [86] R. Merino-Martínez, P. Sijtsma, A. Rubio Carpio, R. Zamponi, S. Luesutthiviboon, A. Malgoezar, M. Snellen, C. Schram, and D. Simons. Integration methods for distributed sound sources. *International Journal of Aeroacoustics*, 18:1475472X1985294, 06 2019. doi:10.1177/1475472X19852945.
- [87] R. Merino-Martínez, P. Sijtsma, M. Snellen, T. Ahlefeldt, J. Antoni, C. J. Bahr, D. Blacodon, D. Ernst, A. Finez, S. Funke, T. F. Geyer, S. Haxter, G. Herold, X. Huang, W. M. Humphreys, Q. Leclère, A. Malgoezar, U. Michel, T. Padois, A. Pereira, C. Picard, E. Sarradj, H. Siller, D. G. Simons, and C. Spehr. A review of acoustic imaging methods using phased microphone arrays. *CEAS Aeronautical Journal*, 10(1):197–230, Mar 2019. doi:10.1007/s13272-019-00383-4.
- [88] Roberto Merino-Martinez, Gert Herold, Mirjam Snellen, and Robert Dougherty. Assessment and comparison of the performance of functional projection beamforming for aeroacoustic measurements. In *Berlin Beamforming Conference*, 03 2020. URL: www.bebec.eu/fileadmin/bebec/downloads/bebec-2020/papers/BeBeC-2020-S07.pdf.
- [89] A. Michalke. On the effect of spatial source coherence on the radiation of jet noise. *Journal of Sound and Vibration*, 55(3):377–394, 1977. doi:https://doi.org/10.1016/S0022-460X(77)80020-5.

- [90] Ulf Michel. Influence of source interference on the directivity of jet mixing noise. In *13th AIAA/CEAS Aeroacoustics Conference (28th AIAA Aeroacoustics Conference)*. American Institute of Aeronautics and Astronautics, may 2007. doi:10.2514/6.2007-3648.
- [91] Ulf Michel. The role of source interference in jet noise. In *15th AIAA/CEAS Aeroacoustics Conference (30th AIAA Aeroacoustics Conference)*. American Institute of Aeronautics and Astronautics, may 2009. doi:10.2514/6.2009-3377.
- [92] Depuru Mohan, K. N., Peter Manovski, Reinhard Geisler, Janos Agocs, Thomas Ahlefeldt, Matteo Novara, Daniel Schanz, Stefan Haxter, Daniel Ernst, Carsten Spehr, and Andreas Schroeder. Aeroacoustic analysis of a mach 0.9 round jet using synchronized microphone array and shake-the-box 3d lagrangian particle tracking measurements. In *AIAA AVIATION Forum*. American Institute of Aeronautics and Astronautics, June 2017. doi:10.2514/6.2017-3862.
- [93] E.-A. Müller, editor. *Mechanics of Sound Generation in Flows*. IUTAM Symposia. Springer-Verlag Berlin Heidelberg, August 1979.
- [94] Attila Balázs Nagy, Jan Delfs, and Gareth J. Bennett. Aeroacoustics research in europe: The ceas-asc report on 2020 & 2021 highlights. *Journal of Sound and Vibration*, 534:117002, 2022. doi:https://doi.org/10.1016/j.jsv.2022.117002.
- [95] Arnold Neumaier. Complete search in continuous global optimization and constraint satisfaction. *Acta Numerica*, 13:271-369, 2004. doi:10.1017/S0962492904000194.
- [96] Stefan Oerlemans and Pieter Sijtsma. Acoustic array measurements of a 1:10.6 scaled airbus a340 model. In *10th AIAA/CEAS Aeroacoustics Conference*. American Institute of Aeronautics and Astronautics, may 2004. doi:10.2514/6.2004-2924.
- [97] Sebastian Oertwig, H. Siller, and Stefan Funke. Sodix for fully and partially coherent sound sources. In *Berlin Beamforming Conference*, 2022. URL: www.bebec.eu/fileadmin/bebec/downloads/bebec-2022/papers/BeBeC-2022-S10.pdf.
- [98] Roman Paryz. Upgrades at the NASA langley research center national transonic facility. In *50th AIAA Aerospace Sciences Meeting including the New Horizons Forum and Aerospace Exposition*. American Institute of Aeronautics and Astronautics, jan 2012. doi:10.2514/6.2012-102.
- [99] F. Pedregosa, G. Varoquaux, A. Gramfort, V. Michel, B. Thirion, O. Grisel, M. Blondel, P. Prettenhofer, R. Weiss, V. Dubourg, J. Vanderplas, A. Passos, D. Cournapeau, M. Brucher, M. Perrot, and E. Duchesnay. Scikit-learn: Machine learning in Python. *Journal of Machine Learning Research*, 12:2825-2830, 2011.
- [100] Junenette L. Peters, Christopher D. Zevitas, Susan Redline, Aaron Hastings, Natalia Sizov, Jaime E. Hart, Jonathan I. Levy, Christopher J. Roof, and Gregory A. Wellenius. Aviation noise and cardiovascular health in the united states: a review of the evidence and recommendations for research direction. *Curr. Epidemiol. Rep.*, 5(2):140-152, apr 2018. doi:10.1007/s40471-018-0151-2.
- [101] Wagner Gonçalves Pinto, Michaël Bauerheim, and Hélène Parisot-Dupuis. Deconvoluting acoustic beamforming maps with a deep neural network. *INTER-NOISE and NOISE-CON Congress and Conference Proceedings*, 263(1):5397-5408, aug 2021. doi:10.3397/in-2021-3084.
- [102] Ludwig Prandtl and O.G. Tietjens. *Applied hydro and aeromechanics*. Dover, 1957.
- [103] J. Quest. ETW - high quality test performance in cryogenic environment. *AIAA-2000-2260, 21st Aerodynamic Measurement Technology and Ground Testing Conference*, 2000. doi:10.2514/6.2000-2206.

- [104] D. Quinlan and M. Krane. Aeroacoustic source identification using frequency dependent velocity scaling. In *Aeroacoustics Conference*, State College, PA, USA, 1996. AIAA and CEAS. doi:10.2514/6.1996-1743.
- [105] Hans-Georg Raumer. *Analysis of an Inverse Source Problem with Correlation Data in Experimental Aeroacoustics*. PhD thesis, University of Göttingen, 08 2021. doi:10.53846/goediss-8783.
- [106] Hans-Georg Raumer, Carsten Spehr, Thorsten Hohage, and Daniel Ernst. Weighted data spaces for correlation-based array imaging in experimental aeroacoustics. *JSV*, 494:115878, mar 2021. doi:10.1016/j.jsv.2020.115878.
- [107] Ennes Sarradj. Three-dimensional acoustic source mapping with different beamforming steering vector formulations. *Advances in Acoustics and Vibration*, 2012:1–12, 2012. doi:10.1155/2012/292695.
- [108] Ennes Sarradj. Three-dimensional gridless source mapping using a signal subspace approach. In *Berlin Beamforming Conference*, 2022.
- [109] R. Schmidt. Multiple emitter location and signal parameter estimation. *IEEE Transactions on Antennas and Propagation*, 34(3):276–280, 1986. doi:10.1109/TAP.1986.1143830.
- [110] Christophe Schram and Gareth J. Bennett. Aeroacoustics research in europe: The ceas-asc report on 2022 highlights. *Journal of Sound and Vibration*, page 117895, 2023. doi:10.1016/j.jsv.2023.117895.
- [111] Gideon Schwarz. Estimating the dimension of a model. *The Annals of Statistics*, 6(2):461–464, 1978.
- [112] Bernhard Schölkopf, Alexander Smola, and Klaus-Robert Müller. Nonlinear component analysis as a kernel eigenvalue problem. *Neural Computation*, 10(5):1299–1319, 1998. doi:10.1162/089976698300017467.
- [113] P. Sijtsma. Experimental techniques for identification and characterisation of noise sources. Technical report, NLR, 2004. URL: <https://reports.nlr.nl/server/api/core/bitstreams/9108ade9-4d4a-4d4a-a979-ddec2ff3079f/content>.
- [114] P. Sijtsma. CLEAN based on spatial source coherence. *Int. J. Aeroacoustics*, 6:357–374, 2007. doi:10.1260/147547207783359459.
- [115] P. Sijtsma. Acoustic beamforming for the ranking of aircraft noise. Technical report, NLR, 2012. URL: <https://reports.nlr.nl/server/api/core/bitstreams/af7a34bb-38ad-403e-b331-9d9a82102771/content>.
- [116] Pieter Sijtsma, Roberto Merino-Martinez, Anwar MN Malgoezar, and Mirjam Snellen. High-resolution CLEAN-SC: Theory and experimental validation. *International Journal of Aeroacoustics*, 16(4-5):274–298, jul 2017. doi:10.1177/1475472x17713034.
- [117] Pieter Sijtsma, Stefan Oerlemans, Tim G. Tibbe, Tobias Berkefeld, and Carsten Spehr. Spectral broadening by shear layers of open jet wind tunnels. In *20th AIAA/CEAS Aeroacoustics Conference*. American Institute of Aeronautics and Astronautics (AIAA), 2014. doi:10.2514/6.2014-3178.
- [118] Simoudis. *Second International Conference on Knowledge Discovery & Data Mining*. AAAI Press, 1996.
- [119] Dale A. Smith, Antonio Filippone, and George N. Barakos. Noise source analysis in counter-rotating open rotors. *AIAA J.*, 60(3):1783–1796, 2022. doi:10.2514/1.J060886.

- [120] P.T. Soderman, F. Kafyeke, J. Boudreau, N.J. Burnside, S.M. Jaeger, and R. Chandrasekharan. Airframe noise study of a bombardier CRJ-700 aircraft model in the NASA Ames 7-by 10-foot wind tunnel. *Int. J. Aeroacoustics*, 3(1):1–42, 2004. doi:10.1260/147547204323022248.
- [121] P.T. Soderman, F. Kafyeke, J. Boudreau, N.J. Burnside, S.M. Jaeger, and R. Chandrasekharan. Airframe noise study of a bombardier CRJ-700 aircraft model in the NASA ames 7-by 10-foot wind tunnel. *Int. J. Aeroacoustics*, 3(1):1–42, jan 2004. doi:10.1260/147547204323022248.
- [122] A. Sommerfeld. Die greensche funktion der schwingungsgleichung. *Jahresbericht der Deutschen Mathematiker-Vereinigung*, 21:309–352, 1912.
- [123] C. Spehr and T. Ahlefeldt. Comparison of microphone array measurements in the closed test section of LSWT and ETW. *CEAS Aeronaut*, 10(1):267–285, 2019. doi:10.1007/s13272-019-00386-1.
- [124] Robert Stoker, Yueping Guo, Craig Streett, and Nathan Burnside. Airframe noise source locations of a 777 aircraft in flight and comparisons with past model-scale tests. In *9th AIAA/CEAS Aeroacoustics Conference and Exhibit*, page 3232, 2003. doi:10.2514/6.2003-3232.
- [125] Takao Suzuki. L1 generalized inverse beam-forming algorithm resolving coherent/incoherent, distributed and multipole sources. *Journal of Sound and Vibration*, 330(24):5835–5851, nov 2011. doi:10.1016/j.jsv.2011.05.021.
- [126] M. Terracol, E. Manoha, C. Herrero, E. Labourasse, S. Redonnet, and P. Sagaut. Hybrid methods for airframe noise numerical prediction. *Theor. Comput. Fluid Dyn.*, 19(3):197–227, jun 2005. doi:10.1007/s00162-005-0165-5.
- [127] M. Terracol, E. Manoha, and B. Lemoine. Investigation of the unsteady flow and noise generation in a slat cove. *AIAA J.*, 54(2):469–489, 2016. doi:10.2514/1.J053479.
- [128] Robert L. Thorndike. Who belongs in the family. *Psychometrika*, pages 267–276, 1953.
- [129] James R. Underbrink. Aeroacoustic phased array testing in low speed wind tunnels. In Thomas J. Mueller, editor, *Aeroacoustic Measurements*, pages 98–217. Springer Berlin Heidelberg, Berlin, Heidelberg, 2002. doi:10.1007/978-3-662-05058-3_3.
- [130] M.C. Vanderveen, B.C. Ng, C.B. Papadias, and A. Paulraj. Joint angle and delay estimation (JADE) for signals in multipath environments. In *Conference Record of The Thirtieth Asilomar Conference on Signals, Systems and Computers*, volume 2, pages 1250–1254. IEEE Comput. Soc. Press, 1996. doi:10.1109/acssc.1996.599145.
- [131] P. Virtanen, R. Gommers, T. E. Oliphant, M. Haberland, T. Reddy, D. Cournapeau, E. Burrowski, P. Peterson, W. Weckesser, J. Bright, S. J. van der Walt, M. Brett, J. Wilson, K. J. Millman, N. Mayorov, A. R. J. Nelson, E. Jones, R. Kern, E. Larson, C. J. Carey, Í. Polat, Yu Feng, E. W. Moore, J. VanderPlas, D. Laxalde, J. Perktold, R. Cimrman, I. Henriksen, E. A. Quintero, C. R. Harris, A. M. Archibald, A. H. Ribeiro, F. Pedregosa, P. van Mulbregt, and SciPy 1.0 Contributors. SciPy 1.0: Fundamental Algorithms for Scientific Computing in Python. *Nature Methods*, 17:261–272, 2020. doi:10.1038/s41592-019-0686-2.
- [132] Bieke von den Hoff, Roberto Merino-Martínez, Dick G. Simons, and Mirjam Snellen. Using global optimization methods for three-dimensional localization and quantification of incoherent acoustic sources. *JASA Express Letters*, 2(5):054802, may 2022. doi:10.1121/10.0010456.
- [133] J. E. Ffowcs Williams and L. H. Hall. Aerodynamic sound generation by turbulent flow in the vicinity of a scattering half plane. *Journal of Fluid Mechanics*, 40(4):657–670, 1970. doi:10.1017/S0022112070000368.

-
- [134] World Health Organization. Regional Office for Europe. *Environmental noise guidelines for the European Region*. World Health Organization, 2020. doi:10.2800/686249.
- [135] Pengwei Xu, Elias J. G. Arcondoulis, and Yu Liu. Deep neural network models for acoustic source localization. In *Berlin Beamforming Conference*, 2021. URL: www.bebec.eu/fileadmin/bebec/downloads/bebec-2020/papers/BeBeC-2020-D21.pdf.
- [136] Tarik Yardibi, Jian Li, Petre Stoica, Nikolas S. Zawodny, and Louis N. Cattafesta. A covariance fitting approach for correlated acoustic source mapping. *The Journal of the Acoustical Society of America*, 127(5):2920–2931, 2010. doi:10.1121/1.3365260.
- [137] Manzil Zaheer, Satwik Kottur, Siamak Ravanbakhsh, Barnabas Poczos, Ruslan Salakhutdinov, and Alexander Smola. Deep sets, 2017. doi:10.48550/ARXIV.1703.06114.
- [138] P.A.G. Zavala, W. De Roeck, K. Janssens, J.R.F. Arruda, P. Sas, and W. Desmet. Generalized inverse beamforming with optimized regularization strategy. *Mechanical Systems and Signal Processing*, 25(3):928–939, apr 2011. doi:10.1016/j.ymssp.2010.09.012.
- [139] M. M. Zdravkovich. *Flow around circular cylinders*, volume 1. Oxford university press, 1997.
- [140] Erliang Zhang, Jérôme Antoni, Bin Dong, and Hichem Snoussi. Bayesian space-frequency separation of wide-band sound sources by a hierarchical approach. *The Journal of the Acoustical Society of America*, 132(5):3240–3250, 2012. doi:10.1121/1.4754530.

List of Figures

2.1	Conditioning of the propagation matrix	18
2.2	Outcome of different clustering methods	20
3.1	Generic monopole experimental setup	24
3.2	Monopole assumption error	25
3.3	Do728 model photo	25
3.4	A320 model photo	26
3.5	Embraer model photo	27
4.1	Comparison of the steering vectors	32
4.2	Partially coherent monopole line sources	34
4.3	Partially coherent dipole line sources	35
4.4	Compact source CLEAN-SC solution	37
4.5	Line source with $L_C = 0$ (incoherent) CLEAN-SC solution	38
4.6	Line source with $L_C = \infty$ (coherent) CLEAN-SC solution	38
4.7	Line source with $L_C = 3$ (partially coherent) CLEAN-SC solution	39
4.8	Embraer DP 1, 2, and 3 CLEAN-SC beamforming maps	40
4.9	Embraer spatially integrated spectra	41
4.10	B-CLEAN-SC case 1) results	43
4.11	B-CLEAN-SC case 2) results	44
4.12	B-CLEAN-SC case 3) results	45
4.13	GO (x_1, q) energy map for case 1a)	48
4.14	GO (x_1, q) energy map for case 1b)	49
4.15	GO (x_1, x_2) energy map for case 1a)	49
4.16	GO (x_1, x_2) energy map for case 1b)	50
4.17	GO energy map for case 2a)	50
4.18	GO energy map for case 2b)	51
4.19	GO smallband and broadband energy for case 2c)	51
4.20	CLEAN-SC results for case 3) and 4)	53
4.21	Standard GO results for case 3) and 4)	54
4.22	Broadband GO results for case 3) and 4)	55
4.23	CLEAN-SC results for case 5)	56
4.24	Standard GO results for case 5)	56
4.25	Broadband GO results for case 5)	57
4.26	Broadband LO results for case 5)	58
4.27	Broadband LO results for case 6)	59
4.28	Error metric for baseline model, one source	63
4.29	Error metric for baseline model, five sources	64
4.30	Error metrics for an increasing number of microphones	64
4.31	Error metrics for an increasing number of focus points	65
4.32	Error metrics of section 4.6.2 for the different models	66
4.33	Gridless ANN beamforming architecture	67
4.34	Perm. inv. ANN, case 1) with $N_S = 1$, positional estimation	71
4.35	Perm. inv. ANN, case 1) with $N_S = 1$, SSD	72

4.36 Perm. inv. ANN, case 2) with $N_S = 3$, regression metrics over SSR	72
4.37 Perm. inv. ANN, correct estimations	73
4.38 Perm. inv. ANN, case 3) with $N_S \leq 3$, positional estimation	74
4.39 Perm. inv. ANN, case 3) with $N_S \leq 3$, classification metrics over SSR	75
5.1 Embraer manual ROI definition	78
5.2 Embraer ROI spectra	79
5.3 A320, CLEAN-SC result, 2D & frequency	79
5.4 Do728, CLEAN-SC result, 2D & frequency	81
5.5 A320, 2D CLEAN-SC result	81
5.6 Do728, flap side edge region	83
5.7 A320, SIND solution	84
5.8 Do728, SIND solution	85
5.9 A320, SIND estimation in upstream flap side edge region	86
5.10 A320, SIND estimation in downstream flap side edge region	87
5.11 Do728, SIND estimation in upstream flap side edge region	87
5.12 Do728, SIND estimation in downstream flap side edge region	88
5.13 Do728, SIND estimation in slat region	88
5.14 A320, beamforming map stretch and shift parameters	89
5.15 A320, SIHC result	90
5.16 Do728, SIHC result	91
5.17 A320, comparison of SIND & SIHC at the flap side edge	92
5.18 Do728, comparison of SIND & SIHC at the flap side edge	92
5.19 Do728, comparison of SIND & SIHC at the slat	92
5.20 A320, Mach power scaling of the leading flap side edge SIND result	93
5.21 A320, Mach power scaling of the trailing flap side edge SIND result	93
5.22 Do728, Mach power scaling of the slat SIHC result	94
5.23 Do728, Mach power scaling of the slat track SIHC result	94
5.24 Do728 3D histogram	96
5.25 Do728 SIND 3D exemplary source	96
5.26 Generic data, CLEAN-SC error	97
5.27 Generic speaker 2D CLEAN-SC result	98
5.28 SIND & SIHC PSD errors and SNR over frequency	98
5.29 Histogram of PSD bins not reconstructed by SIND & SIHC	99
6.1 Expert Decision Support System workflow	102
6.2 Do728, normalized source type spectra	104
6.3 A320, Reynolds number effect on source emission	106
6.4 Do728, $Re = 1.4 \times 10^6$, sources at $\alpha = 3^\circ$	108
6.5 Do728, $Re = 1.4 \times 10^6$, sources at $\alpha = 7^\circ$	108
6.6 A320, $Re = 1.4 \times 10^6$, sources at $\alpha = 3^\circ$	109
6.7 A320, $Re = 1.4 \times 10^6$, sources at $\alpha = 7^\circ$	109
6.8 Embraer ROI and spectra result	110
6.9 Do728 modified Strouhal number for slat tones	114
6.10 Do728 Mach power scaling for slat / track sources	115
6.11 Do728 tone detection on slat tones	116
6.12 Do728, spatial movement of sources over Mach number	118
6.13 Comparison of Do728 and A320 features	120
6.14 Do728 feature correlation heatmap	121
6.15 Do728 UMAP feature projection	123
6.16 Do728, resulting cluster number based on the minimum sample	124
6.17 Do728, cluster tree	124
6.18 Do728, mean clustering confidence per label and cluster	125

6.19	Do728, clustering result	126
6.20	Do728, soft cluster confidences of the Krüger slat	126
6.21	Do728 clustering confusion matrix	127
6.22	Do728, histogram of clustering accuracy	128
6.23	A320 clustering confusion matrix	129

List of Tables

3.1	Do728 flow configurations	26
3.2	A320 flow configurations	26
3.3	Embraer flow configurations	28
4.1	Influence of frequency interval size on B-CLEAN-SC	43
4.2	GO cases	48
4.3	Multipole parameters for GO problem	59
4.4	Overview of ANN beamforming research	60
4.5	ANN architectures for benchmark	66
4.6	Perm. inv. ANN, regression metrics	71
4.7	Perm. inv. ANN, variation of sources, regression metrics	73
4.8	Perm. inv. ANN, variation of microphones, regression metrics	73
4.9	Perm. inv. ANN, variation of dropout, regression metrics	74
4.10	Perm. inv. ANN, with and without classification, regression metrics	74
4.11	Perm. inv. ANN, case 3), TP & FN regression metrics	75
5.1	SIND & SIHC parameters	86
5.2	SIND & SIHC errors	98
6.1	Frequency and Mach scaling exponents for Figure 6.2	103
6.2	Do728 modification exponents	108
6.3	Do728 modification exponents	109
6.4	Embraer modification exponents	110
6.5	Aeroacoustic properties and corresponding features	112

Alphabetical Index

A

Artificial Neuronal Network 18, 60–68, 72, 75, 134–136

B

B-CLEAN-SC 39–46, 74, 132, 133, 145
 Beamforming 18, 26–36, 38, 39, 42, 43, 46, 47, 52, 53, 55, 57, 59–62, 66, 71, 77–84, 88, 89, 93, 95, 97, 99, 101–103, 107, 112, 125, 131–144

C

Classification 55, 61, 62, 64, 65, 86, 89, 101, 134–136, 140, 143
 CLEAN-SC 36–42, 44–46, 52–57, 78–82, 84, 87, 95, 97–100, 107, 110, 112, 114, 131–133, 137–139, 141, 142, 146
 Clustering 19, 84, 89, 101, 102, 107, 111, 121, 122, 124, 127–129, 137–139, 143, 144
 Coherence 14–17, 29, 30, 34–36, 38, 39, 42, 52, 58, 134, 142, 143
 CRAFT 125, 127, 129, 140, 143, 144

D

Deconvolution 36, 43, 78, 80, 114
 Dipole 7, 9, 10, 12–14, 29, 34–36, 46, 52, 58, 59, 107, 120, 133, 134, 136, 145, 146

F

Feature 77, 84, 101, 103, 111–113, 115–117, 119–123, 140–145
 Space 101, 122, 123, 140, 143
 Ffowcs-Williams and Hawkings 9, 11
 Flap 81, 106
 Gap 105, 106, 129
 Side Edge 80–83, 86–93, 104–109, 119–123, 128, 132, 137, 138, 141, 142, 144, 145
 Tone 104, 105
 Track 104–106, 108, 109, 137, 138, 145, 146

G

Generalized frequency 11, 12, 108–110
 Exponent 103, 109, 113, 120, 122, 143
 Global Optimization 39, 46–48, 50, 52–58, 133–136

H

HDBSCAN 89–91, 127, 137, 143, 144

L

Lighthill 8, 9, 11
 Local Optimization 57–59, 133, 134

M

Monopole 7, 10, 12, 13, 17, 23–25, 31, 34–37, 46, 48, 49, 52, 53, 55, 57–60, 63, 67, 99, 107, 120, 131, 132, 135, 139
 monopole 9

N

Nacelle 81, 95, 104, 105, 108, 109, 129, 137, 138, 144–146

R

Region Of Interest 53–56, 77–79, 81, 86, 90, 101, 103, 108, 110, 132, 138, 140
 Regression 61–64, 112, 114, 115, 118–120, 122, 134–136, 142

S

Self-similarity 10, 29, 78, 90, 91, 93, 103, 107, 111–114, 119, 120, 122, 140–143
 SIHC 86, 90–94, 97–99, 137–139, 141
 SIND 57, 84–86, 88–93, 97–99, 103, 106, 107, 117, 122, 125, 133, 136–139, 141
 Slat 80, 81, 87, 88, 90–92, 94, 103–107, 113, 115, 119, 120, 122, 123, 128, 129, 136–139, 141, 143–145
 Cove 107–109, 140, 141, 143, 145, 146
 Resonance 104, 106, 119, 122, 128, 144
 Side Edge 82, 104, 105, 107–109, 123, 129, 138, 145
 Tone 91, 92, 102, 104–109, 114, 116, 119, 120, 122, 123, 141, 143, 144
 Track 81, 82, 87–92, 94, 103–109, 115, 119, 122, 123, 128, 129, 132, 137, 138, 140, 142–146
 Steering vector 29–36, 42, 53, 55, 82, 95, 131–133, 138
 Strake 78, 88, 90, 104–109, 119, 122, 137, 138, 141, 142, 144–146
 Tone 104–106, 119, 120, 122

W

Wind tunnel 23, 24, 29, 58, 77, 78, 90, 99, 101, 102, 104, 105, 132, 136–138, 141
 Wing 41, 77, 90, 95, 105, 107, 110, 131, 138, 145
 Tip 90, 104, 105, 107, 108, 123, 129, 137, 138, 145